



Habilitation à Diriger des Recherches

Neutrinos and applications : an oscillating trip

J-E.MARTEAU

Institut de Physique Nucléaire de Lyon
Université de Lyon UCBL – CNRS/IN2P3

marteau@ipnl.in2p3.fr

Soutenue le 03 mars 2015 à l'IPNL

Jury : G.Chanfray, P.U., UCBL, *président*
Y.Déclais, D.R., IPNL
O.Drapier, D.R., LLR, *rapporteur*
H.Pessard, D.R., LAPP, *rapporteur*
D.Gibert, P.CNAP, GR, *rapporteur*



Table des matières

| | |
|--|------------|
| Motivations | 5 |
| I Physique nucléaire théorique | 13 |
| 1 Effets nucléaires dans les interactions neutrino-matière | 17 |
| 1.1 Introduction aux mécanismes de réponses nucléaires | 17 |
| 1.2 Effects of the Nuclear Correlations on the Neutrino-Oxygen Interactions [1] | 24 |
| 1.3 A unified approach for nucleon knock-out, coherent and incoherent pion production in neutrino interactions with nuclei [9] | 38 |
| 1.4 Neutrino and antineutrino quasielastic interactions with nuclei [10] | 59 |
| 2 Restauration de la symétrie chirale | 65 |
| 2.1 Introduction | 65 |
| 2.2 Pion scalar density and chiral symmetry restoration at finite temperature and density [4] | 66 |
| Bibliographie Partie I | 79 |
| II Physique expérimentale des oscillations de neutrinos | 81 |
| 1 Introduction aux oscillations de neutrinos | 85 |
| 2 Expérience de première génération : OPERA et le programme CNGS | 91 |
| 2.1 Introduction | 91 |
| 2.2 OPERA first events from the CNGS neutrino beam, [12] | 93 |
| 2.3 The OPERA global readout and GPS distribution system, [11] | 100 |
| 2.4 Evidence for $\nu_\mu \rightarrow \nu_\tau$ appearance in the CNGS neutrino beam with the OPERA experiment, [26] | 102 |
| 2.5 Cosmic ray physics with the OPERA detector, [14] | 109 |
| 3 Les générations futures : T2K et au-delà | 115 |
| 3.1 Introduction | 115 |
| 3.2 Indication of Electron Neutrino Appearance from an Accelerator-produced Off-axis Muon Neutrino Beam, [31] | 118 |
| 3.3 LBNO-DEMO : Large-scale neutrino detector demonstrators for phased performance assessment in view of a long-baseline oscillation experiment, [54] | 129 |
| 3.3.1 Design concept of the $6 \times 6 \times 6\text{m}^3$ prototype | 129 |
| 3.3.2 Front-end and DAQ readout | 131 |

| | |
|---|------------|
| Bibliographie Partie II | 139 |
| | |
| III Applications transdisciplinaires | 143 |
| | |
| 1 Imagerie médicale : un prototype de tomographe à émission de positrons TEP | 147 |
| 1.1 Introduction | 147 |
| 1.2 From high energy physics large scale distributed optoelectronics readout to medical imaging applications : prototyping a 2-head readout system for micro-PET | 150 |
| | |
| 2 Tomographie muonique de structures géologiques | 171 |
| 2.1 Introduction | 171 |
| 2.2 Geophysical muon imaging : feasibility and limits, [6] | 174 |
| 2.3 Muons tomography applied to geosciences and volcanology, [7] | 188 |
| 2.4 Implementation of sub-nanoseconds TDC in FPGA : applications to time-of-flight analysis in muon radiography, [14] | 197 |
| 2.5 Muon tomography and gravimetry joint inversion, [15] | 215 |
| | |
| Bibliographie Partie III | 235 |
| | |
| Conclusions | 237 |

Motivations

Introduction : de la thèse à OPERA — Mes activités de recherche se situent dans le domaine de la physique des particules, physique des hautes énergies (*High Energy Physics*, *HEP*) et de ses applications transdisciplinaires à l'imagerie médicale puis à l'imagerie de structures géologiques. Plus spécifiquement j'ai débuté en 1996 par une thèse en physique nucléaire théorique sur les interactions des neutrinos avec la matière, puis j'ai été recruté en 1999 sur un poste de maître de conférences expérimentateur en physique des neutrinos. Ce champ d'activités est alors totalement neuf à l'IPNL et après quelques hésitations liées à la méconnaissance des oscillations de neutrinos (dont la découverte n'est annoncée officiellement qu'en 1998...) le groupe s'engage résolument à partir de 2000 dans le programme européen CNGS (*CERN Neutrinos to Gran Sasso*) au sein de la collaboration OPERA (*Oscillation Physics with Emulsion tRacking Apparatus*). Je suis d'ailleurs l'un des éditeurs du *proposal* de l'expérience. Mes activités et mes responsabilités au sein de cette collaboration (notamment celle de *project leader* de l'acquisition de données que j'endosse dès le démarrage du projet) ont pris fin en décembre 2012 lorsque les derniers neutrinos sont émis par le CNGS.

C'est principalement l'arrêt de l'expérience OPERA – un projet de longue haleine proposé en 1999 dans une lettre d'intention, dont les premiers boulons seront vissés en 2003 au Gran Sasso, qui recevra ses premiers neutrinos en 2006 et qui publiera ses premiers retours de physique à partir de 2010 –, qui a motivé la présentation de cette HDR, comme une opportunité de faire un retour et un bilan sur mes activités de recherche, menées parallèlement aux enseignements, ces derniers étant loin d'être réduits à la portion congrue.

La participation de l'IPNL à OPERA prenant fin officiellement en décembre 2013, je peux à présent dégager un temps raisonnable à la valorisation de l'expérience que j'ai acquise dans différents domaines, au sein de collaborations nationales et internationales traitant de sujets allant de la théorie aux applications en imagerie en passant par la physique fondamentale.

Ayant participé à l'encadrement de plusieurs étudiants en thèse dans le cadre d'OPERA (dont un étudiant en responsabilité complète) puis du projet Diaphane (voir plus bas) avec deux étudiants en co-responsabilité, il m'est aussi apparu important de pouvoir fixer un cadre officiel à cette part importante du travail de chercheur.

Les neutrinos encore — Mais OPERA n'est pas l'unique motivation, car au fur et à mesure que l'horizon s'est dégagé quant à la faisabilité de ce projet et la réussite de mes engagements au sein de cette collaboration, que les connaissances de la physique des neutrinos se sont affinées, il est devenu possible, voire souhaitable, de participer à d'autres programmes expérimentaux d'envergure internationale de recherche et de caractérisation des oscillations de neutrinos sur et hors accélérateurs. C'est ainsi qu'à partir de 2008 je me suis engagé, avec le groupe "Neutrinos" de l'IPNL, dans la collaboration T2K (*Tokai To Kamioka*) au Japon et suivi à partir de 2010, date de publication du premier ν_τ observé dans OPERA, les développements du *design study* européen LAGUNA (*Large*

Apparatus studying Grand Unification and Neutrino Astrophysics) puis LBNO (*Long Baseline Neutrino Oscillation*).

Cette extension du spectre de la physique des neutrinos suit la pente naturelle de la compréhension globale du mécanisme des oscillations de neutrinos. Après l'époque pionnière jalonnée d'"anomalies" à la fin de laquelle s'inscrit mon travail de thèse, on passe à la première génération d'expérience de confirmation du mécanisme sur faisceau (K2K au Japon, MINOS aux Etats-Unis, OPERA en Europe). Cette génération d'expériences va s'intéresser à la mise en évidence des oscillations de neutrinos dans le secteur atmosphérique par la mesure de l'oscillation $\nu_\mu \rightarrow \nu_\mu$. La seconde génération d'expériences d'oscillations, T2K au Japon, NOvA aux Etats-Unis, se concentre sur la métrologie fine des paramètres déjà mis en évidence et cherchent les limites de l'angle θ_{13} . En 2012 la mesure de cet angle, à la fois par les expériences réacteurs (Daya Bay en Chine, RENO en Corée, Double Chooz en France) et par T2K, précise le cadre pour les futures expériences de neutrinos (LBNO en Europe, LBNF aux Etats-Unis, Hyper-Kamiokande au Japon) : il s'agit de mesurer la hiérarchie de masses des neutrinos et d'étudier l'existence éventuelle de la violation CP dans le secteur leptonique.

... Et beyond — Mes motivations pour présenter l'H.D.R aujourd'hui sont donc essentiellement liées à la volonté de faire un bilan des diverses activités sur lesquelles je me suis engagé jusqu'ici. Comme indiqué dans le paragraphe précédent, j'ai assumé de lourdes responsabilités, notamment "hardware" au sein de nombreux projets depuis le premier projet expérimental, OPERA, auquel j'ai participé. On a tendance à penser que les neutrinos représentent actuellement pratiquement l'unique fenêtre permettant de voir au-delà du Modèle Standard de la physique des particules (*physics beyond the Standard Model*). Cette fenêtre est motivée notamment par la nécessité d'adapter le mécanisme de génération des masses pour intégrer les neutrinos dans le tableau.

A titre personnel j'ai eu l'opportunité de pouvoir valoriser les développements instrumentaux en opto-électronique et dans le domaine de l'acquisition de données (DAQ) distribuée sur réseau motivés initialement pour les projets neutrinos. Ces développements ont permis de tisser des liens *au-delà* du domaine de la physique des particules. Ainsi j'ai participé à une possible application dans le domaine de l'imagerie médicale par tomographie par émission de positrons (*Positron Emission Tomography, PET*) pour le petit animal au sein de la collaboration ClearPET du consortium *Crystal Clear*. Mais c'est surtout dans le domaine des géosciences que les applications transdisciplinaires trouvent leur meilleur terrain de jeu, puisque depuis 2008 je co-dirige la collaboration Diaphane (CNRS/IN2P3-INSU et Universités de Lyon/Rennes/Paris). Cette collaboration a pour but de réaliser la tomographie par muons cosmiques de structures d'intérêt géologique, telles que des volcans actifs ou des sites souterrains candidats au stockage de longue durée. Le principe de la tomographie est simple (c'est essentiellement celui de la radiographie clinique) puisque l'on réalise une densitométrie de contraste par mesure de l'atténuation du flux de muons cosmiques à travers la structure considérée. L'expérience acquise sur différents terrains nous a permis de mieux comprendre les sources de bruit de fond, de mettre en oeuvre plusieurs techniques innovantes (par exemple la réjection du flux arrière de particules par mesure du temps de vol grâce à un vernier temporel embarqué dans un FPGA) et d'enrichir les domaines d'applications (de la simple radiographie statique au suivi temporel du système hydrothermal d'un volcan actif). Cette activité débouche sur une physique riche (problème inverse élaboré, instrumentation, imagerie 3D ou imagerie couplée) et sur de possibles applications industrielles dans le génie civil. Elle a obtenu le soutien de l'ANR pour la période 2014-2018.

Résumé de carrière — Élève au lycée Louis-le-Grand de 1991 à 1993, puis élève normalien (ENSL) de 1993 à 1997, j'obtiens en 1995 le DEA de Physique Théorique rhône-alpin, l'agrégation de physique en 1996 et démarre une thèse la même année sous la direction de J.Delorme à l'IPNL,

au sein du groupe “théorie”, sur l’étude des interactions neutrinos-noyaux. Je soutiens ma thèse, “De l’effet des interactions nucléaires dans les réactions de neutrinos sur des cibles d’oxygène et de son rôle dans l’anomalie des neutrinos atmosphériques”, en décembre 1998, mention très honorable avec les félicitations du jury et entame une conversion thématique vers la physique des neutrinos expérimentale, les développements opto-électroniques pour des détecteurs à scintillateurs, l’acquisition et l’analyse de données, au sein du groupe “neutrinos” nouvellement formé à l’IPNL par Y.Déclais. Je suis recruté en septembre 1999 sur un poste de maître de conférences de physicien des neutrinos expérimentateur.

Mon étude sur les interactions neutrinos-noyaux est récompensée par le prix jeune chercheur de la ville de Lyon en 2000.

De 1999 à 2001 l’activité du groupe se concentre sur des développements génériques associés à la physique des neutrinos, puis rejoint en 2001 la collaboration OPERA (Oscillation Project with Emulsions tRacking Apparatus) qui vise à étudier les oscillations des neutrinos entre le CERN (Suisse) et le laboratoire souterrain du Gran Sasso (Italie), soit sur une distance de vol de 730km. Après une restructuration notable du groupe en 2002, je deviens responsable de projet en charge du développement, de l’implantation et de l’exploitation du système d’acquisition de données pour la collaboration OPERA. J’occuperai cette charge jusqu’à fin 2013, date de sortie officielle de l’IPNL de la collaboration. En 2010 nous publions avec OPERA l’observation du premier événement candidat d’une oscillation de neutrinos (première mondiale). En parallèle je participe de 2001 à 2004 à un développement transdisciplinaire dans le domaine de l’imagerie médicale : tomographie par émission de positrons appliquée au petit animal. Ce développement se fait au sein de la collaboration ClearPET du consortium international Crystal Clear. En 2004, nous réalisons la seule mesure au monde de coïncidence en configuration dite “phoswich”. En 2006 je profite d’une délégation CNRS pour passer une année complète en Italie, dans les Abruzzes, pour le montage et le *commissioning* de l’expérience OPERA. Cette expérience riche m’a permis de connaître dans le détail l’ensemble du détecteur et d’initier plusieurs analyses de physique “hors-cadre” (détection des oscillations de neutrinos atmosphériques par mesure du temps de vol, thèse de T.Brugière).

En 2008, le groupe “neutrinos” rejoint officiellement la collaboration T2K (Tokai To Kamioka) au Japon, expérience d’oscillations des neutrinos de seconde génération. Etant encore engagé dans OPERA, il s’agit d’une participation limitée à la mise en place d’un détecteur mesurant la composante basse énergie du flux des neutrinos en position proche et à la contribution aux “shifts” de prise de données. En 2012 nous publions avec T2K la mise en évidence des oscillations de neutrinos dans le canal $\nu_\mu \rightarrow \nu_e$, la mesure du paramètre θ_{13} (première mondiale sur accélérateur). Cette implication sur T2K est prolongée à partir de 2010 par un engagement progressif dans les *design study* européens LAGUNA et LBNO.

En 2008 je participe au lancement avec D.Gibert, géophysicien (IPG Paris et Géosciences Rennes), du projet DIAPHANE dont le but est de réaliser la radiographie de structures géologiques (volcans actifs, sites souterrains etc) en mesurant l’atténuation du flux de muons cosmiques. Ce projet voit le jour comme un volet de l’ANR DOMOSCAN. J’assume la responsabilité de la conception et réalisation du détecteur, du système d’acquisition et de l’analyse de données. Le détecteur proposé, bénéficiant de la R&D effectuée pour OPERA, permet d’être opérationnel rapidement. En 2009 nous installons le premier détecteur dans le laboratoire souterrain du Mont-Terri (St-Ursanne, Suisse). Le but est d’effectuer des mesures sur des couches géologiques de densité différente et bien “calibrées”. Le détecteur sera déplacé en différents points de mesures dans le laboratoire souterrain de 2009 jusqu’à fin 2014. Il a permis de nombreux développements méthodologiques et notamment une étude originale de mesure couplée gravimétrie-muons. En 2010 nous réalisons les premières radio-

graphies sur des volcans actifs : le cratère sud de l'Etna (Sicile, Italie) en collaboration avec l'INGV (*Istituto Nazionale di Geofisica e Vulcanologia*, sezione de Catania) et la soufrière de Guadeloupe (Antilles) en collaboration avec l'OVSF (Observatoire de Volcanologie et de Sismologie de Guadeloupe) et le parc national de la Guadeloupe. Une collaboration voit le jour en 2013 avec le laboratoire EOS (*Earth Observatory of Singapore*) pour l'installation d'un détecteur sur le Mayon aux Philippines. Une autre collaboration est établie avec l'IRSN pour installer un détecteur dans le laboratoire souterrain de Tournemire (Aveyron) en France. Il s'agit là encore d'étudier la géologie locale et de comparer la tomographie muons avec les autres méthodes géophysiques (tomographie électrique, gravimétrie etc). Enfin un financement permet d'installer un détecteur en coïncidence avec un LI-DAR pour une étude exploratoire de l'effet des rayonnements dans le mécanisme de la nucléation. Le projet Diaphane obtient un financement ANR en 2014 pour développer l'étude des volcans de l'arc antillais (soufrière de Guadeloupe, Soufrière Hills de Montserrat). Ce projet, d'abord initié comme une valorisation d'un développement instrumental réalisé dans le cadre de la physique des neutrinos, est devenu parfaitement autonome et permet l'émergence d'une nouvelle méthode d'investigation géophysique. Le potentiel de *monitoring* de l'activité d'un volcan phréatique comme la Soufrière de Guadeloupe est à l'étude actuellement. C'est évidemment une étape importante avant d'intégrer la tomographie par muons cosmiques dans le panel des méthodes d'étude et de surveillance des volcans.

Ces travaux ont été récompensés par le prix Jean Thibault en 2012.

Quelques mots sur l'enseignement — Recruté en Septembre 1999 sur un poste de maître de conférences, je me suis dès le début engagé fortement dans les formations préparatoires aux concours d'enseignement : préparation au CAPES (qui sera intégré dans le Master EDSE puis dans le Master MEEF), préparation à l'agrégation externe de physique-chimie de l'ENS de Lyon, préparation à l'agrégation interne de physique-chimie du rectorat de Lyon.

Depuis 2000, j'assume la responsabilité de la préparation à l'agrégation interne de Sciences-physiques. Cette formation s'adresse aux enseignants certifiés déjà en exercice, ayant au moins 5 années d'ancienneté. Elle prévoit une préparation au concours en deux étapes : des épreuves écrites organisées traditionnellement à la fin du mois de janvier et des épreuves orales (exposé et montage) au début du mois d'avril. La formation comprend deux aspects : des cours magistraux et des corrections d'annales de concours pour la préparation de l'épreuve écrite et des travaux pratiques en collaboration avec certains lycées lyonnais. L'organisation de cette formation se fait en collaboration avec le Rectorat de Lyon, l'Université de Lyon (UCBL) et les lycées lyonnais. Elle suppose également la collaboration avec les I.A. et les I.P.R de la discipline. La formation compte en général une vingtaine de stagiaires inscrits à l'année. J'assure au sein de cette formation un enseignement de physique générale (niveau licence) couvrant sur deux années l'ensemble du programme des classes préparatoires aux grandes écoles (CPGE). Depuis 2009, je collabore également avec l'ENS qui propose aux stagiaires disposant d'un congé de formation (et donc sans contrainte sur l'emploi du temps) une formation plus étalée sur la semaine, en marge de la préparation à l'agrégation externe existante. J'y dispense des corrections de leçons et/ou montages. J'interviens régulièrement (20h ETD) à la préparation à l'agrégation externe de l'ENSL pour des corrections de leçons et de montages.

Le reste de mes enseignements est dispensé au sein du département de physique de l'université de Lyon ou dans le cadre de la formation sciences de la matière à l'ENS de Lyon. En particulier, depuis 2008, je suis co-responsable du module de M1 "Physique Nucléaire - Physique des Particules" au sein du Master de Sciences de la Matière de l'ENS. J'y dispense le cours magistral en Physique des Particules et les TD de Physique Nucléaire. Le choix "éditorial" de ce cours s'est porté d'une part sur une approche théorique de l'électrodynamique quantique au plus bas ordre (équations de propagation relativiste, Klein-Gordon et Dirac, introduction à la théorie quantique des champs,

diffusions d'électrons, Bhabha, Møller etc). D'autre part je présente les aspects expérimentaux principaux (mécanismes de détection, instrumentation etc) de ces disciplines à "grands équipements". Cet enseignement permet d'établir un contact direct entre les étudiants normaliens et les disciplines sub-atomiques. C'est ainsi que régulièrement nous recevons des demandes de stages à pourvoir, soit localement, soit à l'étranger.

Ainsi depuis 2000, j'accueille régulièrement des stagiaires de niveau L3 à M2 sur les thématiques proches de la physique des neutrinos ou des applications transdisciplinaires (3 stagiaires L3 en 2004 pour l'imagerie médicale, 1 stagiaire M1 en 2009 pour la tomographie muons). Certains stages M2 ont été poursuivis en thèse, notamment sur OPERA.

Le poids de l'enseignement est important dans le travail de l'enseignant-chercheur et il n'est pas tout le temps aisé de concilier les 192h statutaires avec une participation active aux différentes phases d'un projet, de la conception à l'analyse en passant par le montage et l'instrumentation.

Organisation du manuscrit — Le présent manuscrit est un condensé de quelques articles ou extraits d'articles significatifs illustrant les trois domaines dans lesquels je me suis investi depuis ma thèse : l'étude théorique des effets nucléaires dans les interactions neutrino-matière, les oscillations de neutrinos sur faisceau et enfin les applications transdisciplinaires. Chaque chapitre est précédé d'un résumé succinct de l'activité, en français, et est suivi de la bibliographie complète des articles auxquels j'ai participé.

Remerciements

Mes premiers remerciements vont à mes proches, à mes enfants, Marie, Maxime, Romane, Albane, à Karine, qui ont toujours participé directement ou indirectement à l'intégralité de mes travaux depuis presque deux décennies. Des premiers pas mal assurés dans la thèse jusqu'aux pentes abruptes de la Soufrière sans oublier cette parenthèse dans les Abruzzes.

Ils vont à Ippolite et Jason, qui ont inspiré et motivé ce mémoire. Ils se reconnaîtront et comprendront que leurs coups de griffes et leurs pensées n'ont pas été vains.

La liste des remerciements est évidemment très longue, tant ce métier ne peut s'entendre que collectif et collaboratif. Chercher c'est d'abord un cadre, favorable et motivant. L'IPN de Lyon est le mien et il m'a toujours offert la possibilité de défendre les projets qui me paraissaient dignes d'intérêt. Je remercie donc Guy et ses prédécesseurs, Bernard, Yves, Jean-Eudes, qui ont suivi et soutenu mon parcours. Penser que je vais enfin pouvoir arpenter les couloirs du laboratoire sans craindre le regard courroucé d'un directeur me demandant de soutenir mon HDR est une récompense en soi.

Pour remercier les collègues qui m'ont le plus apporté et avec lesquels travailler est (ou a été) un plaisir, j' imagine que nous sommes attablés dans un de ces lieux familiers qui nous ont accueillis, chercheurs, ingénieurs, techniciens, après une longue journée (ou une nuit) de "manip", en mission. Je les place autour d'une grande table au Fiordigigli, à une terrasse de la marina Rivière-Sens ou aux Deux-Clefs.

Et j' imagine, autour d'une grappa ou d'un planteur, une discussion avec les physiciens qui m'ont le plus impressionné et ont toujours été un exemple. Yves, Dario pour leurs connaissances encyclopédiques des particules et des moyens de les détecter. Pour leur implication dans leurs projets, leur exigence sans borne, leur persévérance. Ce sera sans alcool avec Dominique, mais pas moins intéressant. Avec impertinence et humour, complices d'une pensée vive et alerte, les problèmes les plus complexes sont avec lui toujours réduits à une plus simple expression. Merci pour cette bouffée de physique venue d'ailleurs.

Mettre en valeur la physique, c'est lui donner des outils techniques que l'on peut pousser largement en-dehors des marges d'un cahier des charges strict. À ce jeu, mes collègues ingénieurs et techniciens ont toujours été excellents et je suis toujours admiratif de leur capacité à concrétiser les projets les plus improbables. Ils ont une place de choix à table. Claude pour sa perspicacité, son application et sa persévérance. Serge pour son implication et sa bonne humeur en toutes circonstances. Bruno le taiseux pour sa capacité infinie à tout "debugger". Thierry, Cyrille dont les premiers pas dans OPERA ont accompagné les miens. Jean-Christophe pour le décalage permanent d'un point de vue intelligent et modeste. Sylvain pour sa technicité pointilleuse. Pierrot. Je les remercie d'avoir suivi ces projets et d'en avoir accepté de très nombreuses contraintes.

Je n'oublie pas les autres collègues du labo, chercheurs et services techniques, administratifs et

collectifs avec qui j'ai plaisir de partager un instant. Une pensée particulière pour Sandra et son acolyte Maryté, qui supportent mes frasques administratives.

Je remercie les membres du jury qui m'ont fait l'honneur de lire et de s'intéresser à ces lignes.

J'ai noué de nombreux liens en dehors du cadre, sur OPERA notamment et au travers des autres projets. Je remercie toutes ces personnes que j'ai eu la chance et le bonheur de cotoyer. Ils sont attablés à côté, discutant des problématiques de leur labo et nous échangeons de temps à autre sur nos projets communs. Comme dans toute entreprise humaine, certains contacts sont longs voire impossibles à établir et certaines personnes ont contribué à me faire réaliser que la dureté des relations professionnelles était une réalité. Je ne les remercie pas à proprement parler et les laisse à une table lointaine. Mais ils ont participé à cette petite histoire.

Enfin je remercie tous ceux qui ont suivi ces travaux de loin, la famille et les amis, qui ont prêté une oreille poliment attentive à des problématiques bien étranges et probablement très irréalistes, voire irréelles. Qu'ils sachent que leur présence est toujours capitale.

Première partie

Physique nucléaire théorique

Table des matières

| | | |
|----------|---|-----------|
| 1 | Effets nucléaires dans les interactions neutrino-matière | 17 |
| 1.1 | Introduction aux mécanismes de réponses nucléaires | 17 |
| 1.2 | Effects of the Nuclear Correlations on the Neutrino-Oxygen Interactions [1] | 24 |
| 1.3 | A unified approach for nucleon knock-out, coherent and incoherent pion production in neutrino interactions with nuclei [9] | 38 |
| 1.4 | Neutrino and antineutrino quasielastic interactions with nuclei [10] | 59 |
| 2 | Restauration de la symétrie chirale | 65 |
| 2.1 | Introduction | 65 |
| 2.2 | Pion scalar density and chiral symmetry restoration at finite temperature and density [4] | 66 |
| | Bibliographie Partie I | 79 |

Chapitre 1

Effets nucléaires dans les interactions neutrino-matière

1.1 Introduction aux mécanismes de réponses nucléaires

L’“anomalie” des neutrinos atmosphériques — La problématique posée en 1996 concernait l’analyse des expériences utilisant des détecteurs Cerenkov à eau souterrains (Kamiokande, Super-Kamiokande, IMB) où les neutrinos interagissent avec les noyaux d’oxygène cible. Ces expériences ont permis la mise en évidence des oscillations de neutrinos atmosphériques et les premières mesures des paramètres gouvernant ce mécanisme : angle de mélange θ_{23} et différence des carrés des masses Δm_{23}^2 . La mesure de ces paramètres sera l’objet des programmes dits “long baseline” de première génération (programmes CNGS-OPERA en Europe, NuMI-MINOS aux Etats-Unis, K2K puis T2K au Japon).

Le but de ce travail était principalement de quantifier les effets collectifs nucléaires et la modification qu’ils pouvaient induire dans le spectre d’énergie transférée lors d’une interaction de neutrino, quasi-élastique ou résonante. Les échelles d’énergie mises en jeu dans ces effets collectifs de type “branche pionique” étant de l’ordre de grandeur de la différence des masses des leptons ($m_\mu - m_e \sim 100$ MeV), l’idée était d’étudier leur influence sur la réponse d’un noyau cible à une interaction de ν_μ ou de ν_e et sur l’analyse des résultats obtenus avec un détecteur de type Čerenkov comme Super-Kamiokande. De plus il est rapidement apparu nécessaire d’inclure l’effet des excitations corrélées de type $np - nh$ puisque la composante hadronique de l’état final n’est pas résolue dans un tel détecteur. L’impact sur la sélection des événements, basée sur le nombre d’anneaux Cerenkov reconstruits est important si l’on considère que différents canaux de réactions sont susceptibles de simuler une interaction de type quasi-élastique (population d’événements retenus pour l’analyse expérimentale).

Ces travaux ont permis de démontrer que les effets nucléaires ne pouvaient pas rendre compte de ce qu’on appelait à l’époque “l’anomalie des neutrinos atmosphériques” mais qu’ils sont suffisamment importants pour compliquer notablement l’analyse. A l’époque, où il n’était question que de se convaincre de l’existence des oscillations de neutrinos, les incertitudes sur les sections efficaces, communément admises pour tourner autour de ~ 20 %, n’étaient pas déterminantes. Mais rapidement il a été reconnu que c’était un chantier important pour la communauté scientifique dans son ensemble. C’est ainsi notamment que le cycle de conférences *NuInt (International Workshop on Neutrino-Nucleus Interactions in the Few-GeV region)* a vu le jour et a mis en relief la nécessité de programmes expérimentaux dédiés aux mesures de sections efficaces pour les expériences actuelles de “métrologie” fine des paramètres des oscillations de neutrinos et les futurs programmes de recherche de violation CP dans le secteur leptonique et de mesure de la hiérarchie de masse. Le

modèle développé pendant ma thèse a été largement diffusé au sein de la communauté (séminaires, conférences, publications) et adapté aussi bien à Lyon par M.Martini, M.Ericson, G.Chanfray et moi-même qu'à l'extérieur (il est à la base du générateur *NuWro* développé par le groupe de J.Sobjczyk à Wroclaw en Pologne).

Même si l'hypothèse des oscillations de neutrinos s'est imposée depuis, les questions étudiées dans cette analyse pionnière des interactions neutrino-matière restent d'actualité. Les générateurs les plus utilisés, tels que *NEUT* ou *GENIE* sont développés sur la base d'un modèle de gaz de Fermi incluant les interactions quasi-élastiques, résonantes (production d'un pion), cohérentes (production cohérente d'un pion, dans laquelle le noyau reste au repos), et profondément inélastiques (production de plusieurs pions en voie de sortie). Ils incluent en général une possibilité de réinteraction dans l'état final (*final state interactions* ou *FSI*). Dans les analyses standard (de l'expérience T2K par exemple), les paramètres des sections efficaces sont considérés avec une incertitude à priori allant de 20 % à 40 %. On comprend qu'à l'ère des mesures de précision, il soit nécessaire de pouvoir disposer de modèles pertinents permettant de comprendre l'influence des effets nucléaires dans une gamme d'énergie de l'ordre du GeV.

Prenons une illustration simple. La reconstruction de l'énergie d'un neutrino, essentielle pour des analyses en L/E des résultats obtenus est une problématique très actuelle. La méthodologie a évolué avec le temps mais de nombreux résultats ont été publiés en considérant que toutes les interactions des neutrinos étaient du type quasi-élastique. Dans cette hypothèse, un modèle de gaz de Fermi relativiste conduit à une cinématique relativement simple :

$$E_{\nu}^{QE} = \frac{m_n^2 - (m_p - E_b)^2 - m_{\mu}^2 + 2(m_p - E_b E_{\mu})}{2(m_p - E_b - E_{\mu} + p_{\mu} \cos \theta_{\mu})} \quad (1.1)$$

$$Q_{QE}^2 = 2E_{\nu}^{QE} (E_{\mu} - p_{\mu} \cos \theta_{\mu}) - m_{\mu}^2 \quad (1.2)$$

Dans l'équation précédente on introduit une énergie de liaison empirique E_b qui traduit la présence du potentiel nucléaire. Les résultats expérimentaux, obtenus avec Minerva par exemple, mettent l'accent sur l'insuffisance d'une telle méthode et la nécessité de considérer une cinématique plus réaliste. Or le modèle développé pendant ma thèse a permis de mettre en évidence clairement qu'une large partie des interactions, entre le pic quasi-élastique et la résonance Delta, fait intervenir des états corrélés de type $np - nh$ et par conséquent une cinématique beaucoup plus complexe où plusieurs nucléons peuvent être éjectés du noyau cible. La pertinence des calculs menés à l'époque a conduit le groupe théorie de l'IPNL à maintenir et développer ce modèle pour le confronter à des résultats expérimentaux récents (Minerva, Miniboone, T2K etc), indisponibles à l'époque de ma thèse. Il est l'un des rares à l'heure actuelle à rendre compte des données expérimentales publiées par MiniBoone. Plusieurs "anomalies" dans les spectres expérimentaux observés doivent notamment être réexaminées à la lumière de la phénomologie nucléaire à basse énergie. La souplesse du modèle développé, adapté à différents types de noyaux cibles et sa "quasi-analyticité" en font un outil pertinent dans les études des sections efficaces des neutrinos, qui sont maintenant la clé des expériences dédiées à la recherche de la violation de CP dans le secteur leptonique.

Le formalisme des réponses nucléaires — Le principal objectif de ce travail de recherche, sous la direction de J.Delorme, et en collaboration avec M.Ericson et G.Chanfray, était donc l'extension des calculs de sections efficaces et de taux d'interactions neutrino-oxygène dans un modèle théorique incluant, sur tout le spectre énergétique accessible aux neutrinos atmosphériques, i.e. du pic quasi-élastique à la région de la résonance Delta :

- les corrélations nucléaires à longue portée de type RPA (*Random Phase Approximation*),
- des effets de volume fini grâce à une approximation de densité locale (et par opposition aux calculs réalisés dans des modèles de gaz de Fermi),

-
- les effets de modification de la largeur de résonance du Delta dans le milieu (incluant les canaux non-résonants réductibles à une largeur de Delta),
 - les excitations corrélées de type $np - nh$ dans lesquelles la sonde initiale peut éjecter plusieurs nucléons par exemple.

Le calcul de ces observables physiques utilise un formalisme de réponse nucléaire semi-classique dans les canaux de réaction d'isospin et de spin-isospin (longitudinal et transverse) par lesquels un neutrino se couple au noyau dans une interaction de type courant chargé :

- opérateur de **spin longitudinal** $(\boldsymbol{\sigma} \cdot \mathbf{q}) \tau_a$,
- opérateurs de **spin transverse** $(\boldsymbol{\sigma} \times \mathbf{q}) \tau_a$ et $((\boldsymbol{\sigma} \times \mathbf{q}) \times \mathbf{q}) \tau_a$,
- opérateur de **charge** $\mathbb{I}_\sigma \tau_a$,

où $\boldsymbol{\tau}$ désigne les matrices de Pauli d'isospin et \mathbb{I}_σ la matrice identité dans l'espace de spin. Les excitations $np - nh$ sont paramétrisées grâce à une extrapolation des données expérimentales sur l'absorption des pions sur des paires de nucléons et sur les données des réactions pion-noyau. Les corrélations RPA sont incluses à l'approximation des anneaux (*ring-RPA*) et modifient le spectre des réponses nucléaires de spin-isospin. Les calculs menés dans ce travail ont été confrontés avec succès aux données expérimentales de réaction pion-noyau (test de la voie de spin-isospin longitudinale) et de diffusion (e, e') (test de la voie de spin-isospin transverse).

Notons que la plupart des modèles d'interaction neutrino-matière repose sur la superposition cohérente des réponses d'un gaz de Fermi dans la région quasi-élastique (calcul initial de Llewellynn-Smith), dans la région des résonances (modèle de Rein-Sehgal par exemple) puis dans la région profondément inélastique. Les zones de recouvrement de ces différentes régions spectrales sont en général délicates à décrire proprement sans "double comptage". Ce problème ne se présente pas dans notre modèle qui inclut de manière cohérente tous les processus précédents au premier ordre (réponses "nues") avant de les intégrer dans le jeu des équations de la RPA.

Les fonctions réponse dans chaque canal se déduisent d'une quantité baptisée propagateur de polarisation suivant la relation :

$$R^{\mu\nu}(\omega, \mathbf{q}) = -\frac{1}{\pi} \text{Im}[\Pi^{\mu\nu}(\omega, \mathbf{q}, \mathbf{q})]. \quad (1.3)$$

A l'ordre le plus bas, les réponses nucléaires s'écrivent :

$$\begin{aligned} R_{cc}(\omega, \mathbf{q}) &= -\frac{1}{\pi} \text{Im}[\Pi^0(\omega, \mathbf{q})], \\ R_{ll}(\omega, \mathbf{q}) &= -\frac{1}{\pi} \text{Im}[\Pi^0(\omega, \mathbf{q})], \\ R_{t_it_j}(\omega, \mathbf{q}) &= (\delta_{ij} - \frac{\mathbf{q}_i \mathbf{q}_j}{q^2}) (-\frac{1}{\pi} \text{Im}[\Pi^0(\omega, \mathbf{q})]). \end{aligned} \quad (1.4)$$

où $\Pi^0(\omega, \mathbf{q})$ désigne le propagateur d'excitation particule-trou. Les propagateurs nucléon-trou et delta-trou sont représentés par les graphes de Feynman suivants :

Les effets collectifs sont inclus sous la forme d'un formalisme de type RPA (Random Phase Approximation) et la taille finie des noyaux est prise en compte grâce à une approximation de densité locale (moment de Fermi dépendant de la position). Symboliquement on passe des propagateurs au premier ordre au propagateurs RPA en résolvant l'équation générique :

$$\Pi = \Pi^0 + \Pi^0 V \Pi, \quad (1.5)$$

que l'on représentera diagrammatiquement par la figure ci-après :

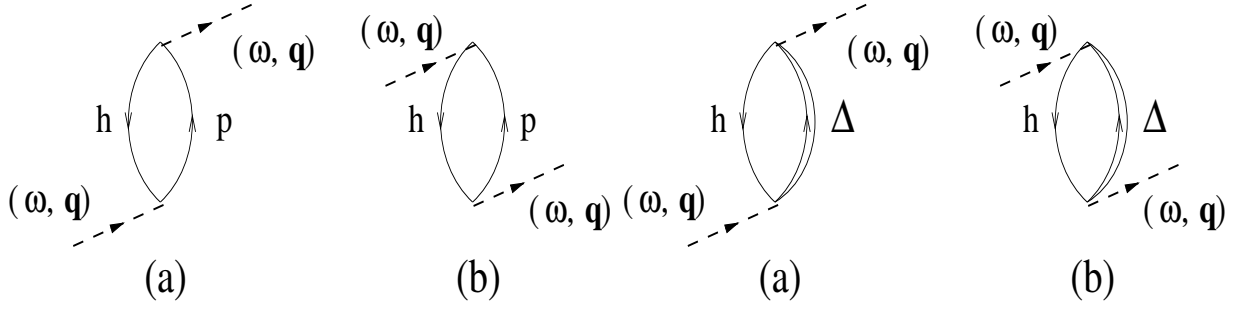


FIGURE 1.1 – *Haut* : propagateurs d’excitation nucléon-h : terme direct (a) et croisé (b). *Bas* : propagateurs d’excitation delta-h : terme direct (a) et croisé (b).

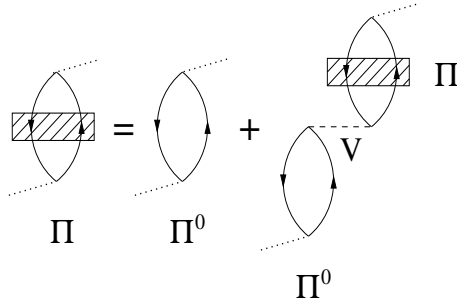


FIGURE 1.2 – *Représentation symbolique de l’approximation des anneaux.*

Le potentiel d’interaction est modélisé, dans le canal de spin-isospin, par des échanges de pions, de rhos et des corrélations de courte portée de type Landau-Migdal. Les effets collectifs de type RPA modifient profondément la réponse longitudinale (apparition de la branche dite “pionique”). Ceci est très clair sur les figures suivantes où l’on compare les réponses nucléaires sans effet collectif et avec effet collectif.

Les sections efficaces neutrino-noyau — La section efficace s’écrit comme une combinaison linéaire des réponses nucléaires :

$$\begin{aligned}
 \frac{\partial^2 \sigma}{\partial \Omega \partial k'} &= \frac{G_F^2 \cos^2 \theta_c (\mathbf{k}')^2}{2 \pi^2} \cos^2 \frac{\theta}{2} \left[G_E^2 \left(\frac{q_\mu^2}{\mathbf{q}^2} \right)^2 R_{\tau}^{NN} \right. \\
 &+ G_A^2 \frac{(M_\Delta - M)^2}{2 \mathbf{q}^2} R_{\sigma\tau(L)}^{N\Delta} + G_A^2 \frac{(M_\Delta - M)^2}{\mathbf{q}^2} R_{\sigma\tau(L)}^{\Delta\Delta} \\
 &+ (G_M^2 \frac{\omega^2}{\mathbf{q}^2} + G_A^2) \left(-\frac{q_\mu^2}{\mathbf{q}^2} + 2 \tan^2 \frac{\theta}{2} \right) (R_{\sigma\tau(T)}^{NN} + 2 R_{\sigma\tau(T)}^{N\Delta} + R_{\sigma\tau(T)}^{\Delta\Delta}) \\
 &\left. \pm 2 G_A G_M \frac{k + k'}{M} \tan^2 \frac{\theta}{2} (R_{\sigma\tau(T)}^{NN} + 2 R_{\sigma\tau(T)}^{N\Delta} + R_{\sigma\tau(T)}^{\Delta\Delta}) \right] \quad (1.6)
 \end{aligned}$$

Les principaux résultats, développés dans les articles suivants, sont la mise en évidence d’une contribution importante des canaux $np - nh$ dans le spectre des sections efficaces, ce qui peut influencer l’analyse des événements neutrinos à basse énergie comme cela a été souligné plus haut et une suppression importante, d’origine cinématique, du canal longitudinal de spin-isospin. Ce dernier effet minimise l’impact de la branche pionique dans les interactions neutrino-noyau.

Réponses longitudinales par nucléon

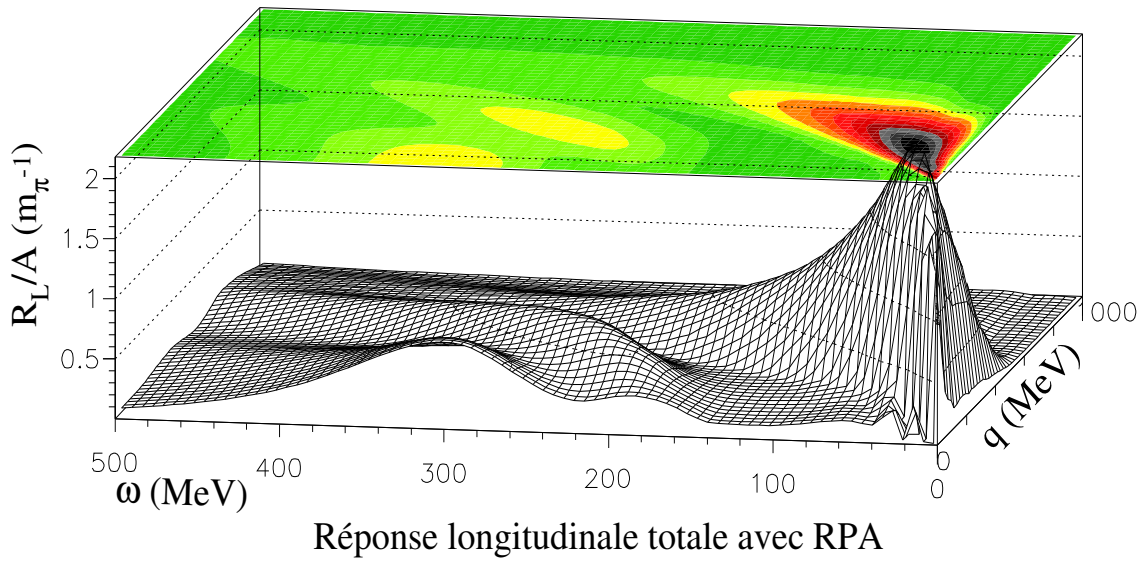
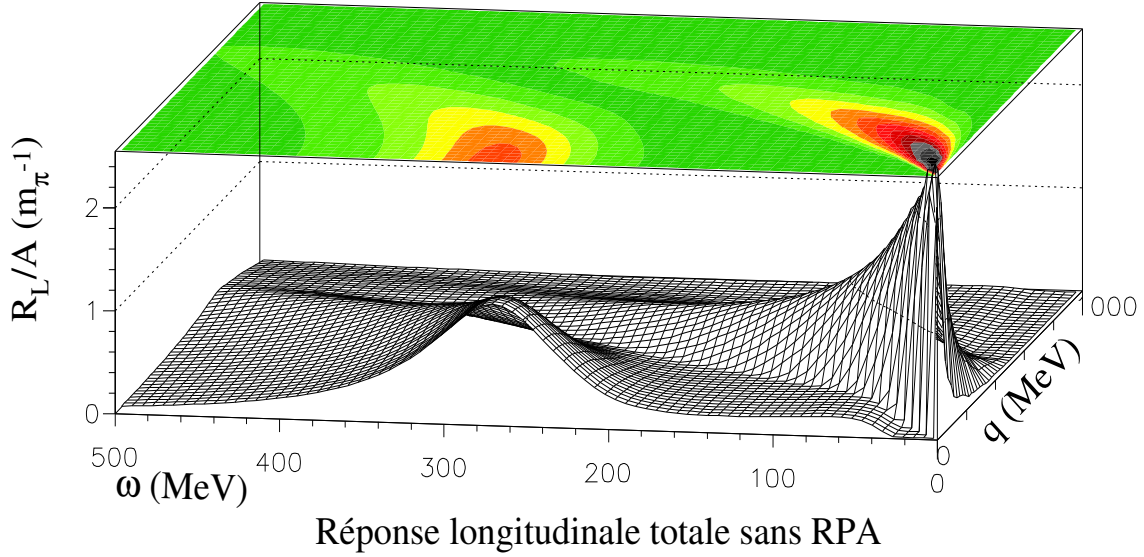
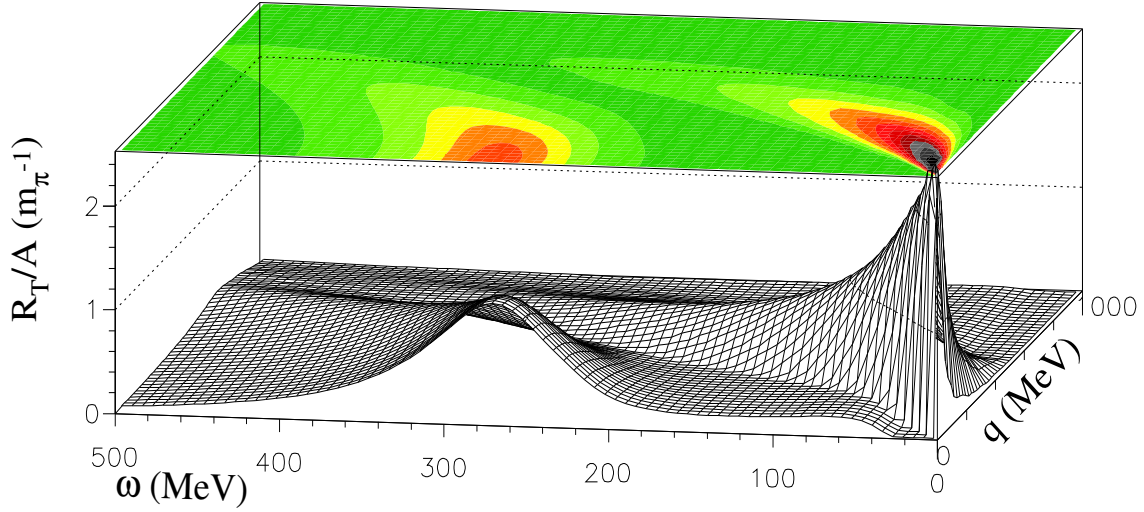
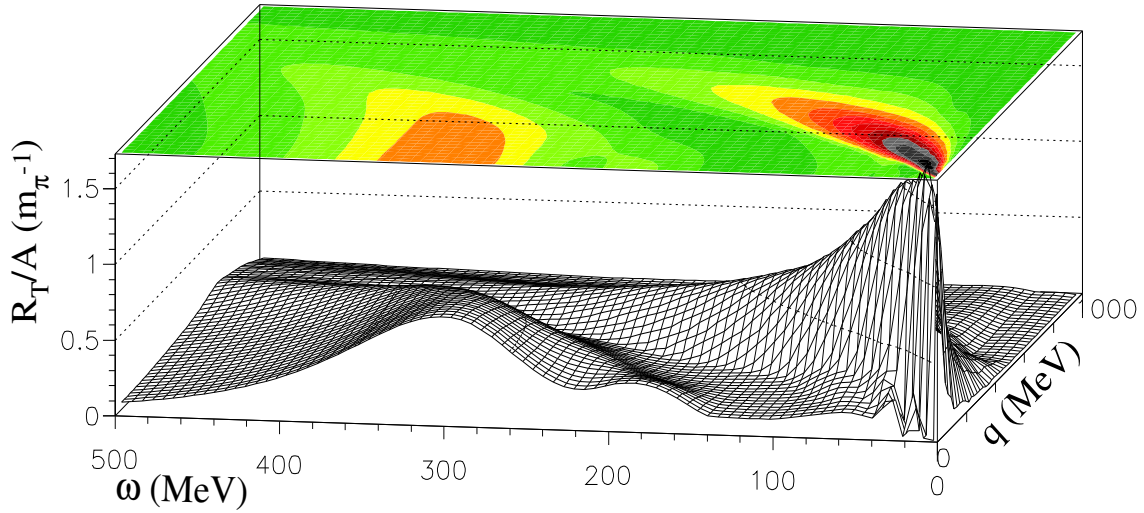


FIGURE 1.3 – Réponses longitudinales par nucléon dans le plan (ω, q) . La projection des réponses sur le plan laisse apparaître le pic quas-élastique démarrant au voisinage de l'origine et la branche du Delta. Dans la réponse RPA cette branche se scinde en une branche supérieure dans la région de genre temps, la branche du Delta collective et une branche inférieure, la branche pionique.

Réponses transverses par nucléon



Réponse transverse totale sans RPA



Réponse transverse totale avec RPA

FIGURE 1.4 – Réponses transverses par nucléon dans le plan (ω, q) . La projection des réponses sur le plan laisse apparaître le pic quas-élastique démarrant au voisinage de l'origine et la branche du Delta. Dans la réponse RPA cette branche du Delta est poussée à bas moment vers les plus grandes énergies de transfert.

Les articles présentés dans les Sections suivantes présentent le formalisme et les principaux résultats obtenus durant ma thèse dans les sections efficaces neutrino-oxygène (*Effects of the Nuclear Correlations on the Neutrino-Oxygen Interactions*, [1]). Ces résultats ont été présentés de nombreuses fois et ont fait l'objet d'autres articles (voir la bibliographie en fin de chapitre). J'ai choisi de mettre en évidence dans les deux articles suivants, une comparaison de ce modèle avec des résultats récents sous l'impulsion de M.Martini et M.Ericson (*A unified approach for nucleon knock-out, coherent and incoherent pion production in neutrino interactions with nuclei*, [9] et *Neutrino and antineutrino quasielastic interactions with nuclei*, [10]). La présentation du formalisme est mise de côté puisqu'elle ne présente aucune nouveauté. On retrouve les principaux résultats concernant les réponses nucléaires, les comparaisons aux données π -noyau. Les sections efficaces quasi-élastiques, de production de pion etc sont confrontées aux résultats expérimentaux de MiniBooNE et SciBooNE notamment et on voit que l'accord est très satisfaisant. Ce domaine de recherche est particulièrement actif à l'ère des mesures de précision qui s'ouvre maintenant avec les futurs projets "mégatonne" (LBNO en Europe, LBNF aux Etats-Unis, Hyper-Kamiokande au Japon). La recherche d'effets fins comme la violation de CP et la hiérarchie de masse, au travers des effets de matière notamment, met en jeu une connaissance accrue des sections efficaces neutrino-noyau. Récemment une comparaison a été faite des résultats de ce modèle aux résultats de MiniBooNE en neutrinos et anti-neutrinos (*Neutrino versus antineutrino cross sections and CP violation*, M.Martini, M.Ericson, arXiv :1501.02442v1). L'accord du modèle, incluant les divers ingrédients détaillés ci-dessus, avec les données souligne une fois encore l'importance des corrélations nucléaires dans l'analyse des interactions neutrino-noyau.

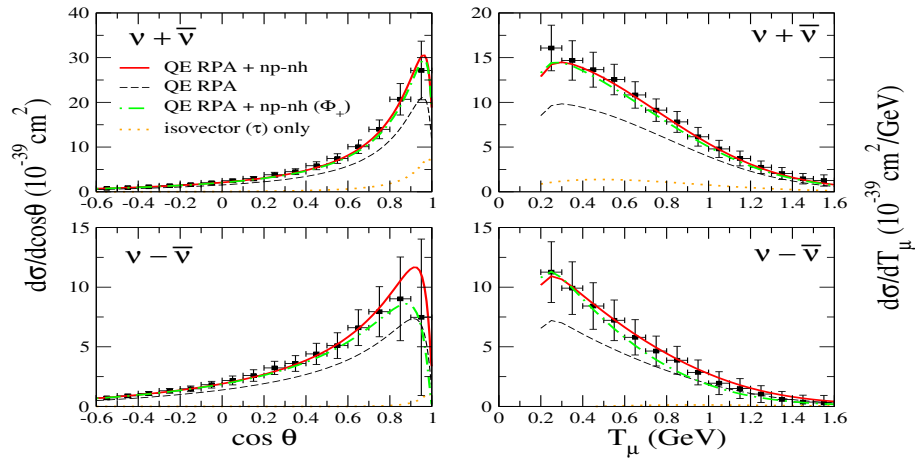


FIGURE 1.5 – Somme et différence de la section efficace différentielle ν et $\bar{\nu}$ par nucléon, moyennée sur le flux, $\frac{d\sigma}{d\cos\theta}$ et $\frac{d\sigma}{dT_\mu}$ pour une cible de carbone. Ligne continue : évaluation RPA complète RPA incluant les canaux d'émission multi-nucléons avec les flux réels ν et $\bar{\nu}$ de MiniBooNE. Ligne hachée : contribution quasi-élastique RPA avec les flux réels ν and $\bar{\nu}$ de MiniBooNE. Ligne intermittente : évaluation RPA complète incluant les canaux d'émission multi-nucléons avec le flux moyen Φ_+ . Ligne pointillée : contribution de la seule réponse isovectorielle.

1.2 Effects of the Nuclear Correlations on the Neutrino-Oxygen Interactions [1]

J. Marteau

*Institut de Physique nucléaire de Lyon,
43 bld du 11 novembre 1918, 69622 Villeurbanne*

Abstract

We perform a calculation of the absolute charged current neutrino-oxygen events rates relevant in the atmospheric neutrino experiments. The inclusive reaction cross-section is split into exclusive channels, which are classified according to the number of Čerenkov rings they produce. The model includes the effects of residual interaction in a RPA scheme with both nucleon-hole and Delta-hole excited states and the effects of $(np-nh)$ excitations ($n=2,3$). Our result is that although the flavor ratio μ/e remains almost unaffected by the nuclear effects considered here and often neglected in the Monte-Carlo simulations, the absolute events rates are subject to important modifications.

PACS 13.15.+gNeutrino interactions; 14.40.-nMesons; 24.30.GdOther resonances

1 Introduction

Neutrino physics is among the hottest topics of particle physics with the recent indications in favor of neutrino oscillations. After the solar neutrino deficit, the apparent anomaly in the ratio of muon to electron atmospheric neutrinos $R_{\mu/e} = (N_{\nu_\mu} + N_{\bar{\nu}_\mu})/(N_{\nu_e} + N_{\bar{\nu}_e})$ observed by (Super-)Kamiokande [1, 2], IMB [3], Soudan-2 [4] and the asymmetry in the zenithal distributions of the μ - type events in Super-Kamiokande [2] have given a strong support to the oscillation hypothesis: $\nu_\mu \longrightarrow \nu_x$ where $\nu_x = \nu_\tau$ (*i.e.* *active-active* transition) or $\nu_x = \nu_s$ (*i.e.* *active-sterile* transition). The solution of the atmospheric neutrinos anomaly in terms of $\nu_\mu \longrightarrow \nu_e$ oscillations has been excluded by the Chooz collaboration [5].

A number of atmospheric neutrinos experiments use large underground water Čerenkov detectors. In these experiments only "one Čerenkov ring" (1 Č.R.) events are retained for the analysis. These events are usually assumed to be produced by quasi-elastic charged current interactions in which a charged lepton is emitted above Čerenkov threshold and leads to one Čerenkov ring. The nucleon which is ejected from the nucleus is in general below threshold and therefore does not produce another ring. The region of energy transfer in processes involving atmospheric neutrinos of ~ 1 GeV extends from the quasi-elastic peak to the Delta resonance region. The evaluation of the nuclear responses in the latter region usually relies on the assumption that the Delta decays into a pion and a nucleon (this is the case for example in ref. [6] where the authors use a relativistic model *à la* Walecka to compute the nuclear response functions). The pion leading to an additional Čerenkov ring,

this charged current event belongs to the two Čerenkov rings (2 Č.R.) class and is rejected by the experimental cuts. Thus theoretical calculations are often limited to the quasi-elastic peak which is treated in Fermi gas models or with more elaborate treatments taking into account the shell structure of the oxygen nucleus and RPA type correlations [7].

However the nuclear dynamics is far more complex than this simple picture. Indeed the pion in the nucleus is a quasi-particle with a broad width and can decay for instance into a *particle-hole* excitation. Therefore the decay of a Delta in the nuclear medium can lead to a nucleon and a *particle-hole* state. In such a process, two nucleons are ejected from the nucleus, none of them producing a Čerenkov ring, and the event belongs to the 1 Č.R. class. Furthermore ($2p$ - $2h$) states may also be directly excited in the nucleus without excitation of the Delta resonance. This process also results in the emission of two nucleons and the event belongs to the 1 Č.R. class. Following these arguments, we perform a full calculation of the neutrino-oxygen cross sections beyond the quasi-elastic assumption, with the identification of the possible final states. This procedure leads to a complete evaluation of the 1 Č.R. events yields in the atmospheric neutrinos experiments and its impact in the description of the retained neutrino events in the detectors has to be investigated.

The starting point of this calculation is the inclusive charged current cross section for the reaction $\nu_l (\bar{\nu}_l) + {}^{16}\text{O} \longrightarrow l^- (l^+) + X$,

$$\begin{aligned} \frac{\partial^2 \sigma}{\partial \Omega \partial k'} &= \frac{G_F^2 \cos^2 \theta_c (\mathbf{k}')^2}{2 \pi^2} \cos^2 \frac{\theta}{2} \left[G_E^2 \left(\frac{q_\mu^2}{\mathbf{q}^2} \right)^2 R_\tau^{NN} \right. \\ &+ G_A^2 \frac{(M_\Delta - M)^2}{2 \mathbf{q}^2} R_{\sigma\tau(L)}^{N\Delta} + G_A^2 \frac{(M_\Delta - M)^2}{\mathbf{q}^2} R_{\sigma\tau(L)}^{\Delta\Delta} \\ &+ (G_M^2 \frac{\omega^2}{\mathbf{q}^2} + G_A^2) \left(-\frac{q_\mu^2}{\mathbf{q}^2} + 2 \tan^2 \frac{\theta}{2} \right) (R_{\sigma\tau(T)}^{NN} + 2 R_{\sigma\tau(T)}^{N\Delta} + R_{\sigma\tau(T)}^{\Delta\Delta}) \\ &\left. \pm 2 G_A G_M \frac{k + k'}{M} \tan^2 \frac{\theta}{2} (R_{\sigma\tau(T)}^{NN} + 2 R_{\sigma\tau(T)}^{N\Delta} + R_{\sigma\tau(T)}^{\Delta\Delta}) \right] \end{aligned} \quad (1)$$

where G_F is the weak coupling constant, θ_c the Cabbibo angle, k and k' the initial and final lepton momenta, $q_\mu = k_\mu - k'_\mu = (\omega, \mathbf{q})$ the four momentum transferred to the nucleus, θ the scattering angle, M_Δ (M) the Delta (nucleon) mass. The plus (minus) sign in eq. (1) stands for the neutrino (antineutrino) case. In a provisional approximation, to be lifted after, we have neglected in eq. (1) the lepton masses and we have kept the leading terms in the development of the hadronic current in p/M , where p denotes the initial nucleon momentum. The electric, magnetic and axial form factors are taken in the standard dipole parameterization with the following normalizations: $G_E(0) = 1.0$, $G_M(0) = 4.71$ and $G_A(0) = 1.25$. We have introduced the inclusive *isospin* (R_τ), *spin-isospin longitudinal* ($R_{\sigma\tau(L)}$) and *spin-isospin transverse* ($R_{\sigma\tau(T)}$) nuclear responses functions (the longitudinal and transverse character of these last two responses refers to the direction of the spin operator with respect to the direction of the transferred momentum):

$$R_\alpha^{PP'} = \sum_n \langle n | \sum_{j=1}^A O_\alpha^P(j) e^{i \mathbf{q} \cdot \mathbf{x}_j} | 0 \rangle \langle n | \sum_{k=1}^A O_\alpha^{P'}(k) e^{i \mathbf{q} \cdot \mathbf{x}_k} | 0 \rangle^* \delta(\omega - E_n + E_0) \quad (2)$$

where the operators have the following forms:

$$O_\alpha^N(j) = \tau_j^\pm, \quad (\boldsymbol{\sigma}_j \cdot \hat{\mathbf{q}}) \tau_j^\pm, \quad ((\boldsymbol{\sigma}_j \times \hat{\mathbf{q}}) \times \hat{\mathbf{q}}) \tau_j^\pm,$$

for $\alpha = \tau, \sigma\tau(L), \sigma\tau(T)$, and

$$O_\alpha^\Delta(j) = (\mathbf{S}_j \cdot \hat{\mathbf{q}}) T_j^\pm, ((\mathbf{S}_j \times \hat{\mathbf{q}}) \times \hat{\mathbf{q}}) T_j^\pm,$$

for $\alpha = \sigma\tau(L), \sigma\tau(T)$. In the above expressions, the superscript P ($P = N$ or Δ) denotes the type of the *Particle-hole* excitations (*Nucleon-hole* or *Delta-hole*) induced by the operator O_α^P . The operators S and T are the usual 1/2 to 3/2 transition operators in the spin and isospin space (for instance see [22]). In this work we neglect the small quadrupole transition connecting the nucleon to the Delta through the pure isospin operator, therefore the isospin response just involves nucleon-hole excitations. Note that we have assumed the existence of a scaling law between the nucleon and Delta magnetic and axial form factors [10]:

$$G_M^*/G_M = G_A^*/G_A = f^*/f,$$

where f^* (f) is the $\pi N \Delta$ ($\pi N N$) coupling constant. For a matter of convenience, we have incorporated the scaling factor $f^*/f = 2.2$ into the responses.

2 Formalism

The evaluation of the nuclear responses is performed within the model developed by Delorme and Guichon for the interpretation of the $(^3\text{He}, t)$ charge exchange experiments [11, 12]. In this model the polarization propagators $\Pi^0(\omega, \mathbf{q}, \mathbf{q}')$ without nuclear correlations are evaluated in a semi-classical approximation to properly take into account the finite size effects. This implies the use of a local Fermi momentum $k_F(r)$ which is calculated by the means of an experimental nuclear density: $k_F(r) = (3/2 \pi^2 \rho(r))^{1/3}$. Note that this procedure differs a little from the pure semi-classical one¹ but it has been found to give better results for the π – nucleus reactions. The "bare" polarization propagators Π^0 (in the following "bare" will mean that the nuclear correlations are switched off) are then used as an input to exactly solve the RPA equations in the ring approximation, as we will develop in the following. In ref. [11, 12] the authors gave satisfactory fits to the set of the experimental data. This model was also confronted to the pion-nuclei experimental results [13] and the agreement obtained for the total and elastic cross sections was remarkably good.

As mentioned above, the first step of the calculation is the evaluation of the bare polarization propagators. A crucial ingredient of the model is the Delta resonance width modified by the nuclear effects. We adopt the parameterization of ref. [14] where the Delta width is split into the contributions of different decay channels: the "quasi-elastic" channel, $\Delta \rightarrow \pi N$, modified by the Pauli blocking of the nucleon and the distortion of the pion, the two-body ($2p$ - $2h$) and three-body ($3p$ - $3h$) absorption channels. This parameterization leads to a good description of pion-nuclear reactions. At resonance we find a Delta width around 130 MeV, a value rather close to the free case. This value reflects the importance of the two- and three-body absorption channels which are large enough to counteract the effect of the Pauli blocking and lead to this overall enhancement of the Delta width. Note furthermore that at resonance the "quasi-elastic" channel modified by the medium effects, is almost equal to the free "quasi-elastic" one. The model of Delorme and Guichon also accounts for the ($2p$ - $2h$) excitations which are not reducible to a modified Delta width. The evaluation of

¹For a pure quantum approach in the low energy part of the nuclear response, applied in the context of terrestrial neutrinos experiments, see ref. [8, 9]

such processes is performed by extrapolating the calculations of two-body pion absorption at threshold given in ref. [15]. We have limited ourselves to the imaginary part of these two-body polarization propagators, the comparison with experimental data such as pion-nucleus scattering or (e, e') scattering giving satisfactory results to that order of approximation. By construction, the bare polarization propagator $\Pi^0(\omega, \mathbf{q}, \mathbf{q}')$ is the sum of the following partial components:

1. NN quasi-elastic (the standard Lindhard function),
2. NN ($2p$ - $2h$),
3. $N\Delta$ and 3'. ΔN ($2p$ - $2h$),
4. $\Delta\Delta$ (πN),
5. $\Delta\Delta$ ($2p$ - $2h$),
6. $\Delta\Delta$ ($3p$ - $3h$),

where the notation N (Δ) stands for Nucleon-hole (Delta-hole) states as previously. The Feynman graphs corresponding to this partial polarization propagators are displayed on fig. (1) with the following conventions: the wiggled lines represent the external probe, the full lines correspond to the propagation of a nucleon (or a hole), the double lines to the propagation of a Delta, the dashed lines to an effective interaction between nucleons and/or Deltas. Finally the dotted lines indicate which intermediate state has to be placed on-shell to obtain the desired partial nuclear response. Note that in the case of $(np$ - nh) polarization propagators the number of graphs is large and we just give one example in the figure.

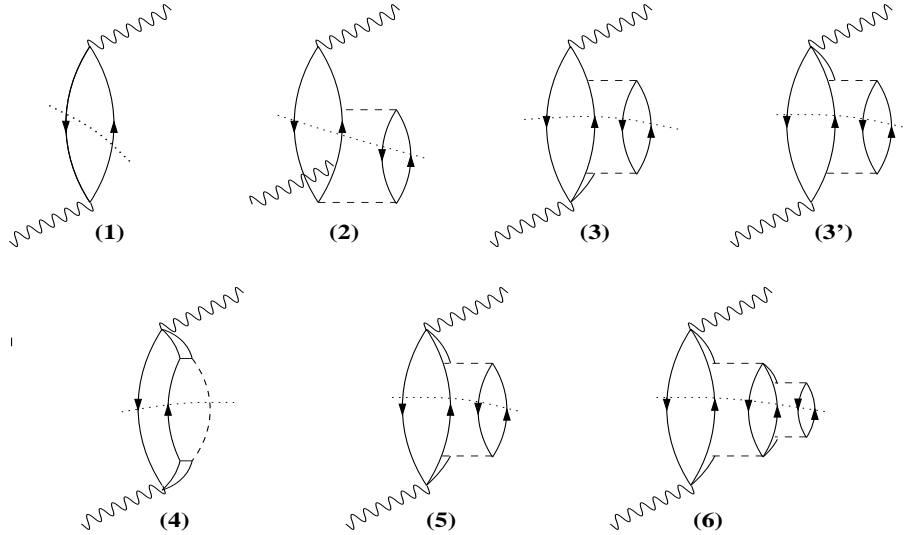


Figure 1: *Feynman graphs of the partial polarization propagators: NN quasi-elastic (1), NN ($2p$ - $2h$) (2), $N\Delta$ ($2p$ - $2h$) (3), ΔN ($2p$ - $2h$) (3'), $\Delta\Delta$ (πN) (4), $\Delta\Delta$ ($2p$ - $2h$) (5), $\Delta\Delta$ ($3p$ - $3h$) (6). The conventions for the various lines drawings are given in the text.*

The bare responses are then given by the standard relations:

$$R^0(k)(\omega, q) = -\frac{1}{\pi} \text{Im}(\Pi^0(k)(\omega, q, q)), \quad (3)$$

with the obvious sum rule:

$$R^0(\omega, q) = -\frac{1}{\pi} \text{Im}(\Pi^0(\omega, q, q)) = \sum_{k=1}^{n_k} R^0(k)(\omega, q), \quad (4)$$

where n_k denotes the number of partial reaction channels ($n_k = 7$ in our model).

Following the method detailed in ref. [11, 12] we include the effects of nuclear correlations by exactly solving the RPA equations in the ring approximation. For instance the inclusive RPA polarization propagators $\Pi(\omega, \mathbf{q}, \mathbf{q}')$ are solution of the generic equation:

$$\Pi = \Pi^0 + \Pi^0 V \Pi \quad (5)$$

where V denotes the effective interaction between *particle-hole* excitations and $\Pi^0(\omega, \mathbf{q}, \mathbf{q}')$ the inclusive bare polarization propagator calculated previously and used here as an input. In the spin-isospin channel the RPA equations couple the L, T and the N, Δ components of the polarization propagators. For the effective interaction relevant in the isospin and spin-isospin channels, we use the standard $\pi + \rho + \delta$ - function parameterization:

$$\begin{aligned} V_{NN} &= (f' + V_\pi + V_\rho + V_{g'}) \boldsymbol{\tau}_1 \cdot \boldsymbol{\tau}_2 \\ V_{N\Delta} &= (V_\pi + V_\rho + V_{g'}) \boldsymbol{\tau}_1 \cdot \mathbf{T}_2^\dagger \\ V_{\Delta N} &= (V_\pi + V_\rho + V_{g'}) \mathbf{T}_1 \cdot \boldsymbol{\tau}_2 \\ V_{\Delta\Delta} &= (V_\pi + V_\rho + V_{g'}) \mathbf{T}_1 \cdot \mathbf{T}_2^\dagger \end{aligned} \quad (6)$$

where in the NN case, for example (the $N\Delta$, ΔN and $\Delta\Delta$ cases are obtained with the appropriate replacements $\sigma \longrightarrow S$):

$$\begin{aligned} V_\pi &= F_\pi^2 \left(\frac{\mathbf{q}^2}{\omega^2 - \mathbf{q}^2 - m_\pi^2} \right) \boldsymbol{\sigma}_1 \cdot \hat{\mathbf{q}} \boldsymbol{\sigma}_2 \cdot \hat{\mathbf{q}} \\ V_\rho &= F_\rho^2 \left(\frac{\mathbf{q}^2}{\omega^2 - \mathbf{q}^2 - m_\rho^2} \right) \boldsymbol{\sigma}_1 \times \hat{\mathbf{q}} \boldsymbol{\sigma}_2 \times \hat{\mathbf{q}} \\ V_{g'} &= F_\pi^2 g' \boldsymbol{\sigma}_1 \cdot \boldsymbol{\sigma}_2 \end{aligned} \quad (7)$$

In the preceding equations, $F_\pi(q)$ and $F_\rho(q)$ are the standard pion-nucleon and rho-nucleon form factors. The values we adopt for the relevant parameters can be found in ref. [13]. In particular we take the "common" Landau-Migdal parameters:

$$f' = 0.6, g'_{NN} = 0.7, g'_{N\Delta} = g'_{\Delta N} = 0.5, g'_{\Delta\Delta} = 0.5$$

The inclusive RPA responses functions are deduced from the corresponding inclusive RPA polarization propagators by the usual relation:

$$R(\omega, q) = -\frac{1}{\pi} \text{Im}(\Pi(\omega, q, q)) \quad (8)$$

We perform the calculation of the partial RPA responses as follows. Starting from the RPA equation (5), we write the imaginary part of $\Pi(\omega, \mathbf{q}, \mathbf{q}')$ in the following form:

$$\text{Im}(\Pi) = |1 + \Pi V|^2 \text{Im}(\Pi^0) + |\Pi|^2 \text{Im}V \quad (9)$$

with $\text{Im}(\Pi^0) = \sum_{k=1}^{n_k} \text{Im}(\Pi^0(k))$. This sum rule gives the different contributions to the inclusive RPA response functions. The first terms in eq. (9) are reminiscent of the bare case. Indeed we recognize the bare partial response functions (apart from the trivial $-\pi$ factor) corrected by a factor involving the inclusive RPA polarization propagator and the effective interaction. The partial RPA response functions, defined by:

$$R(k)(\omega, q) = -\frac{1}{\pi} |1 + \Pi V|^2 \text{Im}(\Pi^0(k)(\omega, q, q)) \quad (10)$$

are represented by the graphs (a) to (d) on fig. (2), where the hatched rings correspond to the inclusive polarization propagator solution of eq. (5), the non hatched rings to the bare partial polarization propagators (the dotted line means that we take the imaginary part of these propagators) and the dashed lines to the effective interaction. It is easy to recover on these graphs the different terms of the development of eq. (10). Note that in the RPA case, a PP' reaction channel ($P, P' = N, \Delta$) gets contributions from every QQ' configurations ($NN, N\Delta, \Delta N, \Delta\Delta$). The last term in eq. (9) corresponds to the "coherent" response function:

$$R_{coh}(\omega, q) = -\frac{1}{\pi} |\Pi|^2 \text{Im} V \quad (11)$$

It is absent of the response spectrum when the effective interaction is switched off. In the domain of energy considered here the sole contribution to this channel comes from the pion exchange. This process corresponds to the emission of a pion on its mass-shell, the nucleus remaining in its ground state. It is represented by the graph (e) on fig. (2) where the dashed line stands for the exchange of a pion. The implications of these partial reaction channels will be discussed in the following sections.

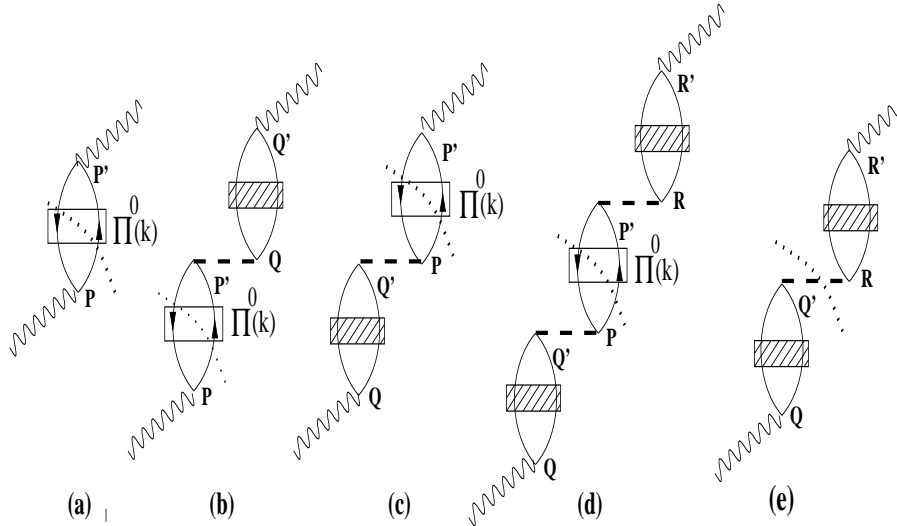


Figure 2: *Graphic representation of the partial RPA response functions. (a)-(d): incoherent partial response functions. (e): coherent partial response function. The hatched rings correspond to the inclusive RPA polarization propagator, the free rings to the partial bare polarization propagators, the dashed line to the effective interaction and the dotted line indicates which intermediate state is placed on-shell.*

3 Cross sections

The next step is the calculation of the neutrino-oxygen cross section. The doubly differential cross section is given in a first approximation by eq. (1). Our final calculation relies on a more complete expression, which we will briefly describe in the following, but the main features remain unchanged. First it is essential to note that the neutrino-nucleus reaction is strongly dominated by the transverse spin-isospin channel. This is clear from eq. (1). Indeed the terms multiplying the transverse responses, depending on the axial and magnetic form factors, have a much larger magnitude than for the longitudinal case. Furthermore the NN quasi-elastic spin-isospin longitudinal response is totally suppressed in the cross section. This suppression arises from an exact cancellation at the top of the quasi-elastic peak between the various terms entering the contraction of the leptonic and the hadronic tensors. This suppression is only partial in the Delta resonance or in the "dip" region (the region intermediate between the quasi-elastic and the Delta peaks). This result is in contradiction with the study of ref. [16] where the relative weights of the transverse to the longitudinal responses were assumed to be 2:1. Note however that the suppression of the NN longitudinal response is no more exact when one considers the complete expression of the doubly differential cross section, which includes the terms involving the charged lepton mass (in fact we consider only the muon mass) and the terms up to order $(p/M)^2$ in the reduction of the hadronic current. The contributions of the NN longitudinal response are then of order $(m_l/M)^2$, where m_l denotes the mass of the charged lepton, and of order (p/M) . These corrections are rather weak. As another source of corrections we have also considered the renormalization of the axial charge by the mesonic exchange currents, because the suppression of the NN longitudinal response involves the time component of the axial current. Following the parameterization of ref. [17] we make the replacement $g_A \rightarrow g_A(1 + \delta)$ in the time component of the axial current. The contribution of the NN longitudinal response is then of order δ^2 . Even with the relatively high value $\delta \sim 0.5$ suggested in ref. [18], the contribution of the NN longitudinal response remains weak. The same conclusion holds for the $N\Delta$ and $\Delta\Delta$ longitudinal responses which are widely dominated by the corresponding transverse ones. Note that in the antineutrino-nucleus reactions the weight of the transverse channel is somewhat reduced because of the change in sign in the interference term. However even in this case, the transverse responses correspond to 75 % of the total, the remaining arising essentially from the NN pure isospin response.

We will now investigate the implications of these global features on the simply differential cross section $\partial\sigma/\partial k'$, which is obtained from the doubly differential cross section by a numerical integration over the solid angle. The great interest of our method is the separation of the inclusive cross section on partial contributions. This separation is simply achieved by the replacement, in the expression of the cross section, of the inclusive response functions with the "exclusive" ones, calculated in the previous section. The results are shown on fig. (3) which displays the simply differential cross section versus the energy transfer, fixing for the sake of illustration a neutrino energy of 700 MeV.

The inclusive cross section is given by the thick curve. It gets its main contribution from the NN quasi-elastic channel (thin full line) which peaks at relatively low energy transfer. For the sake of comparison we have shown the contribution of the NN quasi-elastic channel without RPA (thin long dashed line). We observe that the cross section is reduced and hardened in the RPA case. This result is in full agreement with that of ref. [7]. The shift in strength reflects the dominance of the transverse response. Indeed the Landau-

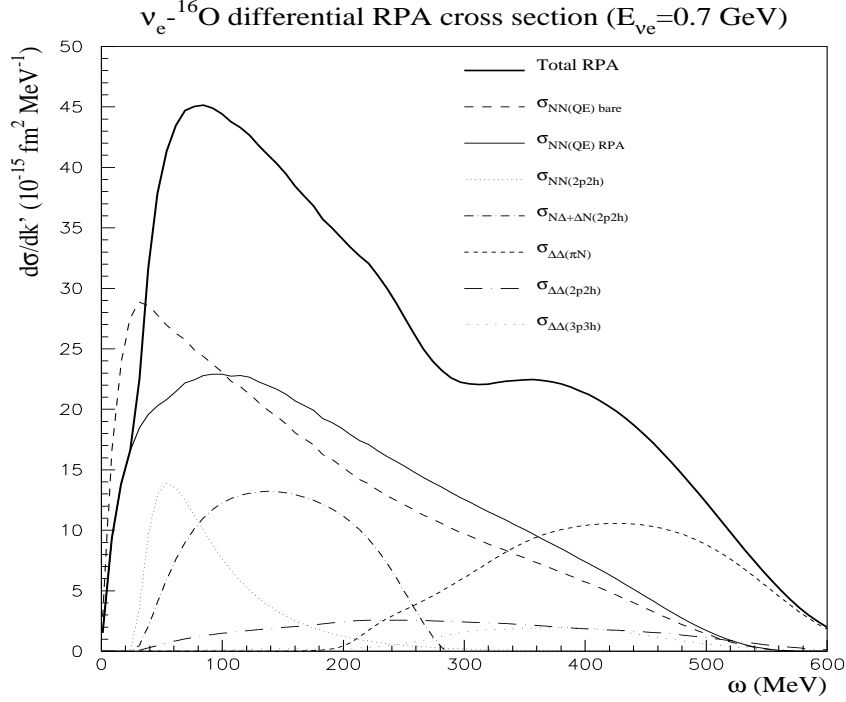


Figure 3: *Differential charged current ν_e - ^{16}O interactions cross-section versus the energy transfer. The thick curve represents the inclusive cross-section. The following exclusive contributions to the inclusive cross-section are displayed: NN (quasi-elastic) (full thin curve), NN (2p-2h) (short dotted curve), $\text{N}\Delta + \Delta\text{N}$ (2p-2h) (short dot-dashed curve), $\Delta\Delta$ (πN) (short dashed curve), $\Delta\Delta$ (2p-2h) (long dot-dashed curve) and $\Delta\Delta$ (3p-3h) (long dotted curve). Also shown is the "bare" NN quasi-elastic cross-section (long dashed curve).*

Migdal interaction is repulsive for all values of the transfer and the ρ -exchange piece is not attractive enough in the domain of energy considered here to counteract this feature. This repulsive effective interaction hardens and reduces the transverse response functions. For instance this conclusion no longer holds in the longitudinal channel where the π -exchange is attractive enough to overcome the Landau-Migdal interaction and to create a collective mode (the so-called *pionic branch* [5,6]). But, as we mentioned previously, the suppression of the longitudinal channel makes the neutrino a poor probe of this pionic mode.

The effect of the RPA correlations are less strong in the others channels and are not shown here. The $\Delta\Delta$ (πN) channel (short dashed curve on the figure) arises at high energy transfer ($\omega \sim 450 \text{ MeV}$). This is in good agreement with the result of the relativistic calculations given in ref. [6] where the Delta was taken into account as a free resonance and where the RPA correlations did not include Delta-hole configurations. The agreement between the two calculations is not surprising. Indeed we use relativistic kinematics for the evaluation of the polarization propagators as in ref. [5,6] and we include the terms up to second order in the (p/M) reduction of the hadronic current as mentioned above. Furthermore the RPA effects on the transverse response in the Delta region, that is at high transfer, are somewhat reduced in the cross section by the form factors and the differences between RPA and bare transverse response functions are very weak at these values of the transfer. Thus our calculations show

that a free Delta resonance gives a rather good approximation of the $\Delta\Delta$ (πN) (or "quasi-elastic") channel. This result corroborates the fact that the "quasi-elastic" Delta width in the nuclear medium is close to the its free value, the Pauli blocking being cancelled by the other mechanisms taken into account.

The most interesting feature of the cross section is the importance of the ($np-nh$) channels. The kinematics of the neutrino-nucleus reaction tends to favor the NN ($2p-2h$) channel (short dotted curve) which peaks at low energy transfer. However the $N\Delta + \Delta N$ ($2p-2h$) channel (short dot-dashed curve) gives a rather large contribution to the inclusive cross section and has an extended spectrum in the "dip" region. Its importance has been pointed out in the (e, e') scattering where it is necessary to reproduce the experimental data in the "dip" region (for example see ref. [19]). Finally note that the $\Delta\Delta$ ($2p-2h$) (long dot-dashed curve) and ($3p-3h$) (long dotted curve) spectra extend over a wide range of energy transfer, while the $\Delta\Delta$ (πN) channel is concentrated in the so-called Delta peak. They give a little contribution to the inclusive cross section (in particular the ($3p-3h$) channel is rather weak) but the extension of their spectra will have important consequences in the specific events yields.

The results obtained in this section show that the inclusive neutrino-oxygen cross section is strongly modified with respect to the free NN quasi-elastic case, which is quite often the sole channel entering into the calculations. In particular we have seen the occurrence of large contributions from the two- and three-body channels. The main effect of the nuclear correlations is the hardening of the NN quasi-elastic channel. They have rather low impact on the others reaction channels and therefore could be legitimately neglected.

4 Events yields

In this section we compute numerically the neutrino-oxygen events yields for a fixed charged lepton momentum:

$$Y(\nu_\alpha + \bar{\nu}_\alpha)(k') = \int_{E_{k'}}^{\infty} dE \left(\Phi_{\nu_\alpha}(E) \frac{\partial\sigma}{\partial k'}(E, k') \Phi_{\bar{\nu}_\alpha}(E) \frac{\partial\bar{\sigma}}{\partial k'}(E, k') \right) \quad (12)$$

where E is the neutrino energy, Φ_ν ($\Phi_{\bar{\nu}}$) the incoming neutrinos (antineutrinos) flux and $\partial\sigma/\partial k'$ ($\partial\bar{\sigma}/\partial k'$) the neutrino-oxygen (antineutrino-oxygen) cross section computed in the previous section. We use the fluxes of Bartol [20] in our calculations for the sake of comparison with the results of ref. [7]. The main feature of these fluxes is their sharp decrease with increasing neutrino energy. Note that several theoretical attempts have been undertaken to compute these atmospheric neutrinos fluxes. The sources of possible differences between three models have been analyzed in ref. [21]. The predictions of these models on the flavor ratio agree at a ~ 5 % degree of accuracy. Anyway the divergences in the absolute fluxes remain rather large (~ 20 %). Furthermore new measurements on the primary cosmic rays fluxes could lead to some modifications with respect to the present situation. The cumulated uncertainties on the neutrino fluxes and on the neutrino-oxygen cross sections could lead to modifications in the experimental analysis, even if they remain unlikely to explain the atmospheric neutrinos anomaly. To perform an analysis of the events yields, we need to classify the partial reaction channels according to the number of Čerenkov ring(s) they produce. This classification has been elaborated within a few rough assumptions. First we consider that every nucleon ejected from the nucleus remains under Čerenkov threshold. In

water, the threshold kinetic energy for a particle of mass m is $E \sim 0.5 m$. For a nucleon, produced through Delta decay or $(2p-2h)$ mechanisms, the assumption is fairly good. On the opposite, we assume that every pion which escapes the nuclear medium produces a Čerenkov ring. The threshold energy for a pion being ~ 70 MeV, this assumption is believed to be reliable. Then the partial reaction channels leading to one Čerenkov ring, in charged current interactions, are the NN quasi-elastic one, which is usually taken into account in the simulations, and the $(np-nh, n>1)$ type channels (both NN , $N\Delta$, ΔN and $\Delta\Delta$). The remaining reaction channels, $\Delta\Delta$ (πN) and coherent pion production, are supposed to lead to at least two Čerenkov rings. The results for the 1 Č.R. events yields, which are relevant in the atmospheric neutrino experiments, are shown on fig. (4) for incident ν_μ and $\bar{\nu}_\mu$, the full curves corresponding to the total 1 Č.R. events yields and the dashed curves to the sole NN quasi-elastic 1 Č.R. events yields. We give the results of the calculations without (thin curves) and with (thick curves) RPA.

First we observe that the RPA tends to reduce the events yields. This is not hard to understand. Indeed the RPA tends to harden the cross sections, *i.e.* to push the strength towards higher energies. But the fluxes decrease with increasing energies and therefore the higher energies are disfavored. This reduction affects mostly the NN quasi-elastic channel in accordance with the result obtained for reaction cross sections. The maximal reduction factor is of the order of 10 %. A more interesting feature is the strong enhancement of the absolute events yields implied by the $(np-nh)$ channels. At the maximum value of the yields, the enhancement of the total yield with respect to the NN quasi-elastic one is around 30 %. This result reflects the main features of the cross sections. Furthermore one must be aware that this result is a lower limit of the true enhancement. Indeed we know that pions can be re-absorbed in the nu-

cleus. Therefore the events produced in the $\Delta\Delta$ (πN) channel can also lead to one Čerenkov ring if the pion does not escape from the nucleus. Thus we can conclude that the RPA 1 Č.R. events yields induced by charged current interactions is globally enhanced with respect to the NN quasi-elastic 1 Č.R. events yields without RPA. The difference between the two calculations could be responsible for the small discrepancy between the experimental and simulated events distributions in Super-Kamiokande ². But we need complementary informations to ensure this conclusion. Indeed it is hard to establish the enhancement factor firmly. Our present analysis leads to a maximum enhancement factor of the order of ~ 20 %. We have

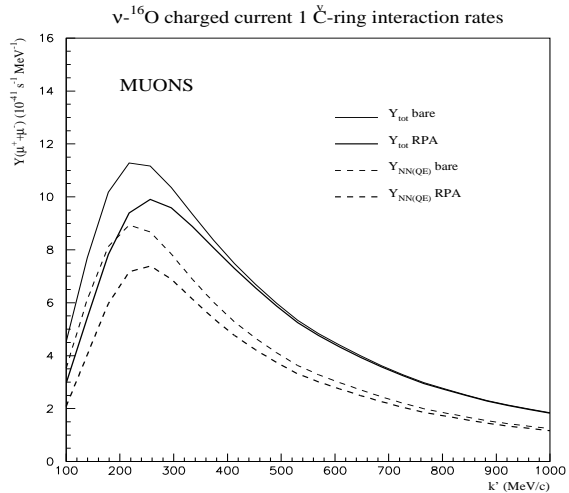


Figure 4: *One Čerenkov $(\nu_\mu + \bar{\nu}_\mu) - {}^{16}\text{O}$ events yields versus the muon momentum. The full curves correspond to the total 1 Č.R. events yields with (thick curve) and without (thin curve) RPA. The dashed curves correspond to the NN quasi-elastic 1 Č.R. events yields with (thick curve) and without (thin curve) RPA.*

²We thank Y. Declais for attracting our attention on this point.

already mentioned that the problem of pion absorption, which is not yet considered in our calculations, could still enhance this factor. We should also be aware that there exists some misidentification problems which could have a more or less large effect. One of the misidentification source, pointed out by the authors of ref. [6], is the "coherent" pion production. Their analysis is based on the assumption that the forward peaked angular distribution of the coherent pions entails the coherent pions to be emitted with a small angle with respect to the charged lepton direction. This could mimic a "shower" which could be interpreted as an $e -$ type event, whatever may be the flavor of the incoming neutrino. Our calculations show that this coherent channel brings a tiny contribution (less than 2 % of the total $\nu_e + \bar{\nu}_e$ events yield) which makes it irrelevant in the atmospheric neutrino anomaly. The suppression of this channel is understandable. Part of it is due to the nuclear form factors effects as discussed for example in [22]. In addition the coherent response manifests itself mainly in the longitudinal spin-isospin channel and we have seen that this channel is suppressed with respect to the transverse one in the neutrino-nucleus reactions. The coherent pions should not be a problem.

The case of the neutral currents is less clear. In charged current interactions, pions ("coherent" or not) lead to, at least, 2 Č.R. events and are excluded from the analysis. But in neutral currents interactions they lead to 1 Č.R. events, because the scattered neutrino does not produce any ring. We have computed the neutral current events yields in each reaction channel, the few differences with respect to the charged current case being easily included in the formalism. The problem arising then is the classification of these $\pi -$ like 1 Č.R. events. Indeed in absence of indication on the experimental π /lepton discrimination efficiency in the water Čerenkov experiments, it is not possible to draw firm conclusions on the role played by the neutral currents. This problem has to be investigated further (for more details on the results of the calculations, see [23]).

Finally we study the evolution of the flavor ratio with the charged lepton momentum:

$$R_{\mu/e}(k') = Y(\nu_\mu + \bar{\nu}_\mu)/Y(\nu_e + \bar{\nu}_e), \quad (13)$$

where Y denotes the events yields defined by eq. (12). We compare the total 1 Č.R. events yields flavor ratio with the NN quasi-elastic 1 Č.R. events yields flavor ratio. The result is shown in table (1) where the ratio of ratios has been calculated for four relevant lepton momentum. There is almost no modification between the two situations. This conclusion strengthens the usual assumption that uncertainties due to nuclear effects cancel when one considers ratios of events rates. Here the maximum effect on the flavor ratio is less than 10 %.

| k' (MeV/c) | $R_{\mu/e}(NN \text{ } q.e.)/R_{\mu/e}(Total)$ |
|--------------|--|
| 100 | 1.060 |
| 150 | 1.040 |
| 250 | 0.999 |
| 400 | 1.001 |

Table 1: *Comparison of the total and NN quasi-elastic 1 Č.R. events yields ratios for four lepton momentum.*

We conclude this work by mentioning the problem of pion emission in neutrino-oxygen interactions. On one side we have shown that the cross sections of the $\Delta\Delta$ ($2p-2h$) and ($3p-$

$3h$) partial channels, which do not lead to pion emission (*non pionic* channels), extend over a broad region in transfer energy, while the *pionic* channel $\Delta\Delta$ (πN) is peaked at high transfer energy (see fig. (3)). On the other side the neutrino flux lowers the weight of the high energies and favors the low energy components of the spectrum. Then the pionic $\Delta\Delta$ channel will be more suppressed by the incident neutrino flux than the non pionic one. This result is shown on fig. (5) where the total $\Delta\Delta$ events yield (full thick curve) is split into its three contributions: (πN) (full thin curve), $2p$ - $2h$ (dashed curve), $3p$ - $3h$ (dotted curve) in the case of μ - type events.

The main result is that the fraction of the non pionic channels over the pionic one is around 50 %. This result remains valid for every values of the lepton momentum. Thus the (np - nh) excitations play an important role in the events yields although their reaction cross sections are relatively low. Finally we would like to point out that some pion production mechanisms, which do not reduce to a simple response function, are still absent of our formalism. For example we have omitted in the production through the vector current, the Kroll-Ruderman and the pion-in-flight terms which play an important role. Improvements to our present calculations are in progress. Nevertheless these limitations of our present calculations do not alter the need of including the effects of the partial $\Delta\Delta$ (np - nh) reaction channels to avoid an overestimation of the number of pions effectively produced in the neutrino-oxygen interactions.

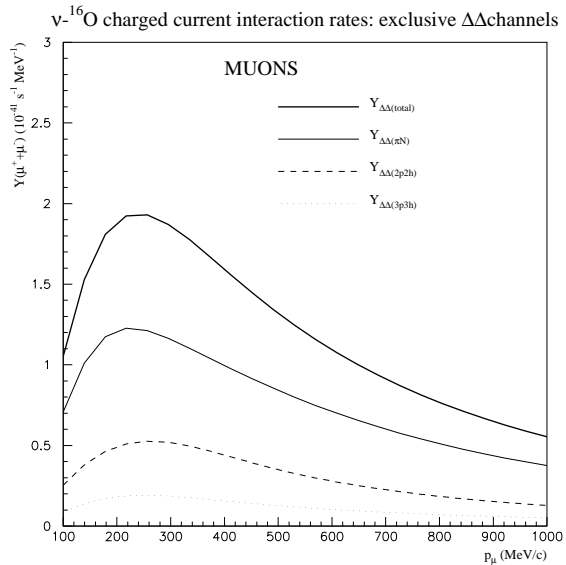


Figure 5: Contributions to the total $\Delta\Delta$ events yield (full thick curve) of the partial channels: (πN) (full thin curve), ($2p$ - $2h$) (dashed line), ($3p$ - $3h$) (dotted line).

5 Conclusion

In this work we have studied the effects of nuclear correlations on the charged current neutrino-oxygen cross sections and events yields in specific exclusive reaction channels. We have shown that besides the quasi-elastic channel the (np - nh , $n=2,3$) excitations also lead to one Čerenkov ring events, which are retained for the analysis of the experiments using large underground water Čerenkov detectors. The enhancement in the one Čerenkov ring events yields is large and could still be increased when some processes, such as pion absorption in nuclei or neutral currents events, are taken into account. It is therefore important to take these nuclear effects into account to perform a calculation of absolute events yields. We have also shown that the flavor ratio $R_{\mu/e}$ is not significantly altered. We have applied our model to others neutrino-nucleus reactions. In particular we have studied the case of iron which is the target-nucleus in the neutrino experiments using calorimeters. The conclusion on the

cross sections are the same than the one presented here in the case of oxygen. However such experiments measure more detailed observables than the water Čerenkov detectors, like the energy and momentum spectra of the particles in the final state. The description of these experiments requires the extension of our model. The present work already shows the necessity of taking into account nuclear correlations involving multi-nucleon excitations.

Acknowledgements

We wish to gratefully acknowledge J. Delorme for his numerous contributions to this work. We are indebted for enlightening discussions and critical reading of the manuscript to J. Delorme, M. Ericson and G. Chanfray. We also thank Y. Declais, P. Lipari and S. Katsanevas for stimulating discussions.

References

- [1] Y. Fukuda *et al.*, Phys. Lett. B**335**, 237(1994); K.S. Hirata *et al.*, Phys. Lett. B**280**, 146(1992).
- [2] Y. Fukuda *et al.*, Phys. Lett. B**433**, (1998) 9; Phys. Rev. Lett. **81**, (1998) 1562.
- [3] R. Becker-Szendy *et al.*, Nucl. Phys. B**38**, 331(1995); Phys. Rev. D**46**, 3720(1992).
- [4] W.W.M. Allison *et al.*, Phys. Lett. B**391**, 491(1997).
- [5] M. Apollonio *et al.*, Phys. Lett. B**420**, 397(1998).
- [6] H. Kim, S. Schramm, C.J. Horowitz, Phys. Rev. C**53**, 3131(1996).
- [7] J. Engel, E. Kolbe, K. Langanke, P. Vogel, Phys. Rev. D**48**, (1993) 3048.
- [8] N. Auerbach, N. Van Giai, O.K. Vorov, Phys. Rev. C**56**, 2368(1997).
- [9] E. KOLBE, K. LANGANKE, S. KREWALD, F.K. THIELEMANN, Nucl. Phys. A**450**, 599(1992); E. KOLBE, K. LANGANKE, F.K. THIELEMANN, P. VOGEL, Phys. Rev. C**52**, 3437(1995).
- [10] G.F. Low, *et al.*, Phys. Rev. **106**, (1957) 1345.
- [11] J. Delorme, P.A.M. Guichon, in *Proceedings of 10^e biennale de physique nucléaire, Aussois, march 6-10, 1989*, rapport LYCEN 8906, p. C.4.1, also in the *Proceedings of the 5th french-japanese symposium on nuclear physics, Dogashima, Izu, september 26-30, 1989*, edited by K. Shimizu and O. Hashimoto, p.66.
- [12] J. Delorme, P.A.M. Guichon, Phys. Lett. B **263**, 157(1991).
- [13] I. Laktineh, W.M. Alberico, J. Delorme, M. Ericson, Nucl. Phys. A**555**, (1993) 237.
- [14] E. Oset, L.L. Salcedo, D. Strottman, Phys. Lett. **165B**, 13(1985).
- [15] K. Shimizu, A. Faessler, Nucl. Ph. A**333**, 495(1980).

- [16] E. Oset, S.K. Singh, Nucl. Phys. A **542**, 587(1992).
- [17] E.K. Warburton, Phys. Rev. C **44**, 233(1991); Phys. Rev. Lett. **66**, 1823(1991).
- [18] I.S. Towner, Phys. Lett. B **233**, 13(1994).
- [19] W. M. Alberico, M. Ericson, A. Molinari, Nucl. Phys. A**379**, 429(1982); Ann. Phys. (N.Y.) **154**, 356(1984).
- [20] G. Barr, T.K. Gaisser, T. Stanev, Phys. Rev. D**39**, 3532(1989).
- [21] T.K. Gaisser, M. Honda, K. Kasahara, H. Lee, S. Midorikawa, V.A. Naumov, T. Stanev, Phys. Rev. D**54**, 5578(1996).
- [22] T. Ericson, W. Weise, *Pions and nuclei*, Oxford Science Publications, 1988.
- [23] J. Marteau, PhD thesis, Université Claude Bernard Lyon-I, report LYCEN T9877.

1.3 A unified approach for nucleon knock-out, coherent and incoherent pion production in neutrino interactions with nuclei [9]

M. Martini^{1,2,3}, M. Ericson^{1,3}, G. Chanfray¹ and J. Marteau¹

¹ Université de Lyon, Univ. Lyon 1, CNRS/IN2P3,
IPN Lyon, F-69622 Villeurbanne Cedex, France

² Università di Bari, I-70126 Bari, Italy

³ Theory Group, Physics Department,
CERN, CH-1211 Geneva, Switzerland

Abstract

We present a theory of neutrino interactions with nuclei aimed at the description of the partial cross-sections, namely quasi-elastic and multi-nucleon emission, coherent and incoherent single pion production. For this purpose, we use the theory of nuclear responses treated in the random phase approximation, which allows a unified description of these channels. It is particularly suited for the coherent pion production where collective effects are important whereas they are moderate in the other channels. We also study the evolution of the neutrino cross-sections with the mass number from carbon to calcium. We compare our approach to the available neutrino experimental data on carbon. We put a particular emphasis on the multi-nucleon channel, which at present is not easily distinguishable from the quasi-elastic events. This component turns out to be quite relevant for the interpretation of experiments (K2K, MiniBooNE, SciBooNE). It can account in particular for the unexpected behavior of the quasi-elastic cross-section.

PACS: 25.30.Pt, 13.15.+g, 24.10.Cn

1 Introduction

Neutrino physics has undergone a spectacular development in the last decade, following the discovery of neutrino oscillations first revealed by the anomaly of atmospheric neutrinos [1]. A number of results on the interaction of neutrinos with matter are now available. Neutrino detectors do not usually consist of pure hydrogen but they involve complex nuclei for instance ^{12}C , as in SciBar [2], where the molecule C_8H_8 is involved, or in MiniBooNE [3] which uses the mineral oil CH_2 . Heavier nuclei are also under consideration for instance in the liquid argon chamber planned for T2K [4, 5]. A number of results have been obtained, for neutral or charged current (K2K, MiniBooNE, SciBooNE) on quasi elastic processes or coherent and incoherent single pion production [6, 7, 8, 9, 10, 11, 12, 13, 14, 15, 16, 17]. The first question is then if our present understanding of neutrino interactions with matter can reproduce the available data. Many works [18, 19, 20, 21, 22, 23, 24, 25, 26, 27, 28, 29, 30, 31, 32, 33, 34, 35, 36] have been devoted to this problem, using various theoretical approaches [37, 38, 39, 40, 41,

42, 43, 44, 45, 46, 47, 48, 49, 50, 51, 52, 53, 54, 55, 56, 57, 58, 59, 60, 61, 62, 63, 64]. In this article we will explore such interactions using the theory of the nuclear response treated in the random phase approximation (RPA) in the quasi-elastic and Delta resonance region including also two and three nucleon knock-out. The formalism is the same as the one used by Marteau [38] in his work on the ν - ^{16}O interaction. The merit of this approach is that, although perfectible in several ways, it describes in a unique frame several final state channels. This technique has been successful in a number of problems involving either weakly interacting probes such as (e,e') scattering or strongly interacting ones such as pion scattering or $(^3\text{He},T)$ charge exchange reaction [65]. We give the cross-sections for pion production, coherent or incoherent, and nucleon knock-out, for neutral or charged currents. We restrict to single pion production ignoring two-pion production processes which, for real photons, lead to a sizable part of the photo-absorption cross-section at energies larger than the Delta resonance, above $\simeq 500$ MeV. Our treatment should thus underestimate the cross-section when multi-pion production starts to show up. Our work ignores as well the meson exchange effects which play a non negligible role [66, 67]. We only take into account the exchange effect in the time component of the axial current, which is known to be important [68]. For single pion production we assume that the dominant production mechanism is via the Delta resonance, ignoring the other resonance excitations, which also limits the energy for the validity of our approach. Beyond quasi-elastic processes and single pion production via Delta excitation we also incorporate several nucleon knock-out through two-particle-two-hole ($2p-2h$) and $3p-3h$ excitations. These will play a crucial role in the comparison with data involving quasi-elastic events.

Among the aims of this work there is the exploration of the evolution of the neutrino-nucleus interaction as the mass number of the nucleus goes from the carbon region to the region of ^{40}Ca . This investigation is motivated by the project of a liquid argon chamber in the T2K experiment which raises the question if one keeps control of the understanding of the interaction of neutrinos with matter by going to a medium-weight nucleus such as ^{40}Ar . In order to single out the evolutions linked to the nuclear size we have chosen as element of comparison an isoscalar nucleus in the ^{40}Ar region, namely ^{40}Ca . For the coherent process which per nucleon fades away in heavy nuclei, the evolution is relatively rapid but should remain under control as our theory is particularly well adapted to this channel. The other exclusive channels, in particular the incoherent pion production, are sensitive to final state interaction not automatically included in our approach. This leaves some uncertainty in the evolution between the mass 12 and the mass 40 region for this channel.

Our article is organized as follows: Section 2 introduces the formalism of the response functions treated in the random phase approximation (RPA). Section 3 discusses the various final state channels. In Sec. 4 we compare these predictions with the available data. In Sec. 5 we provide a summary and conclusion of the present work.

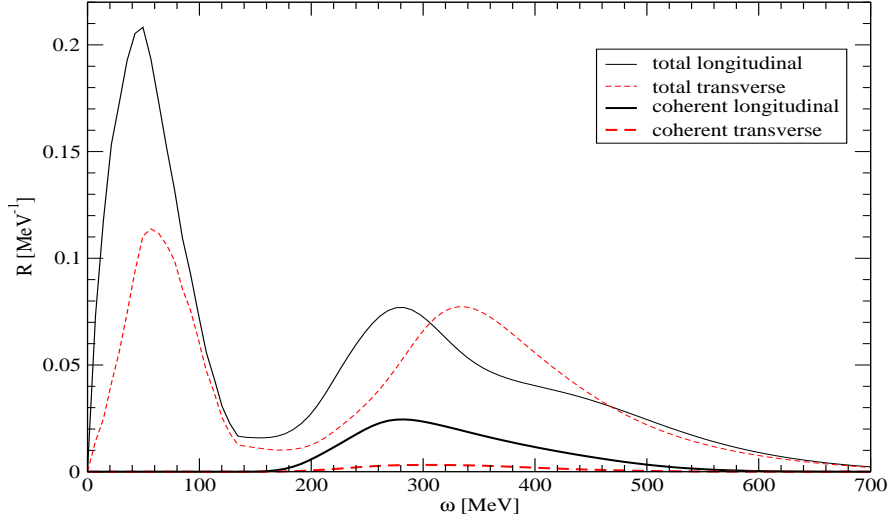


Figure 5: Longitudinal and transverse total responses of ^{12}C at fixed $q = 300 \text{ MeV}/c$ as a function of ω . The coherent part of the responses is also shown.

3 Results

3.1 Coherent cross-section

Several types of responses enter the total neutrino cross-section, isovector, spin-isospin: transverse or longitudinal. The last quantity is naturally associated with the coherent process, since it has the same coupling as the pion. The production by a transverse spin coupling requires a transverse-longitudinal conversion which is partly suppressed. This difference is illustrated in Fig. 5 where the total responses, longitudinal and transverse, of ^{12}C are displayed as a function of the energy transferred to the nuclear system for a fixed three-momentum $q = 300 \text{ MeV}/c$. The coherent component, much larger in the longitudinal case, is also shown.

Figure 6 illustrates the evolution with the nuclear size of the coherent part of the longitudinal response *per nucleon* as a function of the energy at fixed momentum for some nuclei, ^{12}C , ^{16}O , ^{40}Ca and also for a fictitious piece of isospin symmetric nuclear matter with the density profile of lead. Two features emerge, the first one is that its magnitude decreases in “lead”, as expected : the coherent response per nucleon vanishes in nuclear matter when the polarization propagators become diagonal in momentum space. The second is that the coherent response is not peaked at the energy $\omega_\pi = (q^2 + m_\pi^2)^{1/2}$ where the mismatch between the incident energy and that of the physical outgoing pion is smallest. Instead it is reshaped by the collective features of the longitudinal response with the appearance of two collective branches on each side of the pion line. This is more apparent in the case of the (fictitious) lead.

As a test of our description of the coherent responses we have investigated the elastic scattering of pions on nuclei in the Delta region, related to the coherent part of the spin-isospin longitudinal response through :

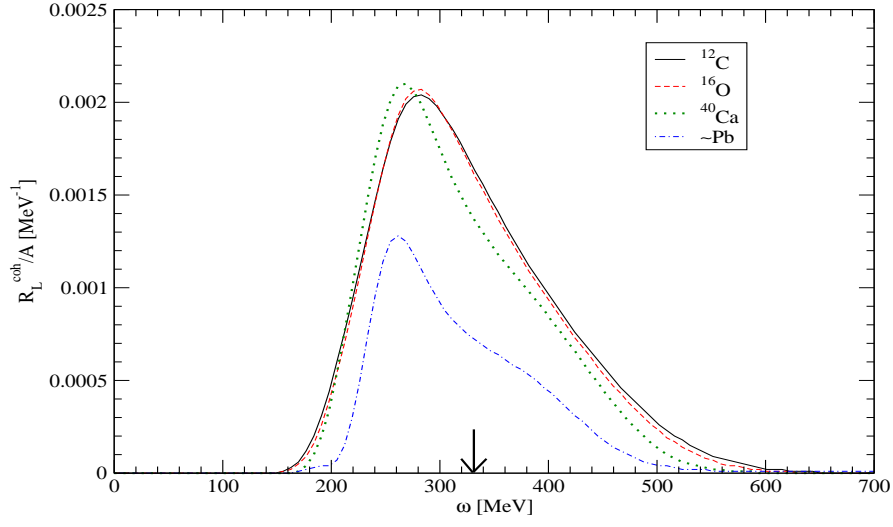


Figure 6: Evolution with the mass number of the coherent longitudinal response per nucleon at fixed $q = 300$ MeV/ c as a function of ω . The arrow indicates the energy for on-shell pion.

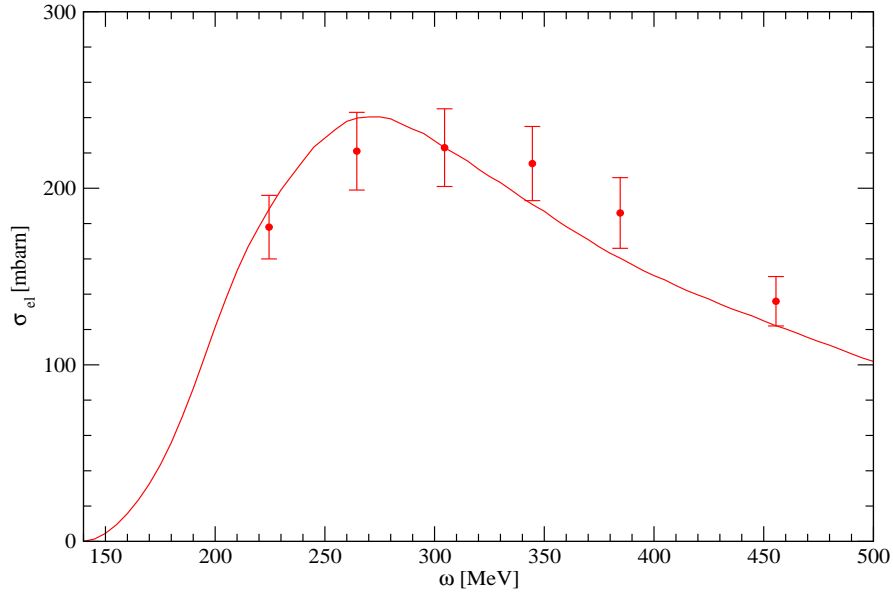


Figure 7: π^- - ^{12}C elastic cross-section as a function of pion energy.

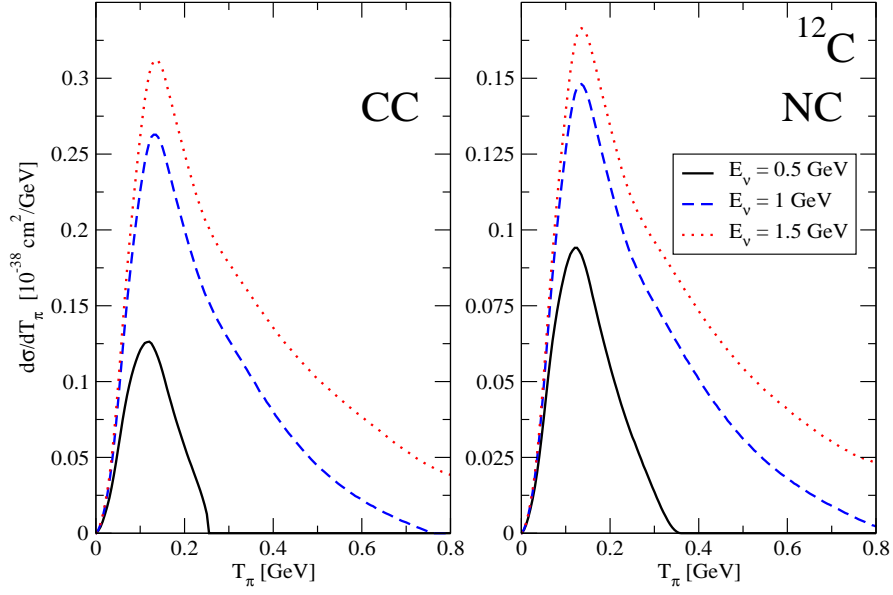


Figure 8: Charged and neutral current coherent pion production differential cross-section off ^{12}C versus pion kinetic energy for several ν_μ energies.

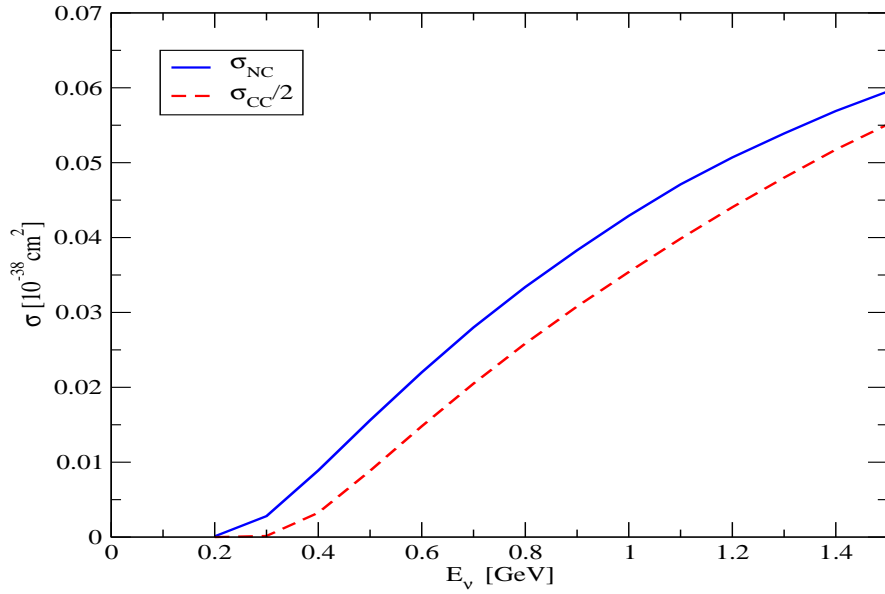


Figure 9: Total CC (divided by 2) and NC ν_μ -induced coherent pion production cross-sections in ^{12}C as a function of neutrino energy.

$$\sigma^{elas}(\omega) = \left(\frac{g_r}{2M_N} \right)^2 \pi q_\pi R_L^{coh}(\omega, q_\pi) \quad (11)$$

where $q_\pi^2 = \omega^2 - m_\pi^2$ and R_L^{coh} refers to the coherent part of the longitudinal response. The resulting cross-section in the case of ^{12}C is shown in Fig.7 together with the experimental points from Ref.[76]. The agreement with data is satisfactory. A similar accuracy can be expected for the coherent response which enters the neutrino cross-section, at least in the energy region for the produced pion where we have tested our model (*i.e.*, between $\omega \simeq 220$ and $\simeq 450\text{MeV}$). The elastic cross-section which depends on the longitudinal response is particularly sensitive to collective effects in this channel known to be important. The replacement of the bare response by the RPA one leads to a different energy behavior, the collective effects producing a softening of the response, characteristic of the collective nature of the longitudinal channel.

Figure 8 displays our evaluations of the neutrino coherent cross-section on ^{12}C as a function of the pion kinetic energy, both for charged and neutral current, for several neutrino incident energies. The resulting total coherent cross-sections are displayed in Fig.9.

The suppression of the meson exchange correction in the time component of the axial current, $G_A^* \rightarrow G_A$, produces a moderate $\simeq 10\%$ increase of the cross-section.

The data available on the coherent production by neutrino concern its ratio to the total cross-section and to the total pion production. We will then postpone the comparison with experimental data after the discussion of the various other channels.

3.1.1 Adler's theorem

In the forward direction where $q = \omega$ and for vanishing lepton mass, only the spin longitudinal response contribution survives. As it also enters in pion scattering, it is possible to relate the forward neutrino cross-section to the cross-section of physical pions, apart from a difference in kinematics: $q = \omega$ (soft pions) for neutrinos, instead of $q = q_\pi = \sqrt{\omega^2 - m_\pi^2}$ for physical pions. This difference becomes less relevant at large energies. This is the content of Adler's theorem [77]. The coherent channel, which is completely dominated by the longitudinal response, offers the best application of this theorem, while for the other channels the transverse component, which bears no relation to pion scattering, quickly takes over as soon as one moves away from the forward direction. This theorem has been used in the approach of Refs. [18] [29] [31] to evaluate the coherent neutrino-nucleus cross-section. This is not our aim here. We want to illustrate the link between the forward direction coherent neutrino cross-section and the elastic pion-nucleus one. For the coherent cross-section Adler's relation writes

$$\left(\frac{\partial^2 \sigma}{\partial \Omega \partial \omega} \right)_{\theta=0}^{coh} = \frac{G_F^2 \cos^2 \theta_c}{\pi^3} f_\pi^2 \frac{E_\nu - \omega}{\omega} \sigma^{elas}(\omega), \quad (12)$$

where $f_\pi = 93.2 \text{ MeV}$ is the neutral pion decay constant. Introducing the experimental values for the elastic cross-section taken from Ref.[76] we obtain the points shown in Fig. 10 together with our predicted curve. The agreement is rather good. It deteriorates at small energies when the kinematical difference between soft and physical pions becomes

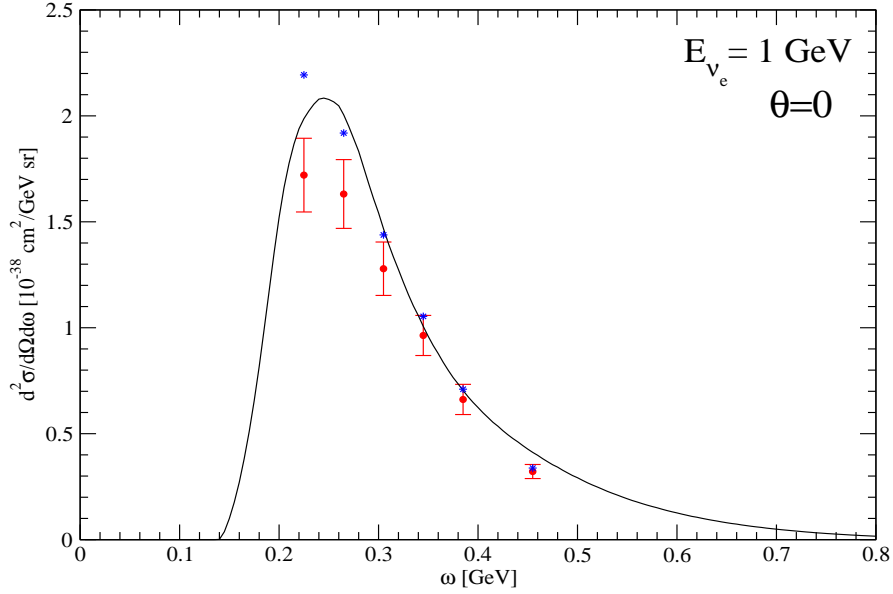


Figure 10: ν_e - ^{12}C coherent cross-section in the forward direction. Continuous line: our result. Circles: deduced, according to Adler's relation of Eq. (12), from the experimental values for the elastic cross-section taken from Ref. [76]. Stars: introducing into the r.h.s. of Eq. (12) the multiplicative factor $\frac{\omega}{q_\pi}$.

substantial. A natural correction can be performed with the introduction into the r.h.s. of Eq.(12) of a multiplicative factor $\frac{\omega}{q_\pi}$ as suggested by the relation of Eq.(11) between R_L and $\sigma^{elas.}$. The corresponding corrected points are also shown in Fig. 10 extending somewhat the region of agreement. The use of the Adler relation becomes problematic at energies near threshold. For small neutrino energy ($E_\nu < 0.5$ GeV) this region has more weight in the total coherent cross-section.

The Adler relation thus provides a good test for our evaluation of coherent neutrino cross-section in the forward direction. We believe that the extrapolation to the non-forward direction as performed in our model should be under control.

3.2 Pion-nucleus cross-sections

The various partial cross-sections for physical pions on nuclei constitute a precious piece of information. Elastic cross-section has already been introduced as a test for the coherent cross-section. The total cross-section for pions on the nuclei is given by an expression similar to Eq.(11) with the full polarization propagator replacing the coherent piece

$$\sigma^{tot}(\omega) = \left(\frac{g_r}{2M_N} \right)^2 \pi q_\pi R_L(\omega, q_\pi). \quad (13)$$

The corresponding cross-section is displayed in Fig.11 together with the experimental points. We will show that in the same way the inelastic cross-section provides some

information on the incoherent pion production by neutrinos and the absorptive cross-section on the multi-nucleon channels. Figure 11 displays the various partial channels (but the elastic one, previously shown) which contribute to the π^+ cross-section on ^{12}C , namely the inelastic pion scattering channel (which is the incoherent scattering with a π^+ in the final state) and the absorptive one. We also display the sum of the incoherent pion (including charge exchange) and true absorption (multi-nucleon channels) cross-sections. The experimental points are taken from Ashery *et al.* [76]. To reduce the clutter, we have not explicitly plotted the charge-exchange cross-section which, in our approach, is one fifth of the inelastic π^+ cross-section and is consistent with the experimental data. While the elastic cross-section was well reproduced, our approach overestimates the π^+ inelastic channel in the peak region and largely underestimates the absorptive channel. We attribute this deficiency to the absence of pion final state interaction as the pion can be reabsorbed on its way out the nucleus. It can also undergo charge exchange process but this is a smaller effect. As a counterpart the absorptive multi-nucleon production is underestimated, as is apparent in Fig.11. The sum of the two channels is instead reasonably well reproduced in the peak region.

These limitations also affect the incoherent neutrino-nucleus cross-section but we stress that, in contradistinction, our description for the coherent channel automatically contains the final state interactions and no further correction is needed. The total neutrino cross-section is also obviously not affected. With the information on the pion energy spectrum in neutrino interactions (that our calculation does not provide) it would be possible to estimate at each energy an attenuation factor for the incoherent neutrino production from the difference between our calculation and inelastic data for physical pions. For instance, for ^{12}C at $E_\nu = 1$ GeV, a rough evaluation of the overall correction for the incoherent production cross-section with the information on the pion spectrum [78] results in a moderate reduction of $\simeq 15\%$. A similar attenuation was found in oxygen at $E_\nu = 500$ MeV and $E_\nu = 750$ MeV [43]. A larger correction is obviously expected for calcium.

3.3 Quasi-elastic and multi-nucleon channels

The quasi-elastic (QE) channel corresponds to a single nucleon knock-out. In the quasi-elastic process the space-like character is pronounced as the quasi-elastic peak occurs at $\omega \simeq \mathbf{q}^2/(2M_N)$, hence the distribution in $Q^2 = \mathbf{q}^2 - \omega^2$ is rather broad [9]. At zero order only R^{NN} contributes to this channel. In the RPA chain instead $R^{N\Delta}$ and $R^{\Delta\Delta}$ also participate. For instance the lowest order contribution of $R^{N\Delta}$ is illustrated in Fig. 12.

In contrast to the coherent channel, the quasi-elastic one is totally dominated by the transverse response. The longitudinal contribution is suppressed by a cancellation between the space and time components of the axial current, as observed by Marteau [38] and shown in Appendix A.1 for vanishing lepton mass and neglecting the Fermi momentum. Numerically its contribution is indeed very small. We have tested our semi-classical approximation on the bare QE $\nu_e - ^{12}\text{C}$ cross-section through a comparison with the one obtained by Martini *et al.* [53] in the continuum shell model where the mean field is produced by a Woods-Saxon well. Our result is very similar in shape and magnitude to the one of [53] but for a displacement in energy of 27 MeV. This reflects the inclusion of the nucleon separation energy in the continuum shell model, which is ignored in our

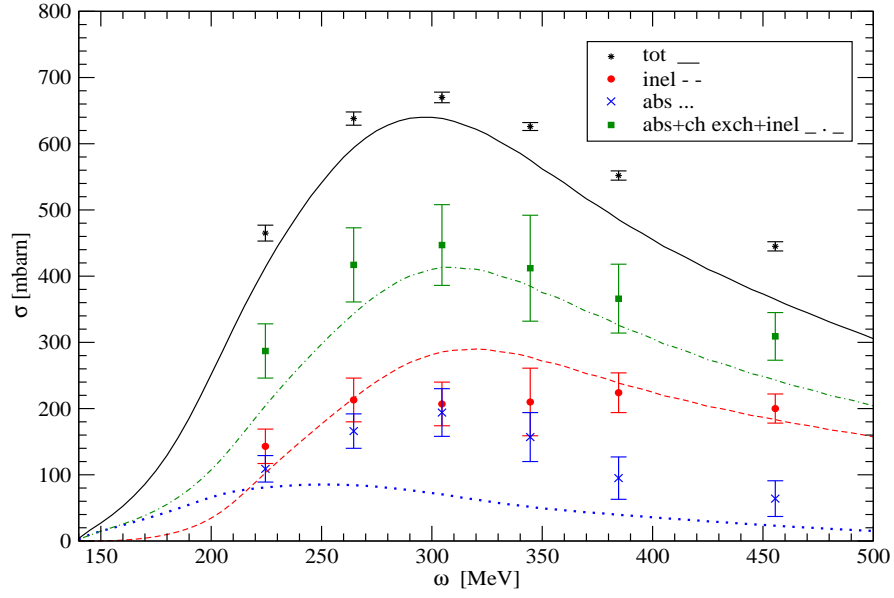


Figure 11: Partial and total π - ^{12}C cross-sections.

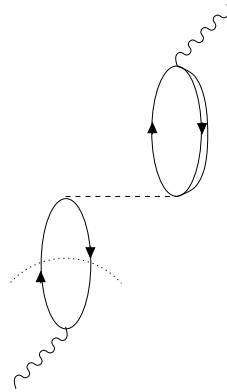


Figure 12: Lowest order contribution of $R^{N\Delta}$ to the quasi-elastic channel.

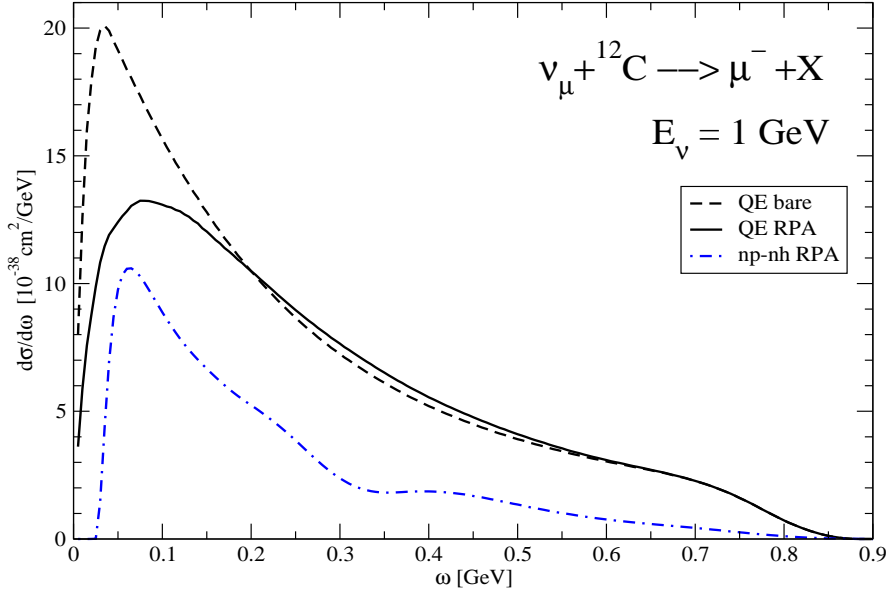


Figure 13: Differential CC $\nu_\mu - {}^{12}\text{C}$ cross-section versus the energy transfer for quasi-elastic process (bare and RPA) and multi-nucleon emission ($np - nh$).

approximation.

The quasi-elastic cross-section is displayed in Fig. 13 as a function of the energy transfer for neutrino energy $E_\nu = 1$ GeV, both in the bare case and in the RPA one. The RPA influence produces a reduction, as expected from the repulsive character of the particle-hole interaction, which prevails in the transverse channel. This reduction is mostly due to the interference term $R^{N\Delta}$ which is negative (Lorentz-Lorenz effect [79]).

The total quasi-elastic charged current and neutral current cross-section are plotted in Figs.14 and 15 as a function of the neutrino energy. In Figs. 13, 14 and 15 we also display the sum of the two- and three-nucleon knock-out cross-sections, which represents a sizable fraction of the quasi-elastic one. Singling out the genuine quasi-elastic process requires the insurance that no more than one proton is ejected. This question will appear in the comparison with data. Among the various contributions to the multi-nucleon channel the ones which do not reduce to a modification of the Δ width are dominant. The accumulation of $2p-2h$ strength at low energy is an artifact of the simplified extrapolation that we use in this channel. In Section 4.3 this point is discussed in more detail and another method for the parametrization, with an explicit momentum dependence, is introduced. It modifies the ω dependence of $\frac{d\sigma}{d\omega}$, spreading the strength over a larger energy region, but does not substantially affect the energy integrated cross-section.

Coming now to the evolution of these channels between ${}^{12}\text{C}$ and ${}^{40}\text{Ca}$ we compare the corresponding RPA differential cross-sections per neutron for the two nuclei in Fig. 16. One can see that the evolution of this quantity with the mass number is quite weak in the QE case. It is also weak in the multi-nucleon channel although it should increase faster with density than the quasi-elastic one. However, between a light system such as ${}^{12}\text{C}$ and ${}^{40}\text{Ca}$ the evolution is moderate. Only in the case of deuteron one expects the

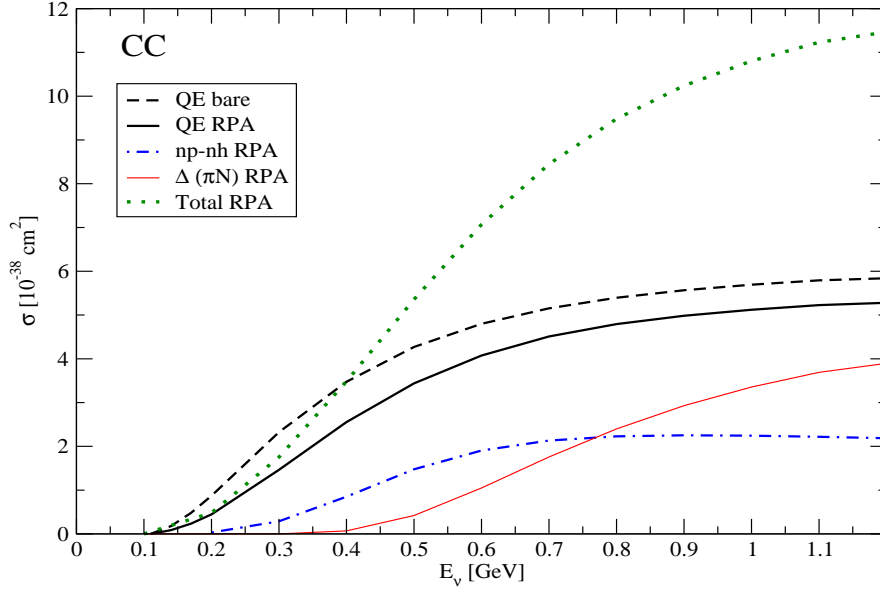


Figure 14: CC $\nu_\mu - {}^{12}\text{C}$ QE, multi-nucleon ($np - nh$), incoherent pion emission and total cross-section as a function of neutrino energy.

multi-nucleon knock-out to be appreciably smaller in view of the loose binding of the system.

3.4 Incoherent pion emission

The pion arises from the pionic decay of the Delta leaving the nucleus in a $p - h$ excited state. For the nuclei that we consider this cross-section is much larger than the coherent one. As compared to a free nucleon the emission probability is already appreciably reduced in the bare case by the change in the Delta width. Moreover the RPA effects, which are moderate, also tend to a small reduction. The reduction due to the modification of the Delta width has a counterpart in the presence of a component of multi-nucleon knock-out. Charged current and neutral current cross-sections for incoherent pion emission for all possible charges are represented in Fig.14 and 15 as a function of neutrino energy. Moreover these figures summarize all previous results for the other channels and also give the total cross-sections.

On the other hand, Fig.16 compares the neutrino differential cross-section per neutron in the various channels as a function of the energy transfer, ω , for the cases of ${}^{12}\text{C}$ and ${}^{40}\text{Ca}$ and for a neutrino energy $E_\nu = 1$ GeV. The two sets of curves are very similar. We can conclude that, at the level of our approximation, *i.e.*, without final state interaction, it is possible to extrapolate smoothly from ${}^{12}\text{C}$ to the region of ${}^{40}\text{Ar}$. Only the coherent cross-section presents a significant variation, illustrated in Fig.17.

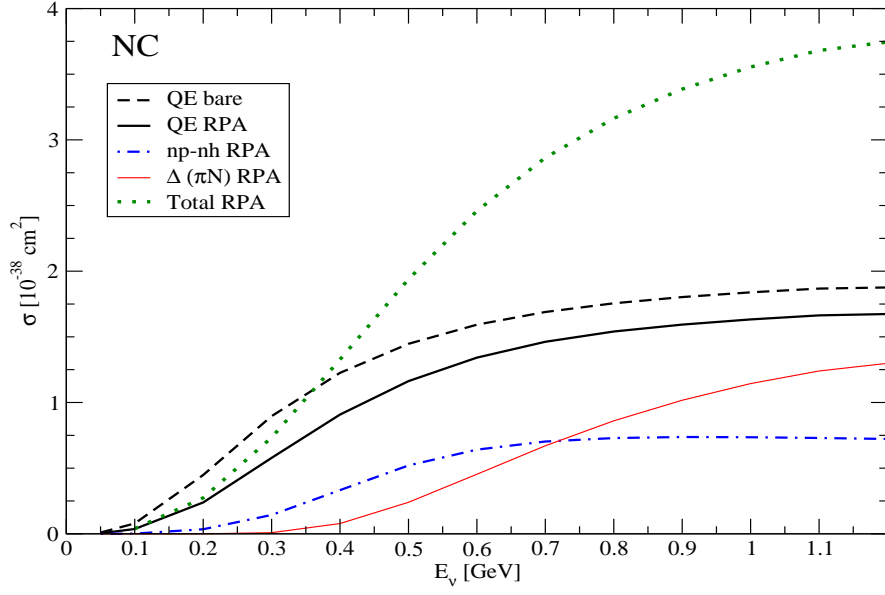


Figure 15: NC $\nu_\mu - {}^{12}\text{C}$ QE, multi-nucleon ($np - nh$), incoherent pion emission and total cross-section as a function of neutrino energy.

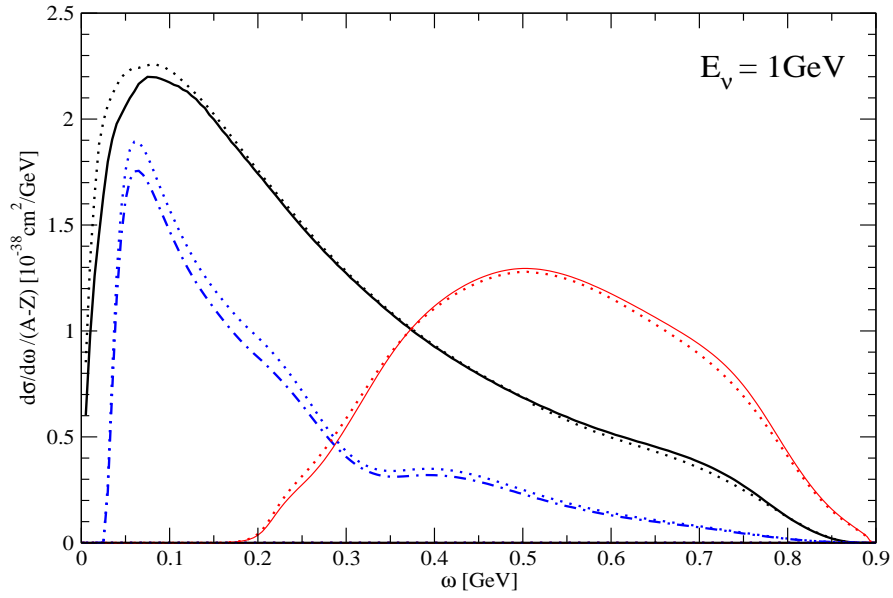


Figure 16: RPA differential CC cross-sections per neutron in the different channels for ${}^{12}\text{C}$ (same convention-line as Figs.13,14,15), and ${}^{40}\text{Ca}$ (dotted lines).

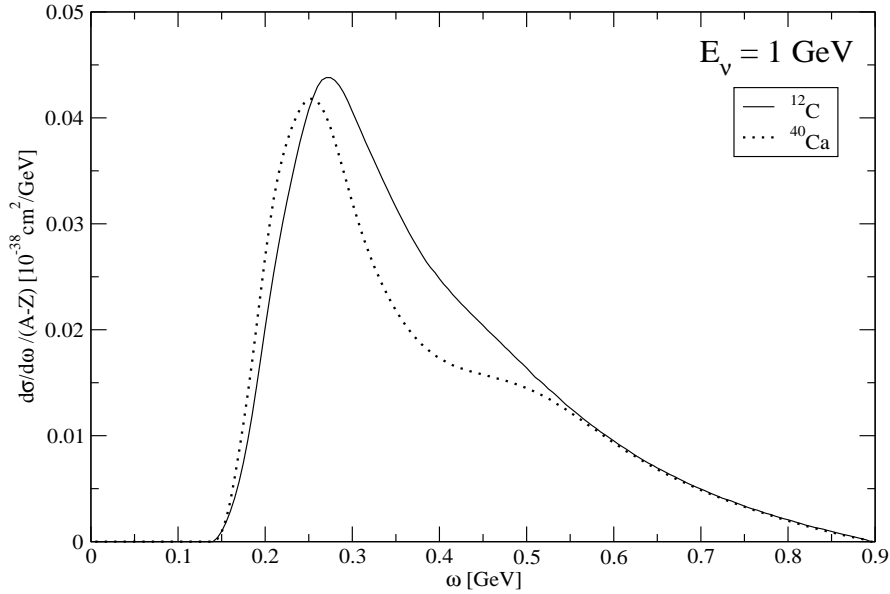


Figure 17: Differential CC cross-sections per neutron in the coherent channel for ^{12}C (continuous line), and ^{40}Ca (dotted line).

4 Comparison with data

4.1 Coherent pion production

Experimental data concern ratios between different cross-sections. The first indication of coherent pion production by neutral current was given by MiniBooNE [10], that found the ratio of coherent to total π^0 production to be $0.195 \pm 0.011 \pm 0.025$. In this experiment the neutrino flux is spread in energy with a peak at $\simeq 700\text{MeV}$ [13]. Our approach leads to a lower number, namely 0.06, which is difficult to reconcile with experimental data, a problem that other groups also face. It has been suggested in Ref.[27] that MiniBooNE, which uses Rein-Sehgal model [80] for data analysis, possibly overestimates the π^0 coherent cross-section. In a preliminary report [81] the experimental value given for this cross-section is $7.7 \pm 1.6 \pm 3.6 \cdot 10^{-40} \text{ cm}^2$. Our result for this cross-section averaged on the MiniBooNE flux [13], $2.8 \cdot 10^{-40} \text{ cm}^2$, is compatible with the experiment in view of the large experimental errors.

On the other hand for charged current, two experimental groups have given upper limits for the ratio of coherent pion production to the total cross-section. The K2K collaboration gives a limit of $0.60 \cdot 10^{-2}$ averaged over a neutrino flux with a mean energy of 1.3 GeV [7]. More recently, the SciBooNE collaboration found for the same quantity $0.67 \cdot 10^{-2}$ at neutrino energy of 1.1 GeV [12] and $1.36 \cdot 10^{-2}$ at neutrino energy of 2.2 GeV. We report in Fig.18 our prediction for this quantity. Since our approach is appropriate for a limited neutrino energy range we keep in the comparison only the lowest energy SciBooNE point. Our curve is just compatible with the experimental bound.

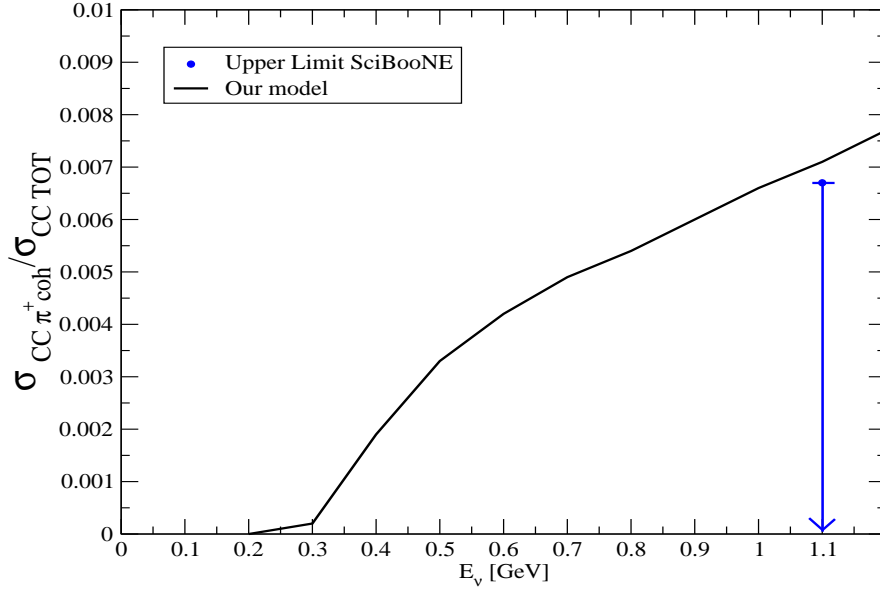


Figure 18: Ratio of the ν_μ -induced charged current coherent π^+ production to total cross-section as a function of neutrino energy.

4.2 Total pion production

Another measured quantity is the ratio of π^+ production to quasi-elastic cross-section for charged current. The MiniBooNE collaboration has used a CH_2 target. In order to compare with ANL [82] and K2K [11] data, they presented the results with an isoscalar rescaling correction [14]. The issue of pion loss by final state interaction, which is not incorporated in our description, has also been taken into account by MiniBooNE who corrects data for this effect. We can thus compare our π^+ over quasi-elastic ratio (solid line in the upper panel of Fig.19) to the final-state-interaction-corrected MiniBooNE results. Our curve incorporates the small coherent cross-section; the incoherent pion one is multiplied by the isospin factor $5/6$ to single out π^+ contribution. Our curve is fully compatible with experimental data.

As an additional information, MiniBooNE also gives a ratio more directly related to the measurements, namely the ratio of pion-like events (defined as events with exactly one μ^- and one π^+ escaping the struck nucleus) and quasi-elastic signal (defined as those with one μ^- and no pions). In our language the last quantity represents the total $Np - Nh$ ($N = 1, 2, 3$, including the quasi-elastic for $N = 1$) exclusive channel. We have compared this second experimental information to the ratio between our calculated pion production (which however ignores final state interactions) and our total $Np - Nh$ contribution to the total charged current neutrino cross-section (lower panel of Fig.19). There is an appreciable difference between the two curves of Fig.19: the one in the lower panel is reduced due to a large $2p-2h$ component in the $Np - Nh$ cross-section, which increases the denominator. The comparison with the experiment shows an agreement up to $E_\nu \simeq 1.2$ GeV. Final state interactions for the pion, which are not included, are expected to reduce

our result at the level of 15 %, still maintaining an agreement.

A new result has been presented at NuInt09 by SciBooNE [16]. It is the ratio of the total neutral current π^0 production cross-section to the total charged current cross-section at the mean neutrino energy of 1.16 GeV. They obtain the preliminary value:

$$\frac{\sigma(NC \pi_0)}{\sigma(CC_{TOT})} = (7.7 \pm 0.5(\text{stat.})_{-0.5}^{+0.4}(\text{sys.})) \cdot 10^{-2}. \quad (14)$$

Our prediction for this quantity, including coherent contribution and a factor 2/3 for NC incoherent pion production to single out π^0 contribution is:

$$\frac{\sigma(NC \pi_0)}{\sigma(CC_{TOT})} = 7.9 \cdot 10^{-2}, \quad (15)$$

which fully agrees with data.

A general comment on the comparison with data: nearly all the ratios that have been discussed, except the final-state-interaction-corrected MiniBooNE result of the upper panel of Fig.19, are sensitive to the presence of the $np - nh$ ($n = 2, 3$) component in the cross-section. Since the size magnitude is not so well tested, we can investigate what becomes the comparison with data in the extreme situation when we totally suppress this contribution. For the last ratio discussed we obtain

$$\frac{\sigma(NC \pi_0)}{(\sigma(CC_{TOT}) - \sigma(CC_{np-nh}))} = 9.8 \cdot 10^{-2}, \quad (16)$$

appreciably above the experimental value.

As for the SciBooNE upper limit of the ratio of the π^+ coherent to total charged current cross-section, our prediction at $E_\nu=1.1$ GeV, which was $0.71 \cdot 10^{-2}$, without $np-nh$ becomes $0.89 \cdot 10^{-2}$, further above the experimental bound of $0.67 \cdot 10^{-2}$.

4.3 Quasi-elastic cross-section

A new preliminary result on absolute cross-sections has been presented by the MiniBooNE collaboration [15]. This group gives in particular the absolute value of the cross-section for “quasi-elastic” events, averaged over the neutrino flux and as a function of neutrino energy. The comparison of these results with a prediction based on the relativistic Fermi gas model using the standard value of the axial cut-off mass $M_A = 1.03$ GeV/ c^2 reveals a substantial discrepancy. In the same model a modification of the axial cut-off mass from the standard value to the larger value $M_A = 1.35$ GeV/ c^2 is needed to account for data. A similar conclusion holds for the Q^2 distribution [8] [9]. The introduction of a realistic spectral function for the nucleon does not alter this conclusion [32].

As a possible interpretation we question here the real definition of quasi-elastic events. As already discussed above, the nuclear medium is not a gas of independent nucleons, correlated only by the Pauli principle, but there are additional correlations. The ejection of a single nucleon (denoted as a genuine quasi-elastic event) is only one possibility, and one must in addition consider events involving a correlated nucleon pair from which the partner nucleon is also ejected. This leads to the excitation of 2 particle-2 hole ($2p - 2h$)

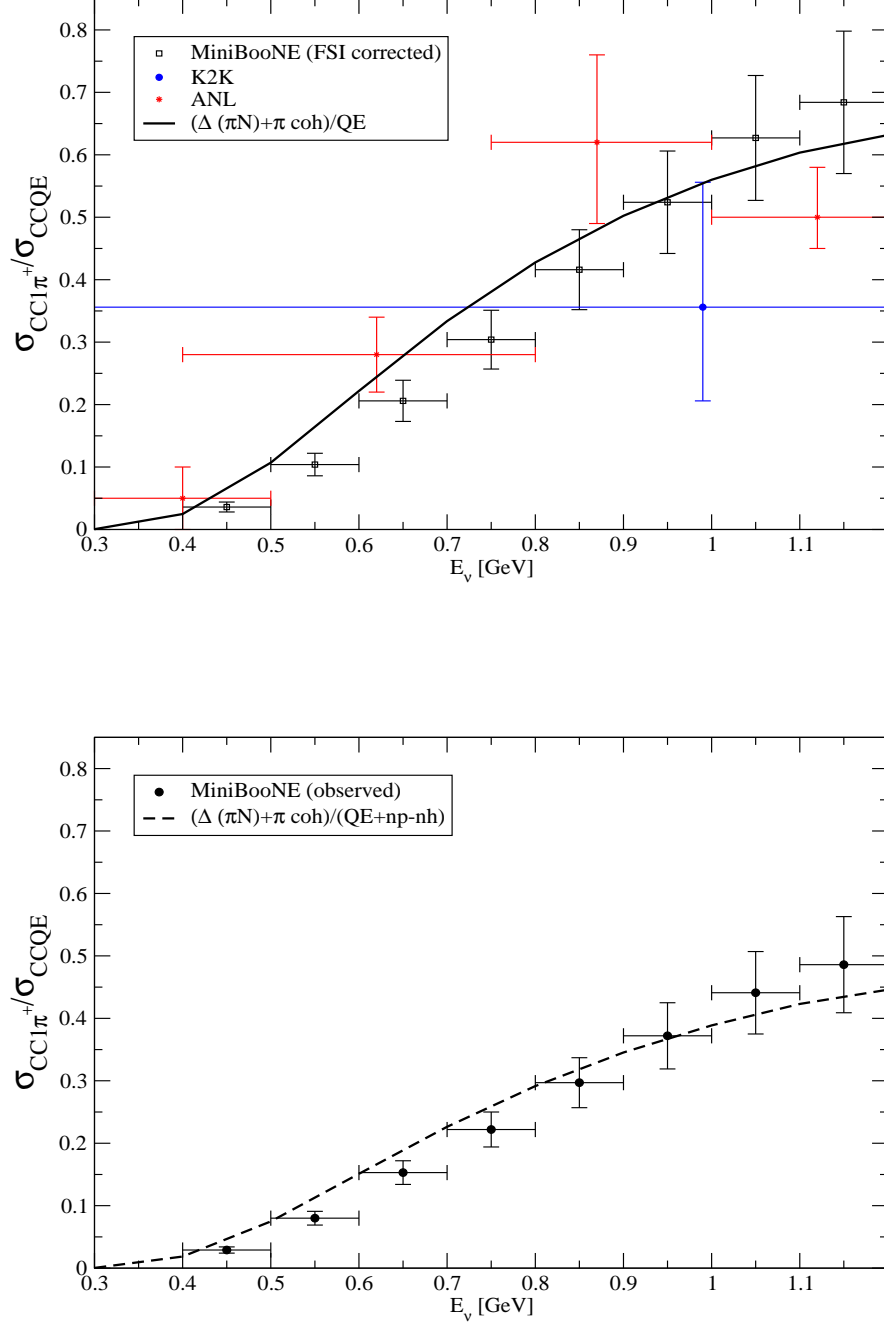


Figure 19: Ratio of the ν_μ -induced charged current one π^+ production to quasi-elastic cross-section as a function of neutrino energy.

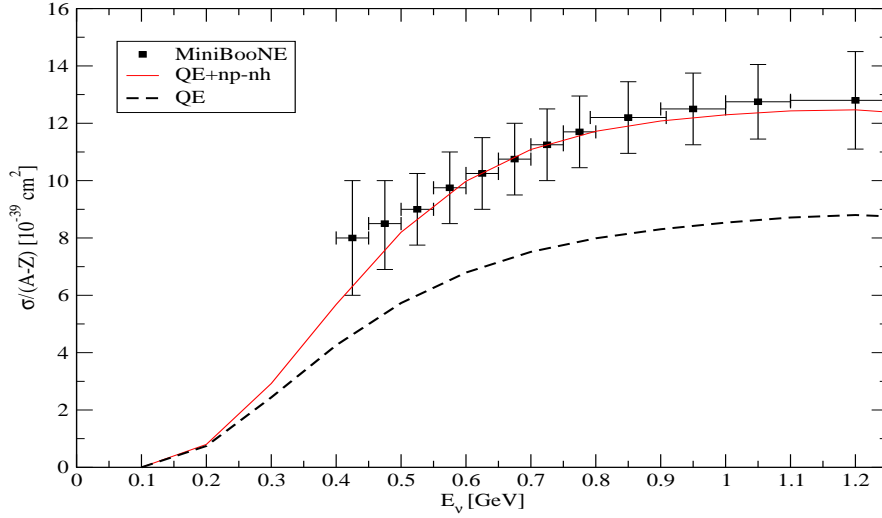


Figure 20: “Quasi-elastic” ν_μ - ^{12}C cross-section per neutron as a function of neutrino energy. Dashed curve: pure quasi-elastic ($1p-1h$) cross-section; solid curve: with the inclusion of $np-nh$ component. The experimental MiniBooNE points are taken from [15].

states which have been abundantly discussed throughout this work. In the spin-isospin channel the correlations, mostly the tensor ones, add $2p-2h$ strength to the $1p-1h$ events [66]. At present, in neutrino reactions, such events cannot be experimentally distinguished from the genuine quasi-elastic events and must be considered simultaneously. Notice that the standard lower value of the axial mass, $M_A=1.03 \text{ GeV}/c^2$, results from deuterium bubble chamber experiments. In this case the effect of tensor correlation is also present but at a lower level since deuteron is a dilute system. Our sum of the combined ^{12}C quasi-elastic cross-section and the $2p-2h$ one is displayed in Fig.20. This prediction fits the experimental data excellently, better than expected in view of the uncertainties of our $2p-2h$ cross-section. As for the flux averaged “quasi-elastic” cross-section per neutron the experimental value is $9.4 \cdot 10^{-39} \text{ cm}^2$ (with a normalization error of 11%). Our prediction for this quantity is $6.3 \cdot 10^{-39} \text{ cm}^2$ without $2p-2h$ contribution and $9.0 \cdot 10^{-39} \text{ cm}^2$ including it, a value more in touch with the experimental one.

In view of the importance of the issue we want to investigate if this large $2p-2h$ contribution is a genuine effect and not an artifact of the particular parametrization that we have used for the bare $2p-2h$ channel. For this, we introduce a different approach which exploits a microscopic evaluation by Alberico *et al.* [66] of the $2p-2h$ contribution to the transverse magnetic response of (e, e') scattering. It does not have the shortcomings of our previous parameterizations which have no momentum dependence. In the previous case the maximum of the $2p-2h$ response R_{2p-2h}^{NN} always lies at low energy, $\omega \simeq 50 \text{ MeV}$, irrespective of the momentum, separating at large momentum from the quasi-elastic peak which instead gets shifted at larger energies. A similar feature exists in the $N\Delta$ part. This is not realistic and below we sketch a possible way for improvements. The aim is to extract the $2p-2h$ responses from the results of Alberico *et al.* [66], although they

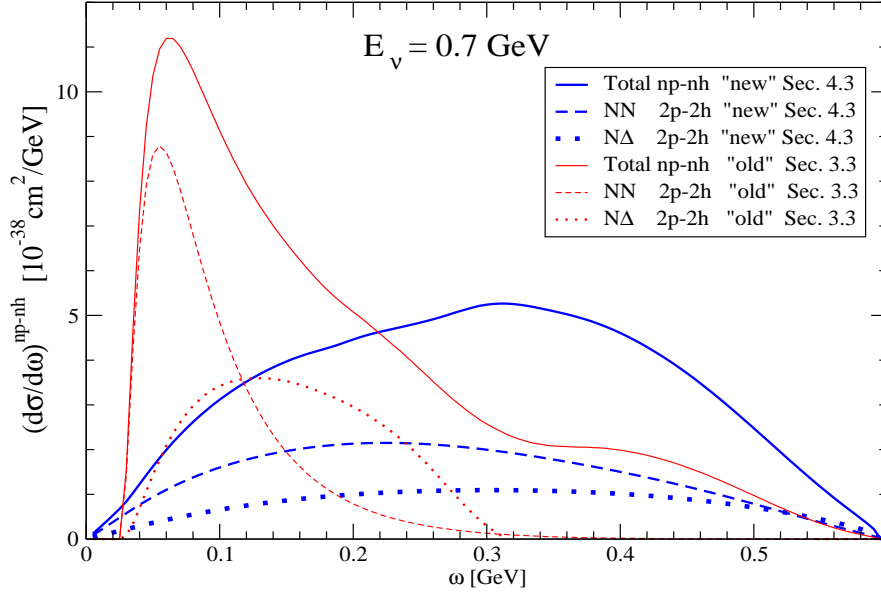


Figure 21: Comparison between the CC ν_μ ^{-12}C $np - nh$ ($n = 2, 3$) differential cross-sections deduced from the two different parameterizations of the $2p - 2h$ components. Thin lines: parametrization of Sec.3.3 and used throughout the whole article (denoted “old”); bold lines: parametrization of Sec.4.3 (“new”).

are available for a limited set of momenta and energies and they concern iron instead of carbon. We have thus performed extrapolations both to cover all the kinematical region of neutrino reactions and to go to the ^{12}C case. For the set of $R_{\sigma\tau(T)}(\omega, q)$ values that we could extract [66] we have observed an approximate scaling behavior with respect to the variable $x = \frac{q^2 - \omega^2}{2M_N\omega}$. A parametrization of the responses in terms of this variable allows the extrapolation needed to cover the full neutrino kinematical region and we have now the new responses, $R_{2p-2h}^{NN}(\omega, q)$ and $R_{2p-2h}^{N\Delta}(\omega, q)$ in all the range. For the $\Delta\Delta$ part, which is not well covered in [66] we have kept the previous parametrization, which already presents a proper q dependence owing to the contribution of the in-medium Δ width [70]. Another remark is in order. The evaluation of Ref.[66] of the $2p - 2h$ channel does not reproduce pion absorption in nuclei at threshold, as observed by the authors. It gives a too large value for the absorptive p -wave optical potential parameter [75], $\text{Im}C_0 \simeq 0.18m_\pi^{-6}$, instead of the best fit value $\text{Im}C_0 \simeq 0.11m_\pi^{-6}$. To be as consistent as possible with our previous parametrization, which comes from pion absorption, we have applied to our scaling function the reduction factor $\frac{0.11}{0.18}$. The nuclear mass dependence is taken care of with the introduction of the Lvinger factor, L , which fixes the number of quasi-deuteron pairs in the nucleus defined as $L \propto ZN/A$. We rescale the iron results by a factor r , ratio of the Lvinger factors, for the two nuclei. It is $r = 0.8$ according to the A dependence of the Laget formula [83] or a similar value, $r \simeq 0.75$ from [84]. Altogether the global reduction factor applied to the iron scaling function is $\simeq 0.5$.

Since in the previous case the RPA have little effect on the $2p - 2h$ component, we introduce directly the bare new $2p - 2h$ quantities in the neutrino cross-section. The

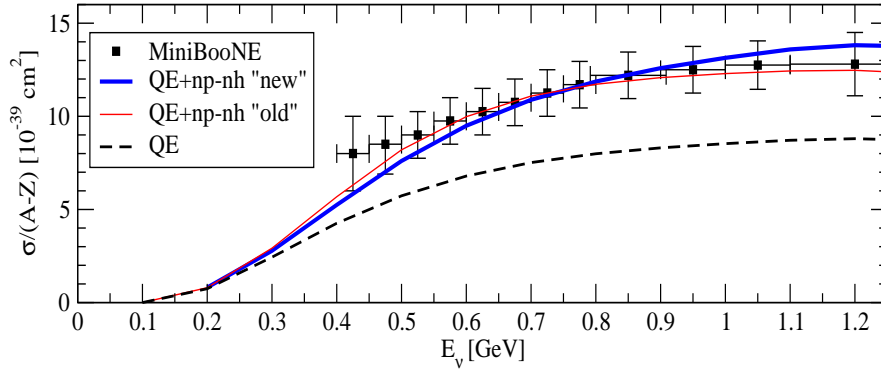


Figure 22: Same as Fig.20 including also our curve (QE + $np - nh$ “new”) with the new parametrization for the $2p - 2h$ component (bold line).

influence of the new modelization of the $2p - 2h$ is displayed in Fig. 21 where the bare partial and total $np - nh$ differential CC neutrino cross-sections at $E_\nu = 0.7$ GeV are shown both for the previous parametrization and for the new one. The energy behaviors are quite different, the NN contribution is no longer localized at small energies but is spread over the whole energy range, a more realistic feature. A similar behavior occurs for $N\Delta$ part. However the integral over the energy, $\sigma_{np-nh}(E_\nu)$, is practically not modified. As a consequence adding this contributions to the quasi-elastic cross-section we reach a similar conclusion as before about the important role of the multi-nucleon channel, as illustrated in Fig. 22.

It indicates that, in the nuclear medium, neutrino in this energy range do not interact only with individual nucleons but also with pairs of nucleons, mostly $n - p$ pairs correlated by the tensor interaction. The spin dependent part of the neutrino interaction with such a pair is stronger than with the same two nucleons when isolated. This increase manifests itself through the $2p - 2h$ strength which adds to the $1p - 1h$ part, an effect simulated by an increase of the axial cut-off mass. Quantitatively a confirmation on the theoretical side of the exact magnitude through a detailed microscopic calculation of the bare $2p - 2h$ response, which will then be inserted in our RPA formalism, would be helpful. Also an experimental identification of the final state would be of a great importance to clarify this point. In particular the charge of the ejected nucleons will be quite significant. Since tensor correlations involve $n - p$ pairs, the ejected pair is predominantly $p - p$ for charged current and $n - p$ for neutral current. This predominance has the same origin as for p-wave π^- absorption by nuclei where $n - n$ emission is favored over $n - p$ emission [72, 79].

5 Summary and Conclusion

We have studied neutrino interactions with light nuclei which enter the targets of present or future experiments. Our theoretical tool is the theory of the nuclear response treated in the random phase approximation (RPA), a well established technique for the treatment of electromagnetic or weak interactions with nuclei and which have been used also

for strongly interacting probes. The crucial element of the RPA treatment is the $p - h$ interaction, in particular for the spin-isospin one, which has been taken from the accumulated knowledge on the spin-isospin responses. The main merit of this approach is to allow unified description of various channels. It has some limitations which restrict the energy range of the neutrino to a region below $\simeq 1.2$ GeV. For instance the only nucleonic resonance incorporated in the description is the Delta resonance. Multi-pion production is also ignored, as well as most meson exchange effects. Moreover, although both the Delta propagator and the center-of-mass correction are the relativistic one, not all relativistic effects are included in a systematic way.

The final states considered are the quasi-elastic, $2p - 2h$, $3p - 3h$ ones, and coherent or incoherent pion production. Some channels have the problem that final state interactions are not incorporated. This is the case for incoherent pion emission where the produced pion can be absorbed on its way out of the nucleus leading to a multi-nucleon state. Incoherent pion production is therefore overestimated and the multi-nucleon channel accordingly underestimated. This effect is visible in the scattering of physical pions on ^{12}C in the region of the Delta peak. For a light nucleus such as ^{12}C the effect is limited but it becomes more serious in heavier nuclei. Our method should be supplemented by an evaluation of the final state interaction, for instance by a Monte Carlo method [61],[85].

The coherent channel is particularly interesting although it represents only a small fraction of the total pion emission. It does not suffer from the previous limitations as final state interactions are automatically incorporated in the RPA treatment which is particularly suited for this channel. Moreover, it is the only channel which is dominated by the isospin spin-longitudinal response where collective effects are very pronounced while they remain moderate in the other channels. The difference between the first order term with one bubble (with Delta excitation) and the full RPA chain is quite large. In this context we have used as a test of our spin longitudinal response the experimental data on elastic pion scattering in the Delta region. It offers a direct test of the forward coherent neutrino cross-section to which it is linked through the Adler theorem. Except for low pion energies near threshold ($\omega \leq 200$ MeV) where Adler's theorem fails, the elastic cross-section can be used to extract the forward neutrino coherent cross-section as in the method of Rein-Sehgal.

For the evolution of the partial cross-sections with mass number in order to reach the ^{40}Ca region, our description indicates that, apart from the coherent pion production which evolves differently, the other partial cross-sections scale essentially as the nucleon number. Final state interactions obviously will destroy this scaling.

We have compared our predictions with the available experimental data. Our ratio for the coherent pion production over the total neutrino cross-section is just compatible with the experimental upper limit. Another test concerns the ratio for charged currents π^+ production to the quasi-elastic cross-section. A delicate point in the experiments concerns the definition of a quasi-elastic process and its separation from $np - nh$ which the experiment does not distinguish. In one set of data a correction is applied to obtain a genuine quasi-elastic cross-section and it is corrected as well for final state interaction. In another set of results a generalized quasi-elastic is introduced, defined as events with only one lepton. In this case our $2p - 2h$ and $3p - 3h$ should be added to the quasi-elastic component. Both lead to successful comparisons with the two sets of experimental

data. Further data involve a ratio of neutral current π^0 production to the total neutrino cross-section for charged currents. Here again our evaluation agrees with data. It is quite encouraging that the comparison with present experimental data is essentially successful.

A distinct feature of our approach, and one of our significant results, is the large $2p-2h$ component. It affects all the measured ratios discussed in this work. At the present level of accuracy we have not found in these ratios any contradiction to its presence. It is also supported by preliminary data on the absolute neutrino quasi-elastic cross-section on carbon. We suggest that the proposed increase of the axial mass from the standard value to a larger one to account for the quasi-elastic data, reflects the presence of a polarization cloud, mostly due to tensor interaction, which surrounds a nucleon in the nuclear medium. It translates into a final state with ejection of two nucleons, which in the present stage of the experiments is indistinguishable from the quasi elastic final state. Although the existence of such $2p-2h$ component is not in question, for a fully quantitative evaluation we plan to improve the description of the multi-nucleon final states by a microscopic treatment. Future precision experiments, such as T2K, will be able to identify final states, namely $p-p$ pairs for charged current and $n-p$ pairs for neutral current, and bring an experimental elucidation of this intriguing effect.

Acknowledgments

We thank Luis Alvarez-Ruso, Dany Davesne, Torleif Ericson and Alfredo Molinari for stimulating discussions.

1.4 Neutrino and antineutrino quasielastic interactions with nuclei [10]

M. Martini,¹ M. Ericson,^{2,3} G. Chanfray,² and J. Marteau²

¹CEA/DAM/DIF, 91297 Arpajon, France

²Université de Lyon, Univ. Lyon 1, CNRS/IN2P3, IPN Lyon, F-69622 Villeurbanne Cedex, France

³Theory Group, Physics Department, CERN, CH-1211 Geneva, Switzerland

We investigate the interaction of neutrinos and antineutrinos with nuclei. We explore in particular the role played by the multinucleon excitations which can contaminate the quasielastic cross section. For neutrinos the multinucleon term produces a sizable increase of the quasielastic cross section. Part of the effect arises from tensor correlations. For antineutrinos this influence is smaller owing to the axial-vector interference which increases the relative importance of the terms which are not affected by these multinucleon excitations.

PACS numbers: 25.30.Pt, 13.15.+g, 24.10.Cn

The progresses of neutrino experimental physics have allowed the measurement of several partial cross sections in the interaction with nuclei. Most data concern ratios of cross sections [1–7] but some absolute values are now available [8–10]. In particular the MiniBooNE collaboration has measured the neutrinos charged current (CC) quasielastic (QE) cross section on ^{12}C for a neutrino beam with average energy of 788 MeV [10]. In this work ejected nucleons are not detected and the quasielastic cross section is defined as the one for processes in which only a muon is detected in the final state. However it is possible that in the neutrino interaction a pion produced via the excitation of the Δ resonance escapes detection, for instance because it is reabsorbed in the nucleus, leading to multinucleon emission. In this case it simulates a quasielastic process. The MiniBooNE analysis of the data corrects for this possibility via a Monte-Carlo evaluation of this process. The net effect amounts to a reduction of the observed quasielastic cross section. After application of this correction the quasielastic cross section thus defined still displays an anomaly as compared to a relativistic Fermi gas prediction. The prediction which is sensitive to the cut-off mass of the axial form factor fits the data provided a modified axial form factor is introduced in the calculation, with an increase of the axial cut-off mass from the accepted value $M_A = 1.03$ GeV to the value $M_A = 1.35$ GeV; otherwise the calculated cross section is too small [10].

On the theoretical side Martini *et al.* [11] have drawn the attention to the existence of additional sources of multinucleon emission which are susceptible to produce an apparent increase of the “quasielastic” cross section. Their evaluation, although approximate, of this contribution shows that it is able to account for this apparent increase. It stresses in particular the role played by the NN tensor correlations in this enhancement. In clarifying this point we will be naturally led to explore the corresponding effect in the case of antineutrinos. We will show that antineutrinos can provide a useful test of the origin of this anomaly, which is the aim of the present work.

In our approach, the same as that of Ref. [11], the neutrino cross section on nuclei is expressed in terms of the nuclear response functions treated in the random phase

approximation (RPA). The only nucleon resonance taken into account is the Δ one. Several responses enter this interaction, as exemplified below in a simplified expression of the charged current cross section where the lepton mass is ignored and the Δ width is taken to zero. It reads :

$$\begin{aligned} \frac{\partial^2 \sigma}{\partial \Omega \partial k'} = & \frac{G_F^2 \cos^2 \theta_c (\mathbf{k}')^2}{2 \pi^2} \cos^2 \frac{\theta}{2} \left\{ G_E^2 \left(\frac{q_\mu^2}{q^2} \right)^2 R_\tau^{NN} \right. \\ & + G_A^2 \frac{(M_\Delta - M)^2}{2 q^2} R_{\sigma\tau(L)}^{N\Delta} + G_A^2 \frac{(M_\Delta - M)^2}{q^2} \\ & \times R_{\sigma\tau(L)}^{\Delta\Delta} + \left(G_M^2 \frac{\omega^2}{q^2} + G_A^2 \right) \left(-\frac{q_\mu^2}{q^2} + 2 \tan^2 \frac{\theta}{2} \right) \\ & \times \left[R_{\sigma\tau(T)}^{NN} + 2 R_{\sigma\tau(T)}^{N\Delta} + R_{\sigma\tau(T)}^{\Delta\Delta} \right] \pm 2 G_A G_M \frac{k+k'}{M} \\ & \times \tan^2 \frac{\theta}{2} \left[R_{\sigma\tau(T)}^{NN} + 2 R_{\sigma\tau(T)}^{N\Delta} + R_{\sigma\tau(T)}^{\Delta\Delta} \right] \left. \right\} \quad (1) \end{aligned}$$

where G_F is the weak coupling constant, θ_c the Cabbibo angle, k and k' the initial and final lepton momenta, $q_\mu = k_\mu - k'_\mu = (\omega, \mathbf{q})$ the four momentum transferred to the nucleus, θ the scattering angle, M_Δ (M) the Δ (nucleon) mass. The plus (minus) sign in Eq. (1) stands for the neutrino (antineutrino) case. The existence of this axial-vector interference term is crucial in the present work. The various responses are related to the imaginary part of the corresponding full polarization propagators :

$$R(\omega, q) = -\frac{\mathcal{V}}{\pi} \text{Im}[\Pi(\omega, q, q)]. \quad (2)$$

They are related to the inelastic cross section for a given coupling. For instance for the isospin operator :

$$\begin{aligned} R_\tau = & \sum_n \langle n | \sum_{j=1}^A \tau(j) e^{i \mathbf{q} \cdot \mathbf{x}_j} | 0 \rangle \\ & \times \langle n | \sum_{k=1}^A \tau(k) e^{i \mathbf{q} \cdot \mathbf{x}_k} | 0 \rangle^* \delta(\omega - E_n + E_0). \quad (3) \end{aligned}$$

Similar expressions apply to the other transition operators. An analogous expression applies for a transition to

a state with a Δ excitation which enters the spin-isospin responses. In this case the operators are :

$$O_{\sigma\tau(L)}^\Delta(j) = (\mathbf{S}_j \cdot \hat{\mathbf{q}}) T_j^\pm, \quad O_{\sigma\tau(T)}^\Delta(j) = (\mathbf{S}_j \times \hat{\mathbf{q}})^i T_j^\pm. \quad (4)$$

In the case of a spin operator the index L or T refers to the direction of the spin, longitudinal or transverse, with respect to the momentum \mathbf{q} . In the expression (1) the upper indices, N or Δ , refer to the type of particles, nucleon or Δ , excited by the weak current at the two ends of the RPA chain (see Fig.1). In the present numerical evaluations we employ, instead of Eq. (1), the full expressions given in the Appendix A of our previous publication [11] for which we refer for more details.

We have treated these responses in the ring approximation of the RPA so as to account for collective effects. A limitation of our description is that it does not incorporate final state interactions such as for instance the possibility for a real pion produced by the neutrino to be reabsorbed in the nucleus leading to multinucleon ejection. This fraction of the produced pions would thus be counted in the “quasielastic” events. These events have been subtracted in the MiniBooNE analysis through their Monte Carlo evaluation. Hence our theory can be confronted to their corrected experimental results.

To lowest order the quasielastic cross section is given by the terms in R^{NN} , whether coming from the isovector interaction, R_τ^{NN} , or from the isospin spin-transverse one, $R_{\sigma\tau(T)}^{NN}$. The isospin spin-longitudinal one is suppressed, for a vanishing lepton mass, by a cancellation between the space and time components of the axial current [11], which is the reason why it is not explicitly written in Eq.(1). In the actual calculation its small quasielastic contribution is taken into account. It also contribute to the multinucleon ejection term. In the RPA chain $R^{N\Delta}$ and $R^{\Delta\Delta}$ also contribute to the quasielastic response as illustrated in Fig.1. The collective effects produce a mild suppression of the quasielastic response due to the repulsive nature of the residual interaction. The effect that we want to discuss here is of a different nature. It concerns the multinucleon ($np - nh$) ejection in neutrino interactions other than that due to final state interaction. Here several sources of multinucleon emission enter our description and all type the responses R^{NN} , $R^{N\Delta}$ and $R^{\Delta\Delta}$ contribute. Examples are given in Fig. 2. One of these multinucleon sources arises from the modification of the Δ width in the nuclear medium (Fig.2 (d)). This effect was introduced and parametrized by Oset and Salcedo [12] in the case of real pion or photon absorption. We have used their parametrization of the modified width, although the kinematics of neutrino interaction is different since we are in the space-like region, which could be a source of uncertainty. For the other terms not reducible to a modification of a Δ width of which some examples are shown in Fig.2 we have used a parametrization of Delorme and Guichon [13]. They exploited a calculation by Shimizu and Faessler [14] of the absorptive part of the p-wave pion-nucleus optical potential at threshold, which writes $(4\pi/2m_\pi) \vec{\nabla} \cdot \text{Im}C_0 \rho^2 \vec{\nabla}$ [15]. It is known

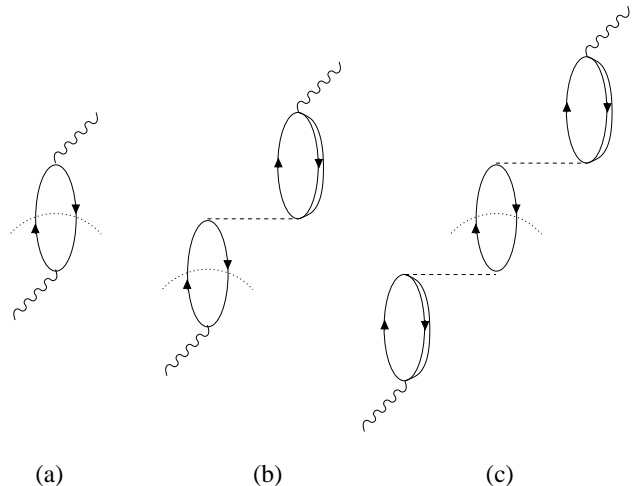


FIG. 1: Examples of contributions to the quasielastic cross section. Lowest order contribution from : (a) R^{NN} ; (b) $R^{N\Delta}$ and (c) $R^{\Delta\Delta}$. The wiggled lines represent the external probe, the full lines correspond to the propagation of a nucleon (or a hole), the double lines to the propagation of a Δ and the dashed lines to an effective interaction between nucleons and/or Δ s. The dotted lines show which particles are placed on-shell.

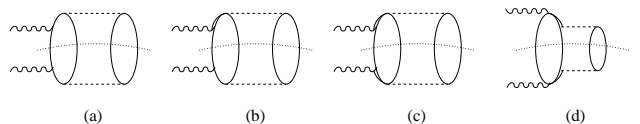


FIG. 2: Examples of contributions to the two nucleon ejection term. From : (a) R^{NN} ; (b) $R^{N\Delta}$; (c) and (d) $R^{\Delta\Delta}$. Diagram (d) represents an example of modification of the Δ width in the medium.

that the absorption mechanism of pions is a two-nucleon one which means that in the final state two nucleons are ejected. In the many-body language this is a two particle-two hole ($2p - 2h$) excitation. In Ref. [14] the absorption is described by three types of terms (see Fig.2). The first one (Fig.2 (a) with pion lines replacing the weak current ones as in the next diagrams) arises from the nucleon-nucleon correlations, essentially from the tensor correlations. Another one involves a Δ excitation (Fig.2 (c)). The third one is an interference between the nucleon correlation and Δ terms as in Fig.2 (b). In these graphs the coupling of the pion to the nucleon involves the pion momentum and is of the spin isospin type, $\vec{\sigma} \cdot \vec{q} \vec{\tau}$, for the nucleon and a similar expression for Δ excitation. In the optical potential the pion momentum is expressed by the gradient, the remaining part of the optical potential with the parameter $\text{Im}C_0$ then provides the nuclear $2p - 2h$ bare responses to a probe which couples to the spin and isospin of the nucleon. In principle it is a spin longitudinal coupling but as this term represents a short range effect there is no difference in the bare case (*i.e.* before

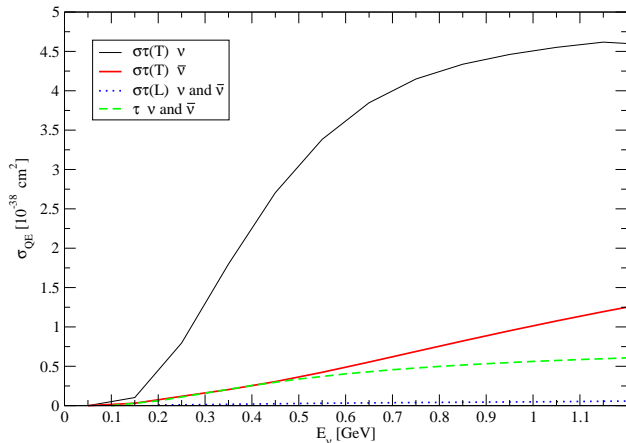


FIG. 3: Various response contributions to the ν_μ and $\bar{\nu}_\mu$ - ^{12}C charged current genuine quasielastic cross section. Isovector (τ) and isospin spin-longitudinal ($\sigma\tau$ (L)) components are identical for ν_μ and $\bar{\nu}_\mu$.

the RPA chain) between longitudinal and transverse spin couplings. Therefore it applies to the bare magnetic part of the vector current and to both the spin-transverse and spin-longitudinal parts of the axial current. The pion absorption calculation of Ref.[14] is performed for threshold pion, i.e. for a vanishing three-momentum and an energy $\omega = m_\pi$, which does not correspond to the neutrino situation. Delorme *et al.* [13] have then introduced in each absorption graph the corresponding energy dependence to obtain the bare $2p-2h$ responses to be inserted in the RPA chain needed for neutrino interaction. However they have completely ignored the momentum dependence. They have left apart the graph (d) of Fig.2 since it corresponds to a modification of the Δ width which is taken into account separately through the parametrization of Oset *et al.* [12]. In a first approach we have used the procedure of Delorme *et al.* as such in order to evaluate the bare $2p-2h$ components to be inserted in the RPA chain for the evaluation of the neutrino cross section. In our resulting $2p-2h$ cross section the modification of the Δ width is not a dominant effect; it adds a small $2p-2h$ component (plus a $3p-3h$ one). It turned out that our overall multinucleon contribution, when added to the genuine quasielastic cross section, was able to account for the anomaly without modification of the axial cut-off mass as already reported in Ref.[11].

Since our parametrization of the $2p-2h$ piece from the extrapolation of pion absorption is questionable, as it ignores in particular any momentum dependence, we have also investigated the effect with our second parametrization [11] of the $2p-2h$ contribution beyond the one which is reducible to a modification of the Delta width. In the second approach we have used a microscopic calculation of Alberico *et al.* [16] specifically aimed at the evaluation of the $2p-2h$ contribution to the isospin spin-transverse response, measured in inclusive (e, e') scattering. Their

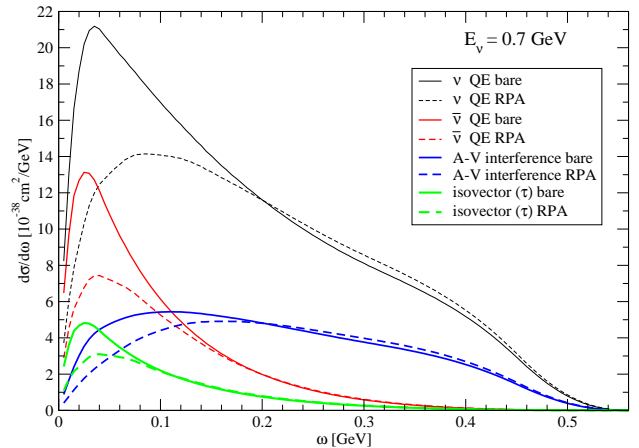


FIG. 4: Differential CC ν_μ and $\bar{\nu}_\mu$ - ^{12}C cross sections versus the energy transfer.

basic graphs are similar to those of Shimizu and Faessler. In principle this way of evaluation is definitely more satisfactory since the kinematical variables are correctly incorporated but the results of Ref.[16] are available only for a limited set of energy and momenta. We have extended this range to cover the neutrino one through an approximate extrapolation. We refer to [11] for the details. The result was that the distribution in the energy transfer ω of the differential neutrino cross section is largely modified with a more realistic distribution but once integrated in energy the difference is small. The corresponding neutrino and antineutrino total “quasielastic” cross sections are practically unchanged.

Now from the way in which this $2p-2h$ contribution is built, the corresponding coupling of the weak current to the nucleon or Δ is a spin isospin one. It is then clear that this $2p-2h$ term only affects the magnetic and axial responses which enter the neutrino cross section. In the expression (1) these are the terms in G_A^2, G_M^2 and the interference term in $G_A G_M$. The isovector response (term in R_τ) instead is not affected. This difference is the basis for the test that we propose to help elucidate the origin of the anomaly. The principle is simple. For antineutrinos the interference term in $G_M G_A$ produces a suppression of the spin isospin response contribution, while it enhances it for neutrinos. In the neutrino case the contribution from the spin isospin terms largely dominates the isovector one. If the suppression of the spin isospin part for antineutrinos by the interference term modifies the balance in such a way that the role of the isovector response in the cross section becomes appreciable, the relative role of the $2p-2h$ part will be smaller for antineutrinos. We will show below that this is indeed the case. Figure 3 displays the various components to the genuine quasielastic (single nucleon ejection) cross section on ^{12}C as a function of the energy both for muon neutrinos and antineutrinos. The isovector part is identical in the two cases, as well as the isospin spin-longitudinal one. The isospin

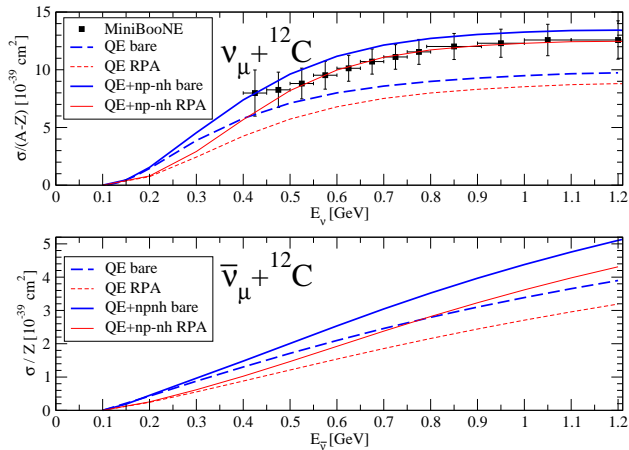


FIG. 5: ν_μ (upper panel) and $\bar{\nu}_\mu$ (lower panel) ^{12}C CC “quasielastic” cross sections per neutron and per proton with and without the multinucleon component as a function of neutrino energy. The experimental points are taken from [10].

spin-transverse one instead changes considerably between neutrinos and antineutrinos due to the interference term with an appreciable reduction in the antineutrino case. As a consequence the isovector relative contribution to the total cross section becomes quite significant for antineutrinos which opens the possibility of an experimental test. Such details are visible in Fig. 4 where the differential cross section $\frac{d\sigma}{d\omega}$ at $E_\nu=700$ MeV is shown in the bare and RPA case, both for neutrinos and antineutrinos. In the same figure the axial-vector interference term is displayed as well as the isovector component illustrating the importance of the latter in the antineutrino case. A remark on the collective nature is in order at this stage. One notices the suppression produced by the RPA which follows from the repulsive character of the residual interaction. It is more pronounced at small energies. The interference term which spreads over all the energy range is therefore less affected by RPA. The antineutrino cross section which peaks at low energies is instead very sensitive to the suppression by the collective RPA effects. Once integrated over the energy transfer the reduction at a typical energy $E_\nu=700$ MeV is somewhat larger for antineutrinos than for neutrinos. A comparison between the two is affected by this difference. This could lead to a source of uncertainty in the comparison as the RPA effects which depend on the residual interaction have not been tested in this momentum regime. However we will show below that it does not prevent the comparison to be significant for our purpose.

We now turn to the generalized “quasielastic” cross section which includes the multinucleon contribution. The neutrino and antineutrino genuine and generalized “quasielastic” cross section are plotted in Fig.5 both in the bare and RPA case. As was already discussed in Ref.[11] the agreement with the MiniBooNE experimental neutrino data [8, 10] is better when the $np-nh$ com-

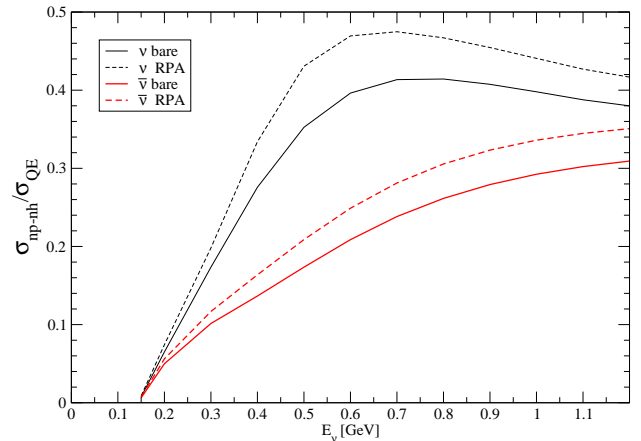


FIG. 6: Ratio of multinucleon component of “quasielastic” cross section on ^{12}C to the single nucleon one for ν_μ and $\bar{\nu}_\mu$ as a function of neutrino energy.

ponent is added to the genuine QE cross section, whether in the free or in the RPA case. Our prediction for the generalized neutrino “quasielastic” cross section shows only a moderate sensitivity to the collective aspects. For antineutrinos instead the sensitivity to RPA is somewhat larger but it does not hide the important point that the relative importance of the $2p-2h$ term is smaller for antineutrino. This is illustrated in Fig.6 which shows the ratio of the multinucleon component to the single nucleon one with and without RPA. In both cases, we find that the ratio for antineutrino is reduced as compared to the neutrino one by a factor 1.7 at $E_\nu=700$ MeV. In order to eliminate the uncertainties related to the neutrino energy reconstruction, we give in Table 1 values of quasielastic and multinucleon cross sections on ^{12}C , as well as their sum, averaged over the respective neutrino [10] and antineutrino [17] MiniBooNE fluxes, so as to provide quantities more in touch with an experimental analysis. We give these quantities both in RPA and in the free case and various situations are possible. For instance, if our RPA description holds, the ratio of the generalized “quasielastic” cross section, which is the measured cross section, to a theoretical free Fermi gas model is 1.22 for neutrinos and 0.99 for antineutrinos, significantly lower. If the extreme case where RPA effects are totally absent the corresponding ratios are 1.37 for neutrinos and 1.25 for antineutrinos. In all cases the antineutrino numbers are smaller and the difference may be detectable, which offers an experimental test. For neutrinos the fit to the quasielastic data in a relativistic Fermi gas description required an appreciable increase of the axial cut-off mass [10]. For antineutrinos the increase needed to account for the data in the same model should be smaller since the relative role of multinucleon ejection is reduced. This difference offers a possible way to shed light on the origin of the anomaly. Of course the difference which occurs owing to the fact that the target is

| | ν | | | $\bar{\nu}$ | | |
|------|-------|-------|----------|-------------|-------|----------|
| | QE | np-nh | QE+np-nh | QE | np-nh | QE+np-nh |
| bare | 7.46 | 2.77 | 10.23 | 2.09 | 0.52 | 2.61 |
| RPA | 6.40 | 2.73 | 9.13 | 1.60 | 0.47 | 2.07 |

TABLE I: MiniBooNE flux-integrated CC ν_{μ} - ^{12}C and $\bar{\nu}_{\mu}$ - ^{12}C total cross sections per neutron and per proton respectively in unit of 10^{-39} cm^2 . The experimental CCQE ν_{μ} - ^{12}C value measured by MiniBooNE is $9.429 \times 10^{-39} \text{ cm}^2$ with a total normalization error of 10.7 % [10].

not pure carbon but CH_2 affects exclusively antineutrino cross section reducing trivially the importance of nuclear effects. It has to be taken into account to reach a significant comparison between neutrino and antineutrino cross sections.

Finally we would like to comment on the absence of final state interactions in our evaluation. In addition to the absorption of a produced pion it also ignores the possibility for an ejected nucleon to interact with the nucleus emitting another nucleon which leads to a final state with two nucleon ejected, the same type of final state as was discussed in this work. For the final state interaction effect all responses are concerned and not only the spin isospin ones. This has been taken into account by Benhar and Meloni [18] using a spectral function which describes the single particle dynamics in an interacting system, deduced from experimental $(e, e'p)$ data. Their conclusion is that this inclusion cannot explain the enhancement of the measured neutrino quasielastic cross section. Although the final states are the same, $(2p-2h)$, we are dealing in the present work to a different type of correlations. These are ground state correlations, mostly tensor ones which affect only the spin isospin responses,

producing an enhancement of the spin isospin sum rule which is reflected in an increase of the “quasielastic” cross section. The rest is due to the Δ excitation or the interference between the two. These also obviously belong exclusively to the spin isospin sector, which is the basis of our test through a comparison between neutrinos and antineutrinos. A fully realistic calculation should include both the spectral function effect and the ground state correlations or Δ ones.

In summary we have studied the quasielastic neutrino and antineutrino cross section in the case of the MiniBooNE experiment where multinucleon ejection is not distinguishable from single nucleon production. The “quasielastic” cross section thus defined contains a certain proportion of $2p-2h$ and $3p-3h$ excitations. This proportion is large for neutrinos, which may be the interpretation of the increase in the axial cut-off mass needed to describe the data in the relativistic Fermi gas. For antineutrinos we predict a smaller role of the $2p-2h$ component. The reason is that the vector-axial interference term produces a suppression of the spin isospin response contribution to the cross section leaving a larger role for the isovector response which is not affected by the $2p-2h$ component. An experimental confirmation of this difference would signal the fact that the excess cross section belongs to the spin-isospin channel, thus displaying the role played by the tensor correlations in neutrino nucleus interactions.

The antineutrino mode which is actively investigated for the general problems of neutrino oscillations and CP violation is also of great relevance for the understanding of the neutrino nucleus interactions.

We thank D. Davesne, T. Ericson, G.T. Garvey and T. Katori for useful discussions.

-
- [1] S. Nakayama *et al.* [K2K Collaboration], Phys. Lett. B **619**, 255 (2005).
[2] M. Hasegawa *et al.* [K2K Collaboration], Phys. Rev. Lett. **95** 252301 (2005).
[3] A. A. Aguilar-Arevalo *et al.* [MiniBooNE Collaboration], Phys. Lett. B **664**, 41 (2008).
[4] A. Rodriguez *et al.* [K2K Collaboration], Phys. Rev. D **78**, 032003 (2008).
[5] K. Hiraide *et al.* [SciBooNE Collaboration], Phys. Rev. D **78** 112004 (2008).
[6] A. A. Aguilar-Arevalo *et al.* [MiniBooNE Collaboration], Phys. Rev. Lett. **103**, 081801 (2009).
[7] Y. Kurimoto *et al.* [SciBooNE Collaboration], Phys. Rev. D **81**, 033004 (2010).
[8] T. Katori [MiniBooNE Collaboration], AIP Conf. Proc. **1189**, 139 (2009).
[9] A. A. Aguilar-Arevalo *et al.* [MiniBooNE Collaboration], Phys. Rev. D **81**, 013005 (2010).
[10] A. A. Aguilar-Arevalo *et al.* [MiniBooNE Collaboration], arXiv:1002.2680 [hep-ex].
[11] M. Martini, M. Ericson, G. Chanfray and J. Marteau, Phys. Rev. C **80**, 065501 (2009).
[12] E. Oset and L. L. Salcedo, Nucl. Phys. A **468** 631 (1987).
[13] J. Delorme, P.A.M. Guichon, in *Proceedings of 10^e biennale de physique nucléaire, Aussois, France, March 6-10, 1989*, LYCEN report 8906, p. C.4.1.
[14] K. Shimizu and A. Faessler, Nucl. Phys. A **333** 495 (1980).
[15] T. E. O. Ericson and W. Weise, *Pions and Nuclei, The International Series of Monographs on Physics* (Clarendon, Oxford, UK, 1988), Vol. 74.
[16] W. M. Alberico, M. Ericson and A. Molinari, Annals Phys. **154**, 356 (1984).
[17] A. A. Aguilar-Arevalo *et al.* [MiniBooNE Collaboration], Phys. Rev. D **79**, 072002 (2009).
[18] O. Benhar and D. Meloni, Phys. Rev. D **80**, 073003 (2009).

Chapitre 2

Restauration de la symétrie chirale

2.1 Introduction

À la fin de ma thèse j'ai participé à la publication d'un article appliquant le formalisme des réponses nucléaires dans un contexte différent, celui de la restauration de la symétrie chirale [4]. Le paramètre d'ordre dans ce cas est le condensat de quarks $\{\bar{q}q\}$ dont on cherche à prédire l'évolution dans la matière hadronique dense et chaude, c'est-à-dire en fonction de T et ρ .

Dans le modèle utilisé ici le condensat de quarks est lié à la valeur d'attente du champ pionique (eq.(2)), dont le calcul fait intervenir la réponse de spin-isospin longitudinale (eq. (4)), analogue à celle que nous avons calculée pour les interactions neutrino-noyau. Elle est donc évaluée à l'approximation des anneaux de la RPA et en incluant la résonance Delta et les excitations $np - nh$. L'évolution en fonction de la température et de la densité baryonique est évaluée au niveau des fonctions réponses nues et RPA.

Le principal résultat obtenu dans cette étude est que les pions virtuels jouent un rôle essentiel, même à des densités baryoniques faibles, dans la densité scalaire pionique. Ils sont même une composante essentielle dans un domaine de température allant jusqu'à $T \sim 150$ MeV. La vertu essentielle du formalisme des réponses nucléaires est encore une fois de pouvoir effectuer une évaluation quantitative d'observables physiques que l'on peut in fine confronter aux valeurs expérimentales.

2.2 Pion scalar density and chiral symmetry restoration at finite temperature and density [4]

G. Chanfray^a, D. Davesne^a, J. Delorme^a, M. Ericson^{a,b} and J. Marteau^a

^a*Institut de Physique Nucléaire de Lyon, IN2P3-CNRS et Université Cl. Bernard,
43, Bvd. du 11 novembre 1918, F-69622 Villeurbanne Cedex, France*

^b*CERN, Theory Division, CH-1211 Geneva 23, Switzerland*

Abstract

This paper is devoted to the evaluation of the pionic scalar density at finite temperature and baryonic density. We express the latter effect in terms of the nuclear response evaluated in the random phase approximation. We discuss the density and temperature evolution of the pionic density which governs the quark condensate evolution. Numerical evaluations are performed.

Introduction

Pions play a crucial role in chiral symmetry restoration, due to their Goldstone boson character. The amount of restoration is measured by the modification of the order parameter, i.e. the quark condensate density, with respect to the vacuum value. In this context the evaluation of the expectation value of the squared pion field, linked to the scalar density of pions ρ_S^π by $\rho_S^\pi = m_\pi \langle \Phi^2 \rangle$, is of a great interest. For a single nucleon this quantity governs the total amount of chiral symmetry restoration of pionic origin, according to [1,2]:

$$\frac{m_\pi^2}{2} \int d^3\vec{x} \langle N | \Phi^2(x) | N \rangle = 2m_q \int d^3\vec{x} \langle N | \Delta^\pi \bar{q}q(x) | N \rangle = \Sigma_N^\pi = \frac{m_\pi}{2} N_\pi, \quad (1)$$

where N_π is the scalar number of pions in the nucleon cloud, Σ_N^π is the part of the nucleon Σ commutator of pionic origin and $\langle N | \Delta^\pi \bar{q}q(x) | N \rangle$ represents the corresponding modification of the quark condensate with respect to the vacuum value. Similarly, in a uniform nuclear medium of density ρ , or in a heat bath, the evolution of the quark condensate originating from the pions is linked, to one-pion loop order, to the average value $\langle \Phi^2 \rangle$ by :

$$\frac{\Delta^\pi \langle \bar{q}q(\rho, T) \rangle}{\langle \bar{q}q(0, 0) \rangle} = -\frac{\langle \Phi^2 \rangle}{2f_\pi^2}. \quad (2)$$

The same quantity $\langle \Phi^2 \rangle$ governs also the quenching factor, $1 - \langle \Phi^2 \rangle / 3f_\pi^2$, of coupling constants such as the nucleonic axial coupling constant g_A or the pion decay one f_π , originating from pion loops, which is the counterpart of the mixing of axial and vector currents [3,4]. This type of quenching has to be seen as a manifestation of chiral symmetry restoration and should also apply to the case of ρ meson excitation by virtual photons as enters in relativistic heavy ion collisions. It is therefore interesting to evaluate the quantity $\langle \Phi^2 \rangle$ in the conditions of such experiments. Now, the fireball which is the source of the dileptons contains, besides thermal pions, a significant residual baryonic background. We have therefore to understand how the pion density evolves at finite values of both temperature and baryonic chemical potential. The first order approximation for the quantity $\langle \Phi^2 \rangle$ adds the values for a pure heat bath and for a cold baryonic medium, writing with obvious notations :

$$\langle \Phi^2 \rangle(\rho, T) = \langle \Phi^2 \rangle_T(\rho = 0) + \langle \Phi^2 \rangle_\rho(T = 0). \quad (3)$$

However this approximation is likely to be crude since the temperature has an effect on the pion density of the nuclear medium and on the other hand the presence of the baryonic background modifies the number of pions thermally excited. As an illustration of the second point, the pion density in the baryonic vacuum is fixed by the Bose-Einstein factor which is $(e^{\omega_k/T} - 1)^{-1}$ for pions of momentum \vec{k} , with $\omega_k = \sqrt{\vec{k}^2 + m_\pi^2}$. In the nuclear medium the pion becomes a quasi-particle with a broad width. It can decay for instance into a particle-hole pair which has a smaller energy than the free pion. Its excitation is then favored by the thermal factor. There is therefore a mutual influence between temperature and density that we will investigate.

The article is organized as follows. In the first section we evaluate the pion density of a nuclear medium at zero temperature. We relate this quantity to the nuclear response to a pion-like excitation. We evaluate this response in the RPA scheme, taking also into account the two particle-two hole ($2p$ - $2h$) excitations. Within this framework, we study the deviation with respect to the independent nucleon approximation. In the second section we introduce the effect of the temperature through the modification of the nuclear responses. In the third section we incorporate the influence of the finite baryonic chemical potential in the heat bath case.

1 Pion scalar density in the cold nuclear medium

This quantity was discussed in relation to the quark condensate modification by Chanfray and Ericson [1]. They discussed its deviations with respect to free nucleons, introducing the nuclear response to pion-like excitation, treated in the static case $M_N \rightarrow \infty$. The extension to the non-static situation can be performed through the time-ordered graphs of Fig. 1 where the cross represents the point at which the pions are created or annihilated. The pion momentum is denoted q and ω is the excitation energy of the nuclear system in the intermediate state. The sum of the four graphs leads to the following expression which has also been derived with a different method in Ref. [5] :

$$Eq.\langle\Phi^2\rangle = \frac{\rho}{A} 3 \frac{g_{\pi NN}^2}{4M_N^2} \int \frac{d^3q}{(2\pi)^3 2\omega_q^2} \int_0^\infty d\omega \left[\frac{1}{(\omega + \omega_q)^2} + \frac{1}{\omega_q} \frac{1}{(\omega + \omega_q)} \right] v^2(Q^2) R_L(\omega, \mathbf{q}) \quad (4)$$

where $Q^2 = \omega^2 - \mathbf{q}^2$, $v(Q^2)$ is the form factor of the pion vertex for which we use a monopole form :

$$v(Q^2) = \frac{\Lambda^2 - m_\pi^2}{\Lambda^2 - Q^2}. \quad (5)$$

Finally, R_L represents the spin-isospin longitudinal response function :

$$R_L(\omega, \mathbf{q}) = \sum_n |\langle n | \sum_{i=1}^A \sigma_i \cdot \mathbf{q} \tau_i^a e^{i\mathbf{q} \cdot \mathbf{r}_i} | 0 \rangle|^2 \delta(\omega - E_n). \quad (6)$$

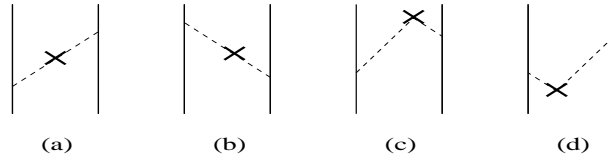


Fig. 1. *Time-ordered graphs for pion exchange.*

In the actual calculation, we add in the response R_L the excitation of the Delta resonance with the standard replacement :

$$\sigma_i \cdot \mathbf{q} \tau_i^a \longrightarrow \frac{g_{\pi N\Delta}}{g_{\pi NN}} \mathbf{S}_i \cdot \mathbf{q} (T_i^a)^\dagger \quad (7)$$

where \mathbf{S}^\dagger (\mathbf{T}^\dagger) is the spin (isospin) transition operator connecting the spin (isospin) $\frac{1}{2}$ and $\frac{3}{2}$ states [6]. Note that for a matter of convenience we have incorporated in this operator the ratio of the $\pi N\Delta$ and πNN coupling constants. We have also assumed the same form factors, $v(Q^2)$, at the πNN vertex and at the $\pi N\Delta$ vertices. Finally we recall the link between the response function and the polarization propagator $\Pi(\omega, \mathbf{q}, \mathbf{q}')$ which we will use in the following :

$$R(\omega, \mathbf{q}) = -\frac{V}{\pi} \text{Im}\Pi(\omega, \mathbf{q}, \mathbf{q}) \quad (8)$$

We will first discuss the result for the free nucleon.

1.1 Free nucleon.

In the nucleon case, where the response R_L reduces to a simple expression, Eq. (4) provides for the (scalar) pion number N_π in the nucleon cloud :

$$\begin{aligned}
N_\pi &= m_\pi \int d^3\vec{x} \langle N | \Phi^2(\mathbf{x}) | N \rangle \\
&= m_\pi 3 \frac{g_{\pi NN}^2}{4M^2} \int \frac{d^3q}{(2\pi)^3} \mathbf{q}^2 \left\{ \frac{1}{\omega_q} \left[\frac{1}{2\omega_q} \frac{1}{(\varepsilon_q + \omega_q)^2} + \frac{1}{2\omega_q^2} \frac{1}{(\varepsilon_q + \omega_q)} \right] v^2(Q^2) \right. \\
&\quad \left. + \frac{4}{9} \left(\frac{g_{\pi N\Delta}}{g_{\pi NN}} \right)^2 \int_0^\infty \frac{d\omega}{\omega_q} \left[\frac{1}{2\omega_q} \frac{1}{(\omega + \omega_q)^2} + \frac{1}{2\omega_q^2} \frac{1}{(\omega + \omega_q)} \right] v^2(Q^2) \left(-\frac{1}{\pi} \text{Im} \frac{1}{\omega - \omega_\Delta + i\frac{\Gamma_\Delta}{2}} \right) \right\}. \quad (9)
\end{aligned}$$

In the above equation we have used the following notations : $\varepsilon_q = \mathbf{q}^2/2M_N$ and $\omega_\Delta = M_\Delta - M_N + \mathbf{q}^2/2M_\Delta$. The energy dependence of the Delta width Γ_Δ is taken from the analysis of the pion-nucleon scattering [6].

Our numerical inputs for the evaluation of N_π are defined as follows. Without form-factor the integrals diverge linearly. The resulting value is then quite sensitive to the cut-off function. We stress, however, that the specific case of the single nucleon is not the purpose of this paper. It is for us an element of comparison to introduce the nuclear effects. Since we want to restrict the calculation to a region where nuclear effects are reasonably under control, we have limited the integrals to : $q = 1$ GeV and $\omega = 1$ GeV. The parameters are chosen so as to obtain a value $\Sigma_N^\pi = \frac{1}{2}m_\pi N_\pi = 30$ MeV which is well in the accepted range [7–9]. This is achieved with $\Lambda = 1$ GeV and $(g_{\pi N\Delta}/g_{\pi NN})^2 = 3.8$.

1.2 Infinite nuclear matter.

We now turn to the case of infinite nuclear matter. In order to evaluate the response functions, we use the method of Delorme and Guichon [10] who calculated the zero order response in the local density approximation and then solved exactly the RPA equations. Their zero order response function also includes the $2p$ - $2h$ excitations. The corresponding Feynman diagrams of such processes are displayed in Fig. 2.

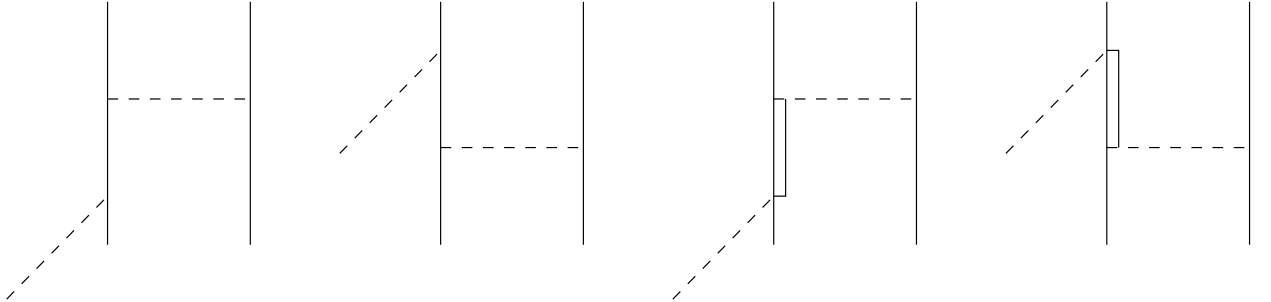


Fig. 2. *Feynman diagrams for the 2p-2h processes. The double line represents the Delta resonance.*

They are calculated in two steps. First we single out the contributions which reduce to a medium modification of the Δ self-energy, for which the parametrization of Ref. [11] is used. This parametrization includes some $3p$ - $3h$ excitation states as well. For the rest we use the results of Shimizu-Faessler [12] who evaluated the two nucleons p-wave pion absorption at threshold ($\omega = m_\pi$), from which the Δ self-energy part, already taken into account, is separated out. As for each

the remaining contributions, an energy extrapolation suggested by the many-body diagrammatic interpretation is performed.

We solve the RPA equations in the ring approximation : $\Pi = \Pi^0 + \Pi^0 \mathcal{V} \Pi$. Here \mathcal{V} is the particle-hole (p - h) interaction with the standard formulation : $\mathcal{V} = V_\pi + V_{g'}$ where the second piece is the short-range Landau-Migdal part. More explicitly with our definition of the response, \mathcal{V} reads :

$$\mathcal{V} = \frac{v^2(Q^2)}{\mathbf{q}^2} \left(\frac{\mathbf{q}^2}{Q^2 - m_\pi^2} + g' \right). \quad (10)$$

The corresponding Landau-Migdal parameters g' are different in the various channels : g'_{NN} for the NN sector, $g'_{\Delta\Delta}$ for the Δ one, $g'_{N\Delta}$ for the mixing of NN and ΔN excitations. We adopt the following values:

$$g'_{NN} = 0.7, \quad g'_{N\Delta} = g'_{\Delta\Delta} = 0.5. \quad (11)$$

The results are illustrated on Fig. 3 which shows the energy dependence of the zero order and RPA responses, for a fixed value of the momentum $q = 300$ MeV. The bare response presents a low-energy peak corresponding to the NN^{-1} excitation and a high-energy one (ΔN^{-1} excitations). The figure displays the RPA enhancement of the low energy peak, introduced by Alberico et al.

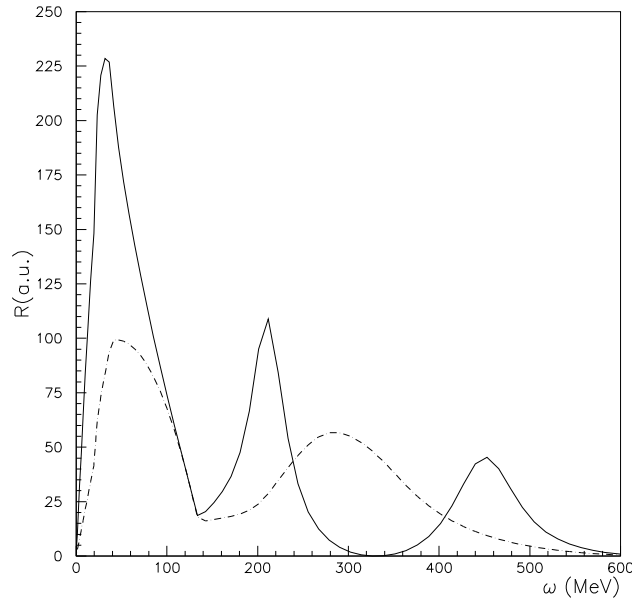


Fig. 3. Response function per nucleon at normal nuclear density as a function of the energy for a fixed momentum $q = 300$ MeV. The dot-dashed and continuous lines represent respectively the zero order and RPA responses.

[13], which arises from the attractive nature of the p - h interaction. It also displays the collective behaviour of the Δ excitation with a splitting into two branches.

Once the energy and momentum integrations are performed, we find, as in Ref. [1], a moderate increase as compared to the free nucleon value, with the values per nucleon at normal nuclear density :

$$\tilde{\Sigma}_N^\pi \equiv \Sigma_A^\pi/A = 38.5 \text{ MeV} \text{ and } N_A^\pi/A = 0.55 \quad (12)$$

versus 30 MeV and 0.40 respectively for the free nucleon. The quantity $\tilde{\Sigma}_N^\pi$ is the (medium modified) effective sigma commutator.

More precisely, we decompose the response function Π (accordingly Σ^π) into four types, depending on the kind of states which are excited at each external vertices : NN , $N\Delta$, ΔN and $\Delta\Delta$ (Fig. 4). The density evolution of the different components of the sigma commutator are represented on

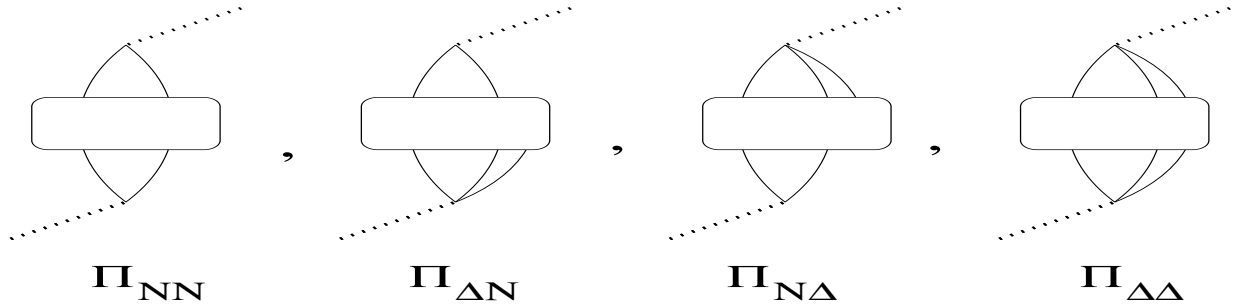


Fig. 4. *Symbolic representation of the NN , ΔN , $N\Delta$ and $\Delta\Delta$ response functions. The Delta resonance is represented by the double line.*

Fig. 5 both without and with RPA. Notice that, in absence of the RPA, there is already a contribution of the $N\Delta$ channel at finite density due to the $2p$ - $2h$ excitations. The overall RPA increase of the sigma commutator mainly comes from that of the $\Sigma_{N\Delta} + \Sigma_{\Delta N}$ parts. These last quantities embody the mixing of the ΔN^{-1} configurations into the NN^{-1} ones. This is well known to be responsible for the enhancement of the low energy response (*i.e.* the NN^{-1} excitations) [14].

2 Inclusion of temperature

2.1 Influence on the virtual pion cloud

We now introduce the temperature, *via* the Matsubara formalism : all the integrals over energy are replaced by an infinite sum over Matsubara frequencies. For the NN^{-1} sector, the generalized Lindhart function (the imaginary part of which is proportional to the response function) at finite temperature is discussed in textbooks (see e.g. Ref. [15]). The result is the replacement of the Heaviside functions that characterize the occupation of fermion states at zero temperature by the Fermi-Dirac distributions. We have generalized this procedure to particle with width and applied it to Δ - N^{-1} , N - Δ^{-1} and Δ - Δ^{-1} rings. The generalized Lindhart function L_{ab-1} for a process

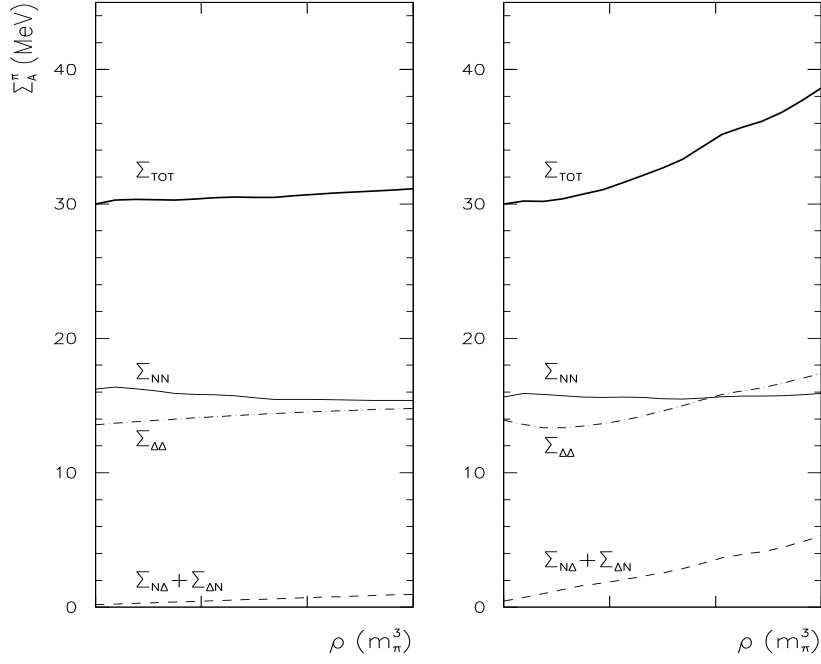


Fig. 5. *Density evolution of the different components of the effective sigma commutator: left (right) figure is without (with) RPA.*

involving a particle of type (a) and a hole of type (b) is found to be :

$$L_{ab^{-1}}(\omega, \vec{q}) = -\frac{N_{S,I}}{4\pi^2} \int k^2 dk d(\cos \theta) \frac{f(\omega_k^b)(1 - f(\omega_{k+q}^a))}{\omega - \omega_{k+q}^a + \omega_k^b + \frac{i}{2}\Gamma^a(\omega_k^b + \omega) + \frac{i}{2}\Gamma^b(\omega_{k+q}^a - \omega)} \quad (13)$$

$$-\frac{f(\omega_k^b)(1 - f(\omega_{k+q}^a))}{\omega + \omega_{k+q}^a - \omega_k^b + \frac{i}{2}\Gamma^a(\omega_k^b - \omega) + \frac{i}{2}\Gamma^b(\omega_{k+q}^a + \omega)} \quad (14)$$

where $N_{S,I}$ is a constant arising from the summation of spin and isospin and $\Gamma^{a,b}(\omega)$ represents the width of the particle of type (a,b) for an energy ω . The occupation number of hadron species a is :

$$f(\omega_k^a) = \frac{1}{\exp(\frac{\omega_k^a - \mu}{T}) + 1} \quad (15)$$

where μ is the (common) chemical potential for baryons, the value of which fixes the baryonic density ρ at a given temperature. As implicitly stated before, we limit ourselves to nucleons and deltas *i.e.* $\rho = \rho_N + \rho_\Delta$.

Concerning the Δ width, things are somewhat more complicated. In the medium, the pionic decay channel $\Delta \rightarrow \pi N$ is partly suppressed due to Pauli blocking. At the same time, other channels open, the pion being replaced by $1p-1h$, $2p-2h$, etc... At normal density and zero temperature

the pionic channel remains dominant according to Ref. [11]. It represents approximately 75% of the total width ($\simeq 90$ MeV to be compared with 120 MeV at the resonance energy) and the non-pionic decay channels only the remaining 25%. In view of the difficulties of a full calculation of the temperature effects, we have adopted the simplified following strategy : we have kept the parametrization of Ref. [11], derived at $T = 0$, for the non-pionic decay channel. We have introduced the temperature effects *via* the Matsubara formalism only for the main pionic part of the width.

The Figure 6 displays the temperature evolution of the zero order response function. The dashed line, which represents the $T = 0$ case, exhibits the $N-N^{-1}$ and $\Delta-N^{-1}$ structures. Increasing temperature tends to wash out more and more these peaks. At the same time an overall suppression effect occurs. Note that the Δ branch is less affected by the temperature because of the higher

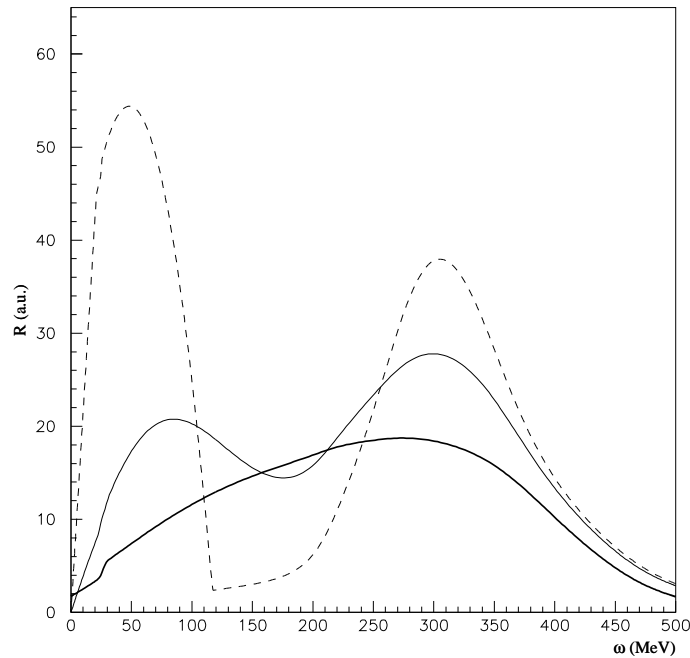


Fig. 6. Zero order response at a baryonic density equal half nuclear matter density ($\rho = 0.25m_\pi^3$) as a function of energy for a fixed momentum $q = 300$ MeV for three temperatures. Dashed lines : $T = 0$. Thin full line : $T = 50$ MeV. Thick full line : $T = 150$ MeV.

energies involved. In the RPA case (see Fig. 7) , one observes a similar behavior : an important general decrease and the loss of the lower energy structures.

We now turn to the question of the thermal pions present in the heat bath.

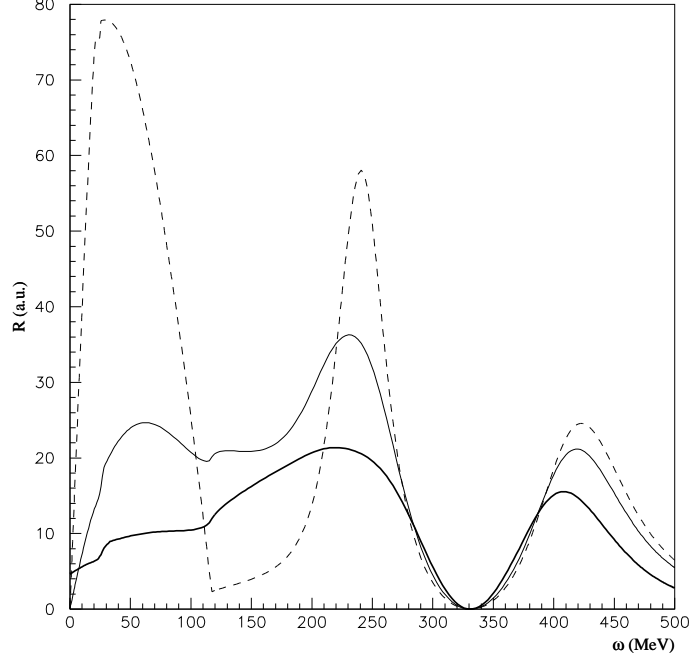


Fig. 7. *Same as before but for the RPA response.*

2.2 Inclusion of thermal pions.

The effects previously discussed concerned only the modification, due to the temperature, of the virtual pion density present in the nuclear medium. At finite temperature, thermally excited pionic modes (quasi-pions) are also present and they give an additional contribution to the pion scalar density. Here for a better illustration we give the result for $\langle \Phi^2 \rangle / 2f_\pi^2$ which according to Eq.(2) governs the amount of chiral symmetry restoration of pionic origin:

$$\begin{aligned}
\frac{\langle \Phi^2 \rangle}{2f_\pi^2} &= \frac{\rho}{A} \frac{3}{2f_\pi^2} \frac{g_{\pi NN}^2}{4M_N^2} \int \frac{d^3q}{(2\pi)^3} \int_0^\infty d\omega \left(\frac{1}{2\omega_q^2(\omega + \omega_q)^2} + \frac{1}{2\omega_q^3(\omega + \omega_q)} \right) v^2(Q^2) R_L(\omega, \mathbf{q}) \\
&\quad + \frac{3}{2f_\pi^2} \int \frac{d^3q}{(2\pi)^3} \int_0^\infty d\omega n(\omega) \left(-\frac{2}{\pi} \right) \text{Im } D(\omega, \mathbf{q}) \\
&\equiv \frac{\rho \tilde{\Sigma}_B^\pi}{f_\pi^2 m_\pi^2} + \frac{\langle \Phi^2 \rangle_T}{2f_\pi^2}
\end{aligned}$$

where $n(\omega) = 1 / (\exp(\omega/T) - 1)$ is the Bose occupation factor and $D(\omega, \mathbf{q})$ the quasi-pion propagator. The second identity defines the quantities $\tilde{\Sigma}_B^\pi$ and $\langle \Phi^2 \rangle_T$, associated respectively with the first and second pieces of the r.h.s. of the above equation: $\tilde{\Sigma}_B^\pi$ represents an effective, temperature dependent, sigma commutator per baryon, whereas $\langle \Phi^2 \rangle_T$ is the scalar density of quasi-pions thermally excited.

3 Results

In order to display the condensate evolution, all the forthcoming figures show its relative decrease, *i.e.* the quantity $\Phi^2/2f_\pi^2$ according to Eq. (2). We stress again that the points of interest are the influence of temperature on the nuclear pionic cloud contribution, the influence of the baryonic density on the thermal pions one and finally how large is the deviation from the additive approximation of Eq. (3).

We first present on Fig. 8 the contribution of the virtual pion cloud alone alone (term in $\tilde{\Sigma}_B^\pi$). Each box shows the temperature evolution at fixed baryonic density. It illustrates the suppression effect of the temperature which originates in the quenching of the nuclear response previously mentioned. The increase with baryonic density observed in this figure reflects the obvious fact that the pionic density follows the baryon one.

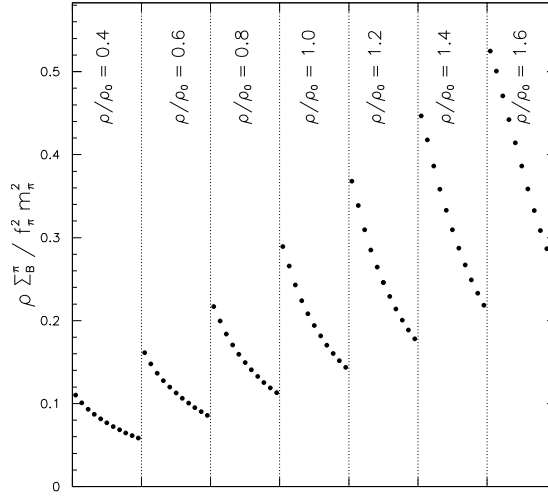


Fig. 8. *Relative decrease of the condensate coming from the virtual pion cloud part as a function of the density and the temperature. Each box corresponds to a fixed density as indicated. The density increases by steps of $0.2\rho_0$ from left to right between 0.4 and $1.6\rho_0$. In each box the points correspond to temperature increases by steps of $0.10m_\pi$ between 0.05 and $1.05m_\pi$.*

In Figure 9 we present in the same fashion the condensate decrease due to thermal pions alone (term in $\langle\Phi^2\rangle_T/2f_\pi^2$). The iso-temperature curves show the influence of the baryonic density which pushes down the quasi-pion excitation energy, thus increasing their thermal excitation.

Finally in the last figure (Fig. 10) we present the sum of both contributions. The competition between the variations of both terms with respect to the temperature is the source of the observed parabolic type shape. For comparison, we have plotted in open circles the approximation of Eq. (3) where the effect of the thermal pions at zero density is simply added to that of the pion cloud at zero temperature. This approximation does not display the hollow shape of the exact calculation: it overestimates the latter by at most 15% in the medium part of the temperature range we

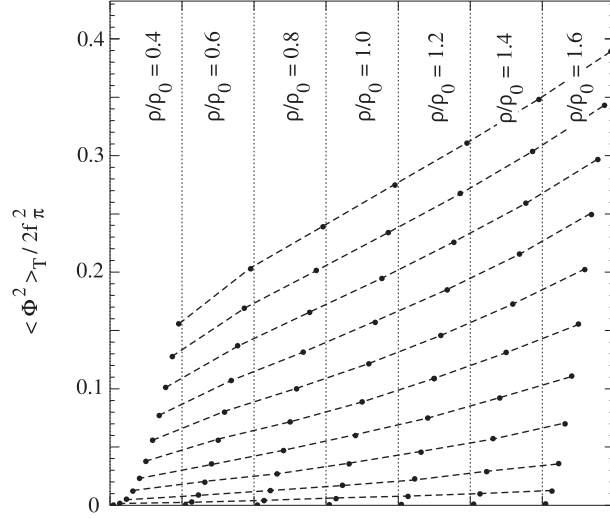


Fig. 9. Same as the preceding figure but for the thermal pions. As a guidance in order to display the influence of the density on the thermal pions, points of equal temperature are joined by a dashed line.

have considered, the deviation becoming quite small beyond $T \approx 90$ -100 MeV. In this region the decrease of the pionic cloud contribution with temperature (Fig. 8) practically compensates the enhancement of the thermal excitations by density effects. The most important conclusion which can be drawn from Fig. 10 is that, due to the nuclear pions, the pion scalar density is much larger than in the absence of nuclear effects, already for densities of the order of $0.6 \rho_0$.

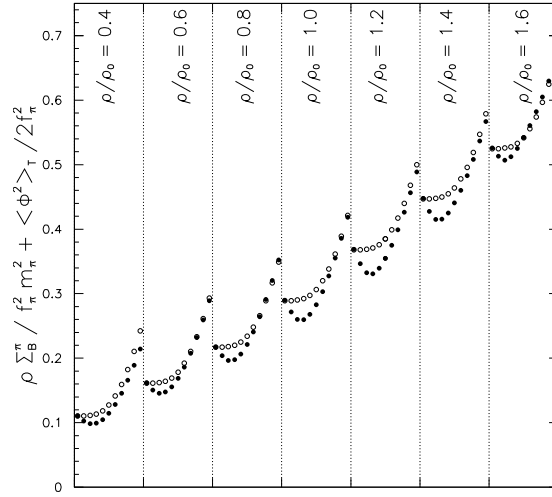


Fig. 10. Sum of both contributions of the virtual pion cloud and the thermal pions (black circles). For comparison the open circles represent the additive approximation of Eq. (3)

Conclusion.

In conclusion we have studied the evolution of the quark condensate of pionic origin under the simultaneous influence of the baryonic density and temperature. It is related to the scalar pionic density which comes on the one hand from the virtual nuclear pions and on the other hand from the thermally excited ones. We have expressed the first contribution in terms of the nuclear response to a pion-like excitation and evaluated it for the case of nuclear matter in the RPA scheme, first at zero and then at finite temperature. We have shown that the RPA produces a sizeable enhancement ($\approx 30\%$), while instead the temperature washes out the peaks and suppresses the nuclear response, hence decreasing the virtual pion density.

As for the thermally excited pions we have shown that the presence of the baryonic background appreciably enhances their number. The cause has to be found in the lowering of the quasi-pion excitation energies, which favours their thermal excitation. When the densities of both types of pions are added, the mutual influences which go in opposite directions cancel their effects to a large extent. In the density and temperature domain that we have explored, the additive assumption of Eq. (3) which neglects the mutual influence is a good approximation. It deviates from the exact result by no more than 15%, the deviation being maximum around $T \approx 50$ MeV. At this T value the additive approximation slightly overestimates the pionic density.

Our study has shown that, even at moderate baryonic density, the virtual nuclear pions are a major component of the overall scalar pion density. As an example, at nuclear matter density, they dominate in the temperature range we have considered, *i.e.* up to at least $T \approx 150$ MeV. Since the pion is the agent for the mixing of the vector and axial correlators, the consequence of our study is that the existence of a baryonic background, if any, should not be ignored in this mixing.

References

- [1] G. Chanfray and M. Ericson, Nucl. Phys. **A556** (1993) 427.
- [2] G. Chanfray, M. Ericson and J. Wambach, Phys. Lett. **B388** (1996) 673.
- [3] M. Dey, V.L. Eletsky and B.L. Ioffe, Phys. Lett. **B252** (1990) 620.
- [4] G. Chanfray, J. Delorme and M. Ericson, Nucl. Phys. **A637** (1998) 421.
- [5] G. Chanfray and D. Davesne, Nucl. Phys. **A646** (1999) 125.
- [6] T. Ericson and W. Weise, *Pions and nuclei* (Oxford Science Publications, Clarendon Press, Oxford 1988).
- [7] M. Birse and J. Mc Govern, Phys. Lett. **B292** (1992) 242.
- [8] I. Jameson, G. Chanfray and A.W. Thomas, Journal of Physics **G18** (1992) L159.
- [9] G. Chanfray, J. Delorme and M. Ericson, Phys. Lett. **B455** (1999) 39.
- [10] J. Delorme and P.A.M. Guichon, Phys. Lett. **B264** (1991) 157; more details and earlier references can be found in the unpublished report LYCEN 8906 (1989).
- [11] E. Oset, L.L. Salcedo and D. Strottman, Phys. Lett. **B165** (1985) 13.
- [12] K. Shimizu and A. Faessler, Nucl. Ph. **A306** (1978) 311; *ibid.* **A333** (1980) 495.
- [13] W.M. Alberico, M. Ericson and A. Molinari, Phys. Lett. **92B** (1980) 153.
- [14] M. Ericson, in *Proc. International School "Mesons, isobars, quarks and nuclear excitations, Erice" 1983*, edited by D. Wilkinson (Pergamon Press 1983).
- [15] A.L. Fetter and J.D. Walecka, *Quantum theory of many-particle systems* (McGraw-Hill, New York 1971).

Bibliographie

- [1] Effects of the Nuclear Correlations on the Neutrino-Oxygen Interactions, J. Marteau Eur.Phys.J.A5 :183-190, 1999.
- [2] Nuclear effects in neutrino nucleus interactions, J. Marteau, J. Delorme, M. Ericson, Nucl.Instrum.Meth. A451 (2000) 76-80.
- [3] Nuclear correlation effects in neutrino oxygen interactions and the atmospheric neutrino anomaly, J. Marteau, J. Delorme, Magda Ericson, Nucl.Phys. A663 (2000) 783-786.
- [4] Pion Scalar Density and Chiral Symmetry Restoration at Finite Temperature and Density, G. Chanfray, D. Davesne, J. Delorme, M. Ericson, J. Marteau, Eur.Phys.J. A8 (2000) 283-289.
- [5] Neutrino-Oxygen interactions : role of nuclear physics in the atmospheric neutrino anomaly, J. Marteau, J. Delorme, M. Ericson, Proceedings of the XXXIVth Rencontres de Moriond "Electroweak interactions and unified theories", LYCEN-9956.
- [6] Nuclear correlation effects in neutrino-nucleus interactions, J. Marteau, Nucl.Phys.Proc.Suppl. 112 (2002) 203-209 & Nucl.Phys.Proc.Suppl. 112 (2002) 98-105.
- [7] Comparison of predictions for nuclear effects in the Marteau model with the NUX+FLUKA scheme, J.A.Nowak et al 3rd International Workshop on Neutrino-Nucleus Interactions in the Few-GeV Region, 17-21 March, Gran Sasso (Italy), Proceedings of the conference.
- [8] Neutrino interactions with nuclei, M.Martini, G.Chanfray, M.Ericson, J.Marteau, LYCEN-2009-09, Sep 2009, arXiv :0909.0642, 6th International workshop on Neutrino-Nucleus Interactions in the Few-GeV Region (NuInt'09), May 18th - 22nd, 2009, Sitges, Barcelona (Spain), AIP Conf.Proc.1189 :323-326,2009.
- [9] A unified approach for nucleon knock-out, coherent and incoherent pion production in neutrino interactions with nuclei, M.Martini, M.Ericson, G.Chanfray, J.Marteau, Phys.Rev.C80 :065501,2009.
- [10] Neutrino and antineutrino quasielastic interactions with nuclei, M. Martini, M. Ericson, G. Chanfray, J. Marteau, Journal Ref : Phys.Rev.C81 :045502, 2010.

Deuxième partie

Physique expérimentale des oscillations
de neutrinos

Table des matières

| | | |
|----------|---|------------|
| 1 | Introduction aux oscillations de neutrinos | 85 |
| 2 | Expérience de première génération : OPERA et le programme CNGS | 91 |
| 2.1 | Introduction | 91 |
| 2.2 | OPERA first events from the CNGS neutrino beam, [12] | 93 |
| 2.3 | The OPERA global readout and GPS distribution system, [11] | 100 |
| 2.4 | Evidence for $\nu_\mu \rightarrow \nu_\tau$ appearance in the CNGS neutrino beam with the OPERA experiment, [26] | 102 |
| 2.5 | Cosmic ray physics with the OPERA detector, [14] | 109 |
| 3 | Les générations futures : T2K et au-delà | 115 |
| 3.1 | Introduction | 115 |
| 3.2 | Indication of Electron Neutrino Appearance from an Accelerator-produced Off-axis Muon Neutrino Beam, [31] | 118 |
| 3.3 | LBNO-DEMO : Large-scale neutrino detector demonstrators for phased performance assessment in view of a long-baseline oscillation experiment, [54] | 129 |
| 3.3.1 | Design concept of the $6 \times 6 \times 6\text{m}^3$ prototype | 129 |
| 3.3.2 | Front-end and DAQ readout | 131 |
| | Bibliographie Partie II | 139 |

Chapitre 1

Introduction aux oscillations de neutrinos

Généralités — Les oscillations de neutrinos désignent le phénomène par lequel un neutrino, actif, produit dans un état de saveur déterminé (ν_e , ν_μ ou ν_τ) va se projeter dans un état de saveur différente de sa saveur initiale après avoir parcouru une distance donnée. Le phénomène d'oscillation des neutrinos se manifeste soit par l'apparition d'un excès d'une nouvelle saveur dans les données (mode 'apparition') soit par un déficit de la saveur initiale attendue (mode "disparition"). La condition nécessaire et suffisante d'obtention des oscillations est l'existence d'états de masse définis pour les neutrinos, ce qui rompt avec la théorie du Modèle Standard et qui implique un mécanisme non-standard de génération des masses.

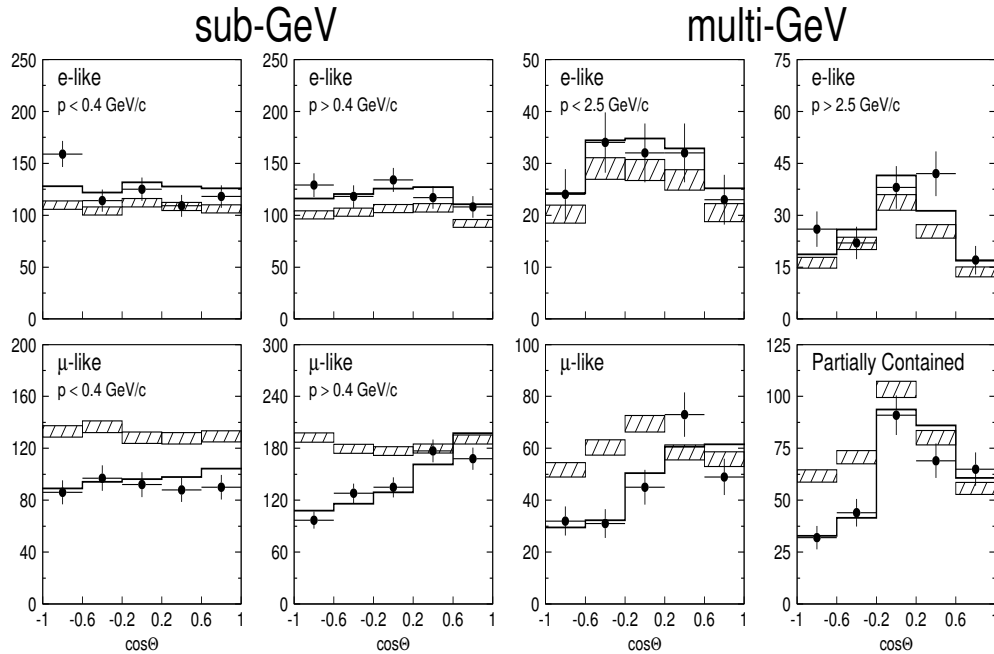


FIGURE 1.1 – Distributions zénithales des événements de type électronique et muonique "sub-GeV" et "multi-GeV". Ces distributions sont données pour différentes coupures cinématiques sur le moment du lepton détecté. Les rectangles hachurés correspondent aux attentes des calculs Monte-Carlo sans oscillation de neutrino. Les lignes pleines correspondent aux oscillations $\nu_\mu \rightarrow \nu_\tau$.

Les oscillations de neutrinos ont fait l'objet de nombreuses études depuis le postulat de leur existence, sur le modèle des oscillations $\nu \leftrightarrow \bar{\nu}$. Historiquement présent sous forme de diverses “anomalies” expérimentales relevées lors de l'étude des neutrinos d'origine naturelle – neutrinos solaires et atmosphériques –, le phénomène a été progressivement confirmé par des expériences sur faisceaux et auprès de réacteurs nucléaires. Si la fin du siècle dernier marque un tournant avec la proclamation de la première observation des oscillations de neutrinos atmosphériques (Super-Kamiokande, 1998, dont l'analyse historique dans le canal atmosphérique est montrée sur la figure ci-avant), la décennie passée a été riche en confirmations expérimentales tant dans le secteur des atmosphériques que celui des neutrinos solaires.

Formalisme — Le formalisme des oscillations de neutrinos est simple. Les états propre de l'interaction faible (ν_α , $\alpha = (e, \mu, \tau)$) et les états propres de masse (ν_i , $i = (1, 2, 3)$) sont reliés par une matrice unitaire U telle que $|\nu_\alpha\rangle = \sum_i U_{\alpha i} |\nu_i\rangle$. La matrice U n'étant pas diagonale, elle va permettre des transitions entre différents saveurs de neutrinos lors de leur propagation dans l'espace-temps.

Considérons un neutrino créé par interaction faible de courant chargé à $t = 0$ et $x = 0$ comme un état propre de saveur $|\nu_\beta\rangle$. Quand il va se propager, l'opérateur d'évolution va permettre de développer des phases correspondant aux différents états propres de masse dont il est la combinaison linéaire :

$$|\nu_\alpha(t, x)\rangle = \sum_i U_{\alpha i} e^{-i(E_i t - p_i x)} |\nu_i\rangle$$

L'amplitude de probabilité de le détecter après propagation comme un état propre de saveur $|\nu_\beta\rangle$ est :

$$\begin{aligned} A(\nu_\alpha \rightarrow \nu_\beta) &= \langle \nu_\beta | \nu_\alpha(t, x) \rangle \\ &= \sum_{i,j} U_{\beta j}^* U_{\alpha i} e^{-i(E_i t - p_i x)} \langle \nu_j | \nu_i \rangle \\ &= \sum_i U_{\beta i}^* U_{\alpha i} e^{-i(E_i t - p_i x)} \\ &\simeq \sum_i U_{\beta i}^* e^{-i(E_i - p_i)x} U_{\alpha i} \end{aligned}$$

où dans la dernière équation on a fait l'hypothèse que les neutrinos sont ultra-relativistes ($t \simeq x$). Dans cette dernière équation, on voit que l'amplitude de transition est une somme de contributions des différents états propres de masse.

Pour simplifier le traitement des oscillations, on fait en général l'hypothèse que le neutrino est créé soit avec une impulsion bien définie soit avec une énergie bien définie. Dans les deux cas cela viole le principe d'incertitude de la mécanique quantique. Un traitement rigoureux nécessite l'utilisation de paquets d'ondes. Le traitement simplifié donne cependant la même réponse. Par exemple si le neutrino est créé dans un état d'énergie bien définie E , alors l'impulsion de l'état propre de masse ν_i est $p_i = \sqrt{E^2 - m_i^2} \simeq E - m_i^2/2E$. L'amplitude de transition si les neutrinos sont détectés à une distance L de la source, s'écrit alors :

$$A(\nu_\alpha \rightarrow \nu_\beta) \simeq \sum_i U_{\beta i}^* e^{-i(m_i^2 L)/2E} U_{\alpha i}$$

En définissant $\Delta m_{ij}^2 \equiv m_i^2 - m_j^2$, on peut écrire la probabilité de transition sous la forme :

$$\begin{aligned}
P(\nu_\alpha \rightarrow \nu_\beta) &= |A(\nu_\alpha \rightarrow \nu_\beta)|^2 \\
&= \delta_{\alpha\beta} - 4 \sum_{i>j} \text{Re}(U_{\alpha i}^* U_{\beta i} U_{\alpha j} U_{\beta j}^*) \sin^2 \left(\frac{\Delta m_{ij}^2 L}{4E} \right) \\
&\quad + 2 \sum_{i>j} \text{Im}(U_{\alpha i}^* U_{\beta i} U_{\alpha j} U_{\beta j}^*) \cos^2 \left(\frac{\Delta m_{ij}^2 L}{4E} \right)
\end{aligned}$$

Dans le cas d'oscillations entre deux saveurs (par exemple : $\nu_e \leftrightarrow \nu_\mu$), la matrice de mélange se réduit à une matrice de rotation à un paramètre θ :

$$U = \begin{pmatrix} \cos \theta & \sin \theta \\ -\sin \theta & \cos \theta \end{pmatrix},$$

et la probabilité de transition s'écrit alors :

$$P(\nu_\mu \rightarrow \nu_e) = \sin^2(2\theta) \sin^2\left(\frac{\Delta m^2 L}{4E}\right).$$

On introduit la longueur d'oscillation : $L_{\text{osc}}[m] = 2\pi \frac{2E}{\Delta m^2} \simeq 2.48 \frac{E[\text{MeV}]}{\Delta m^2[\text{eV}^2]}$. La figure suivante illustre les différents cas qui peuvent se présenter :

- $L \ll L_{\text{osc}}$: les neutrinos n'ont pas le temps d'osciller
- $L \gg L_{\text{osc}}$: l'oscillation très rapide du neutrinos est en général lavée par la résolution du détecteur. La probabilité de transition ne varie plus avec la distance : $P(\nu_\mu \rightarrow \nu_e) = \frac{1}{2} \sin^2 2\theta$
- $L \sim L_{\text{osc}}$: on est sensible aux oscillations.

De façon à être sensible à la plus grande plage en Δm^2 possible, on va utiliser différents types de sources (différentes énergies) et détecter les neutrinos à différentes distances.

Dans un formalisme à 3 saveurs de neutrinos et en introduisant les angles de mélange θ_{12} , θ_{13} , θ_{23} et la phase δ_{CP} de violation de CP (en omettant les phases de Majorana), la matrice unitaire 3×3 U (matrice *PMNS* pour Pontecorvo-Maki-Nakagawa-Sakata) s'écrit :

$$U = \begin{pmatrix} U_{e1} & U_{e2} & U_{e3} \\ U_{\mu 1} & U_{\mu 2} & U_{\mu 3} \\ U_{\tau 1} & U_{\tau 2} & U_{\tau 3} \end{pmatrix} = \begin{pmatrix} 1 & 0 & 0 \\ 0 & c_{23} & s_{23} \\ 0 & -s_{23} & c_{23} \end{pmatrix} \begin{pmatrix} c_{13} & 0 & s_{13}e^{-i\delta} \\ 0 & 1 & 0 \\ -s_{13}e^{i\delta} & 0 & c_{13} \end{pmatrix} \begin{pmatrix} c_{12} & s_{12} & 0 \\ -s_{12} & c_{12} & 0 \\ 0 & 0 & 1 \end{pmatrix}$$

où c_{ij} et s_{ij} représentent respectivement $\cos(\theta_{ij})$ et $\sin(\theta_{ij})$. Les trois matrices sont associées couramment aux secteurs "atmosphérique" (angle θ_{23}), "solaire" (angle θ_{12}), et "réacteurs" (angle θ_{13}).

Résultats marquants — Le niveau actuel de compréhension de la matrice $PMNS$ est impressionnant si on le compare à celui qui prévalait en 1998, date de la proclamation de l’existence des oscillations de neutrinos dans le secteur des neutrinos atmosphériques par la collaboration Super-Kamiokande. Les 3 angles de mélange sont aujourd’hui mesurés et les inconnues restant sont l’existence éventuelle de la violation de CP dans le secteur leptonique (mesure de la δ_{CP} – ou des – phase(s) δ_{CP}) et la hiérarchie des masses : “mass hierarchy” ou MH (a-t-on $m_1^2 > m_3^2$ ou $m_3^2 > m_1^2$?).

Dans le secteur des neutrinos atmosphériques on retiendra les confirmations apportées par les programmes “long baseline” : K2K (KEK-to-Kamioka, 2001*) puis T2K (Tokai-to-Kamioka, 2008) au Japon, MINOS aux Etats-Unis (2005) et le CNGS (CERN-Neutrino-to-Gran Sasso, 2006) en Europe. Ces expériences ont permis de compléter la connaissance des paramètres θ_{23} et Δm_{23}^2 soit en mode “disparition” (observation d’un déficit de neutrinos par rapport aux prévisions théoriques) soit en mode “apparition” (détection directe des produits de l’oscillation). À ce titre l’expérience OPERA sur le faisceau CNGS joue un rôle singulier puisqu’elle a été la première, en 2010, à observer directement une oscillation de neutrino (ν_τ issu de l’oscillation d’un ν_μ du faisceau).

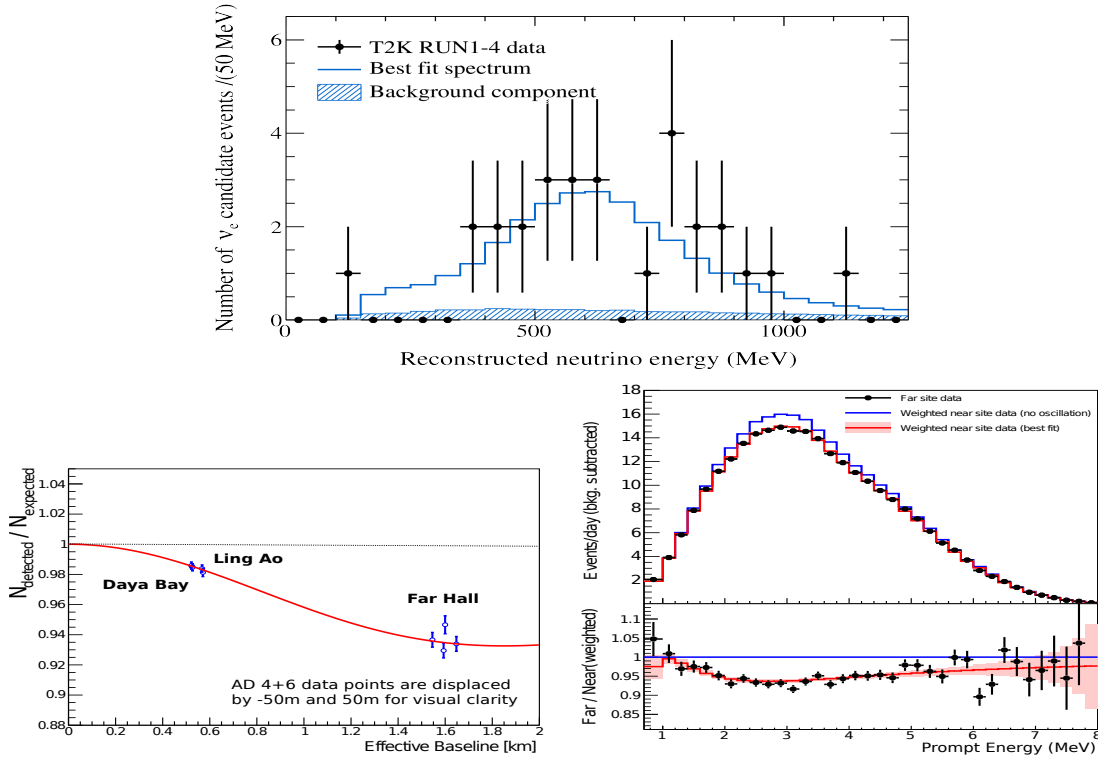


FIGURE 1.2 – En haut : spectre en énergie des candidats ν_e observés dans T2K. En bas, à gauche, rapport des événements $\bar{\nu}_e$ observés sur attendus dans les 3 halls expérimentaux de Daya Bay, en fonction de la distance de vol. En bas, à droite, figure supérieure : spectre mesuré après soustraction du bruit de fond au site lointain, comparé au spectre attendu après extrapolation des résultats des sites proches. En bas, à droite, figure inférieure : rapport des quantités précédentes.

Dans le secteur des neutrinos solaires on retiendra que les “anomalies” des neutrinos solaires (expériences radio-chimiques Chlore, Gallex, Sage) ont couru pendant quelques décennies avant d’être finalement confirmées par plusieurs expériences complémentaires. D’une part l’expérience SNO (Sudbury-Neutrino-Observatory, 2000) au Canada, sensible à différents canaux d’interaction des neutrinos solaires (par courant chargé, neutre ou diffusion élastique) permet de singulariser le com-

*. Les dates indiquées sont les dates des premiers run de physique.

portement des neutrinos électroniques et des neutrinos des autres saveurs. D'autre part l'expérience KamLAND au Japon (2002), sensible aux paramètres d'oscillation du secteur solaire grâce à la mesure des neutrinos d'un ensemble de réacteurs nucléaires japonais, confirme l'oscillation et apporte une mesure précise des paramètres θ_{12} et Δm_{21}^2 .

Dans le secteur des "réacteurs", les expériences Daya Bay en Chine, puis RENO en Corée et enfin Double Chooz en France annoncent en 2012 la mesure du dernier angle de mélange θ_{13} , juste sous la limite fixée par l'expérience Chooz en 1998. Cette information capitale pour le futur de la physique des neutrinos est confirmée pendant l'été 2012 de manière totalement indépendante, sur faisceau, par la collaboration T2K, dans le canal d'apparition $\nu_\mu \rightarrow \nu_e$. Les deux premières mondiales que constituent l'observation, en mode apparition, des oscillations de neutrinos $\nu_\mu \rightarrow \nu_\tau$ par OPERA en 2010 puis $\nu_\mu \rightarrow \nu_e$ par T2K en 2012, ont permis d'ancrer profondément le modèle des oscillations de neutrinos dans le cadre théorique de la physique des particules. Elles constituent la seule ouverture actuelle pour une physique au delà du Modèle Standard validée expérimentalement. Les deux analyses ayant permis la mesure du paramètre θ_{13} sont rappelées dans la Figure 1.2 (T2K, en haut droite, Daya Bay[†], en bas).

La matrice de mélange leptonique se ramène après analyse globale des données publiées après la conférence NOW 2014[‡] à :

$$|U| = \begin{pmatrix} 0.801 \rightarrow 0.845 & 0.514 \rightarrow 0.580 & 0.137 \rightarrow 0.158 \\ 0.225 \rightarrow 0.517 & 0.441 \rightarrow 0.699 & 0.614 \rightarrow 0.793 \\ 0.246 \rightarrow 0.529 & 0.464 \rightarrow 0.713 & 0.590 \rightarrow 0.776 \end{pmatrix}.$$

Les paramètres des oscillations de neutrinos ont les valeurs suivantes (d'après la même référence) :

| | Normal Ordering ($\Delta\chi^2 = 0.97$) | | Inverted Ordering (best fit) | | Any Ordering |
|---|---|-----------------------------|------------------------------|-----------------------------|--|
| | bfp $\pm 1\sigma$ | 3σ range | bfp $\pm 1\sigma$ | 3σ range | 3σ range |
| $\sin^2 \theta_{12}$ | $0.304^{+0.013}_{-0.012}$ | $0.270 \rightarrow 0.344$ | $0.304^{+0.013}_{-0.012}$ | $0.270 \rightarrow 0.344$ | $0.270 \rightarrow 0.344$ |
| $\theta_{12}/^\circ$ | $33.48^{+0.78}_{-0.75}$ | $31.29 \rightarrow 35.91$ | $33.48^{+0.78}_{-0.75}$ | $31.29 \rightarrow 35.91$ | $31.29 \rightarrow 35.91$ |
| $\sin^2 \theta_{23}$ | $0.452^{+0.052}_{-0.028}$ | $0.382 \rightarrow 0.643$ | $0.579^{+0.025}_{-0.037}$ | $0.389 \rightarrow 0.644$ | $0.385 \rightarrow 0.644$ |
| $\theta_{23}/^\circ$ | $42.3^{+3.0}_{-1.6}$ | $38.2 \rightarrow 53.3$ | $49.5^{+1.5}_{-2.2}$ | $38.6 \rightarrow 53.3$ | $38.3 \rightarrow 53.3$ |
| $\sin^2 \theta_{13}$ | $0.0218^{+0.0010}_{-0.0010}$ | $0.0186 \rightarrow 0.0250$ | $0.0219^{+0.0011}_{-0.0010}$ | $0.0188 \rightarrow 0.0251$ | $0.0188 \rightarrow 0.0251$ |
| $\theta_{13}/^\circ$ | $8.50^{+0.20}_{-0.21}$ | $7.85 \rightarrow 9.10$ | $8.51^{+0.20}_{-0.21}$ | $7.87 \rightarrow 9.11$ | $7.87 \rightarrow 9.11$ |
| $\delta_{CP}/^\circ$ | 306^{+39}_{-70} | $0 \rightarrow 360$ | 254^{+63}_{-62} | $0 \rightarrow 360$ | $0 \rightarrow 360$ |
| $\frac{\Delta m_{21}^2}{10^{-5} \text{ eV}^2}$ | $7.50^{+0.19}_{-0.17}$ | $7.02 \rightarrow 8.09$ | $7.50^{+0.19}_{-0.17}$ | $7.02 \rightarrow 8.09$ | $7.02 \rightarrow 8.09$ |
| $\frac{\Delta m_{3\ell}^2}{10^{-3} \text{ eV}^2}$ | $+2.457^{+0.047}_{-0.047}$ | $+2.317 \rightarrow +2.607$ | $-2.449^{+0.048}_{-0.047}$ | $-2.590 \rightarrow -2.307$ | $\begin{bmatrix} +2.325 \rightarrow +2.599 \\ -2.590 \rightarrow -2.307 \end{bmatrix}$ |

TABLE 1.1 – Paramètres d'oscillations à 3 saveurs d'après un fit global, après la conférence NOW 2014. Les résultats sont obtenus en laissant libres les flux de réacteurs et en incluant les données réacteurs dont la longueur de vol est $L \lesssim 100$ m. Les nombres dans la première (2nde) colonne sont obtenus en supposant la hiérarchie de masse normale NO ou inversée (IO). Dans la 3ème colonne cette hiérarchie est laissée libre. On note que $\Delta m_{3\ell}^2 \equiv \Delta m_{31}^2 > 0$ pour NO et $\Delta m_{3\ell}^2 \equiv \Delta m_{32}^2 < 0$ pour IO.

[†]. arXiv :1311.4114 et arXiv :1501.04991

[‡]. arXiv :1409.5439v2

Fenêtre(s) sur le futur — Les projets futurs ont recentré leur programme sur la recherche de la violation de CP dans le secteur leptonique et la détermination de la hiérarchie de masse. Ces paramètres peuvent être mesurés par une expérience sur faisceau, dans les canaux d'apparition $\nu_\mu \rightarrow \nu_e$ et $\bar{\nu}_\mu \rightarrow \bar{\nu}_e$, lorsqu'on inclut les effets d'ordre supérieur induits par le parcours des neutrinos électroniques dans la matière.

Pour mettre ceci en évidence, supposons dans un premier temps que l'on ait $\delta_{CP} = 0$. La probabilité d'apparition des ν_e dans le vide s'écrit alors au premier ordre :

$$P(\nu_\mu \rightarrow \nu_e) \simeq \sin^2 2\theta_{13} \cdot \sin^2 \theta_{23} \cdot \sin^2 (\Delta m_{31}^2 L / 4E).$$

Lorsque les neutrinos se propagent dans la matière elle devient :

$$P(\nu_\mu \rightarrow \nu_e) \simeq \sin^2 2\theta_{13} \cdot \frac{\sin^2 \theta_{23}}{(A-1)^2} \cdot \sin^2 ((A-1)\Delta m_{31}^2 L / 4E)$$

où $A = \sqrt{2}G_F N_e \frac{2E}{\Delta m_{31}^2}$ et N_e représentant la densité électronique du milieu traversé. On voit que cette expression dépend du signe de Δm_{31}^2 et donc de la hiérarchie de masse. Le paramètre A change aussi de signe pour des neutrinos et des antineutrinos ce qui implique que des effets d'augmentation de la probabilité dans un mode se traduiront par des effets de diminution dans l'autre.

On peut résumer l'ensemble de ces conditions avec la probabilité d'oscillation complète :

$$\begin{aligned} P(\nu_\mu \rightarrow \nu_e) \simeq & 4c_{13}^2 s_{13}^2 s_{23}^2 \left\{ 1 + \frac{a}{\Delta m_{31}^2} \cdot 2(1 - 2s_{13}^2) \right\} \sin^2 \frac{\Delta m_{31}^2 L}{4E} \\ & + c_{13}^2 s_{13} s_{23} \left\{ -\frac{aL}{E} s_{13} s_{23} (1 - 2s_{13}^2) + \frac{\Delta m_{21}^2 L}{E} s_{12} (-s_{13} s_{23} s_{12} + c_\delta c_{23} c_{12}) \right\} \sin \frac{\Delta m_{31}^2 L}{2E} \\ & - 4 \frac{\Delta m_{21}^2 L}{2E} s_\delta c_{13}^2 s_{13} c_{23} s_{23} c_{12} s_{12} \sin^2 \frac{\Delta m_{31}^2 L}{4E} \end{aligned}$$

où $c_{ij} = \cos \theta_{ij}$, $s_{ij} = \sin \theta_{ij}$, $c_\delta = \cos \delta_{CP}$, $s_\delta = \sin \delta_{CP}$, et $a = 2\sqrt{2}G_F n_e E$, avec n_e représentant la densité électronique du milieu traversé. La probabilité correspondante pour les anti-neutrinos s'obtient en remplaçant $\delta_{CP} \rightarrow -\delta_{CP}$ et $a \rightarrow -a$. On voit sur l'expression précédente que les effets de violation de CP sont modulés par les 3 autres angles de mélange et qu'il en résulte des dégénérescences compliquées. La stratégie de la collaboration LAGUNA-LBNO en Europe est de combiner différentes mesures (spectre en énergie pour les premier et second maxima) en mode disparition et apparition avec la meilleure résolution possible et de comparer les résultats pour les neutrinos et les antineutrinos. La technique des chambres à projection temporelle (*TPC*) a été sélectionnée à la suite d'un *design study* achevé en août 2014, comme étant la plus performante dans ce contexte. Une présentation du programme est donnée dans le second chapitre de cette partie. C'est sur ce programme que j'ai décidé de poursuivre mon engagement dans la physique des neutrinos après avoir participé aux premières mesures en mode apparition des oscillations de neutrinos.

Chapitre 2

Expérience de première génération : OPERA et le programme CNGS

2.1 Introduction

Le but de l'expérience OPERA comprenant 150 physiciens et une trentaine d'instituts de recherche en Europe et au Japon est la détection, dans le laboratoire souterrain du Gran Sasso (Laboratori Nazionali del Gran Sasso) des neutrinos ν_τ issus de l'oscillation de neutrinos ν_μ produits au CERN (faisceau CNGS) et donc la signature du mécanisme d'oscillation des neutrinos dans le secteur "atmosphérique", l'amélioration de la précision sur les paramètres d'oscillation en cas de signal positif ($|\Delta m_{23}^2|$ et $\sin^2 2\theta_{23}$) et des limites sur θ_{13} par l'étude du canal $\nu_\mu \longrightarrow \nu_e$.

OPERA est un détecteur hybride constitué d'émulsions nucléaires avec une résolution intrinsèque sub-millimétrique complétées d'un trajectographe à scintillateurs et d'un spectromètre magnétisé. Les détecteurs électroniques ont pour but de déclencher le marquage en temps de l'événement, de sélectionner le volume de cible (segmenté en "briques") à "scanner" par microscopie (processus différé dans le temps), et d'effectuer la reconstruction de l'événement (identification de particule, reconstruction des impulsions et énergies, des trajectoires, mesure des charges).

L'IPNL a eu une action particulièrement visible dans OPERA depuis le démarrage de l'expérience avec notamment la responsabilité totale du développement du système d'acquisition de données (DAQ) et de distribution d'horloges pour synchroniser l'ensemble des capteurs. Ce développement pionnier d'un système de capteurs intelligents distribués sur réseau a fait l'objet d'un dépôt de brevet. *Project leader* pour le DAQ depuis 2002, j'ai assuré la pleine responsabilité de cette partie du détecteur (seul physicien en charge) ainsi que le suivi qualité de la prise de données depuis le premier run de commissioning à l'automne 2005 jusqu'à l'arrêt du faisceau neutrinos fin 2012. Cette acquisition a été développée entièrement à l'IPNL en collaboration avec le service électronique (C.Girerd, C.Guérin, S.Gardien) et le service informatique (T.Descombes, B.Carlus, C.Aufranc).

Techniquement un processeur Ethernet risc-32 (MCM 4+16, ETRAX 100LX produit par AXIS) est placé sur une carte digitale à la sortie de l'électronique front-end pour le pré-traitement des données et le marquage temporel et communique par réseau l'ensemble des données au niveau supérieur de traitement. Ce processeur est implanté sur une carte mezzanine, commune à tous les sous-détecteurs, comportant également un séquenceur (de type FPGA) et une FIFO. Le marquage en temps des événements est effectué à une précision de 10ns (horloge locale du FPGA) et les horloges sont synchronisées sur le GPS. L'ensemble des cartes électroniques a été conçu et testé à l'IPNL pour un total de 100,000 canaux de lecture. La chaîne de transmission de l'horloge commune

à tous les capteurs, verrouillée sur le GPS, a également été développée à l'IPNL, de même que la suite logicielle d'acquisition de données basée sur CORBA pour la gestion d'objets distribués et d'Oracle pour le stockage des données. J'ai encadré la thèse de T.Brugière sur la validation du système d'acquisition et l'analyse des données sur et hors faisceau (étude des performances dans la détection des neutrinos atmosphériques).

En 2010 OPERA a publié l'observation du premier candidat ν_τ dans les données collectées en 2008-2009. Cette mesure constitue une première mondiale puisqu'il s'agit de la première "apparition" d'un produit des oscillations de neutrinos, toutes les indications expérimentales précédentes étant basées sur une "disparition" de neutrinos après comparaison des flux mesurés en position proche et lointaine. Avec une statistique finale correspondant à $4.0 \cdot 10^{20}$ p.o.t. ("protons on target"), le nombre d'événements d'oscillations de neutrinos détecté à présent s'élève à 4.

Les quatre articles présentés ici décrivent le détecteur dans son ensemble et les premiers événements détectés (*OPERA first events from the CNGS beam*, [12]), le système d'acquisition de données et de distribution d'horloges (*The OPERA global readout and GPS distribution system*, [11]), puis l'observation du troisième candidat ν_τ (*Evidence for $\nu_\mu \rightarrow \nu_\tau$ appearance in the CNGS neutrino beam with the OPERA experiment*, [26]). Enfin le dernier article montre une analyse de physique hors faisceau (*Cosmic ray physics with the OPERA detector*, [14]) conduite en exploitant les performances du système d'acquisition du détecteur.

2.2 OPERA first events from the CNGS neutrino beam, [12]

J.Marteau for the OPERA collaboration
*Institut de Physique Nucléaire de Lyon - UCBL-IN2P3, 4 rue E.Fermi,
69622 Villeurbanne, France*

The aim of the OPERA experiment is to search for the appearance of the tau neutrino in the quasi pure muon neutrino beam produced at CERN (CNGS). The detector, installed in the Gran Sasso underground laboratory 730 km away from CERN, consists of a lead/emulsion target complemented with electronic detectors. A report is given on the detector status (construction, data taking and analysis) and on the first successful 2006 neutrino runs.

Introduction

In the last decades solar and atmospheric neutrino experiments observed deficits in the measured fluxes which are all well reproduced in a neutrino oscillations model, implying non vanishing, not degenerate neutrino masses and neutrino mixing. Within such hypothesis weak interactions eigenstates differ from the mass eigenstates. The mixing can be parametrized in an unitary matrix whose parameters (3 angles and 1 or 3 phases depending on the Dirac or Majorana nature of neutrinos) associated to the square masses differences Δm^2 drive the amplitude of the disappearance ($P(\nu_\alpha \rightarrow \nu_\beta)$) or survival ($P(\nu_\alpha \rightarrow \nu_\alpha)$) probabilities. The major experimental results for solar neutrinos come from radiochemic experiments^{1,2,3} or large Čerenkov detectors^{4,5,6,7}. For atmospheric neutrinos they come from Čerenkov and calorimeters^{8,9}. These results were confirmed with reactor^{10,11} and long baseline experiments^{12,13}. All these experiments are however of “disappearance” type, they compare the measured flux at a far distance with either one at a close position (in the case of long baseline experiments) or with the predicted one (in the reactor, “solar” and “atmospheric” experiments).

The OPERA experiment¹⁴ has been designed to perform an unique appearance observation of the oscillation products to confirm (or infirm) the neutrino oscillation hypothesis in the atmospheric sector through the $\nu_\mu \rightarrow \nu_\tau$ channel and also to set limits on the θ_{13} angle through the $\nu_\mu \rightarrow \nu_e$ channel. This article reports the first observed neutrino events from the CNGS (CERN to Gran Sasso) beam by the OPERA experiment.

1 The OPERA experiment

1.1 The CNGS programme

The CNGS¹⁵ programme of neutrino beam from CERN to Gran Sasso has been approved in 1999. OPERA was approved as “CNGS1 experiment” in 2001. From CERN to Gran Sasso the neutrinos time of flight is 2.44 ms and their average direction makes a 3° angle w.r.t. the horizontal due to the earth curvature. The main features of the beam have been presented in

details in this conference¹⁶. The beam has been optimized to maximize the number of τ events in the detector (convolution of the neutrino flux, the disappearance probability $P(\nu_\mu \rightarrow \nu_\tau)$ and the detection efficiency). The neutrino average energy is 17 GeV. The $\bar{\nu}_\mu$ contamination is $\sim 4\%$, the ν_e ($\bar{\nu}_e$) is $< 1\%$ and the number of ν_τ is negligible. The expected beam intensity is $4.5 \cdot 10^{19}$ p.o.t./year.

1.2 The detection technique

The challenge of the experiment is to measure the appearance of ν_τ from ν_μ oscillations through CC τ interactions. The events induced by the short-lived τ have a characteristic topology (with a “kink” due to the presence of undetected neutrinos in the τ decay) but extends over $\sim mm^3$ typical volumes.

ECC technique The detector should therefore match a large mass for statistics, a high spatial resolution and high rejection power to limit background contamination. These requirements are satisfied using the proven ECC (Emulsion Cloud Chamber) technique which already worked successfully in the DONUT experiment¹⁷. The passive target consists of lead plates. Particles are tracked in nuclear emulsions films with a sub-micrometric intrinsic resolution. 57 emulsions films are assembled and interspaced with 56 lead plates 1 mm wide in a detector basic cell called “brick”. A brick is a 12.7×10.2 cm² object with a thickness along the beam direction of 7.5 cm (about 10 radiation lengths). Its weight is about 8.3 kg. Bricks are assembled in 31 walls (52×64 bricks) separated by electronic detectors planes to trigger the event and identify the brick with the interaction vertex.

The readout sequence of OPERA events is quasi-online. Once identified the brick is extracted from the detector, emulsions are developed and scanned by automatic microscopes. Scanning performs detailed tracking, vertex location, particle identification, momentum measurement through Multiple Coulomb Scattering, decay kink search. The data are complemented with the momentum, energy and charge measurements done by the electronic detectors.

Expected performances At the expected nominal beam intensity and for five years data taking a total of 31000 charged and neutral current interactions is expected in the nominal mass target of OPERA. Among these 95 (214) CC ν_τ interactions are expected for oscillation parameter values $\Delta m_{23}^2 = 2(3) \times 10^{-3}$ eV² and $\sin^2 2\theta_{23} = 1$. The overall detection efficiencies have been estimated in Monte Carlo simulations upgraded by dedicated tests (vertex searches, e/π and π/μ separation, large angle muon scattering...). The nominal expected number of τ events ranges from 11 to 16 events with the same parameters sets. The physics channel considered so far are $\tau \rightarrow e$, $\tau \rightarrow \mu$ and $\tau \rightarrow h$ (1 or 3 prongs). The background is expected to be < 1 . In the sub-dominant $\nu_\mu \rightarrow \nu_e$ channel OPERA should, in the same run conditions, set a limit of $\sin^2 2\theta_{13} < 0.06$ (90% C.L.)¹⁸ assuming $\Delta m^2 = 2.5 \cdot 10^{-3}$ eV².

1.3 The OPERA detector

The OPERA detector is divided into two Super-Modules consisting of a target section followed by a muon spectrometer (see Picture 1). The target section is made of 31 brick walls each one being followed by a highly segmented scintillator tracker plane. A large VETO plane is placed in front of the detector to further discriminate beam events from horizontal cosmics. The construction of the experiment started in Spring 2003. The two instrumented magnets were completed in May 2004 and beginning of 2005 respectively. In Spring 2006 all scintillator planes were installed.

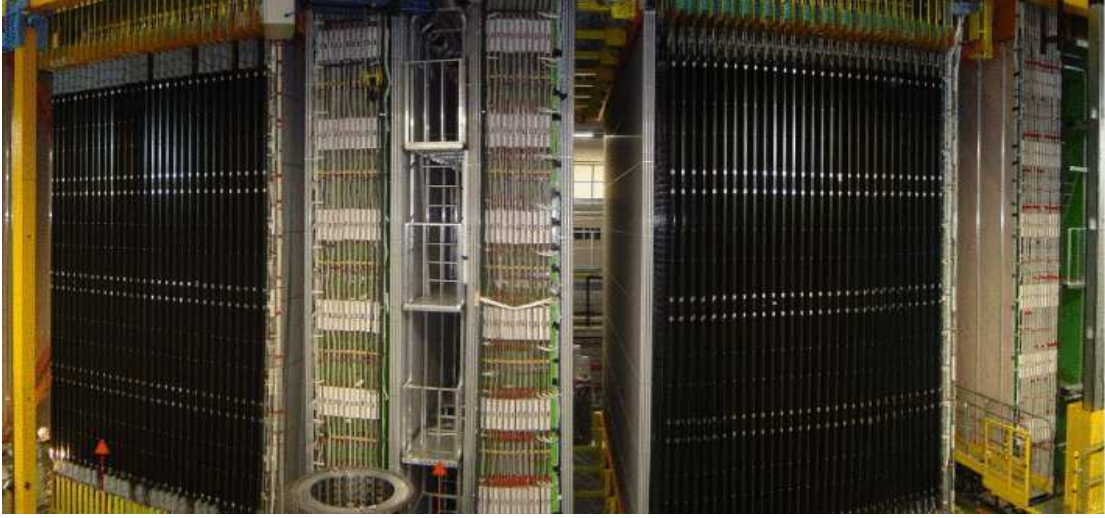


Figure 1: Side view of the OPERA detector. The two target modules, 31 bricks walls spaced by black covered scintillator biplanes, are separated by the first spectrometer, 6 stations of drift tubes upstream, between and downstream the two arms of a dipolar magnet instrumented with RPC.

The electronic detectors The target tracker covers a total area of 7000 m^2 and is built of 32000 scintillator strips, each 7 m long and of $25 \text{ mm} \times 15 \text{ mm}$ cross section. Along the strip, a wavelength shifting fiber of 1 mm diameter transmits the light signals to both ends, read out by 992 multi-anode (64 channels) PMT's from Hamamatsu. A 32 channel front-end electronics ASIC¹⁹ has been developed which allows individual gain corrections (with a dynamic range of $1 \div 4$) and auto-triggered readout sequence in a standard dual shaper scheme (fast and slow) and track & hold logic.

The muon spectrometer consists of a large $8 \times 8 \text{ m}^2$ dipolar magnet delivering a magnetic field of 1.55 T and instrumented with RPC's and drift tubes. Each magnet arm consists of twelve 5 cm thick iron slabs, alternating with RPC planes. This sandwich structure allows the tracking in the magnetic field to identify the muons and to determine their momentum. In addition the precision tracker²⁰ measures the muon track coordinates in the horizontal plane. It is made of 8 m long drift tubes with an outer diameter of 38 mm. The charge misidentification is expected to be 0.1 % - 0.3 % in the relevant momentum range which is efficient enough to minimize the background originating from the charmed particles produced in ν_μ interactions. With the muon spectrometer a momentum resolution of $\Delta p/p \leq 0.25$ for all muon momenta p up to a maximum of $p = 25 \text{ GeV}/c$ can be achieved.

"Bricks" production In total ~ 200000 bricks should be nominally produced and installed in OPERA. The production is performed by a dedicated apparatus called Brick Assembly Machine (BAM) installed in Gran Sasso. It is a chain of different stations (for piling, pressing, wrapping etc) using robots operating in dark rooms with controlled environment. The production is around ~ 2 bricks per minute. Once bricks are produced they are placed in dedicated mechanical structures called drums (9 rows of 26 bricks) and inserted from there to the detector by the Brick Manipulating System (BMS). The BMS has two equivalent structures (one per side) consisting of a brick storage place (carousel) where the drums are exchanged and a moving robot along the side of the experiment. The mobile part of the BMS can reach the desired row and plane with a sub-millimetric accuracy. The robot has a mobile bridge on which the bricks are pushed inside the detector by a pushing arm to their desired position. The brick extraction is performed by a

vacuum sucker located on the front of a small vehicle.

2 Data taking and analysis

DAQ and on-line analysis The OPERA DAQ system is based on a so-called “smart” sensor concept on an Ethernet network. The principle is to implement a local micro-processor as close as possible to the front-end electronics and to access it for configuration and/or data transmission through Ethernet. The core of this architecture is a small processor board which hosts a sequencer (FPGA of the Altera cyclone family), a micro-processor (32 bits RISC Etrax100lx processor from Axis) and an intermediate FIFO. The FPGA manages the full readout sequence, the data timestamping with a 10 ns accuracy, the data formatting and pre-processing (pedestals and zero suppression, local histogramming) and the data transfer to the intermediate buffer. The processor runs “sensor” applications communicating with “daq” servers and developed within the CORBA framework implemented in C++.

Each sensor is plugged to a sub-detector specific motherboard and is seen as a standard Ethernet node over a large network. In total 1153 sensors are connected for a total of 100000 readout channels. The synchronization of each individual clock is performed through a specific bi-directional bus starting from a GPS PCI board developed on purpose. A common 20 MHz clock embedding specific signals is sent to the sensors with a measurement of time propagation delays for off-line correction.

Data analysis and reconstruction is performed continuously on-line within the Opera software framework based on ROOT.

Off-line emulsion scanning After development emulsions are scanned by automatic microscopes whose nominal speed is higher than $\sim 20 \text{ cm}^2/\text{h}$ per emulsion layer ($44 \mu\text{m}$ thick). There are two different approaches developed by the OPERA collaboration, in Europe (ESS²¹, based on software image reconstruction) and in Japan (S-UTS²² based on hard-coded algorithms). Next picture displays an example of both systems. The scanning sequence proceeds with the division of the emulsion thickness into ~ 16 tomographic images by focal plane adjustment, images digitization and track finding algorithms. Track grains are identified and separated from “fog” grains and associated into “micro-tracks”. Examples of reconstructed tracks during 2006 runs will be given below.

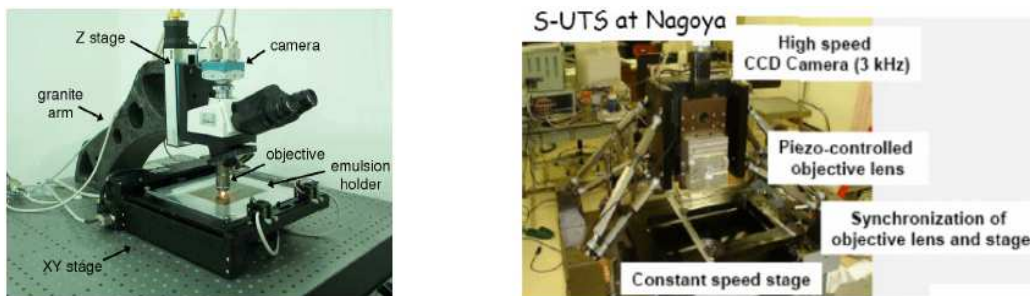


Figure 2: Pictures of one of the ESS microscopes (left) and of the S-UTS (right).

3 First CNGS neutrino events

Beam structure reconstruction During the first CNGS run in August 2006 319 neutrino events were collected with an estimated systematic error of 5% (see Fig.3 left for a typical

display). The events were selected by a comparison of their absolute timestamps w.r.t. the beam time information in quite large coincidence window (1ms). The beam spill time structure reconstructed in OPERA is displayed in Fig.3 (right).

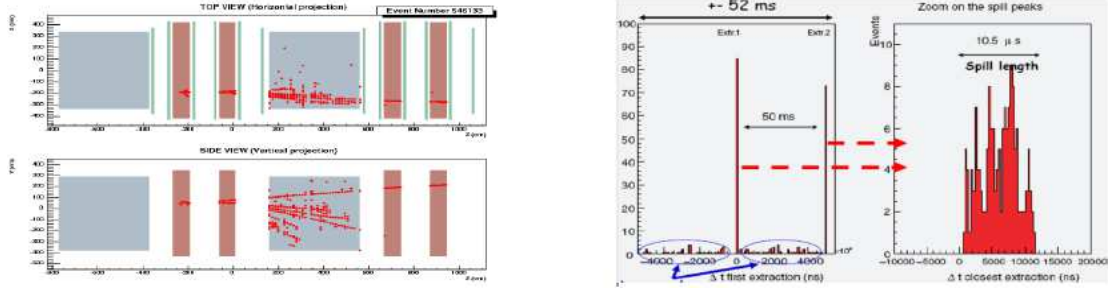


Figure 3: Left: event display of a neutrino interaction in the spectrometer. Right : timing distribution of beam related events. The 2 CNGS fast extractions, separated by 50 ms are clearly reconstructed. The right plot focuses on one of the two extractions. The typical width reconstructed ($\sim 10\mu s$) is coherent with the expectations.

Cosmics vs neutrino events Beam events have an average direction close to the horizontal one (3.3° angle) whereas cosmics have large angles distributions. This is shown in the distributions of Fig. 4. A gaussian fit to the central distribution leads to a mean angle of $3.4 \pm 0.3^\circ$ in agreement with the expected value.

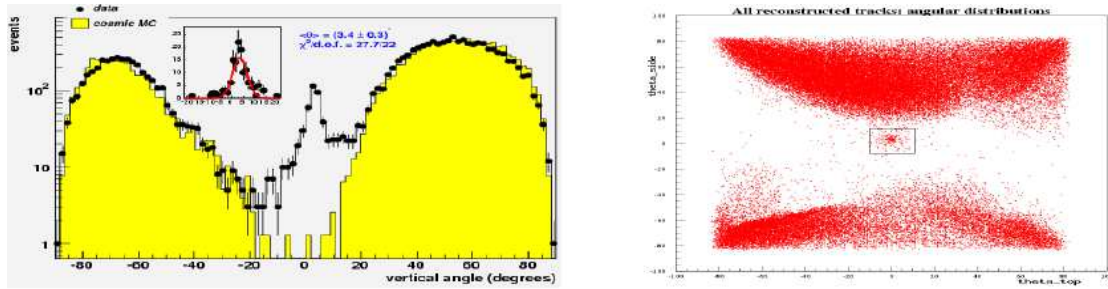


Figure 4: Left: angular distribution w.r.t. horizontal direction of events reconstructed with the spectrometer RPC (black points) compared to MC expectations for cosmics only (yellow histogram). Right: scatter plot of side and top projection angles wrt horizontal direction reconstructed with the target tracker. Beam events appear in the central zone of those distributions.

Emulsions matching Some clean tracks have been followed in emulsion sheets inside the detector. A typical display of the hits reconstructed in the emulsions and in the TT is given in Fig. 5.

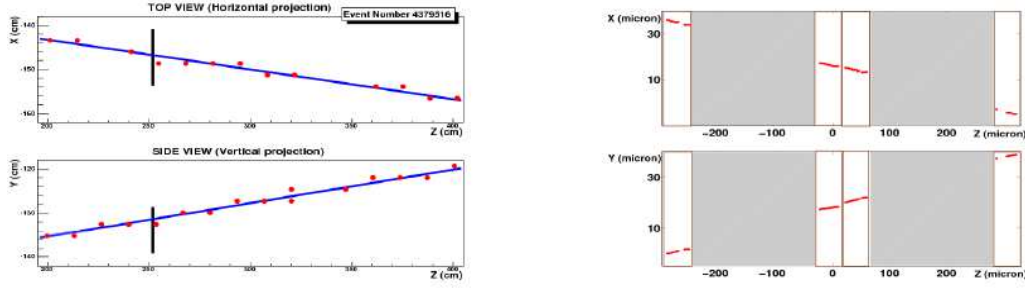


Figure 5: Left: display of one event with the muon passing through the emulsion sheet detector plane. Right: display of the corresponding 4 micro-tracks reconstructed in the emulsion.

Conclusions and perspectives

OPERA performed the first detection of neutrino events from the long baseline CERN CNGS beam in the underground Gran Sasso laboratory. 319 neutrino-induced events were collected for an integrated intensity of 7.6×10^{17} p.o.t. in agreement with the expectations. The reconstructed zenith-angle distributions and the time structure of the events demonstrate the capability of the electronic detectors, build up during the last three years, to reach the experiment goals. The association of tracks between electronic detectors and emulsion sheets has been also successfully performed. The collaboration is facing the last large effort of brick production and insertion and is preparing next neutrinos runs in fall 2007 for physics commissioning.

Acknowledgments

I would like to acknowledge the cooperation of all the members of the OPERA Collaboration and thank the organizers of the conference for the invitation.

References

1. R. Davis, Prog. Part. Nucl.Phys. **32**, 13(1994);
2. T. Kirsten *et al.*, [GALLEX collaboration], *Neutrino 98*, Nucl. Phys. **B** (Proc. Suppl.).
3. V. Gavrin *et al.*, [SAGE collaboration], *Neutrino 98*, Nucl. Phys. **B** (Proc. Suppl.).
4. Y. Fukuda *et al.* [Super-Kamiokande Collaboration], Phys. Rev. Lett. **81**, 1562 (1998); J. Hosaka *et al.*, Phys. Rev. D **74**, 032002 (2006).
5. K. S. Hirata *et al.* [KAMIOKANDE-II Collaboration], Phys. Lett. B **205**, 416 (1988).
6. R. Becker-Szendy *et al.*, Nucl. Phys. **B38**, 331(1995).
7. Q.R. Ahmad *et al.* [SNO collaboration], Phys.Rev.Lett. **87** (2001) 071301; Q.R. Ahmad *et al.* [SNO collaboration], Phys.Rev.Lett. **89** (2002) 011301&011302.
8. W. W. M. Allison *et al.* [SOUDAN2 Collaboration], Phys. Lett. B **449**, 137 (1999); W. W. M. Allison *et al.*, Phys. Rev. D **72**, 052005 (2005).
9. S. P. Ahlen *et al.* [MACRO Collaboration], Phys. Lett. B **357**, 481 (1995); M. Ambrosio *et al.*, Eur. Phys. J. C **36**, 323 (2004).
10. M. Apollonio *et al.* [CHOOZ Collaboration], Eur. Phys. J. C **27**, 331 (2003).
11. T. Araki *et al.*, [KamLAND Collaboration], Phys.Rev.Lett. **94** (2005) 081801.
12. M. H. Ahn *et al.* [K2K Collaboration], Phys. Rev. D **74**, 072003 (2006).
13. D.G. Michael *et al.* [MINOS Collaboration], arXiv:hep-ex/0607088.
14. M. Guler *et al.* [OPERA Collaboration], CERN-SPSC-2000-028; Y. Declais *et al.*, CERN-SPSC-2002-029 SPSC-059.

15. CNGS project: <http://proj-cngs.web.cern.ch/proj-cngs/>.
16. E.Gschwendtner, proceedings of this conference.
17. K. Kodama *et al.* [DONUT Collaboration], Phys. Lett. B **504**, 218 (2001).
18. M. Komatsu *et al.*, *J. Phys.* **G29**, 443 (2003).
19. A. Lucotte *et al.*, Nucl. Instrum. Meth. A **521**, 378 (2004).
20. R. Zimmermann *et al.*, Nucl. Instr. Meth. **A 555**, (2005), 435-450.
21. N. Armenise *et al.*, Nucl. Instrum. Meth. A **551**, 261 (2005);
M. De Serio *et al.*, Nucl. Instrum. Meth. A **554**, 247 (2005);
L. Arrabito *et al.*, arXiv:physics/0604043, to be published in Nucl. Instrum. Meth. A.
22. S. Aoki *et al.*, Nucl. Instrum. Meth. B **51**, 466 (1990);
T. Nakano, PhD Thesis, University of Nagoya (1997);
T. Nakano [CHORUS Collaboration], *International Europhysics Conference on High-Energy Physics* (HEP 2001), Budapest, Hungary, 12-18 July 2001.

2.3 The OPERA global readout and GPS distribution system, [11]

J. Marteau^{*,a}, the OPERA collaboration¹

^aIPNL, Université de Lyon, Université Lyon 1, CNRS/IN2P3, 4 rue E. Fermi 69622 Villeurbanne cedex, France

Abstract

OPERA is an experiment dedicated to the observation of ν_μ into ν_τ oscillations in appearance mode using a pure ν_μ beam (CNGS) produced at CERN and detected at Gran Sasso. The experiment exploits a hybrid technology with emulsions and electronics detectors [1]. The OPERA readout is performed through a triggerless, continuously running, distributed and highly available system. Its global architecture is based on Ethernet-capable smart sensors with microprocessing and network interface directly at the front-end stage. A unique interface board is used for the full detector reading out ADC-, TDC- or Controller-boards. All the readout channels are synchronized through a GPS-locked common bidirectional clock distribution system developed on purpose in a PCI format. It offers a second line to address all channels and the off-line synchronization with the CNGS to select the events.

Key words: DAQ and data management, Readout systems, Distributed smart sensors, Ethernet-based DAQ systems

PACS: 07.05.Hd, 07.05.Kf, 07.05.Wr, 07.07.Df

1. Global data readout architecture

OPERA is optimized for the τ neutrino detection. Detector's target consists of lead-emulsions bricks walls followed by scintillator tracker planes (Target Tracker referred to as TT) to trigger and locate the events and it is complemented by two muon magnetic spectrometers (drift tubes referred to as HPT and RPC tracker). The overall data rate is dominated by cosmics and ambient radioactive background while the neutrino interactions are well localized in time in correlation with the CNGS beam spill. The synchronization with the CNGS beam spill is done off-line via the GPS. The detector remains sensitive during the inter-spill time and the DAQ system runs continuously in a triggerless mode.

The data readout system has been designed to sort the data through Ethernet at the earliest stage of each sub-detector. The global DAQ is build like a standard Ethernet network whose nodes are the "Ethernet Controller Mezzanines" (ECM) plugged on Controller Boards (CB). These boards are designed to interface and control each sub-detector specific F/E electronics, to sort the data to the Event Building WorkStation (EBWS), to handle monitoring and slow control from the Global Manager through the same Ethernet processors.

Target Tracker The readout of the TT PMTs (Hamamatsu 64 pixels H8804-mod1) is performed via multi-channels front-end chips designed at LAL the signals of which are digitized and pre-processed on a custom motherboard developed at the IPNL. The F/E chips are self-triggering and allow to compensate the pixel-to-pixel gain spread of the MaPMT. A common threshold is set on a chip, which makes the OR of the 32 channels to provide a trigger output signal whenever one channel at least is

over threshold.

Spectrometer Each spectrometer has two sensitive elements: 22 RPC planes and 3 pairs of drift tubes stations located upstream, in the middle and downstream of a dipolar magnet. The electronics of these 2 trackers is placed on the top of the experiment. It consists in VME-like boards collected in VME crates and power supply stations. The F/E electronics of one RPC plane is divided into 9 F/E boards readout serially by one Controller Board that receives the trigger signals (defined by the fast OR of 32 channels). Each drift tube station is readout by a TDC board which receives a common stop from the OR of two nearby RPC planes.

Computing The EBWS consists of commercial PC's receiving data from the Ethernet network. The distributed client/server software is based on the CORBA (Common Object Request Broker Architecture) standard which is a well established Object Oriented application [2]. It offers a global framework which links the applications running on the sensors, on the EBWS and on the Manager. The on-line data storage is performed by a database cluster (Oracle 11.1 RAC) with two dedicated servers.

Network The global DAQ network is divided into 2 parts : the Ethernet network from the EBWS to each Ethernet Controller (used for data transfer but also for detector configuration, monitoring & slow control) and the clock distribution system from the Central Clock Unit synchronized on the GPS to each sensor (used for the synchronization of all the nodes local clocks)

2. Ethernet Controller Mezzanine

The aim of the ECM is to provide a **common interface** between the F/E of the various sub-detectors and the overall DAQ system. The physical form of the mezzanine has been chosen for the ease of integration (see Figure 1). The mezzanine can

^{*}Corresponding author

Email address: j.marteau@ipnl.in2p3.fr (J. Marteau)

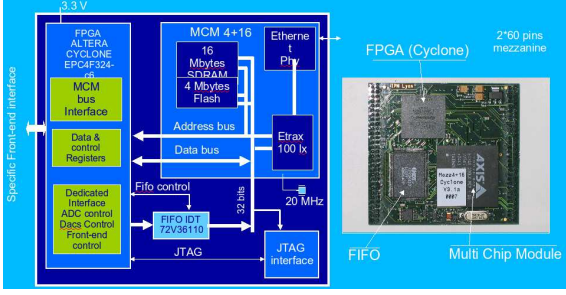


Figure 1: Ethernet Controller Module: schematics and physical view.

be seen as an external component to be plugged on the Controller Boards and that can be (re)-configured to the specifications of each sub-detectors [3, 4, 5]. The Ethernet controller is the core of the board. It includes a sequencer (FPGA from the Cyclone ALTERA family), an external FIFO and a microprocessor (ETRAX 100LX from AXIS) with an Ethernet interface. The FPGA performs the sequencing of the readout (clocks, R/O registers, digital I/O), the local data pre-processing (zero suppression, event validation through external trigger on request), event time stamping (via a local fine counter at 100 MHz synchronized with the global distributed clock), data transfer to the external FIFO, interface with the Ethernet processor. The Ethernet processor is an ASIC based on the ETRAX 100LX from AXIS. It is a 32-bit RISC CPU with Linux 2.4 operating system and Ethernet interface supporting data transfer rates up to 200 Mbits/s [6]. The chip is embedded in a Multi Chip Module (MCM) which includes in a single chip the ETRAX100lx core plus 4 Mbytes of flash memory, 16 Mbytes of SDRAM and an Ethernet transceiver. The MCM gets the data in a time scheduled job from the FIFO, performs local processing and transfers the data to the EBWS.

3. Clock distribution system

A global clock is mandatory to synchronize all the nodes of the distributed system. The general features of the system are close to Ref.[7], in particular the bi-directionality of the system allows the control of the signal reception and the measurement of the propagation time with acknowledgement signals. The clock distribution system starts from the GPS control unit which synchronizes a 20MHz clock with the signal of the GPS and sends the clock + encoded commands via an optical fibre. The signal is then converted into electrical format and distributed to the "clock master cards" through M-LVDS bus. Each of these cards deserialize the commands and the clock, and distribute both of them to the clock unit of each controller board through another M-LVDS bus. The PPS sent to each sensor is used to reset the local fine counters after correction of the time propagation delay. Since the PPS transmission time is recorded and locked with the GPS, the absolute event timestamp is assigned as the sum of that time and the value of the local 100MHz clock running on the ECM. This timestamp accuracy allows monitoring the beam spill structure (Figure 2) and to perform physics studies in parallel to the neu-

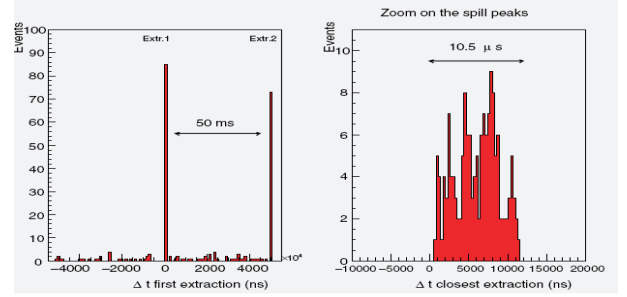


Figure 2: CNGS beam time structure seen in OPERA

trino oscillations using particles ToF (cosmic rays physics, atmospheric neutrinos etc). A crucial point to extract the beam events is the intercalibration between CERN and LNGS GPS systems. Both have comparable performance (± 100 ns accuracy) and their single units are in both cases based on a GPS system + Rb clock although build by different manufacturers (Symmetricom for CERN, ESAT for LNGS). Dedicated tests were performed to check for relative offsets and time stability of the two systems [8]. The two systems are able to track each other within ± 23 ns over long periods.

4. Conclusion

The OPERA global readout system is the first fully Ethernet-based data acquisition system using the "smart sensors" concept. Commissioned during the first CNGS run in summer 2006, it is running continuously with a high availability and efficiency. During the 2008 physics run, around 10,000 neutrino interactions have been recorded in time coincidence with the CNGS, among which 1,700 interactions in the target. Emulsions analysis is being performed by automatic scanning stations [9].

References

- [1] "The detection of neutrino interactions in the emulsion/lead target of the OPERA experiment", N. Agafonova, et al. (OPERA Collaboration), arXiv:0903.2973, accepted for publication in JINST.
- [2] <http://www.corba.org>
- [3] "Ethernet DAQ core mezzanine, User Manual", C.Girerd, OPERA internal note, December 22, 2002.
- [4] "Ethernet network based DAQ and smart sensors for the OPERA long-baseline neutrino experiment", C.Girerd et al, LYCEN 2000-109, IEEE Nuclear Science Symposium and Nuclear Imaging Conference, Lyon, October 15 - 20, 2000.
- [5] "The scintillator option for the OPERA target tracker: results on the read-out", L.Chaussard et al, OPERA internal note, July 06, 2001.
- [6] <http://developer.axis.com/products/etrax100lx/>
- [7] "Numerical clock distribution for Antares", Ch.Olivetto, F.Rhethore, 3LCM-01-01C, August 16, 2000.
- [8] "Inter-laboratory synchronization for the CNGS project", J. Serrano, P. Alvarez Sanchez, J. Lewis and D. Autiero, Prepared for 10th European Particle Accelerator Conference (EPAC 06), Edinburgh, Scotland, 26-30 Jun 2006
- [9] "The European Scanning System for the Measurement and Analysis of OPERA Neutrino Interactions with Nuclear Emulsions", M.Ieva, these proceedings.

2.4 Evidence for $\nu_\mu \longrightarrow \nu_\tau$ appearance in the CNGS neutrino beam with the OPERA experiment, [26]

(The OPERA Collaboration)

3

I. INTRODUCTION

The OPERA experiment is designed to perform a crucial test of neutrino oscillations aiming at the direct observation of the appearance of τ neutrinos in a ν_μ beam. Using atmospheric neutrinos, the Super-Kamiokande experiment recently reported the evidence for a ν_τ appearance signal on a statistical basis and with a low signal-to-noise ratio [1]. The OPERA apparatus has the capability of detecting the ν_τ charged-current interactions on an event-by-event basis and with an extremely high signal-to-noise ratio. A positive evidence from OPERA can prove that the $\nu_\mu \rightarrow \nu_\tau$ transition is the mechanism underlying the disappearance of muon neutrinos at the atmospheric scale [2], thus providing essential support to the establishment of the 3-flavour mixing scheme.

To accomplish this task, several ingredients are required: a high-energy neutrino beam, a long baseline and a kt-scale detector with sub-micrometric resolution. The CERN Neutrinos to Gran Sasso (CNGS [3]) beam was designed to deliver muon neutrinos with a mean energy of 17 GeV to the Gran Sasso underground laboratory (LNGS) where the detector is installed at a distance of 730 km. The contaminations of $\bar{\nu}_\mu$ and $\nu_e + \bar{\nu}_e$ charged current interactions at LNGS, relative to the number of ν_μ charged current interactions, are respectively 2.1% and 0.9%. The contamination from prompt ν_τ is negligible.

The OPERA detector [4] is composed of two identical supermodules, each consisting of an iron spectrometer downstream of a target section. The target has a mass of about 1.2 kt and a modular structure with approximately 150000 target units, called bricks. A brick is made of 56 1 mm-thick lead plates, acting as targets, interleaved with 57 nuclear emulsion films, used as micrometric tracking devices. Each film is composed of two 44 μm -thick emulsion layers on both sides of a 205 μm -thick plastic base. Bricks are arranged in walls interleaved with planes of scintillator strips forming the Target Tracker (TT). The magnetic spectrometers, which consist of iron magnets instrumented with Resistive Plate Chambers (RPC) and Precision Drift Tubes (PT), are used for the measurement of the muon charge and momentum. For each event, the information provided by the electronic detectors allows assigning to each brick a probability to contain the neutrino interaction vertex.

In a recent publication [5] the ν_τ appearance analysis was described in detail, explaining the selection of signal candidate events and the assessment of efficiencies and backgrounds. In the following, the experimental procedure is briefly summarised along with the description of a third ν_τ candidate.

II. DATA SAMPLE

The CNGS beam has run for five years, from 2008 till the end of 2012, delivering a total of 17.97×10^{19} protons on target yielding 19505 neutrino interactions recorded in the targets.

A neutrino interaction is classified as being either charged current-like (1μ) or neutral current-like (0μ) by using the electronic data of the TT and the spectrometers. The neutrino interaction vertex brick predicted by the electronic detector data is extracted from the target by an automatic brick manipulator system. If the scanning of a dedicated pair of emulsion films (Changeable Sheets, CS), acting as an interface between the brick and the TT, yields tracks related to the neutrino interaction, the emulsion films of the brick are developed and distributed to the different scanning laboratories of the collaboration. Their analysis provides the three-dimensional reconstruction of the neutrino interaction and of possible secondary decay vertices of short-lived particles with micrometric accuracy.

The sample of events considered in our previous publication [5] consisted of:

- all the 0μ events collected and searched for in the two most probable bricks for the 2008-2009 runs and in the most probable one for the 2010-2011 runs,
- all the 1μ events with $p_\mu < 15$ GeV/c collected and searched for in the two most probable bricks for the 2008-2009 runs and in the most probable one for the 2010 run.

Two ν_τ candidate events in the hadronic decay channels were observed: the first in the 2009 run data with a one-prong topology [6], the second in the 2011 run data with a three-prong topology [5].

The analysis was then performed on the most probable bricks of 1μ events with $p_\mu < 15$ GeV/c collected during the 2011 and 2012 runs. A ν_τ candidate event in the muonic decay channel was observed in this data sample.

III. THE NEW ν_τ CANDIDATE EVENT

Figure 1 shows the electronic detector display of this new event; the neutrino vertex brick (highlighted) is well contained in the target region. An isolated, penetrating track is reconstructed in the electronic detectors: the particle

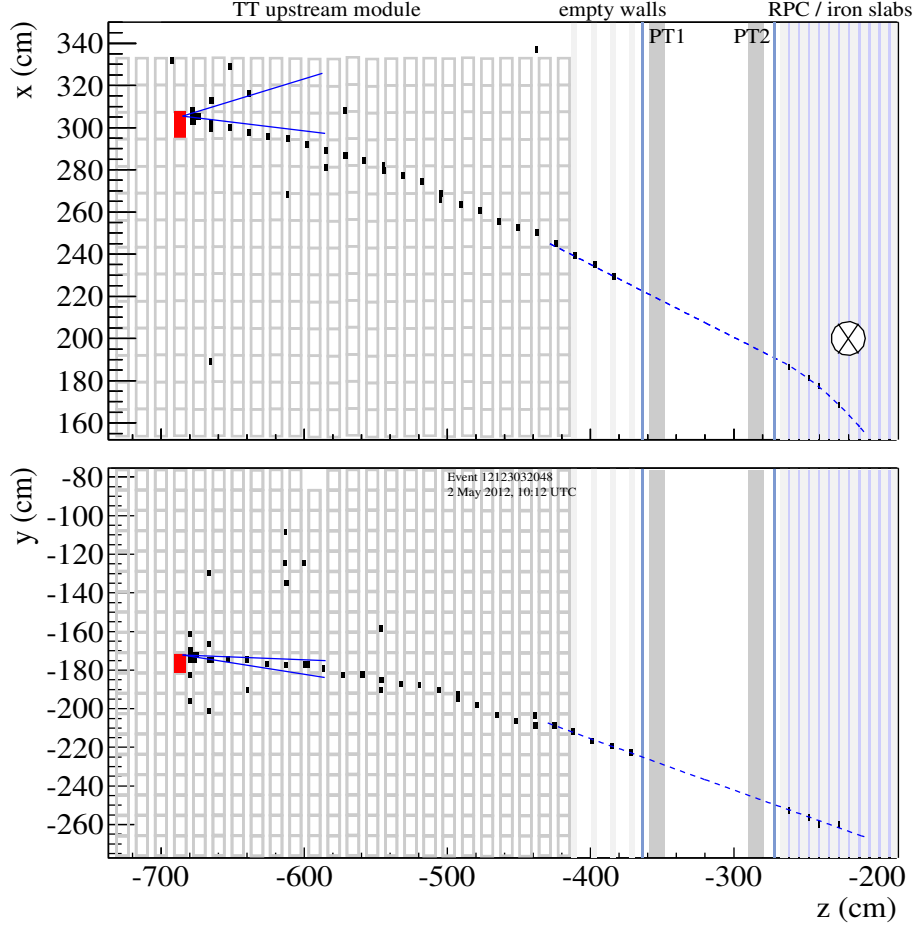


FIG. 1. Electronic detector display of the new ν_τ candidate event. The blue solid lines represent the linear extrapolation of tracks measured in the emulsion films of the vertex brick. The dashed blue lines show the fit of the most downstream hits according to the model: $x(z) = p_{0x} + p_{1x}(z - z_0) + p_{2x}(z - z_0)^2$ with $z_0 = -267.826$ cm. The quadratic term parameter is $p_{2x} = (-0.00389 \pm 0.00069) \text{ cm}^{-1}$ and the fit χ^2/ndf is 2.6/4.

is recorded in 24 planes of the TT and crosses 6 RPC planes before stopping in the spectrometer. This range corresponds to 1650 g/cm^2 of material.

Four RPC planes have hits associated to the track in both projections (Fig. 1). The time spread of the RPC hits is within 20 ns. The efficiency of the RPC planes was monitored with cosmic ray tracks and muons from neutrino interactions in the rock [7].

The muon momentum at the interaction vertex is accurately estimated from the range of the particle in the electronic detector: a Kalman filter-based algorithm yields a value of $p_\mu = (2.8 \pm 0.2) \text{ GeV}/c$. The momentum estimate resulting from a measurement of Multiple Coulomb Scattering (MCS) [8] in the downstream brick, based on the emulsion data, leads to a compatible value of $3.1^{+0.9}_{-0.5} \text{ GeV}/c$.

For events to be retained as candidates in the $\tau \rightarrow \mu$ decay channel the charge of the secondary muon track must either be measured to be negative or be undetermined. This requirement is applied in order to minimize the background from charged current ν_μ interactions with production of a charmed particle decaying to a positive muon and where the primary negative muon goes undetected.

The charge measurement is performed using the bending of the track in the magnetised iron given by the four available RPC hits.

For this event, no hits could be recorded by the PT planes (grey rectangles in Fig. 1) due to an inefficiency of the trigger (the trigger is given by a 2 out of 3 majority of the first RPC plane within the magnet and two upstream dedicated RPC planes, the so-called XPC planes [4]).

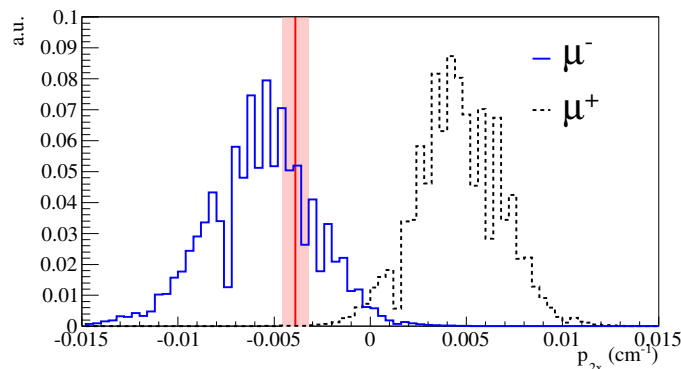


FIG. 2. Distributions of p_{2x} for a Monte Carlo sample of μ^- and μ^+ . The vertical solid line represents the measured value and the vertical band corresponds to the 1σ confidence interval. The visible structures are due to the pitch of the RPC readout which introduces a discretisation effect.

As the last brick-filled wall is followed by three double layers of TT planes (and essentially no other material, see Fig. 1), the slope of the track at the entrance of the spectrometer could be determined with the needed precision.

The relative alignment of RPC and TT planes in the x and y directions was determined using muons from interactions of neutrinos in the rock (horizontal tracks) and cosmic ray muons (sensitive also to vertical displacements). In both cases, the resulting alignment is accurate at the mm level. The errors on the measurement points were computed assuming uniform probability density across the strips that have a width of 2.6 cm (x) and 3.5 cm (y) for RPC detectors and 2.64 cm for the TT. The uncertainty related to MCS has also been taken into account.

The TT and RPC hits are fitted with a simple analytical model consisting of a straight line in the field-free region matched to a parabola in the magnetised region (Fig. 1). The fitted parabola bends towards smaller x (see Fig. 1 top) corresponding to a negative charge. The quadratic parameter is nonzero at 5.6σ significance. The associated momentum at the spectrometer entrance is compatible with the one measured from range.

For this event, the charge misidentification probability was estimated by means of a Monte Carlo simulation. Muons of either charge were sampled using a uniform momentum distribution. A gaussian smearing of the incoming direction was applied to account for the measurement error in the three most downstream TT layers. Only those muons stopping in the same slab observed for the event and with hits within a time window of 30 ns were selected, giving a sample of negative (positive) muons with an average momentum of 613 MeV/c with a 48 MeV/c r.m.s. (540 MeV/c with a 26 MeV/c r.m.s.). The strip read-out was simulated using the efficiency observed in real data. The resulting distributions of the quadratic term p_{2x} for the μ^- and μ^+ samples are shown in Fig. 2. The fraction of μ^+ for which the bending is reconstructed as negative and that mimics a μ^- is 2.5%, but for only 0.063% of the μ^+ the bending is more negative than the observed one. The measured p_{2x} is compatible with the peak value of the distribution for the μ^- sample. For this event, the sign of the charge of the secondary muon is thus univocally determined to be negative. The efficiency of the RPC chamber downstream of the iron slab layer in which the muon is assumed to have stopped is 93%. If the muon had actually stopped in the next layer with this RPC plane being inefficient, then its momentum would have been larger by only 75 MeV/c, the precision in its charge determination remaining unaffected.

IV. EVENT TOPOLOGY AND KINEMATICS

The scanning of the CS films of the interaction brick yielded a track matching the muon direction. A converging pattern of more tracks was also found, reinforcing the conditions for event validation.

The neutrino interaction occurred well inside the brick with respect to the longitudinal direction, $3.3 X_0$ from its downstream face. All tracks possibly related to the interaction were searched for in the brick with an angular acceptance up to $\tan\theta = 1$. The display of the event as reconstructed in the brick is shown in Fig. 3.

The primary vertex (V_0) is given by two tracks: the τ lepton candidate and a hadron track (p_0) having a distance of closest approach of $(0.5 \pm 0.5) \mu\text{m}$. An electromagnetic shower produced by a γ -ray and pointing to this primary vertex has also been observed. The τ lepton decay occurs in the plastic base of the film immediately downstream of the primary vertex, after a flight length of $(376 \pm 10) \mu\text{m}$. The longitudinal coordinate of the decay vertex (V_1) with respect to the downstream face of the lead plate containing the primary vertex (z_{dec}) is $(151 \pm 10) \mu\text{m}$.

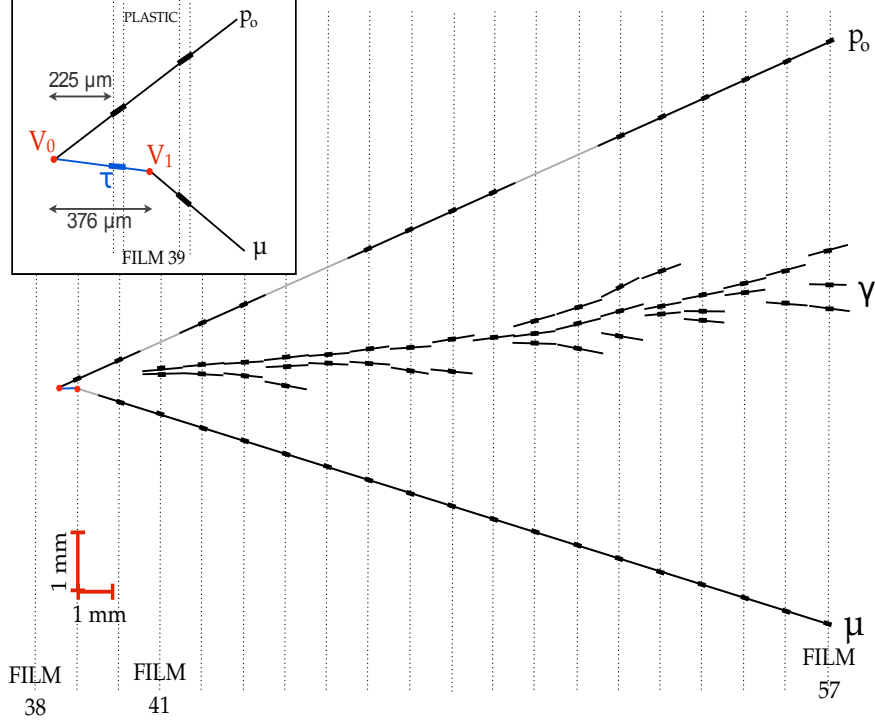


FIG. 3. Display of the new ν_τ candidate event in the xz projection: tracks τ and p_0 come from the primary vertex; the τ candidate decays in the plastic base of film 39, track d_1 is the τ decay daughter identified as a muon. The starting point of the shower generated from the γ is visible in film 41. The inset contains a zoomed view of the primary and decay vertex region.

The kinematical quantities of the tracks measured in the emulsion films are given in the following:

- track p_0 has a momentum $p_{p_0} = (0.90^{+0.18}_{-0.13})$ GeV/ c , measured by MCS. It was found in the CS films. It was followed into the downstream brick where it disappears after having crossed 18 lead plates. No charged particle track could be detected at the interaction point. It is classified as a hadron by its momentum-range correlation [5];
- track d_1 is the τ decay daughter. Its angle with the τ lepton track (θ_{kink}) is (245 ± 5) mrad. The impact parameter with respect to the primary vertex is (93.7 ± 1.1) μm . The track, found also on the CS films, agrees with the muon track reconstructed in the electronic detectors in both momentum ($\Delta p = 0.3^{+0.9}_{-0.5}$ GeV/ c) and angle ($\Delta\theta = 18 \pm 25$ mrad);
- the shower originating from a γ -ray conversion has an energy of $(3.1^{+0.9}_{-0.6})$ GeV. The conversion to an e^+e^- pair is observed 2.1 mm ($0.36 X_0$) downstream of the primary vertex to which it points with an impact parameter of (18 ± 13) μm . It is incompatible with originating from the secondary vertex, the impact parameter being (96 ± 12) μm .

A scanning procedure [9] with an extended angular acceptance (up to $\tan\theta = 3.5$) did not reveal any additional large-angle primary track that could be left by a muon or an electron.

In a dedicated search in the 19 films downstream of the primary vertex and in the 10 most upstream films of the downstream brick (more than $5 X_0$ in total), no further γ -ray shower within a slope acceptance of $\tan\theta < 1$ and an energy above 500 MeV could be found. The single γ -ray detected at the primary vertex can be interpreted as coming from the decay of a π^0 with the other γ being undetected.

In the plane transverse to the beam direction, the angle between the τ candidate direction and the sum of the transverse momenta of the other primary particles (p_0 and γ) is $\Delta\phi_{\tau H} = (155 \pm 15)^\circ$ (see Fig. 4). The transverse momentum at the secondary vertex (p_T^{2ry}) amounts to (690 ± 50) MeV/ c . The scalar sum of the momenta of all the particles is $p_{sum} = (6.8^{+0.9}_{-0.6})$ GeV/ c .

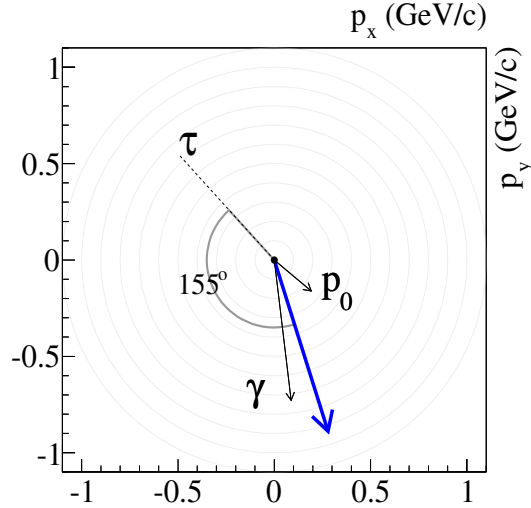


FIG. 4. The τ lepton direction (dashed line) and the momenta of the other primary particles (p_0 and γ -ray) in the plane transverse to the CNGS beam. The blue arrow is the sum of the transverse momenta of the p_0 track and of the γ -ray.

| Variable | Selection ($\tau \rightarrow \mu$) | Measurement |
|-----------------------------|--------------------------------------|---------------|
| θ_{kink} (mrad) | > 20 | 245 ± 5 |
| z_{dec} (μm) | < 2600 | 151 ± 10 |
| p_μ (GeV/c) | $[1, 15]$ | 2.8 ± 0.2 |
| p_T^{2ry} (MeV/c) | > 250 | 690 ± 50 |

TABLE I. Selection criteria for ν_τ candidate events in the $\tau \rightarrow \mu$ decay channel along with the values measured for the candidate event. Variables are defined in the text.

In Tab. I the values of the kinematical variables for this event are reported along with the predefined selection criteria [5] for the $\tau \rightarrow \mu$ channel. Besides satisfying all the selections, the variables are well within the domain of the expected signal, see Fig. 5.

V. EXPECTATIONS AND STATISTICAL SIGNIFICANCE

The method used for the estimation of signal and background was recently discussed [5]. With respect to those results, here is also taken into account the extension of the analysed sample to the 1μ events of the 2011 and 2012 runs with $p_\mu < 15$ GeV/c (presently completed at 56%).

The total sample of analysed events is 5272 giving an expected ν_τ signal in all decay channels of 1.7 events ($\Delta m_{23}^2 = 2.32 \times 10^{-3}$ eV² and $\sin^2 2\theta_{23} = 1$), out of which 0.54 in the $\tau \rightarrow \mu$ decay channel.

For the background evaluation, the full sample of 1μ events was conservatively accounted for, although it is not yet completely analysed. The additional background only affects the $\tau \rightarrow \mu$ decay channel which increases from 0.011 ± 0.05 ([5]) to 0.021 ± 0.010 events, accordingly rising the total background to 0.184 ± 0.025 events. The background in the $\tau \rightarrow \mu$ channel is dominated by the contribution of large-angle muon scattering in lead (about 80%) followed by charmed particle decays (20%), the background from hadronic interactions with a fake-muon being negligible [5].

Accounting for the fact that the signal-to-background ratio is different for each decay channel, the following method was adopted: four Poissonian random integers are extracted, one for each decay channel in the background-only hypothesis. The p -values of the single channels (obtained as the integral of the Poisson distribution for values larger or equal to the observed number of candidates) are combined into an estimator $p^* = p_\mu p_e p_h p_{3h}$. By counting the fraction of extractions for which $p^* \leq p^*(\text{observed})$, the procedure allows excluding the absence of a $\nu_\mu \rightarrow \nu_\tau$ oscillation signal with a significance of 3.4σ ($p\text{-value} = 2.9 \times 10^{-4}$).

Finally, it should be noted that the new candidate is in a region of the parameter space that is free from background:

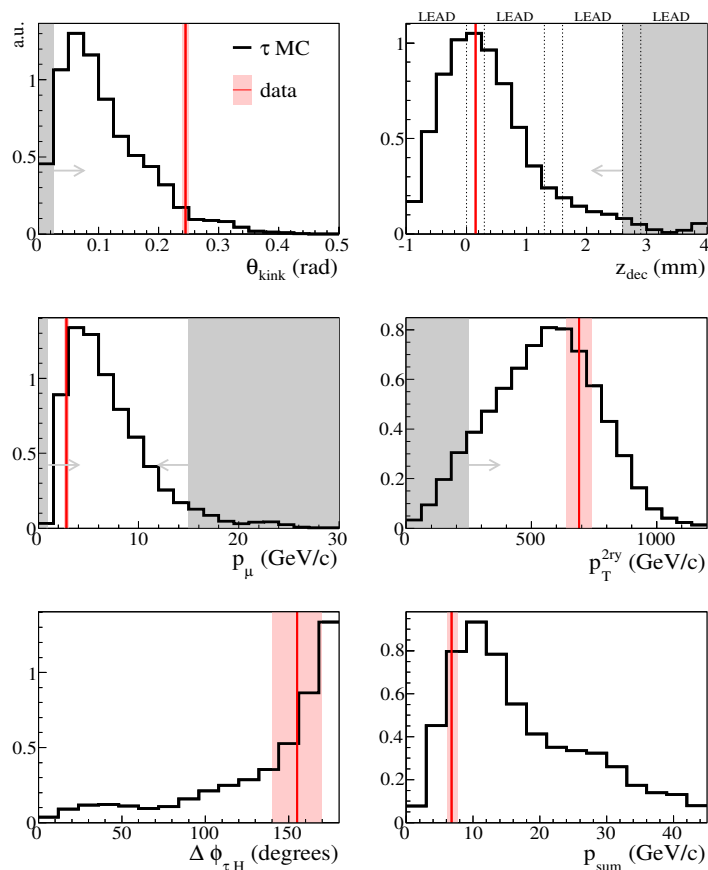


FIG. 5. Monte Carlo distribution of the reconstructed kinematical variables (see the text) for the $\tau \rightarrow \mu$ decay channel. Red lines show the measured values and red bands their uncertainty. Grey areas cover the regions excluded by the selection cuts.

the τ decay occurs in a low-density and low- Z material (the plastic base) and with a transverse momentum at the secondary vertex of 690 MeV/c, thus highly disfavouring the hypothesis of a large-angle muon scattering.

VI. CONCLUSIONS

The results of a ν_τ appearance analysis on an extended sub-sample of the neutrino interactions collected by the OPERA experiment in the CNGS run years 2008 to 2012 are reported. A ν_τ candidate event in the $\tau^- \rightarrow \mu^-$ decay channel was observed. A measurement of the negative charge of the τ lepton candidate, consistent with what is expected for the $\nu_\mu \rightarrow \nu_\tau$ oscillation, has been performed for the first time. With the present statistics and the observation of three ν_τ candidates, the absence of a signal from $\nu_\mu \rightarrow \nu_\tau$ oscillations is excluded at 3.4σ .

ACKNOWLEDGEMENTS

We thank CERN for the successful operation of the CNGS facility and INFN for the continuous support given to the experiment through its LNGS laboratory. We acknowledge funding from our national agencies. Fonds de la Recherche Scientifique-FNRS and Institut InterUniversitaire des Sciences Nucléaires for Belgium, MoSES for Croatia, CNRS and IN2P3 for France, BMBF for Germany, INFN for Italy, JSPS, MEXT, QFPU - Global COE programme of Nagoya University) and Promotion and Mutual Aid Corporation for Private Schools of Japan for Japan, SNF, the University of Bern and ETH Zurich for Switzerland, the Russian Foundation for Basic Research (grant 12-02-12142 ofim), the Programs of the Presidium of the Russian Academy of Sciences (Neutrino physics and Experimental and theoretical researches of fundamental interactions), and the Ministry of Education and Science of the Russian Federation for

Russia, the National Research Foundation of Korea Grant No. 2011-0029457 and TUBITAK for Korea, the Scientific and Technological Research Council of Turkey, for Turkey. We thank the IN2P3 Computing Centre (CC-IN2P3) for providing computing resources.

- [1] K. Abe *et al.*, Phys. Rev. Lett. **110**, 181802 (2013).
- [2] Y. Fukuda *et al.*, Phys. Rev. Lett. **81**, 1562 (1998).
- [3] R. Bailey *et al.*, CERN-SL-99-034-DI. INFN-AE-99-05 (1999), addendum to CERN 98-02, INFN-AE-98-05.
- [4] R. Acquafredda *et al.*, JINST **4**, P04018 (2009).
- [5] N. Agafonova *et al.*, Accepted by JHEP (2013), arXiv:1308.2553 [hep-ex].
- [6] N. Agafonova *et al.*, Phys. Lett. **B691**, 138 (2010).
- [7] A. Bertolin *et al.*, OPERA public note 161 (2013), <http://operaweb.lngs.infn.it/Opera/publicnotes/note161.pdf>.
- [8] N. Agafonova *et al.*, New J. Phys. **14**, 013026 (2012).
- [9] T. Fukuda *et al.*, JINST **8**, P01023 (2013).

2.5 Cosmic ray physics with the OPERA detector, [14]

T. BRUGIERE*

*Universit Claude Bernard, Lyon I,
Institut de Physique Nuclaire de Lyon,
Lyon, FRANCE*

** E-mail: brugiere@ipnl.in2p3.fr*

OPERA is a long-baseline neutrino experiment located in the Hall C of the underground Gran Sasso Laboratory at an average depth of 3.8 km.w.e., corresponding to muon energies at surface higher than 1.5 TeV. In this paper we focus on the potentialities of OPERA used as a cosmic ray detector. We report on the measurement of the atmospheric muon charge ratio, on the analysis of upgoing muons induced by atmospheric neutrinos and on the large cosmic showers inducing coincidences between different experiments in Gran Sasso.

Keywords: long baseline experiments, neutrino oscillations, atmospheric muons

1. Introduction

OPERA is a hybrid detector designed to identify the τ lepton via the topological observation of its decay in nuclear emulsions (providing an intrinsic micrometric resolution) complemented with electronic detectors (scintillator planes in the target section and dipolar muon spectrometers) to trigger on the events, locate the interaction volume and measure the muons momentum and charge. OPERA is taking data since the commissioning run in 2006 and recorded up-to-now around 25,000 events from the CNGS beam.¹

2. Atmospheric neutrinos

The timing system of the OPERA target tracker (TT) allows a t.o.f. analysis of the cosmic particles and an identification of the up-going atmospheric-neutrino induced muons.⁵ The acceptance for through-going tracks is however limited (roughly 1/10 of MACRO) for events crossing the spectrometer. The TT consists of 62 planes of 512 scintillator strips readout at both ends by a Hamamatsu 64 channels MaPMT in auto-trigger mode. Each front-end

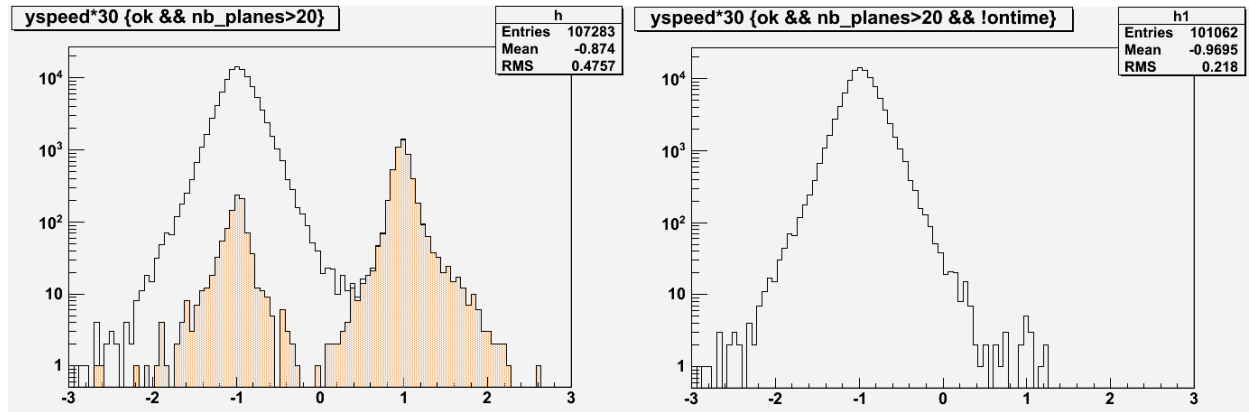


Fig. 1. “speed-side”, (left) with on-time events (orange), (right) only off-time events

electronics channel is divided into a slow shapper for charge measurement and a fast shaper for triggering and timestamping. The GPS-locked clock distribution system gives timestamp accuracy of 10ns. All propagation delays induced in the fibres and the timing distribution system are accounted for in the off-line analysis.

Appropriate runs are selected according to the average cosmics event rate. The total livetime after cut is 433.3 effective days during the 2008 and 2009 runs.

Tracks are reconstructed through a Hough transform algorithm and standard methods with pivot points for tracking and fitting. Other cuts are applied on the tracks length in the TT and the timing information content (requiring typically one timing information available in each direction).

From a full Monte Carlo simulation based taking Honda flux inputs, 11.3 events are expected.

Fig.1 displays the distributions of the “speed-side” convoluting the $1/\beta = c/v$ variable with the track slope sign. Conventionnaly upward(downward)-going and downward-going particles have positive (negative) speed-side. Given the slope of the CNGS beam w.r.t. the horizontal ($\sim +3.3^\circ$) almost all on-time events have a positive speed side. This part is rejected using also time coincidence with CERN. Off-time up-going events, with a cut $0.75 < 1/\beta < 1.25$, are selected as atmospheric neutrino events. A total of 15 events is retained as atmosheric neutrinos induced muons, compatible with the expectations.

3. Atmospheric muon charge ratio

The muon charge ratio (R_μ) is an important observable to understand the physics of cosmic ray interactions in atmosphere (e.g. high energy hadronic

interactions in the forward region) and to constraints theoretical models. Since most of the primary cosmic rays are protons, there is a positive charge excess in the hadronic showers and hence in the penetrating component : in the energy range from a few hundred MeV to 300 GeV we get $R_\mu = N_{\mu^+}/N_{\mu^-} \approx 1.27$.² As energy increases, the fraction of muons coming from kaon decays also increases, and since strong interaction production channels lead to a K^+/K^- higher than π^+/π^- , the muon charge ratio is expected to rise.³ This effect is balanced when the zenith angle increases since mesons have larger probability to decay in the deeper and less dense atmosphere and therefore the fraction of muons from pion decays increases. We also expect that muons in high multiplicity events, produced by heavier primaries and coming from small Feynman X_F , exhibit a smaller charge ratio.³ The measurement of R_μ at high energies is therefore important to constrain models of forward particle production. Air showers experiments are not sensitive to the hadroproduction at high X_F , while the interpretation of underground, underwater and underice data strongly relies on its modeling.

The results presented here are based on data recorded during the CNGS Physics Run, from June 18 until November 10, 2008 (113.4 equivalent days livetime after cuts). The detector ran in the standard configuration, with the magnetic field directed along the vertical axis in the first arm of both spectrometers, and opposite to the vertical axis in the second arm of both spectrometers. Moreover, a sample of cosmic ray muons was collected with the magnetic field switched off, in order to correct for the alignment and to evaluate systematic uncertainties. A muon crossing the spectrometer is deflected in the horizontal plane : the charge and momentum reconstruction is performed for tracks crossing at least one magnet arm using the bending angle information ($\Delta\phi$) coming from HPT stations.

Ratio between OPERA and Monte Carlo data rates (R) is : $R_{\text{data}}/R_{\text{MC}} = (95.9 \pm 0.3)\%$. For this analysis, the basic information required for the charge-momentum measurement is at least one reconstructed $\Delta\phi$ angle in each event and we selected tracks whose deflections are above the experimental resolution, ie. $\Delta\phi/\sigma_{\Delta\phi} > 3$. The muon charge ratio has been computed separately for single muon events and multiple muon events. To provide a result independent from the detector features, we unfolded the charge ratio measured value using the charge mis-identification probability η , known with an accuracy of 1%, computed with Monte Carlo. For

single-muon :

$$R_{\text{unf}} = \frac{\eta - (1 - \eta)R_{\text{meas}}}{\eta R_{\text{meas}} - (1 - \eta)} = 1.395 \pm 0.022(\text{stat.})_{0.001}^{+0.011}(\text{syst.}) \quad (1)$$

where $\eta = 0.0282 \pm 0.0018$ is the misidentification probability, defined as the number of wrong charge assignments with respect to the total number of reconstructed muons. For multiple-muon events :

$$Runf = 1.23 \pm 0.10(\text{stat.})_{0.001}^{+0.011}(\text{syst.}) \quad (2)$$

Within the present statistical accuracy, we did not find any indication of charge ratio dependence on the residual underground momentum, rock depth, zenithal angle and azimuthal angle. On the other hand this result is somehow expected⁴ and we can evaluate the rock/zenith dependence of the charge ratio. Considering the parameters fitted in that work and an energy/depth relation obtained by Monte Carlo, we find that muons detected by OPERA are in the region where the kaon contribution is completely saturated. In fact, the Gran Sasso topological map has the unique rock/cos(θ) dependence for which kaon decay contribution is constant with the energy and no further rise in the charge ratio is expected. In this respect, OPERA data constitute an ultimate limit for this kind of measurement.

With the same data sample, using the bending angle information, the underground muon spectrum was measured. To reconstruct the momentum from the $\Delta\phi$ measurement, the energy loss in the iron magnet is taken into account. The MC distribution of true momentum versus reconstructed momentum shows a linear trend until ~ 300 GeV/c. The muon spectrum allows to investigate the primary chemical composition : varying the composition model in MC, the comparison with the measurement should indicate the best one.

4. OPERA-LVD coincidences

We attempted a first search of coincidences between the OPERA and LVD detectors.⁶ The relative position of the two detectors, separated by an average distance of $\sim 170m$, allows an unprecedented analysis of very large cosmic ray showers looking at their penetrating TeV component.

The physics case follows the consideration that TeV muons separated by hundreds of meters are produced in high p_T interactions up in the atmosphere ($p_T > 3GeV/c$) where pQCD can be applied instead of standard phenomenological models usually adopted.⁷

We analysed data of 2008 CNGS run, for a total OPERA-LVD joined live-time of 131.3 days. In a time-window of $15\mu s$ we found 145 events ontime

with CNGS (beam events) and 38 events out of the CNGS spill window (cosmic events).

The first sample of events has a time difference within the $10.5\mu\text{s}$ of the CNGS spill width and is well centered around zero, probing the good inter-calibration accuracy of the detector timing systems. The cosmic ray sample, on the other hand, has a narrow distribution peaked at -573.4 ns with a RMS of 94 ns. The central value of the distribution has a simple interpretation: coincident events are due to single muon events entering horizontally from the OPERA side sticking the LVD detector after 573.4 ns of flight (corresponding to 172 m). The OPERA-LVD direction lies along the so-called Teramo valley, where the mountain profile exhibits a small rock depth even for horizontal directions. Visual inspection using the event displays of both the experiments confirms this conclusion.

This analysis will be extended with the statistics accumulated in the forthcoming runs in order to improve the limits on high p_T events.

5. Conclusions

Cosmic ray physics is performed in parallel to the oscillation physics programme with the OPERA detector. The analysis of neutrino-induced atmospheric muons showed the OPERA capability to tag these kind of events, with the aim of charge discriminate the oscillation signature as soon as new statistics will be accumulated. Results for atmospheric muon charge ratio will be helpful to constrain phenomenological hadronic interaction models in the very forward region. Finally, coincident events between two LNGS experiments have been unambiguously observed, premise to observe high p_T events originated in cosmic ray showers in the forthcoming runs.

References

1. R. Acquafredda et al. [OPERA Collaboration] (JINST 4, P04018, 2009).
2. T. Hebbeker and C. Timmermans (Astropart. Phys. 18, 107, 2002).
3. G. Battistoni, A. Margiotta, S. Muraro, M. Sioli [FLUKA Collaboration] : to appear in the proceedings of ICRC09, 2009.
4. P. Adamson et al. [MINOS Collaboration] (Phys. Rev. D 76, 052003, 2007).
5. P. Adamson et al. [MINOS Collaboration] (Phys. Rev. D 75, 092003).
6. M. Selvi [LVD collaboration] : to appear in the proceedings of ICRC09, 2009.
7. S. R. Klein and D. Chirkin for the IceCube Collaboration (Proc. of the 30th ICRC, Merida, Yucatan, Mexico, 2007).

Chapitre 3

Les générations futures : T2K et au-delà

3.1 Introduction

T2K — (Tokai To Kamioka) comprenant 200 physiciens en Europe, au Japon et en Amérique. La “ligne neutrinos” utilisée est celle de J-Parc à Tokai (Japon), dirigée vers Kamioka où se situe le détecteur lointain Super-Kamiokande. Cette expérience de seconde génération utilise le canal d’oscillations $\nu_\mu \rightarrow \nu_e$ pour la mesure de l’angle θ_{13} et la recherche de phase(s) de violation de CP dans le secteur leptonique. Les premiers tirs sur la cible de la ligne neutrinos ont été effectués en Avril 2009 et les premiers runs de physique ont pris place en 2010. Depuis quatre runs de physique ont été menés à bien et le résultat principal est l’observation de l’apparition de 28 candidats ν_e dans le détecteur lointain. Ceci constitue la seconde observation de l’oscillation de neutrinos en mode “apparition” après celle d’OPERA et des premiers candidats ν_τ et apporte une confirmation de la mesure de Daya Bay (voir introduction) de l’angle de mélange manquant jusque-là, θ_{13} .

Au sein de T2K, et compte-tenu de ses engagements sur OPERA, l’IPNL s’est engagé dans deux axes de recherche : production et opération d’un détecteur à basse énergie de 2010 à 2012 (Low Energy Monitor ou LEM), modèle réduit du trajectographe d’OPERA - utilisant le même système DAQ - et début d’une R&D sur une chaîne de lecture électronique de chambre à projection temporelle (TPC) à argon liquide (LAr). C’est dans ce cadre là qu’un système de synchronisation à travers le réseau a été mis au point et a fait l’objet d’un dépôt de brevet.

LAGUNA-LBNO —. Parallèlement à ces activités au sein de deux grandes collaborations internationales, je me suis engagé avec le groupe Neutrinos de l’IPNL dans le design study FP7 LAGUNA (*Large Apparatus studying Grand Unification and Neutrino Astrophysics*), impliquant 21 contributeurs en Europe (académiques et industriels) et dédié à l’étude de la faisabilité de très grandes infrastructures souterraines pour héberger les détecteurs du futur et aux développements de ceux-ci (LAGUNA-LBNO pour les TPC LAr grand volume).

Ce DS a pour vocation de préparer la 3ème génération d’expériences, après T2K, pour l’étude de la violation CP et des hiérarchies de masse de neutrinos. L’IPNL (physique et services techniques) est engagé dans la R&D sur une chaîne prototype d’électronique de lecture des TPC à Argon Liquide (continuité de T2K) : production d’un ASIC fonctionnant à froid (phase vapeur de l’argon) et d’une électronique d’acquisition haut débit (Ethernet Gigabit) aux standards microTCA/xTCA. Dans le cadre du LABEX LIO, un prototype de TPC LAr pour valider l’ensemble de la chaîne de lecture avec des cosmiques a été d’installé à l’IPNL. Le DS s’est conclu en août 2014 à Helsinki, Finlande, en concluant que le meilleur projet parmi les différentes options étudiées était un détecteur de type TPC double phase à argon liquide (20kt + 50kt) placé dans une mine à 1400m de profondeur (Pyhäsalmi, Finlande), à 2300km du CERN (Genève, Suisse) et 1100km de Protvino (Moscou, Russie).

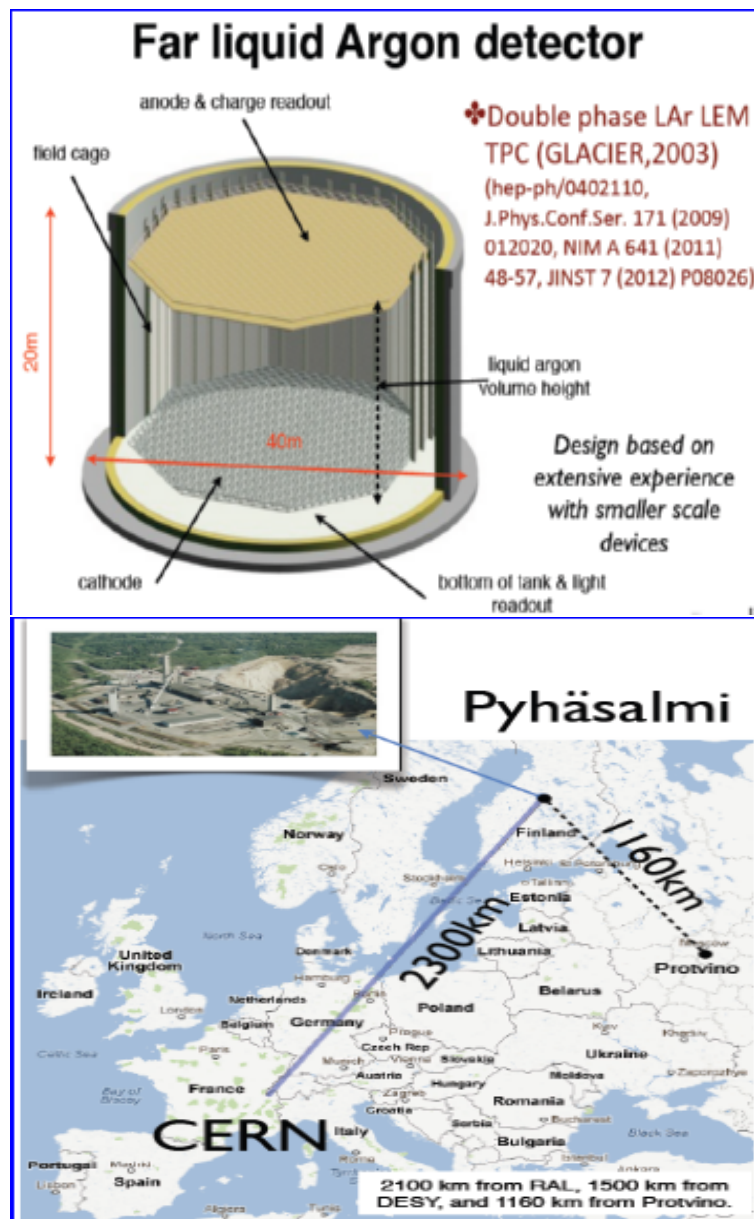


FIGURE 3.1 – En haut : schéma d’une TPC double phase à argon liquide (détecteur GLACIER). En bas : représentation des *baseline* potentielles à partir du CERN et de Protvino pour un détecteur placé dans la mine de Pyhäsalmi.

Avant cette ultime étape de détecteur à l’échelle de la dizaine de kilotonnes, il est prévu de mettre au point un démonstrateur au CERN, dans la West Area. Le détecteur, baptisé WA105, doit permettre de valider l’ensemble du concept, la faisabilité de la détection des électrons de l’ionisation sur de grandes distances dans l’argon ultra pur, l’amplification en phase gazeuse, la chaîne de lecture front-end et back-end. Ce projet est en cours de réalisation au CERN et j’assume la responsabilité de l’acquisition de données pour le détecteur. La solution technique proposée dans ce cas repose sur un système distribué sur réseau, à très haut débit (10GbE), au sein d’un standard industriel, le micro-TCA, très répandu dans l’industrie des télécommunications. Le protocole de transfert de données doit permettre aussi dans une large mesure la synchronisation des différents éléments connectés sur ce réseau et doit s’appuyer sur le brevet déposé lors des premières R&D *Installation de capteurs*

intelligents pour l'acquisition à haut débit de données via le réseau Ethernet, brevet n°04 00468.

Le premier article (*Indication of Electron Neutrino Appearance from an Accelerator-produced Off-axis Muon Neutrino Beam*, [31]) publié par la collaboration T2K relate l'observation des premiers événements d'apparition de ν_e dans le faisceau de ν_μ de J-PARC. Le second article est un extrait du TDR de WA105 (LBNO-DEMO) [54] décrivant le détecteur en général et plus précisément le système d'acquisition proposé par l'IPNL.

3.2 Indication of Electron Neutrino Appearance from an Accelerator-produced Off-axis Muon Neutrino Beam, [31]

(The T2K collaboration)

We report results of a search for ν_e appearance in the T2K experiment [1]. In a three-neutrino mixing scenario, flavor oscillations are described by the PMNS matrix [2, 3], usually parametrized by the three angles θ_{12} , θ_{23} , θ_{13} , and the CP -violating phase δ_{CP} . Previous experiments have observed neutrino oscillations driven by θ_{12} and θ_{23} in the solar (Δm_{12}^2) and atmospheric ($\Delta m_{13}^2 \simeq \Delta m_{23}^2$) sectors [4–9]. In the atmospheric sector, data are consistent with $|\Delta m_{23}^2| \simeq 2.4 \times 10^{-3} \text{ eV}^2$, a normal $\Delta m_{23}^2 > 0$ or inverted $\Delta m_{23}^2 < 0$ mass hierarchy, and $\sin^2 2\theta_{23}$ close to, or equal to unity. Searches for oscillations driven by θ_{13} have been inconclusive and upper limits have been derived [10–13], with the most stringent being $\sin^2 2\theta_{13} < 0.15$ (90%C.L.), set by CHOOZ [14] and MINOS [15].

T2K uses a conventional neutrino beam produced at J-PARC and directed 2.5° off-axis to Super-Kamiokande (SK) at a distance $L = 295 \text{ km}$. This configuration produces a narrow-band ν_μ beam [16], tuned at the first oscillation maximum $E_\nu = |\Delta m_{23}^2| L / (2\pi) \simeq 0.6 \text{ GeV}$, reducing backgrounds from higher energy neutrino interactions.

Details of the T2K experimental setup are described elsewhere [17]. Here we briefly review the components relevant for the ν_e search. The J-PARC Main Ring (MR) accelerator [18] provides 30 GeV protons with a cycle of 0.3 Hz. Eight bunches are single-turn extracted in $5 \mu\text{s}$ and transported through an extraction line arc defined by superconducting combined-function magnets to the production target. The primary beamline is equipped with 21 electrostatic beam position monitors (ESM), 19 segmented secondary emission monitors (SSEM), one optical transition radiation monitor (OTR) and five current transformers. The secondary beamline, filled with He at atmospheric pressure, is composed of the target, focusing horns and decay tunnel. The graphite target is 2.6 cm in diameter and 90 cm ($1.9\lambda_{int}$) long. Charged particles exiting the target are sign selected and focused into the 96 m long decay tunnel by three magnetic horns pulsed at 250 kA. Neutrinos are primarily produced in the decays of charged pions and kaons. A beam dump is located at the end of the tunnel and is followed by muon monitors.

The Near Detector complex [17] located 280 m downstream from the target hosts two detectors. The on-axis Interactive Neutrino GRID (INGRID) accumulates neutrino interactions with high statistics to monitor the beam intensity, direction and profile. It consists of 14 identical 7-ton iron-absorber/scintillator-tracker sandwich modules arranged in 10 m by 10 m crossed horizontal and vertical arrays centered on the beam. The off-axis detector reconstructs exclusive final states to study neutrino interactions and beam properties corre-

sponding to those expected at the far detector. Embedded in the refurbished UA1 magnet (0.2 T), it consists of three large volume time projection chambers (TPCs) [19] interleaved with two fine-grained tracking detectors (FGDs, each 1 ton), a π^0 -optimized detector and a surrounding electromagnetic calorimeter. The magnet yoke is instrumented as a side muon range detector.

The SK water Cherenkov far detector [20] has a fiducial volume (FV) of 22.5 kton within its cylindrical inner detector (ID). Enclosing the ID all around is the 2 m-wide outer detector (OD). The front-end readout electronics allow for a zero-deadtime software trigger. Spill timing information, synchronized by the Global Positioning System (GPS) with < 150 ns precision, is transferred online to SK and triggers the recording of photomultiplier hits within ± 500 μ s of the expected arrival time of the neutrinos.

The results presented in this Letter are based on the first two physics runs: Run 1 (Jan–Jun 2010) and Run 2 (Nov 2010–Mar 2011). During this time period, the MR proton beam power was continually increased and reached 145 kW with 9×10^{13} protons per pulse. The targeting efficiency was monitored by the ESM, SSEM and OTR and found to be stable at over 99%. The muon monitors provided additional spill-by-spill steering information. A total of 2,474,419 spills were retained for analysis after beam and far detector quality cuts, yielding 1.43×10^{20} protons on target (p.o.t.).

We present the study of events in the far detector with only a single electron-like (e -like) ring. The analysis produces a sample enhanced in ν_e charged-current quasi-elastic interactions (CCQE) arising from $\nu_\mu \rightarrow \nu_e$ oscillations. The main backgrounds are intrinsic ν_e contamination in the beam and neutral current (NC) interactions with a misidentified π^0 . The selection criteria for this analysis were fixed from Monte Carlo (MC) studies before the data were collected, optimized for the initial running conditions. The observed number of events is compared to expectations based on neutrino flux and cross-section predictions for signal and all sources of backgrounds, which are corrected using an inclusive ν_μ charged-current (CC) measurement in the off-axis near detector.

We compute the neutrino beam fluxes (Fig. 1) starting from models and tuning them to experimental data. Pion production in (p, θ) bins is based on the NA61 measurements [21], typically with 5–10% uncertainties. Pions produced outside the experimentally measured phase space, as well as kaons, are modeled using FLUKA [22, 23]. These pions are assigned systematic uncertainties on their production of 50%, while kaon production uncertainties,

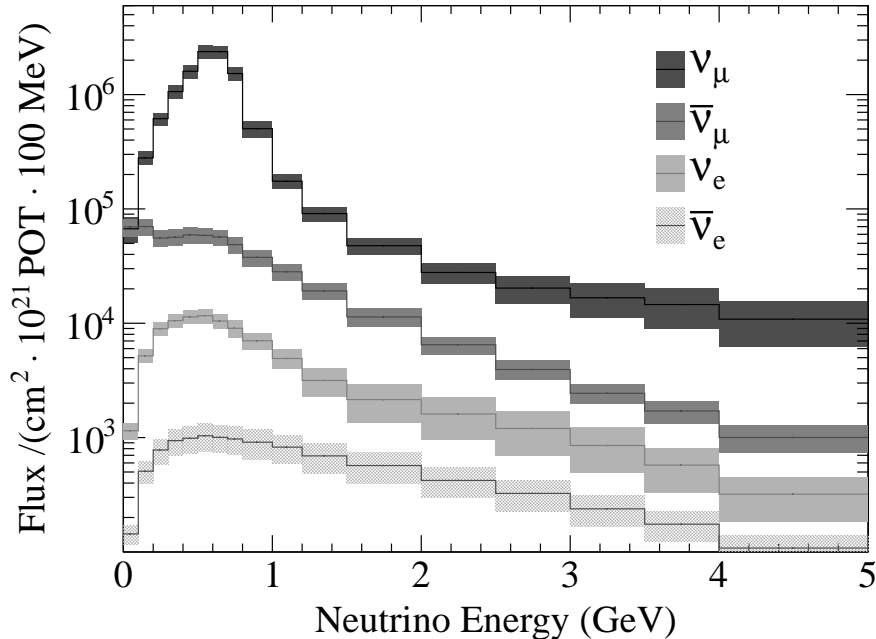


FIG. 1. Predicted neutrino fluxes at the far detector, in absence of oscillations. The shaded boxes indicate the total systematic uncertainties for each energy bin.

estimated from a comparison with data from Eichten *et al.* [24], range from 15% to 100% depending on the bin. GEANT3 [25], with GCALOR [26] for hadronic interactions, handles particle propagation through the magnetic horns, target hall, decay volume and beam dump. Additional errors to the neutrino fluxes are included for the proton beam uncertainties, secondary beamline component alignment uncertainties, and the beam direction uncertainty.

The neutrino beam profile and its absolute rate ($1.5 \text{ events}/10^{14} \text{ p.o.t.}$) as measured by INGRID were stable and consistent with expectations. The beam profile center (Fig. 2) indicates that beam steering was better than $\pm 1 \text{ mrad}$. The correlated systematic error is $\pm 0.33(0.37) \text{ mrad}$ for the horizontal(vertical) direction. The error on the SK position relative to the beamline elements was obtained from a dedicated GPS survey and is negligible. As shown in Fig. 1, the estimated uncertainties of the intrinsic ν_μ and ν_e fluxes below 1 GeV are around 14%. Above 1 GeV, the intrinsic ν_e flux error is dominated by the uncertainty on the kaon production rate with resulting errors of 20–50%.

The NEUT MC event generator [28], which has been tuned with recent neutrino interaction data in an energy region compatible with T2K [29–31], is used to simulate neutrino interactions in the near and far detectors. The GENIE [32] generator provides a separate

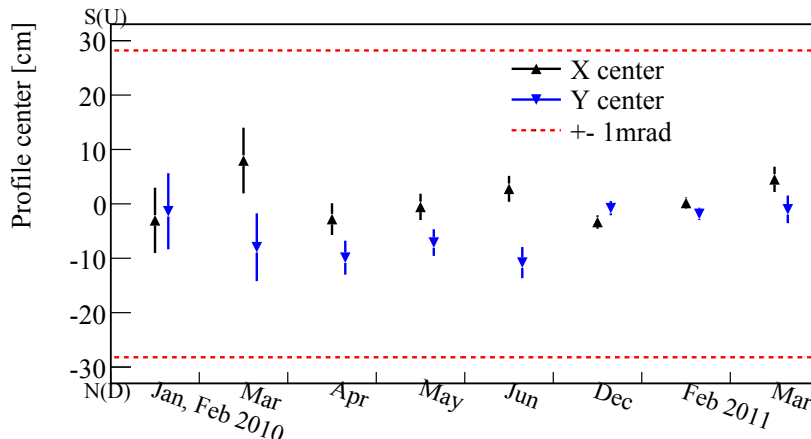


FIG. 2. Beam centering stability in horizontal (x, South–North) and vertical (y, Down–Up) directions as a function of time, as measured by INGRID. Errors shown are only statistical. The dashed lines correspond to a change of beam direction by ± 1 mrad.

TABLE I. Summary of systematic uncertainties for the relative rate of different charged-current (CC) and neutral-current (NC) reactions to the rate for CCQE.

| Process | Systematic error |
|-----------------------|---|
| CCQE | energy-dependent (7% at 500 MeV) |
| CC 1π | 30% ($E_\nu < 2$ GeV) – 20% ($E_\nu > 2$ GeV) |
| CC coherent π^\pm | 100% (upper limit from [27]) |
| CC other | 30% ($E_\nu < 2$ GeV) – 25% ($E_\nu > 2$ GeV) |
| NC $1\pi^0$ | 30% ($E_\nu < 1$ GeV) – 20% ($E_\nu > 1$ GeV) |
| NC coherent π | 30% |
| NC other π | 30% |
| FSI | energy-dependent (10% at 500 MeV) |

cross-check of the assumed cross-sections and uncertainties, and yields consistent results. A list of reactions and their uncertainties relative to the CCQE total cross-section is shown in Table I. An energy-dependent error on CCQE is assigned to account for the uncertainty in the low energy cross-section, especially for the different target materials between the near and far detectors. Uncertainties in intranuclear final state interactions (FSI), implemented with a microscopic cascade model [33], introduce an additional error in the rates (see e.g.

[34]).

An inclusive ν_μ CC measurement in the off-axis near detector is used to constrain the expected event rate at the far detector. From a data sample collected in Run 1 and corresponding to 2.88×10^{19} p.o.t. after detector quality cuts, neutrino interactions are selected in the FGDs with tracks entering the downstream TPC. The most energetic negative track in the TPC is chosen and we require its ionization loss to be compatible with a muon. To reduce background from interactions outside the FGDs, there must be no track in the upstream TPC. The analysis selects 1529 data events (38% ν_μ CC efficiency for 90% purity, estimated from MC). The momentum distribution of the selected muons (Fig. 3) shows good agreement between data and MC. The measured data/MC ratio is

$$R_{ND}^{\mu,Data}/R_{ND}^{\mu,MC} = 1.036 \pm 0.028(\text{stat.})_{-0.037}^{+0.044}(\text{det.syst.}) \pm 0.038(\text{phys.syst.}), \quad (1)$$

where $R_{ND}^{\mu,Data}$ and $R_{ND}^{\mu,MC}$ are the p.o.t. normalized rates of ν_μ CC interactions in data and MC. The detector systematic errors mainly come from tracking and particle identification efficiencies, and physics uncertainties are related to the interaction modeling. Uncertainties that effectively cancel between near and far detectors were omitted.

At the far detector, we extract a fully-contained fiducial volume (FCFV) sample by requiring no event activity in either the OD or in the 100 μs before the event trigger time, at least 30 MeV electron-equivalent energy deposited in the ID (defined as visible energy E_{vis}), and the reconstructed vertex in the fiducial region. The data have 88 such FCFV events that are within the timing range from -2 to $10 \mu\text{s}$ around the beam trigger time. The accidental contamination from non-beam related events is determined from the sidebands to be 0.003 events. A Kolmogorov-Smirnov (KS) test of the observed number of FCFV events as a function of accumulated p.o.t. is compatible with the normalized event rate being constant ($p\text{-value}=0.32$). The analysis relies on the well-established reconstruction techniques developed for other data samples [4]. Forty-one events are reconstructed with a single ring, and eight of those are e -like. Six of these events have $E_{vis} > 100 \text{ MeV}$ and no delayed-electron signal. To suppress misidentified π^0 mesons, the reconstruction of two rings is forced by comparison of the observed and expected light patterns calculated under the assumption of two showers [35], and a cut on the two-ring invariant mass $M_{inv} < 105 \text{ MeV}/c^2$ is imposed. No events are rejected (Fig. 4). Finally, the neutrino energy E_ν^{rec} is computed using the reconstructed momentum and direction of the ring, by assuming

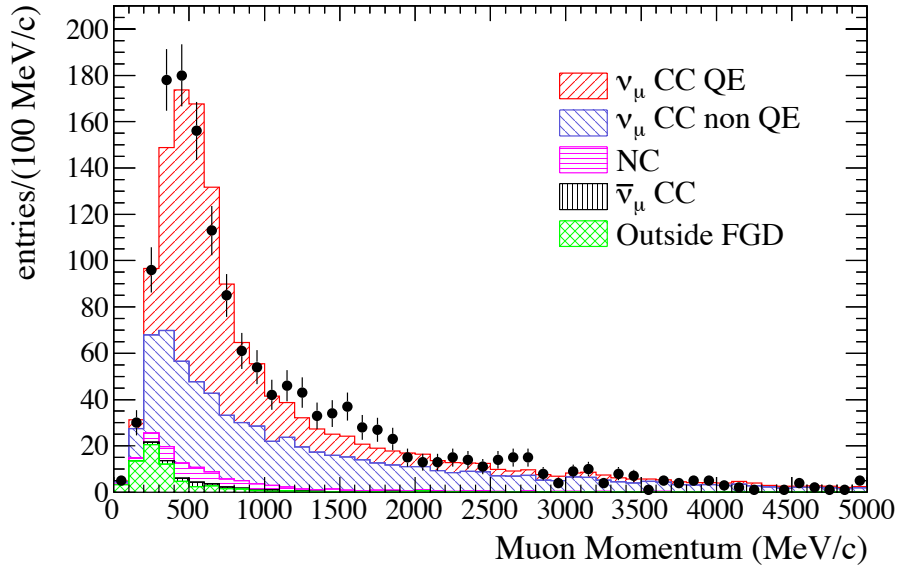


FIG. 3. Measured muon momentum of ν_μ CC candidates reconstructed in the FGD target. The data are shown using points with error bars (statistical only) and the MC predictions are in histograms shaded according to their type.

quasi-elastic kinematics and neglecting Fermi motion. No events are rejected by requiring $E_\nu^{rec} < 1250$ MeV, aimed at suppressing events from the intrinsic ν_e component arising primarily from kaon decays (Fig. 5). The data and MC reductions after each selection criterion are shown in Table II. The ν_e appearance signal efficiency is estimated from MC to be 66% while rejection for $\nu_\mu + \bar{\nu}_\mu$ CC, intrinsic ν_e CC, and NC are $> 99\%$, 77%, and 99%, respectively. Of the surviving background NC interactions constitute 46%, of which 74% are due to π^0 mesons and 6% originate from single gamma production.

Examination of the six data events shows properties consistent with ν_e CC interactions. The distribution of the cosine of the opening angle between the ring and the incoming beam direction is consistent with CCQE events. The event vertices in cylindrical coordinates (R, ϕ, z) show that these events are clustered at large R , near the edge of the FV in the upstream beam direction. A KS test on the R^2 distribution of our final events yields a p -value of 0.03. If this was related to contamination from penetrating particles produced in upstream neutrino interactions, then the ID region outside the FV should show evidence for such events, however this is not observed. In addition, an analysis of the neutrino interactions occurring in the OD volume is consistent with expectations.

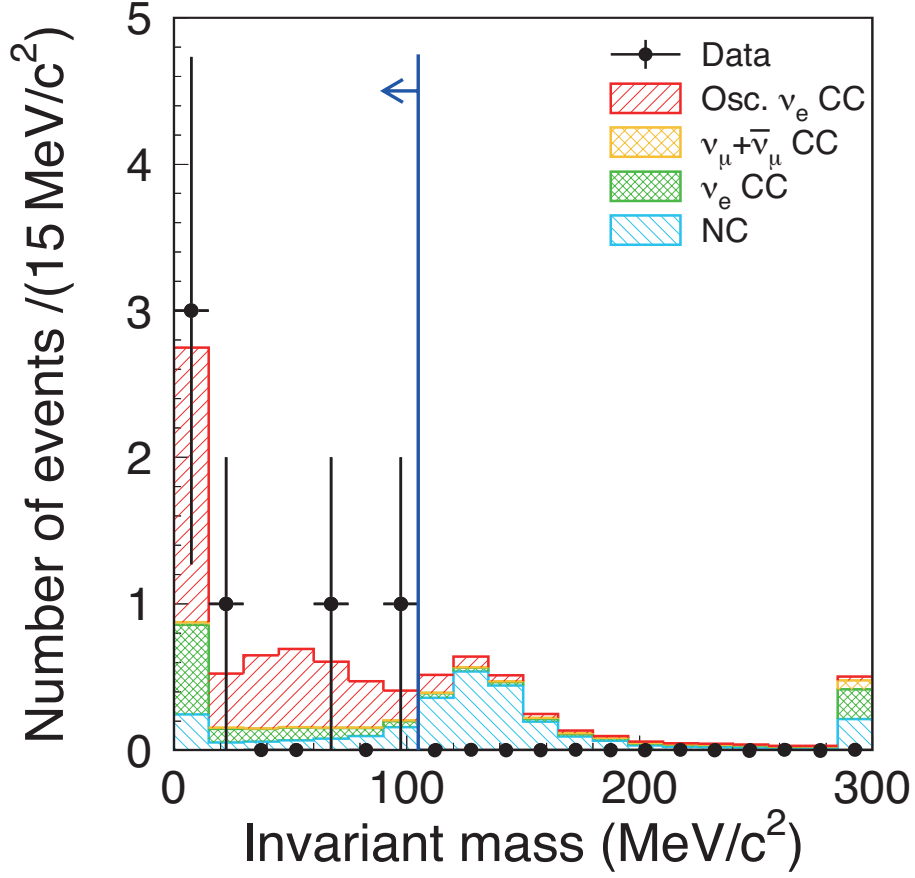


FIG. 4. Distribution of invariant mass M_{inv} when each event is forced to be reconstructed into two rings. The data are shown using points with error bars (statistical only) and the MC predictions are in shaded histograms, corresponding to oscillated ν_e CC signal and various background sources for $\sin^2 2\theta_{13} = 0.1$. The last bin shows overflow entries. The vertical line shows the applied cut at 105 MeV/ c^2 .

To compute the expected number of events at the far detector N_{SK}^{exp} , we use the near detector ν_μ CC interaction rate measurement as normalization, and the ratio of expected events in the near and far detectors, where common systematic errors cancel. Using Eq. 1, this can be expressed as:

$$N_{SK}^{exp} = \left(R_{ND}^{\mu, Data} / R_{ND}^{\mu, MC} \right) \cdot N_{SK}^{MC}, \quad (2)$$

where N_{SK}^{MC} is the MC number of events expected in the far detector. Due to the correlation of systematic errors in the near and far detector samples, Eq. 2 reduces the uncertainty on the expected number of events. Event rates are computed incorporating three-flavor oscillation

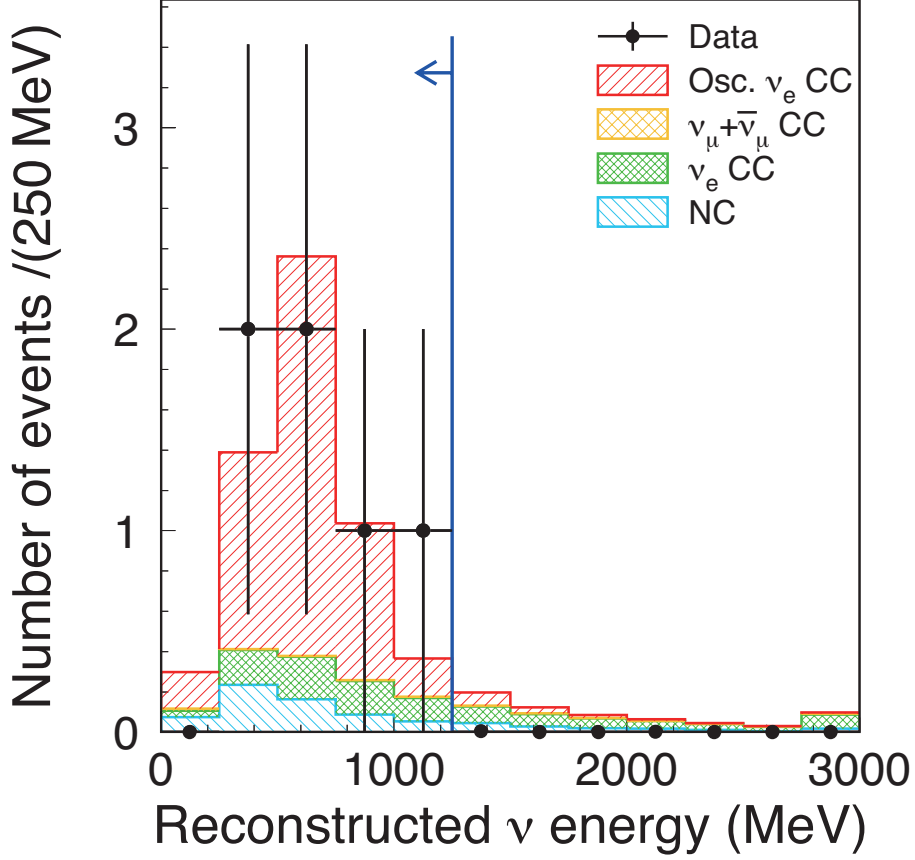


FIG. 5. Same as Fig. 4 for the reconstructed neutrino energy spectrum of the events which pass all ν_e appearance signal selection criteria with the exception of the energy cut. The vertical line shows the applied cut at 1250 MeV.

probabilities and matter effects [36] with $\Delta m_{12}^2 = 7.6 \times 10^{-5} \text{ eV}^2$, $\Delta m_{23}^2 = +2.4 \times 10^{-3} \text{ eV}^2$, $\sin^2 2\theta_{12} = 0.8704$, $\sin^2 2\theta_{23} = 1.0$, an average Earth density $\rho = 3.2 \text{ g/cm}^3$ and $\delta_{\text{CP}} = 0$ unless otherwise noted. The expectations are $0.03(0.03) \nu_\mu + \bar{\nu}_\mu \text{ CC}$, $0.8(0.7)$ intrinsic $\nu_e \text{ CC}$, and $0.1(4.1) \nu_\mu \rightarrow \nu_e$ oscillation events for $\sin^2 2\theta_{13} = 0(0.1)$, and 0.6 NC events. As shown in Table III, the total systematic uncertainty on N_{SK}^{exp} depends on θ_{13} . Neutrino flux uncertainties contribute $14.9\%(15.4\%)$ to the far(near) event rates, but their ratio has an 8.5% error due to cancellations. The near detector $\nu_\mu \text{ CC}$ selection efficiency uncertainty yields $^{+5.6\%}_{-5.2\%}$ and the statistical uncertainty gives 2.7% . The errors from cross-section modeling are dominated by FSI uncertainties and by the knowledge of the $\sigma(\nu_e)/\sigma(\nu_\mu)$ ratio, estimated to $\pm 6\%$. The systematic uncertainties due to event selection in SK were studied with cosmic-ray muons, electrons from muon decays, and atmospheric neutrino events. Their contribution

TABLE II. Event reduction for the ν_e appearance search at the far detector. After each selection criterion is applied, the numbers of observed (Data) and MC expected events of ν_μ CC, intrinsic ν_e CC, NC, and the ν_e CC signal, are given. All MC CC samples include three-flavor oscillations for $\sin^2 2\theta_{13}=0.1$ and $\delta_{\text{CP}} = 0$.

| | Data | ν_μ CC | ν_e CC | NC | $\nu_\mu \rightarrow \nu_e$ CC |
|------------------------------|------|--------------|------------|------|--------------------------------|
| (0) interaction in FV | n/a | 67.2 | 3.1 | 71.0 | 6.2 |
| (1) fully-contained FV | 88 | 52.4 | 2.9 | 18.3 | 6.0 |
| (2) single ring | 41 | 30.8 | 1.8 | 5.7 | 5.2 |
| (3) e -like | 8 | 1.0 | 1.8 | 3.7 | 5.2 |
| (4) $E_{vis} > 100$ MeV | 7 | 0.7 | 1.8 | 3.2 | 5.1 |
| (5) no delayed electron | 6 | 0.1 | 1.5 | 2.8 | 4.6 |
| (6) non- π^0 -like | 6 | 0.04 | 1.1 | 0.8 | 4.2 |
| (7) $E_\nu^{rec} < 1250$ MeV | 6 | 0.03 | 0.7 | 0.6 | 4.1 |

to $\delta N_{SK}^{exp}/N_{SK}^{exp}$ for e.g. $\sin^2 2\theta_{13} = 0.1$ is as follows: 1.4% from the fiducial volume definition, 0.6% from the energy scale and 0.2% from the delayed electron signal tagging efficiency. The π^0 rejection efficiency, studied with a NC π^0 topological control sample combining one data electron and one simulated gamma event, contributes 0.9%. The uncertainty on the acceptance of one-ring e -like events was studied with an atmospheric neutrino sample, adding a contribution of 5% from ring counting and 4.9% from particle identification uncertainties. The performance of muon rejection by the ring particle identification algorithm was investigated using cosmic-ray muons and atmospheric neutrino events, giving 0.3%. The effect from uncertainties in the M_{inv} cut is 6.0%. Combining the above uncertainties, the total far detector systematic error contribution to $\delta N_{SK}^{exp}/N_{SK}^{exp}$ is 14.7%(9.4%) for $\sin^2 2\theta_{13} = 0(0.1)$.

Our oscillation result is based entirely on comparing the number of ν_e candidate events with predictions, varying $\sin^2 2\theta_{13}$ for each δ_{CP} value. Including systematic uncertainties, the expectation is $1.5 \pm 0.3 (5.5 \pm 1.0)$ events for $\sin^2 2\theta_{13} = 0(0.1)$. At each oscillation parameter point, a probability distribution for the expected number of events is constructed, incorporating systematic errors [37], which is used to make the confidence interval (Fig. 6), following the unified ordering prescription of Feldman and Cousins [38].

In conclusion, the observation of six single ring e -like events exceeds the expectation of

TABLE III. Contributions from various sources and the total relative uncertainty for $\sin^2 2\theta_{13}=0$ and 0.1, and $\delta_{\text{CP}} = 0$.

| Source | $\sin^2 2\theta_{13} = 0$ | $\sin^2 2\theta_{13} = 0.1$ |
|--|---------------------------|-----------------------------|
| (1) neutrino flux | $\pm 8.5\%$ | $\pm 8.5\%$ |
| (2) near detector | $+5.6\%$ -5.2% | $+5.6\%$ -5.2% |
| (3) near det. statistics | $\pm 2.7\%$ | $\pm 2.7\%$ |
| (4) cross section | $\pm 14.0\%$ | $\pm 10.5\%$ |
| (5) far detector | $\pm 14.7\%$ | $\pm 9.4\%$ |
| Total $\delta N_{SK}^{exp}/N_{SK}^{exp}$ | $+22.8\%$ -22.7% | $+17.6\%$ -17.5% |

a three-flavor neutrino oscillation scenario with $\sin^2 2\theta_{13} = 0$. Under this hypothesis, the probability to observe six or more candidate events is 7×10^{-3} . Thus, we conclude that our data indicate ν_e appearance from a ν_μ neutrino beam. This result converted into a confidence interval yields $0.03(0.04) < \sin^2 2\theta_{13} < 0.28(0.34)$ at 90% C.L. for $\sin^2 2\theta_{23} = 1.0$, $|\Delta m_{23}^2| = 2.4 \times 10^{-3} \text{ eV}^2$, $\delta_{\text{CP}} = 0$ and for normal (inverted) neutrino mass hierarchy. Under the same assumptions, the best fit points are 0.11(0.14), respectively. For non-maximal $\sin^2 2\theta_{23}$, the confidence intervals remain unchanged to first order by replacing $\sin^2 2\theta_{13}$ by $2 \sin^2 \theta_{23} \sin^2 2\theta_{13}$. More data are required to firmly establish ν_e appearance and to better determine the angle θ_{13} .

We thank the J-PARC accelerator team for the superb accelerator performance and CERN NA61 colleagues for providing essential particle production data and for their excellent collaboration. We acknowledge the support of MEXT, Japan; NSERC, NRC and CFI, Canada; CEA and CNRS/IN2P3, France; DFG, Germany; INFN, Italy; Ministry of Science and Higher Education, Poland; RAS, RFBR and the Ministry of Education and Science of the Russian Federation; MEST and NRF, South Korea; MICINN and CPAN, Spain; SNSF and SER, Switzerland; STFC, U.K.; and DOE, U.S.A. We also thank CERN for their donation of the UA1/NOMAD magnet and DESY for the HERA-B magnet mover system. In addition, participation of individual researchers and institutions in T2K has been further supported by funds from: ERC (FP7), EU; JSPS, Japan; Royal Society, UK; DOE-OJI and DOE-Early Career program, and the A. P. Sloan Foundation, U.S.A.

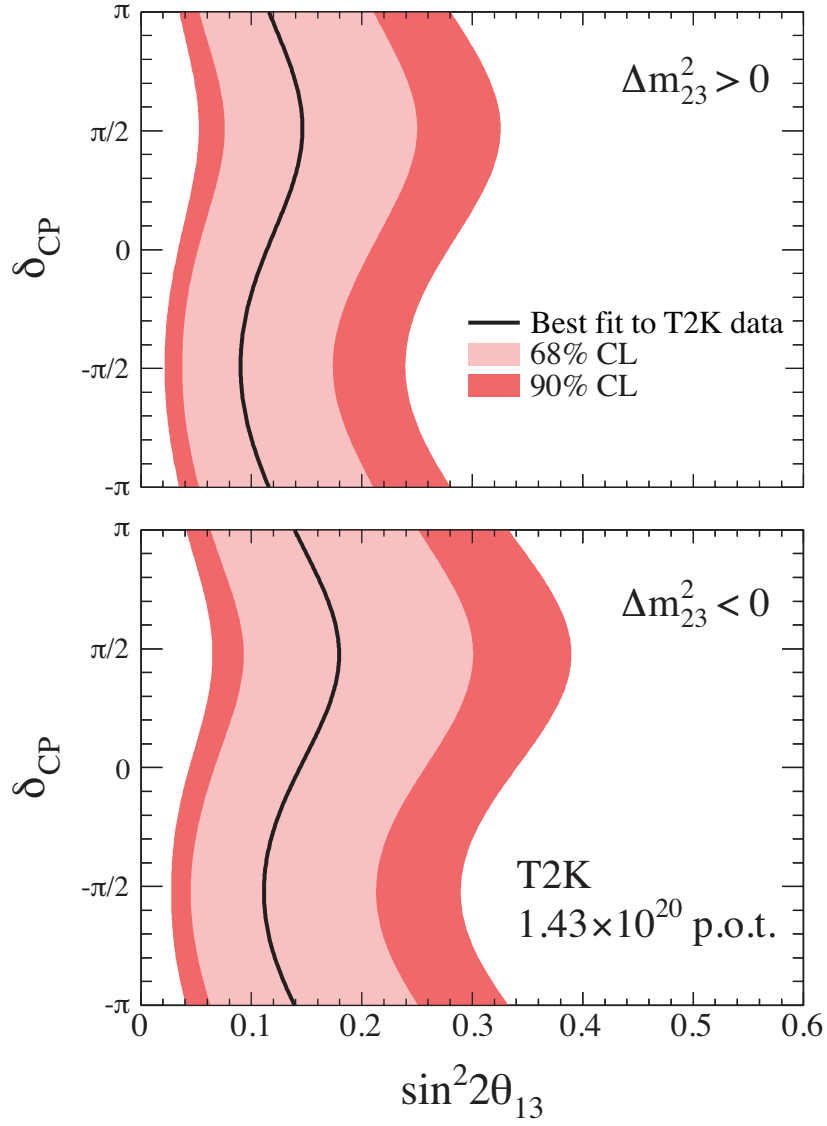


FIG. 6. The 68% and 90% C.L. regions for $\sin^2 2\theta_{13}$ for each value of δ_{CP} , consistent with the observed number of events in the three-flavor oscillation case for normal (top) and inverted (bottom) mass hierarchy. The other oscillation parameters are fixed (see text). The best fit values are shown with solid lines.

3.3 LBNO-DEMO : Large-scale neutrino detector demonstrators for phased performance assessment in view of a long-baseline oscillation experiment, [54]

3.3.1 Design concept of the $6 \times 6 \times 6\text{m}^3$ prototype

The $6 \times 6 \times 6\text{m}^3$ prototype is illustrated in 3.2. Following the GLACIER concept, the LAr detector has the shape of a vertically standing volume, where electrons are drifted vertically towards the liquid-vapor interface, extracted from the liquid into the gas phase, amplified and collected at a segmented anode.

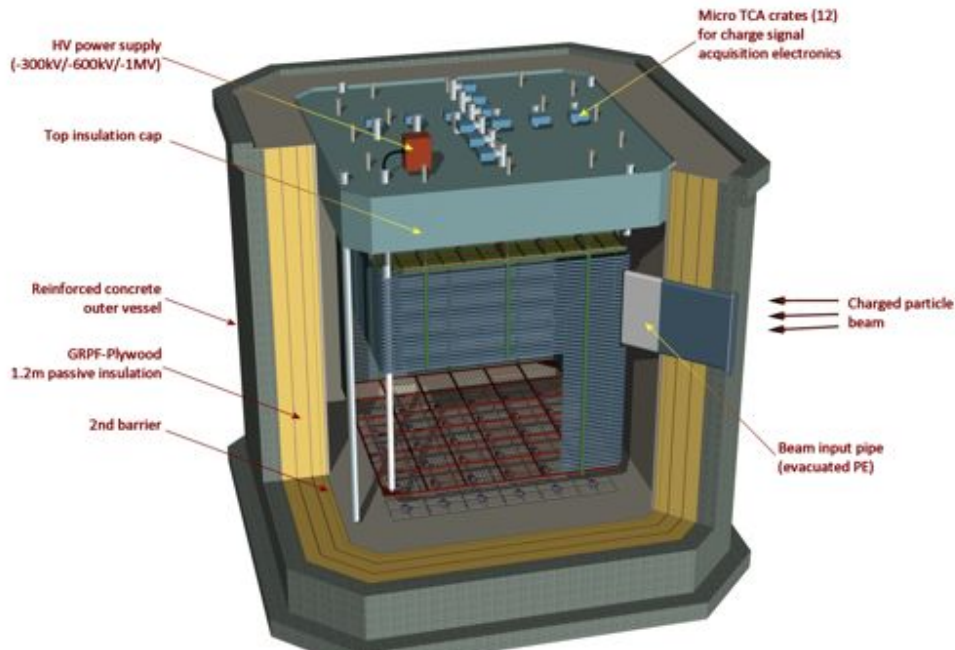


FIGURE 3.2 – Illustration of the $6 \times 6 \times 6\text{m}^3$ with the inner detector inside the cryostat.

The main parameters are summarised in Table 3.1.

| | | |
|--|------------------|-----------------------------|
| Liquid argon density | T/m ³ | 1.38 |
| Liquid argon volume height | m | 7.6 |
| Active liquid argon height | m | 5.99 |
| Hydrostatic pressure at the bottom | bar | 1.03 |
| Inner vessel size (WxLxH) | m ³ | $8.3 \times 8.3 \times 8.1$ |
| Inner vessel base surface | m ² | 67.6 |
| Total liquid argon volume | m ³ | 509.6 |
| Total liquid argon mass | t | 705 |
| Active LAr area | m ² | 36 |
| Charge readout module (0.5 x0.5 m ²) | | 36 |
| N of signal feedthrough | | 12 |
| N of readout channels | | 7680 |
| N of PMT | | 36 |

TABLE 3.1 – Main parameters of the LBNO prototype.

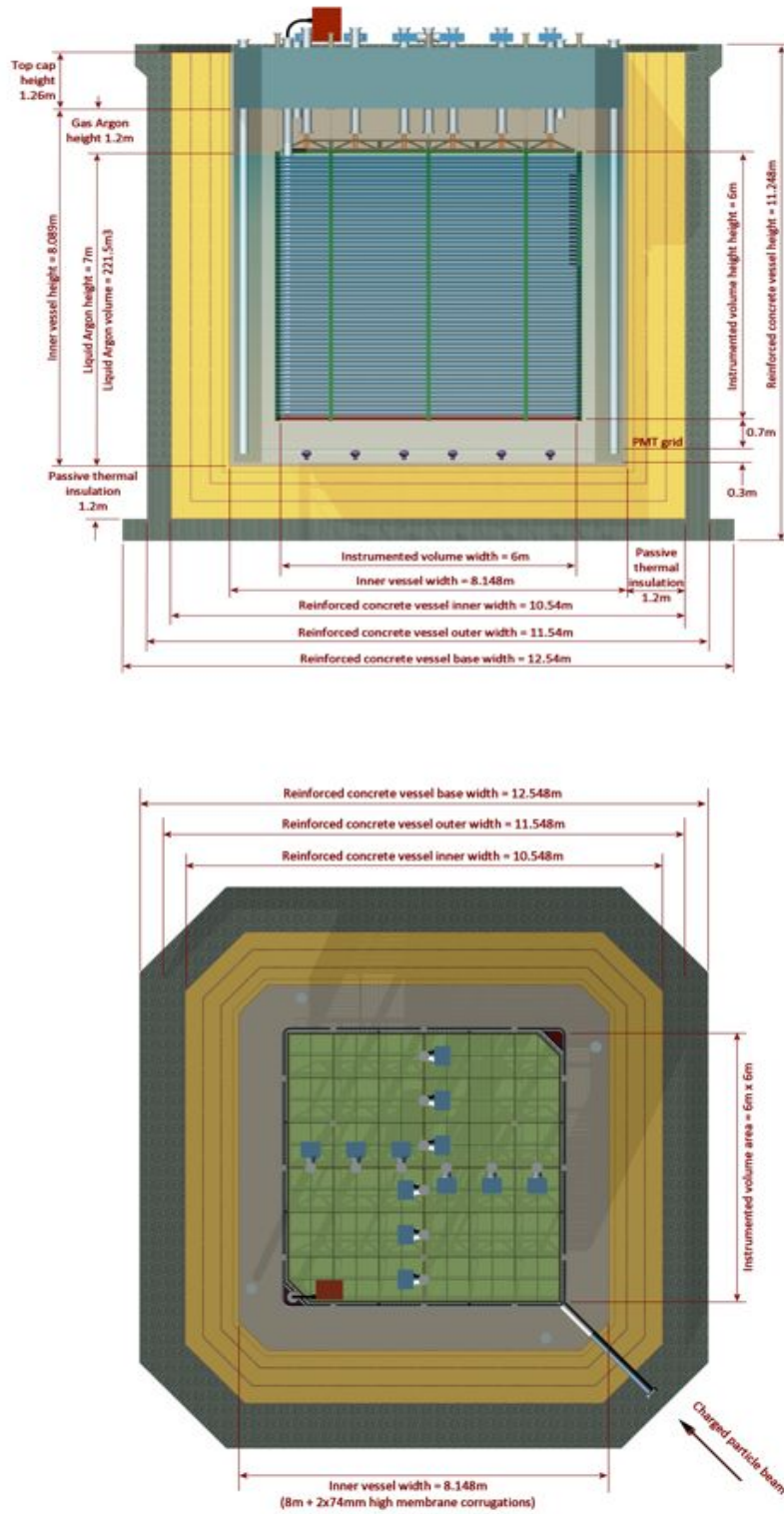


FIGURE 3.3 – Top : plan view section of the 6 × 6 × 6 m³. Bottom : vertical cross section of the 6 × 6 × 6 m³.

The uniform drift field is created by a field cage composed of several equally-spaced stainless-steel tubes, held in place by insulating mechanical structures which are hanged from the top cap of the vessel. The anode deck is also suspended with stainless-steel ropes linked to the top roof. The bottom field is closed by a transparent cathode and the top field by an anode, which also serves as the charge readout. The light readout consists of PMTs uniformly distributed below the cathode.

The detector is configured as a $6 \times 6 \times 6 \text{ m}^3$ liquid argon TPC with liquid-to-gas ionisation electron extraction and multiplication before collection. The ionisation charge is collected in a 2-dimensional readout plane on the top of the volume with an area of $6 \times 6 \text{ m}^2$ and finely segmented with a 3 mm strip pitch. The full active volume of $\sim 216 \text{ m}^3$ is under an uniform electric field $E \simeq 0.5 - 1.0 \text{ kV/cm}$ generated from a bottom cathode plane (also $6 \times 6 \text{ m}^2$) operated at $\simeq 300\text{--}600 \text{ kV}$ and kept uniform by a stack of field shaping electrodes (round pipes along a square path, with rounded corners) polarised at linearly decreasing voltage from the cathode voltage to ground.

The cathode plane is gridded and transparent to light to allow the detection of the scintillation light by an array of photomultipliers located at a distance of $\sim 1\text{m}$ under it. Ionization charge signals are sent to a set of signal feedthroughs (12), located on the top face of the hosting LAr vessel and hosting the cold readout electronics. Other chimneys/feedthroughs are foreseen for HV (1 or 2), top readout plane suspension and level regulation (3), PMT high voltage and signal readout (4), monitoring instrumentation (level, temperature, 1 or 2). The front-end electronics is based on analog preamplifiers implemented in CMOS ASIC circuits for high integration and large scale affordable production. The baseline design is to integrate this electronics on the feed-through flange terminating the chimneys on the roof of the tank, under the insulation layer in order to be cooled to a temperature near that of liquid argon. Cathode and field shaping electrodes are kept in their position by a set of insulating supports/spacers resting on the inner vessel floor. The inner vessel has a cubic shape with chamfered vertical edges. Its walls are built with the so-called corrugate membrane technique, to compensate thermal shrinkage. A manhole and a detail-introduction hole are located in its top face. Thermal insulation is passive, based on GRPF (glass reinforced polyurethane foam) layers, interspersed with pressure distributing layers of plywood. Its thickness and composition are such to reach a residual heat input of 5 W/m^2 . The estimated total heat input including also the losses through the feed-throughs, cables, etc., and introduced by the LAr process, is $\sim 4 \text{ kW}$ at liquid argon temperature, to be dissipated by cryocooler(s). The passive insulation is contained in a reinforced concrete “vessel” with $\simeq 0.5 \text{ m}$ thick walls. The top outer ceiling is made by a framework reinforced stainless steel plane, able to support the inner anode and outer instrumentation (electronics, cryogenics, control).

A charged beam pipe (evacuated) is indicated as crossing the concrete outer vessel and the thermal insulation layers. Its vertical orientation is adapted to the charged beam vertical axis in its last section.

3.3.2 Front-end and DAQ readout

Requirements for the large scale front-end electronics

One of the goals of the WA105 demonstrator is to establish the large scale readout systems being developed for the far site LBNO LAr detectors in a configuration as close as possible to their foreseen final architecture. The large scale deployment of the readout systems in the demonstrator will allow testing their performance with high statistics samples of hadronic interaction showers, their stability and reliability over long time periods and on large data volumes, develop lossless noise-tolerant zero-suppression schemes on real data, as well as optimizing the full integration in the detector. The large number of charge readout channels, needed for the 20-50 kton LAr detector sizes for LBNO with channel count in the range of 500'000 to 1'000'000, naturally called during the last years for R&D efforts in view of the development of large scale readout solutions. These are characterized by high-integration levels, significant cost reduction and aims to performance

improvement. The R&D activities focused on two main axes :

- the developments of cold front-end ASIC electronics ;
- the optimization of the data acquisition system based on modern telecommunication technologies.

Both efforts aim to improving the effectiveness and the integration level of the complete readout chain and to cost reductions for the large number of channels to be implemented in the detector. Shortening of cables needed to bring the analog signals outside the cryostat and reduction of the electronic noise can be achieved using analog amplifiers operating at cryogenic temperatures. The current R&D on the front-end electronics is based on analog preamplifiers implemented in CMOS ASIC circuits for high integration and large scale affordable production. The noise is reduced by exploiting its behaviour as a function of temperature, which has a minimum around 100 K, and thanks to the suppression of the cables used to bring signals outside the cryostat, which otherwise increase the capacitance at the input of the preamplifier. In our present baseline the ASIC analog amplifiers can be integrated on the feed-through flange terminating the chimneys on the roof of the tank, under the insulation layer, in order to be cooled to a temperature near that of liquid argon (see ??). This solution fully preserves all the benefits of the cold electronics, as described above, while guaranteeing at the same time accessibility to the amplifiers without affecting the inner volume containing ultra-pure LAr.

For what concerns the DAQ, solutions based on Ethernet capable “smart sensors” were developed. The “smart sensors” are Ethernet capable front-end DAQ/processing units acquiring large groups of channels. They are integrated with a time distribution system needed to align the data taken by different units operating independently. Data are output on a Ethernet network and collected with a system of switches to a computing farm which builds the events on the bases of the time stamps associated to the data packets by the different sensors. This concept was further developed for the LAr readout, since the time of its first implementation in the OPERA experiment, with the following technical improvements :

1. porting it to the Gigabit Ethernet standard ;
2. adopting FPGA based virtual processors, in order to achieve cheaper implementation costs and become independent on the market of Ethernet capable front-end processors ;
3. integrating the electronics in the micro-TCA form factor, becoming very popular in the world of commercial telecommunication applications ;
4. developing a special time distribution system, derived from the Precise Time Protocol standard, integrated in a synchronous Ethernet network. This time distribution scheme achieves a synchronization accuracy among different nodes at better than 1 ns.

This DAQ scheme allows benefiting of the large-scale integrations developments of the telecommunication industry and decoupling from the market lifetime of commercial processors since it relies on a completely virtual implementation of the processors in the FPGA. A complete setup built out of this R&D was developed in 2010 for 128 channels (See 3.4). The proposed DAQ version for the LBNO prototype detector is an evolution of that system, further increasing the channels density and reducing the costs.

Back-end electronics and DAQ global architecture

The DAQ system uses micro-TCA standards which offers a very compact and easily scalable architecture to manage a large number of channels at low cost. Those constraints are indeed very close to the one existing in the network telecommunication industry. This has been driving the very first developments based on this type of standards in constant technological evolution and applied to large scale neutrino experiments. A generic scheme of the DAQ architecture is displayed in 3.5.



FIGURE 3.4 – Picture of a micro-TCA crate containing DAQ boards with 32 ADC channels/board as developed in 2010.

The main component of this DAQ system is an Advanced Mezzanine Board (AMC) reading out the input signals from the front-end electronics and sending the formatted data through a micro-TCA backplane using a Gigabit or a 10 Gigabit Ethernet link. In the following, details are given on the design of this AMC and the possible alternatives existing to the Ethernet link on the backplane (e.g. PCI express). The connections from the front-end use the Very High Density cable interconnect (VHDCI) standard to minimize the number of cables.

A micro-TCA crate (or shelf) interconnects a fixed number of AMC cards through the backplane to collect the data and send them through a standard 10 Gbe MicroTCA Carrier Hub (MCH) and to distribute a common clock signal issued from a single, stable, GPS-locked Master Clock (MC).

The clock is made available on the backplane through a dedicated AMC (one per crate) which receives it from an external connection, together with the trigger signals (internal trigger from the PMT array and external beam trigger). Those triggers are split and distributed through conventional systems.

A network hierarchical structure is implemented where all crates are interconnected to a dedicated Bittware FPGA processing board (S5-PCIe-HQ, Figure 3.6). This board has two QSFP+ cages to bring the data direct to the FPGA for lowest possible latency. Up-to 8x10Gbe links w/o data loss are available per board. The board performs further data processing, filtering and transmission to the highest level for storage. This type of board is widely used in the massive processing systems and the present generation, based on the Altera Stratix V, will evolve to the Aria X and the Stratix X. This version will be probably available at the time of the construction of the DAQ system.

Programming of the processing board is achievable through the OpenCL software suite where a kernel code allows, on top of a host code, to program directly the FPGA without a classical VHDL synthesis chain. OpenCL is a high level language for massive parallel processing transparent to its hardware implementation (CPUs, GPUs, FPGAs). Under OpenCL FPGAs provide large computing power for data processing at low power consumption. This highly flexible feature is fully adapted to the requirements of the large DAQ systems where conditions of filtering, event building etc... may evolve with time.

The storage is defined as the highest level of the DAQ chain and implies the use of a redundant 2-servers cluster linked to a RAID-5 disks array system.

MicroTCA standard and crates

MicroTCA offers the possibility to interconnect distributed applications while offering a standard, compact and robust form factor with simplified power supply management, cooling and in-

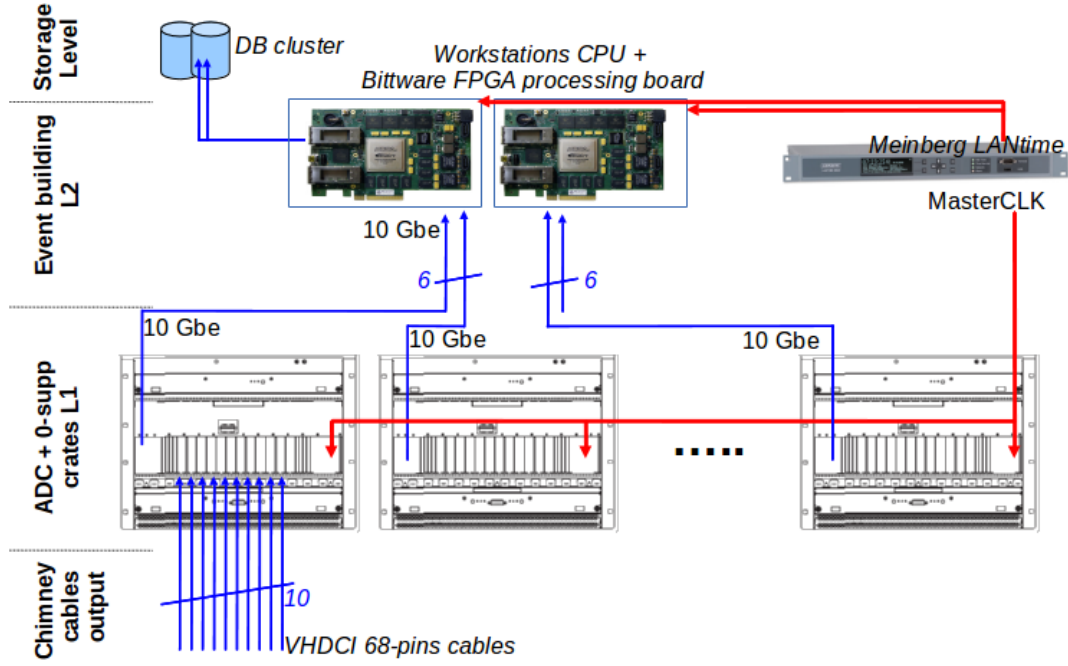


FIGURE 3.5 – Global DAQ scheme. At the bottom the DAQ receives the cables from the F/E electronics. 10 VHDCI cables are connected on each rack. One crate is foreseen per chimney, leading to 12 racks in total for the 1st level (L1). Each crate is connected through a 10Gbe uplink to the next level (L2). The L2 directly connects the racks to the event builder workstation via a 10Gbe network link on a Bittware FPGA processing board. This board may connect up to 8-10Gbe links or 2-40Gbe links. A lossless transmission scheme is therefore foreseen down to the processing board which performs the zero suppression and the event building. A stable common clock is distributed to L1 and L2, as well as the trigger signals (from PMT and beam). The master clock generator may be derived from a Meinberg LANtime generator.

ternal clocks distribution. The microTCA backplane is based on high speed serial links arranged in various possible topologies. Lanes on a microTCA backplane support a large variety of protocols like for example Ethernet 1G or 10G, PCI Express or SRIO.

The boards plugged into a microTCA shelf are called Advanced Mezzanine Card (AMC). Each AMC board is connected to one or two MicroTCA Carrier Hub (MCH) through the backplane serial links which provides a central switch function allowing each AMC to communicate with each other or towards external systems through an uplink access. The backplane also provides the connectivity for the clock distribution allowing the AMC board synchronisation. 3.7 provides a sketch of the backplane technology and its implementation in one retained shelf reference.

The first developments performed for the LAr TPC readout with the microTCA systems were based on the microTCA.1 standard with connections to the user input signals from the front side only. In the baseline option we stay as close as possible to this standard although additional standards have emerged like the microTCA.4 offering the possibility to enter in a crate both from front and rear sides.

In the microTCA.1 baseline option, one has 1 crate per output chimney, handling 640 channels dispatched over 10 AMC. A candidate crate is the 11850-015 8U shelf from Schroff (3.8). We are also considering other references from various providers (like the NATIVE-R9 from NAT) in the spirit of evolving to the microTCA.4 standard. In this case each crate will be located between 2 nearby chimneys. As shown in ??, the crates are implemented on the top layer of the prototype detector. Each brown box features a crate. The inter-chimney distance, of the order of 1 meter, allows this type of crate disposal which minimizes the constraints on cables lengths.



FIGURE 3.6 – FPGA processing board based on Stratix V from Altera. The board features a dual QFP+ cages for 40GigE or 10GigE links, 16 GBytes DDR3 SDRAM, 72 MBytes QDRII/II+, two SATA connectors and is programmable via OpenCL.

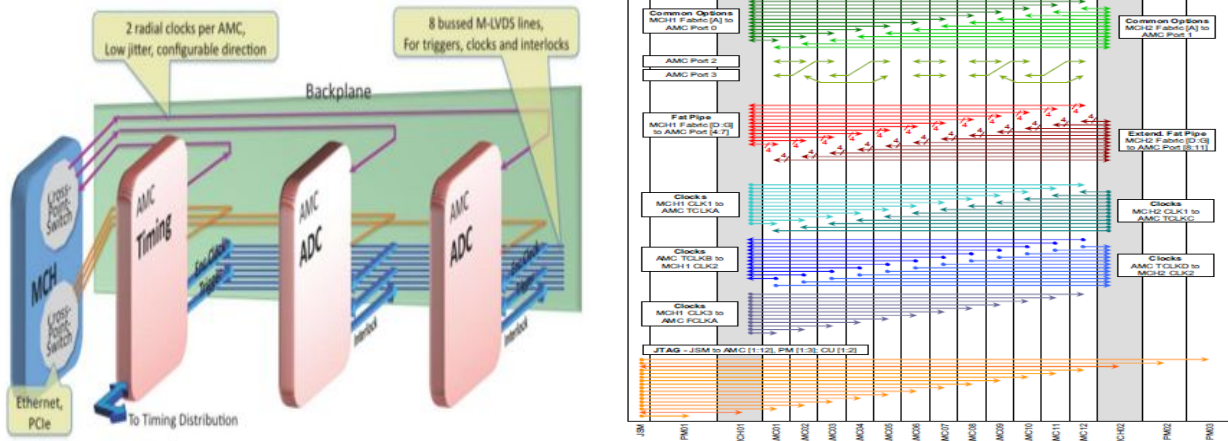


FIGURE 3.7 – Left : global microTCA crate organization. AMC cards (providing basic ADC functions) are connected to the crate controller or MCH which uplinks the external systems. A dedicated AMC for the clock receives dedicated signals (masterclock, trigger signals) from the timing distribution system and transcript them onto the backplane. Right : backplane technology of the Schroff 11850-015 reference.

The main features of the 11850-015 Schroff crate references are listed below :

- 8 U microTCA Shelf, 12+2+3+1 slot for AMC double Mid-size modules,
- 19" rack mountable,
- 12 AMC Double Mid-size slots,
- 2 redundant MicroTCA Carrier Hub (MCH) slots (Double Full-size),
- 2 Power Module (PM) slots (6 HP Double) at the right side,
- 1 Power Module (PM) slots (12 (9) HP Double) at the left side,
- 1 slot for a JTAG module (Double compact),
- 5 splitting kits to install single module in a double slot.

Various MCH references may be used in that design. We selected the NAT MCH with additional hardware for optical fibres connections (NAT-MCH-Base12-GbE, NAT-MCH-XAUIx48, NAT-MCH-UPLNK-SFP+, NAT-MCH-UPLNK-SFP+850). The optical link will go down to the FPGA processing board. This MCH has SRIO (Gen2), PCIe (Gen3), 1GbE and 10GbE (XAUI), central management up to 13 AMCs, 2 cooling units and 4 power modules, e-keying, redundancy and load sharing.



FIGURE 3.8 – Picture of the Schroff 11850-015 8U shelf.

MicroTCA dedicated AMC

AMC board design — The idea is to develop only the user AMC offering the desired functions. The generic functional diagram of the AMC is displayed in 3.9. The AMC chosen is a double-size module (also compatible with microTCA.4 standard) with a single input connector and a 10GbE or PCIe link to the backplane. The input stage performs the 64 channels digitization through 8 8-channels 14-bits ADC readout at a 2.5MHz frequency. The ADC readout sequence is controlled by 2 EP3C40 FPGA from Altera which makes the data available on a double port memory (DPRAM with 9k-samples width from IDT). Two banks (B0/B1) are attached to each channel and work in ping pong mode. The write state machine manages the bank address working as a circular buffer. If no trigger conditions is detected the samples are written continuously into the memory, the oldest ADC being overwritten by the newest ones. The ADC values and the address location in the bank are written into an intermediate FIFO for each bank (B0/B1). If a trigger occurs, the write state machine keeps on storing the event corresponding to the TPC drift. If the second bank is available, the main state machine tells the write state machine to continue to store the samples into this new active bank. The read state machine sets a flag corresponding to the availability of an event in a bank. All the read state machines are interconnected through a token ring like structure. The zero-suppression algorithm is applied on all samples available in the bank, the pedestals (mean and width) being computed on the samples themselves. The recorded samples are then formatted and sent out. These operations are managed by a third FPGA (EP5CE from Altera), which sends the data on the backplane. The baseline option foresees to send the data directly through a 10GbE link (UDP was used in the first prototype). The readout scheme and hardware implementation is very close to the first prototype designed in IPNL (3.9) with slight changes : replacement of the single FPGA by three cost-effective FPGA's and direct implementation of the ADC layer on the motherboard (in the first version ADC's were on a mezzanine board).

ADC readout chain — The analog signals from the F/E ASICs are connected to the AMC front-panel through a 68 pins VHDCI connector. The 8×14 -bits ADC 8 ch. AD9257 ADC from Analog Device, including a serial LVDS output, has been chosen. The translation from single ended to differential signals is performed upstream of the ADC. The readout scheme is displayed on 3.10. This design offers a high integration level required by the large density of input signals.

Data rate requirements

Data reduction — In the present design the useful ADC will be 12-bits resolution and each sample will have 16-bits size. The readout frequency of 2.5 MHz (400ns steps) requires a maximum

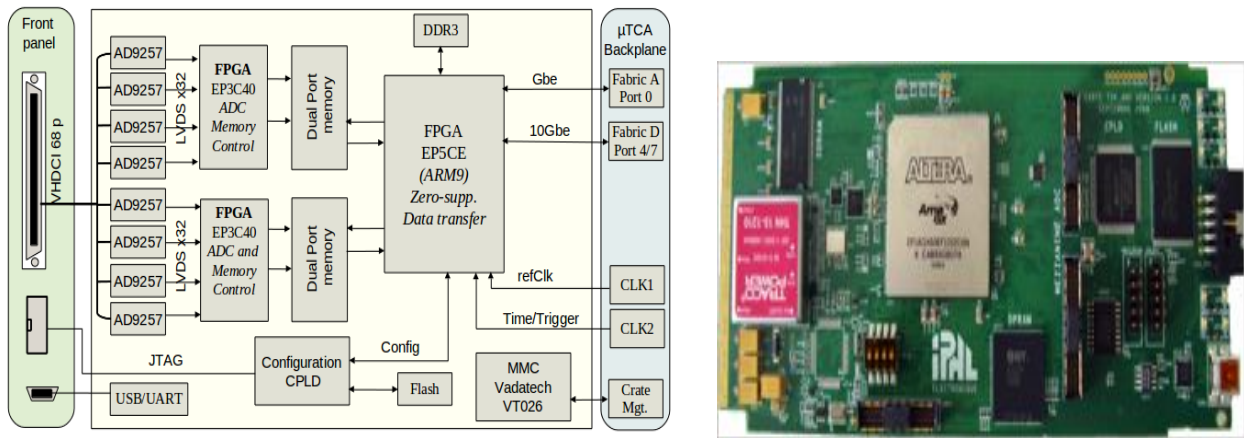


FIGURE 3.9 – Left : AMC bloc diagram scheme. The input stage digitizes the 64 input channels. The ADC readout sequence is controlled via 2 FPGA (one for 32 channels) which handles also the writing into a double bank memory. The management of the trigger input, data output, and link to the backplane if performed by a third FPGA. The link to the backplane may be direct 10GbE or PCI-e. Right : the first AMC version, single height for 32 channels. Present design is an extension of this board.

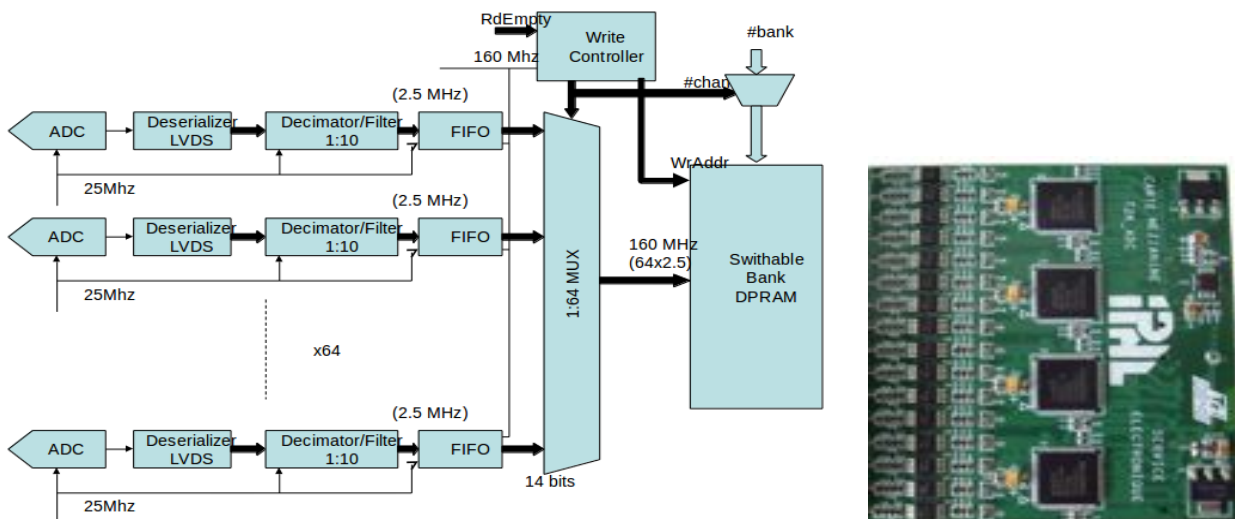


FIGURE 3.10 – Left : ADC readout chain block diagram. The AD amplifier is used to translate the inputs to differential levels. Right : implementation of a 32 channels ADC readout chain in the first prototype version.

of 10k samples for the maximal drift time of 4000 microseconds that we want to cover. Given the 6 microseconds shaping of the F/E electronics for a single hit, one obtains : $6(\mu\text{ s})/400(\text{ns})\sim 15$ useful samples for a single hit over the 10k of a full bank. To be conservative we assume in the following a reduction factor 100 given by the zero suppression algorithm if implemented at the AMC level. In the lossless data transmission scheme we will assume the total 10ksamples.

Data rate constraints — In this context we may compute the saturation limits for one crate and for the full detector. One crate is used to readout a full chimney, that is 640 channels (10 AMC). In the case the zero-suppression is not applied, the maximal affordable data rate to saturate the 10GbE uplink of the crate is therefore : $10(\text{GbE})/(16(\text{bits})\times 640(\text{ch.})\times 10\text{k}(\text{samples}))\simeq 100\text{Hz}$. Since the crates are readout in parallel by the FPGA processing boards, this rate corresponds to the maximal rate for the full detector. This mode is adapted to a beam-only data readout. In the case the zero suppression is applied we may reach a maximal rate of 10kHz, compatible with the surface cosmic rays rate ($\simeq 6\text{kHz}$). In this mode we may readout beam data and cosmoics between the beam cycles.

Bibliographie

- [1] An appearance experiment to search for $\nu_\mu \longrightarrow \nu_\tau$ oscillations in the CNGS beam : experimental proposal, M.Guler et al (OPERA collaboration), CERN-SPSC-2000-028 ; SPSC-P-318 ; LNGS-P-25-2000, LYCEN 2000-165.
- [2] Status report on the OPERA experiment, M.Guler et al, OPERA Collaboration, Aug 2001, CERN-SPSC-2001-025, CERN-SPSC-M-668, LNGS-EXP-30-2001-ADD-1.
- [3] Large liquid-scintillator trackers for neutrino experiments, L. Benussi, N. Bruski, N. D'Ambrosio, Y. Declais, J. Dupraz, J.P. Fabre, V. Fanti, E. Forton, D. Frekers, A. Frenkel et al. NIM A488 (2002) 503-516.
- [4] Request for a Test Exposure of OPERA Targets in the NuMI Beam, K. Kodama et al, FERMILAB-PROPOSAL-0952.
- [5] Electron/pion separation with an Emulsion Cloud Chamber by using a Neural Network, L.Arrabito et al, JINST 2 (2007) P02001.
- [6] First events from CNGS beam detected with the OPERA detector, R.Acquafredda et al (OPERA collaboration), New J.Physics (2006) 8, 303.
- [7] The detection of neutrino interactions in the emulsion/lead target of the OPERA experiment, N. Agafonova et al (OPERA collaboration), JINST 4 (2009) PP06020.
- [8] The OPERA experiment in the CERN to Gran Sasso neutrino beam, R. Acquafredda et al (OPERA collaboration), JINST 4 (2009) P04018.
- [9] Study of the effects induced by lead on the emulsion films of the OPERA experiment, A. Anokhina et al (OPERA collaboration), JINST 3 (2008) P07002.
- [10] Emulsion sheet doublets as interface trackers for the OPERA experiment, A. Anokhina et al (OPERA collaboration), JINST 3 (2008) P07005.
- [11] The OPERA global readout and GPS distribution system, J. Marteau for the OPERA collaboration, Nucl.Instrum.Meth. A617 (2010) 291-293.
- [12] OPERA first events from the CNGS neutrino beam, J.Marteau (for the OPERA collaboration), Proceedings of the XLIInd Rencontres de Moriond session Electroweak Interactions and Unified Theories, La Thuile, 10-17 March 2007 [arXiv :0706.1699].
- [13] The OPERA experiment : a direct search of the $\nu_\mu \longrightarrow \nu_\tau$ oscillations, J.Marteau (for the OPERA collaboration) 11th ICATPP Conference on Astroparticle, Particle, Space Physics, Detectors and Medical Physics Applications, Como 5-9 Oct. 2009 [arXiv :0910.3468].
- [14] Cosmic ray physics with the OPERA Detector, T.Brugière (for the OPERA collaboration) 11th ICATPP Conference on Astroparticle, Particle, Space Physics, Detectors and Medical Physics Applications, Como 5-9 Oct. 2009.
- [15] Oscillations des neutrinos sur et hors faisceau : étude des performances du système d'acquisition d'OPERA, T. Brugière, LYCEN-T-2011-23.
- [16] Nuclear emulsions in the OPERA experiment, OPERA collaboration, Radiat.Meas.44 :840-845,2009.

-
- [17] Measurement of the atmospheric muon charge ratio with the OPERA detector, OPERA collaboration, Eur. Phys. J. C **67** (2010) 25.
 - [18] Observation of a first ν_τ candidate in the OPERA experiment in the CNGS beam, OPERA collaboration, Phys.Lett.B691 :138-145,2010.
 - [19] Study of neutrino interactions with the electronic detectors of the OPERA experiment, OPERA collaboration, New J.Phys.13 :053051,2011.
 - [20] Momentum measurement by the Multiple Coulomb Scattering method in the OPERA lead emulsion target, OPERA collaboration, New J. Phys. 14 013026 doi :10.1088/1367-2630/14/1/013026.
 - [21] Search for $\nu_\mu \rightarrow \nu_\tau$ oscillation with the OPERA experiment in the CNGS beam, OPERA collaboration, New J. Phys. **14** (2012) 033017 [arXiv :1107.2594].
 - [22] Measurement of the neutrino velocity with the OPERA detector in the CNGS beam, OPERA collaboration, JHEP **1210** (2012) 093 [arXiv :1109.4897].
 - [23] Measurement of the neutrino velocity with the OPERA detector in the CNGS beam using 2012 dedicated data, OPERA collaboration, JHEP **1301** (2013) 153 [arXiv :1212.1276].
 - [24] Search for $\nu_\mu \rightarrow \nu_e$ oscillation with the OPERA experiment in the CNGS beam, OPERA collaboration, JHEP **1307** (2013) 004 [Addendum-ibid. **1307** (2013) 085] [arXiv :1303.3953].
 - [25] New results on for $\nu_\mu \rightarrow \nu_\tau$ appearance with the OPERA experiment in the CNGS beam, OPERA collaboration, JHEP **1311** (2013) 036 [Erratum-ibid. **1404** (2014) 014] [arXiv :1308.2553].
 - [26] Evidence for $\nu_\mu \rightarrow \nu_\tau$ appearance in the CNGS neutrino beam with the OPERA experiment, OPERA collaboration, Phys. Rev. D **89** (2014) 5, 051102 [arXiv : 1401.2079].
 - [27] Installation de capteurs intelligents pour l'acquisition à haut débit de données via le réseau Ethernet, brevet n°04 00468 (délivrance n°06/16 du 21.04.06). Licence cédée à un partenaire industriel (11.08) : Société LEAS, ZA la Bâtie, 38330 SAINT ISMIER
 - [28] A detector to monitor the neutrino beam asymmetry at the T2K 280m hall, The 2KM LR monitor subgroup, Experimental proposal submitted to T2K collaboration, 09/2008 ; experimental project KEK-P35.
 - [29] MicroTCA implementation of synchronous Ethernet-Based DAQ systems for large scale experiments, C.Girerd, D.Autiero, B.Carlus, S.Gardien, J.Marteau, W.Tromeur, talk presented at the 2009 Real Time Conference, Beijing, May '09, IEEE proceedings of the conference.
 - [30] The T2K Experiment, K. Abe *et al.*, T2K collaboration, Nucl. Instrum. Meth. A **659** (2011) 106 [arXiv :1106.1238].
 - [31] Indication of Electron Neutrino Appearance from an Accelerator-produced Off-axis Muon Neutrino Beam, K. Abe *et al.*, T2K collaboration, Phys. Rev. Lett. **107** (2011) 041801 [arXiv :1106.2822].
 - [32] Measurements of the T2K neutrino beam properties using the INGRID on-axis near detector, K. Abe *et al.*, T2K collaboration, Nucl. Instrum. Meth. A **694** (2012) 211 [arXiv :1111.3119].
 - [33] First Muon-Neutrino Disappearance Study with an Off-Axis Beam, K. Abe *et al.*, T2K collaboration, Phys. Rev. D **85** (2012) 031103 [arXiv :1201.1386].
 - [34] The T2K neutrino flux prediction, K. Abe *et al.*, T2K collaboration, Phys. Rev. D **87** (2013) 1, 012001 [Addendum-ibid. D **87** (2013) 1, 019902] [arXiv :1211.0469].
 - [35] Measurement of the inclusive ν_μ NuMu charged current cross section on carbon in the near detector of the T2K experiment, K. Abe *et al.*, T2K collaboration, Phys. Rev. D **87** (2013) 9, 092003 [arXiv :1302.4908].

-
- [36] Evidence of electron neutrino appearance in a muon neutrino beam, K. Abe *et al.*, T2K collaboration, Phys. Rev. D **88** (2013) 3, 032002 [arXiv :1304.0841].
 - [37] Measurement of neutrino oscillation parameters from muon neutrino disappearance with an off-axis beam, K. Abe *et al.*, T2K collaboration, Phys. Rev. Lett. **111** (2013) 21, 211803 [arXiv :1308.0465].
 - [38] Observation of electron neutrino appearance in a muon neutrino beam, K. Abe *et al.*, T2K collaboration, Phys. Rev. Lett. **112** (2014) 061802 [arXiv :1311.4750].
 - [39] Recent Results from the T2K Experiment, K. Abe *et al.*, Nucl. Phys. Proc. Suppl. **246-247** (2014) 23.
 - [40] Precise measurement of the neutrino mixing parameter θ_{23} from muon neutrino disappearance in an off-axis beam, K. Abe *et al.*, T2K collaboration, Phys. Rev. Lett. **112** (2014) 18, 181801 [arXiv :1403.1532].
 - [41] Measurement of the intrinsic electron neutrino component in the T2K neutrino beam with the ND280 detector, K. Abe *et al.*, T2K collaboration, Phys. Rev. D **89** (2014) 9, 092003 [Addendum-ibid. D **89** (2014) 9, 099902] [Erratum-ibid. D **89** (2014) 9, 099902 [arXiv :1403.2552].
 - [42] Measurement of the neutrino-oxygen neutral-current interaction cross section by observing nuclear de-excitation γ -rays, K. Abe *et al.*, T2K collaboration, Phys. Rev. D **90** (2014) 7, 072012 [arXiv :1403.3140].
 - [43] Measurement of the inclusive ν_μ charged current cross section on iron and hydrocarbon in the T2K on-axis neutrino beam, K. Abe *et al.*, T2K Collaboration, Phys. Rev. D **90** (2014) 5, 052010 [arXiv :1407.4256].
 - [44] Measurement of the Inclusive Electron Neutrino Charged Current Cross Section on Carbon with the T2K Near Detector, K. Abe *et al.*, T2K Collaboration, Phys. Rev. Lett. **113** (2014) 24, 241803 [arXiv :1407.7389].
 - [45] Neutrino Oscillation Physics Potential of the T2K Experiment, K. Abe *et al.*, T2K Collaboration [arXiv :1409.7469].
 - [46] Search for short baseline ν_e disappearance with the T2K near detector, K. Abe *et al.*, T2K Collaboration [arXiv :1410.8811].
 - [47] Measurement of the ν_μ CCQE cross section on carbon with the ND280 detector at T2K, K. Abe *et al.*, T2K Collaboration [arXiv :1411.6264].
 - [48] Measurements of neutrino oscillation in appearance and disappearance channels by the T2K experiment with 6.6E20 protons on target, K. Abe *et al.*, T2K Collaboration [arXiv :1502.01550].
 - [49] Large underground, liquid based detectors for astro-particle physics in Europe : scientific case and prospects D.Autiero et al, JCAP **0711** (2007) 011 JCAP 11 [arXiv :0705.0116].
 - [50] The LAGUNA design study- towards giant liquid based underground detectors for neutrino physics and astrophysics and proton decay searches, (the LAGUNA collaboration), contribution to the Workshop "European Strategy for Future Neutrino Physics", CERN, Oct. 2009 [arXiv :1001.0077].
 - [51] The LAGUNA project : Towards the giant liquid based detectors for proton decay searches and for low energy neutrino astrophysics, J. Kisiel *et al.* [LAGUNA Collaboration], PoS EPS **-HEP2009** (2009) 283.
 - [52] Expression of Interest for a very long baseline neutrino oscillation experiment (LBNO), A. Stahl *et al.*, CERN-SPSC-2012-021, SPSC-EOI-007.

- [53] The mass-hierarchy and CP-violation discovery reach of the LBNO long-baseline neutrino experiment, S. K. Agarwalla *et al.*, LAGUNA-LBNO Collaboration, JHEP **1405** (2014) 094 [arXiv :1312.6520].
- [54] LBNO-DEMO : Large-scale neutrino detector demonstrators for phased performance assessment in view of a long-baseline oscillation experiment, L. Agostino *et al.*, The LBNO-DEMO - WA105 - Collaboration, CERN-SPSC-2014-013 ; SPSC-TDR-004 [arXiv :1409.4405].
- [55] Optimised sensitivity to leptonic CP violation from spectral information : the LBNO case at 2300 km baseline, S. K. Agarwalla *et al.*, LAGUNA-LBNO Collaboration [arXiv :1412.0593].
- [56] The LBNO long-baseline oscillation sensitivities with two conventional neutrino beams at different baselines, S. K. Agarwalla *et al.*, LAGUNA-LBNO Collaboration [arXiv :1412.0804].
- [57] Procédé de synchronisation temporelle. Equipements principal et secondaire pour la mise en oeuvre de ce procédé, procédé de fonctionnement de ces équipements principal et secondaire, brevet n° 08 57227 (soumission 1000039837 24.10.08).

Troisième partie

Applications transdisciplinaires

Table des matières

| | | |
|----------|--|------------|
| 1 | Imagerie médicale : un prototype de tomographe à émission de positrons TEP | 147 |
| 1.1 | Introduction | 147 |
| 1.2 | From high energy physics large scale distributed optoelectronics readout to medical imaging applications : prototyping a 2-head readout system for micro-PET | 150 |
| 2 | Tomographie muonique de structures géologiques | 171 |
| 2.1 | Introduction | 171 |
| 2.2 | Geophysical muon imaging : feasibility and limits, [6] | 174 |
| 2.3 | Muons tomography applied to geosciences and volcanology, [7] | 188 |
| 2.4 | Implementation of sub-nanoseconds TDC in FPGA : applications to time-of-flight analysis in muon radiography, [14] | 197 |
| 2.5 | Muon tomography and gravimetry joint inversion, [15] | 215 |
| | Bibliographie Partie III | 235 |
| | Conclusions | 237 |

Chapitre 1

Imagerie médicale : un prototype de tomographe à émission de positrons TEP

1.1 Introduction

Contexte général — Cette activité, menée de 2001 à 2004, se proposait, au sein de la collaboration “ClearPET” (dans le consortium Crystal Clear au CERN), d’étudier la faisabilité d’un tomographe à émission de positrons pour le petit animal (micro-PET) avec une précision spatiale meilleure que le millimètre et des temps de pose courts. Ce développement R&D, appuyé sur l’opto-électronique d’OPERA, a permis la seule et unique étude d’une configuration “phoswich” dans laquelle un cristal de type LuAP et un cristal de LSO sont superposés sur le même canal de détection de manière à améliorer la résolution spatiale. La discrimination des cristaux touchés est effectuée sur la composante rapide de leur temps de décroissance par analyse de forme du signal de manière à minimiser le temps d’exposition du sujet. Le cahier des charges à remplir est détaillé ci-dessous.

Ce projet consiste à concevoir, simuler et réaliser un prototype de TEP en ligne pour l’imagerie de cibles de type fantôme PMMA ou animal, placées sur un faisceau d’ion carbone. La réalisation d’un prototype répondant aux contraintes fortes de grande sensibilité et de bon rapport signal sur bruit nécessite de développer les axes suivants :

- Simulation de la chaîne complète de l’expérience allant des caractéristiques du faisceau de la cible et du détecteur jusqu’à la reconstruction des cartes des émetteurs bêta.
- Instrumentation : réalisation, tests et caractérisation de têtes de détection modulaires, incluant d’une part une R&D sur la chaîne optoélectronique et sur la partie acquisition (DAQ) distribuée sur Ethernet et d’autre part la finalisation du transfert de technologies vers la société d’électronique EFS initiée par un FITT en 2003.
- Reconstruction des images avec les contraintes géométriques particulière du TEP en faisceau.

Simulation — La première étape consiste à estimer l’intensité de signal que l’on est susceptible d’obtenir en fonction des paramètres du faisceau. Cette estimation du signal provenant de la fragmentation d’un faisceau de ^{12}C sur un fantôme de PMMA et/ou d’eau peut être obtenue soit à partir des simulations avec SRIM ou LISE, soit à partir des cartographies de β^+ produites par le code FLUKA. Ces cartographies β^+ seront interfacées avec le framework GATE pour simuler la partie détecteur TEP. La deuxième étape consiste à établir la géométrie du prototype en déterminant le diamètre de l’anneau, la segmentation, la taille et le type des cristaux, afin d’obtenir le meilleur compromis entre sensibilité ($\sim 3\%$), rapport signal sur bruit et résolution spatiale (~ 4 mm). Ces simulations sont réalisées dans le cadre de la collaboration OpenGATE qui développe un framework de simulation TEP et SPECT basé sur le code Géant4 (CERN). Une simulation complète

du module de détection composé de photomultiplicateurs Flat Panel et différents assemblages de cristaux sera réalisée afin de contrôler et de valider par des mesures expérimentales : La résolution énergétique et les effets des interactions Compton dans les cristaux par utilisation de l'information de la distribution de charge sur plusieurs pixels. L'effet des temps morts de l'électronique d'acquisition avec coïncidences entre deux modules. Ces travaux nous permettront de mettre au point une simulation précise et réaliste d'une tête modulaire de détection qui pourra être dupliquée et assemblée dans des configurations répondant aux exigences de l'HadronTEP : les meilleurs sensibilité et rapport signal sur bruit attendus.

Instrumentation — Les matériaux scintillateurs destinés à équiper les TEP seront des cristaux à haut rendement lumineux, rapides et suffisamment denses. Deux configurations seront utilisées. Premièrement, les cristaux de LSO seront découpés de manière classique en parallélépipède de 5 x 5 mm de section avec une profondeur de 20 mm afin d'obtenir une bonne sensibilité et en préservant une résolution spatiale de l'ordre 4 mm. Cette dimension correspond parfaitement au pitch des PMT « flat panel » qui possède un très bon coefficient de remplissage et un couplage « one2one » avec l'électronique. La seconde approche consiste à utiliser des blocs de 5 x 5 cm de section (correspondant à la surface du PMT-FP) avec une profondeur de 20 mm, et de calculer l'origine de la scintillation par une modélisation de type « réseau de neurone ». Cette solution a l'avantage de limiter considérablement le coût des cristaux tout en augmentant la sensibilité et en préservant la résolution spatiale.

L'électronique frontale doit accomplir les tâches suivantes : mesurer l'énergie avec une bonne résolution (15%) avec connaissance de la diaphonie inter pixel et un temps mort le plus faible possible (quelques micro-secondes au maximum) mesurer le temps d'arrivée du signal avec une bonne résolution pour pouvoir rejeter les fortuits avec une logique de coïncidences suffisamment stricte (5 nanosecondes) effectuer le pré-traitement, le formatage et l'envoi des données sur le réseau par un processeur Ethernet. En vue d'une application dédiée à un module de détection en imagerie TEP, nous sommes engagés dans un multi-projet de fabrication d'un chip analogique développé pour l'expérience OPERA qui permettra de réduire le temps mort des prototypes actuels et de corriger l'hétérogénéité des gains nécessaire à l'utilisation des MaPMT ou des PMT-FP en TEP. Une version R&D de cette même puce analogique sera spécialement développée pour la lecture des APD afin d'obtenir une meilleure couverture de détection à un coût plus faible et dans un environnement magnétique. Cette R&D pourra être adaptée aux cartes électroniques déjà en cours de transfert vers la société EFS.

La construction du prototype par l'assemblage de têtes modulaires auparavant validées en laboratoire permettra la réalisation d'expériences pour différentes énergies de faisceau à GANIL et à GSI. Des études sur fantôme (eau et PMMA) et petit animal permettront de valider les simulations en terme de sensibilité essentiellement et de confirmer le bon fonctionnement de cette nouvelle instrumentation dans le faisceau.

Les données brutes issues du système d'acquisition seront intégrées dans un format standard LMF (List Mode Format). Ce format permet de stocker les informations concernant la machine, l'acquisition, les types de données et tous les paramètres nécessaires au traitement. Il permet d'enregistrer les événements simples (singles). Les coïncidences seront triées selon une fenêtre temporelle paramétrable et stockées dans un mode liste "coïncidenc". A partir de ce format, il est nécessaire de prévoir une routine de reformatage des données dans un mode sinogramme 2D et 3D. Différents systèmes de corrections des images sont nécessaires tant pour la correction de l'atténuation (on pourra utiliser l'image de scanner X utilisée pour le traitement planning) que pour les corrections des erreurs induites par les événements diffusés et les fortuits. La reconstruction des images devra faire appel

aux nouvelles méthodes analytiques de type MLEM ou OSEM compte-tenu de l'absence de ligne de réponse (anneau incomplet).

L'article présenté donne les principaux résultats obtenus avec un prototype à deux têtes de lecture (deux PMT's), en mode "phoswich" (unique réalisation dans le cadre de la collaboration Clear-PET) et la reconstruction d'une image ponctuelle.

1.2 From high energy physics large scale distributed optoelectronics readout to medical imaging applications : prototyping a 2-head readout system for micro-PET

Authors

Rémi Barbier, Jacques Marteau, E.Pennachio*

Abstract

This paper describes the experimental set-up designed for micro-PET detectors studies and presents the results. The prototype includes 2 smart detection heads composed with scintillating crystals, pixel photo-detector, auto-triggerable front-end electronics and Ethernet capable DAQ processor totally independent and configurable via Ethernet. The electronic readout system based on the “smart sensor” design is inspired by the OPERA experiment of neutrino oscillations detection currently under installation in the Gran Sasso underground laboratory. The two detection heads have been characterized. Different aspects of the development are presented : pulse shape discrimination (PSD) from two different crystals for depth of interaction (DOI) measurement, energy resolution, light sharing, multi-hit studies from Compton events, flood diagram and sodium 22 point source image reconstruction.

** The research of E.P. has been partially supported by the ETOILE Project.*

This work was done in collaboration with:

P. Bouquet, S. Gardien, C. Girerd, C. Guerin, G. Guillot, S. Vanzetto.

Introduction

Main requirements to a small animal PET system are spatial resolution (1.5 mm^3 expected) and sensitivity. Unfortunately increasing the sensitivity by decreasing the gantry radius implies increasing the parallax error which is drastically enhanced with the crystal size. One solution is to perform Depth of Interaction (DOI) measurement from pulse shape discrimination (PSD) of two crystals with different mean decay constants. The project described here has been developed in the Crystal Clear Collaboration (CCC) which promotes DOI measurement through PSD with the so-called “phoswitch” configuration. The phoswitch mode is obtained in our case with 2 different crystals putted one behind the other in the “pointing geometry”. The purpose of this paper is to present the developments performed in 2002-2003 on a two head micro-PET prototypes. The main components of the prototype are:

- lutetium oxides crystals (LSO and LuAP),
- multi anode PMT HR7546 from Hamamatsu,
- electronic readout chain based on an Ethernet “smart sensor” concept¹.

The main goal of such prototype was the evaluation of the full optoelectronic chain performance: crystals light yields, reflectors and packaging performance in real micro-PET conditions, light sharing effects on the reconstructed energy, Compton events selection for image reconstruction. A point source Na image has been obtained to validate the full optoelectronic chain within the off-line coincidence sorting concept.

Experimental setup

-1/ Crystals

The crystals used for the tests were of LuAP type ($\text{LuAlO}_3:\text{Ce}^{3+}$) and LSO type ($\text{Lu}_2\text{SiO}_5:\text{Ce}^{3+}$), which have equivalent stopping power but different decay times: 40 ns for LSO and 20 ns for LuAP. On top of these fast components the LuAP has a slow component of about 400 ns. The crystals also differ by their light yields (LuAP/LSO ~ 10 -50 % depending on the crystals quality). The light yields discrepancy is the major drawback for such phoswitch solution which suffers from single trigger electronic threshold. Details on the production of the LuAP crystals used for these tests can be found in the literature [1].

-2/ Crystal Matrix

The crystal dimension was $2\text{mm} \times 2\text{mm} \times 10\text{mm}$ to match the multi-anode photo-multiplier pixel size of the Hamamatsu HR7546. The 64 crystals were gathered in an 8×8 “matrix”. The one-to-one mapping between crystals and pixels induces severe constraints on the light collection and on the matrices technologies.

The first arises from the relatively large surface/volume ratio, which implies that a lot of light is emitted through the lateral surfaces. Tests show that this represents roughly half of the emitted light. The second comes from the differences in the emission spectra of the 2 crystals (420nm at the emission peak for the LuAP vs. 480nm for the LSO). The reflective index depending on the wavelength, a good compromise has to be found in the type of material if one wants to have the same matrix material for both crystals, which is actually the third constraint. The last constraint comes from the mechanics of both the MaPMT, which imposes an inter-pixel pitch of 0.3mm and of the crystals, which requires the most possible regular shape.

¹ Patent WO2005081121

The first matrix prototype was done in stainless steel and the inner walls were cut with a 0.1mm diameter wire. This gives the best mechanical results (Fig.1, left picture) but a poor light collection. This prototype was then used to build a mould (Fig.2, left picture) in which matrices were then produced (Fig.1, right picture).

Different materials were tested in these matrices (TiO₂ loaded epoxy, Tyvek and Teflon). The best results for the light collection were obtained with Tyvek and Teflon (+40% and +30% respectively for LSO and +25% for LuAP). Matrices studies has been discussed in the paper [1].



Figure 1: Matrix pictures: stainless steel matrix (left) and Teflon matrix (right) obtained with the epoxy mould displayed in Fig.2 (left).

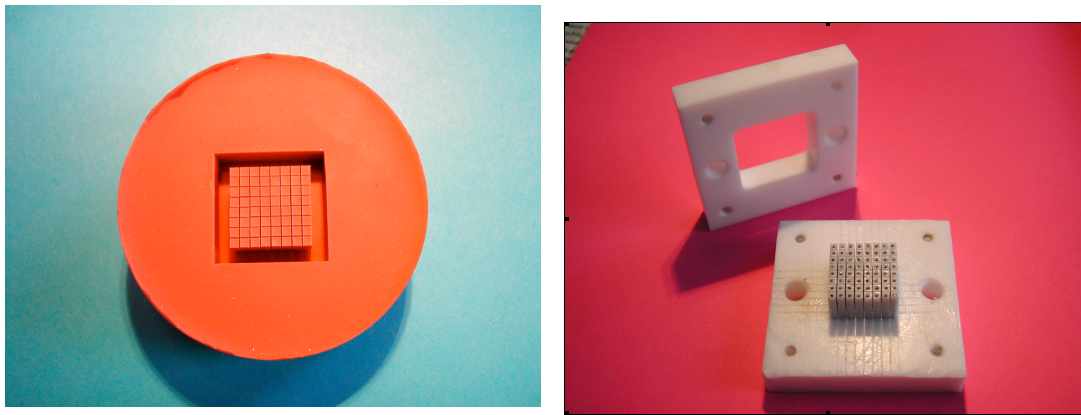


Figure 2: Different mounting system for matrix production: epoxy mould (left) obtained with the stainless steel matrix (Fig. 1) and Teflon template (right) used to gather Tyvek thin foils to wrap the 64 crystals.

-3/ Detection head production

The detection head was composed with one or two matrices (one with LSO crystals and/or one with LuAP crystals) depending on phoswich test was performed or not. The matrices were mechanically mapped on the HR7546 MaPMT. Optical grease was used to enhance the light collection, which was really critical for LuAP prototypes crystals.

The two detection heads with their electronics were aligned along a ring diameter. The ring dimension was set to simulate the final micro-PET gantry (~16 cm). The point Na source (diameter ~3mm) was placed in the centre of the ring. A mechanical rotation of the source

gave 10 data taking period with a 20-degree rotation step to simulate a data taking with a full ring of 18 MaPMT. Fig.3 shows the coincidence set-up that gave us the first image produce with this new auto triggered detection head with off-line coincidence sorting concept.

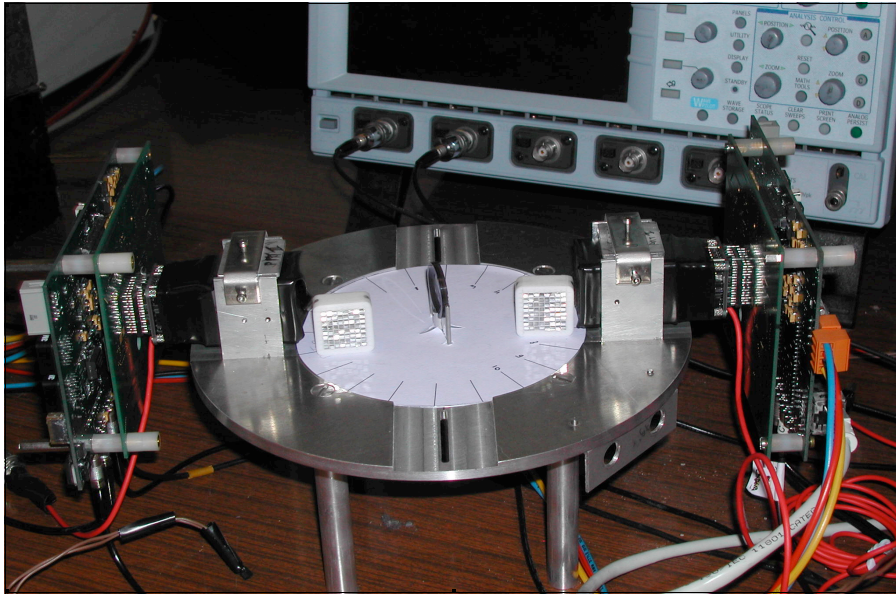


Figure 3: Detection head set-up for matrix tests and off-line coincidence sorting demonstration. The Na source can be seen in the centre.

Readout electronics

-1/ MaPMT tests using a BFOOT system

We perform tests of the MaPMT used in the OPERA experiment with a demonstrator DAQ board – using the BFOOT processor from Agilent – and a commercially available front-end electronics, the VA-TA system from IDEAS. Two board generations were produced and validated to readout HPDs (DEP proximity focusing 61 pixels) and MaPMTs (Hamamatsu) [2]. The 2 boards are shown in Fig.4 : 1st prototype (ORCA board, left) and 2nd prototype (right).

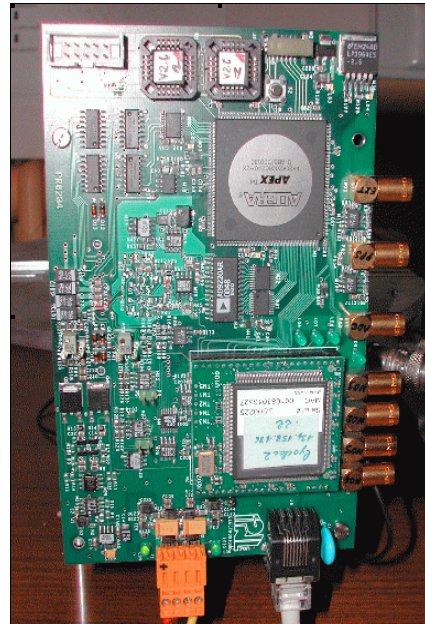
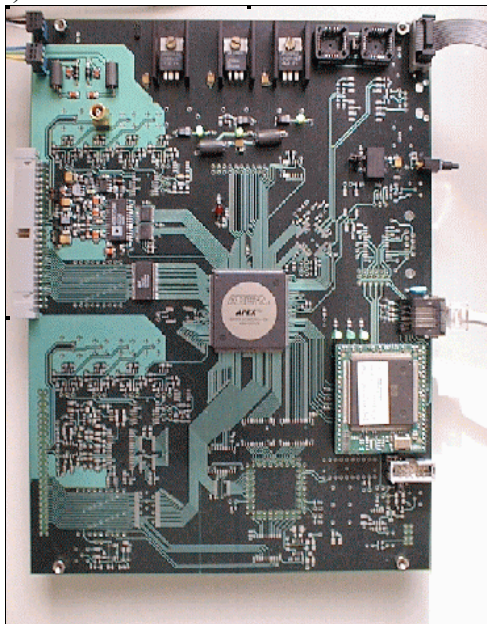


Figure 4: Two board versions using BFOOT Ethernet processor.

The readout sequence is independent of the photo detectors, which have a comparable $\sim 4\text{pF}$ pixel output capacitance: the photo detector charge is readout through a slow shaping time chip – VA32c (low noise and high gain) for HPD readout, VA32hdr11 (High Dynamic Range chip) for MAPMT readout – after a sample/hold logic triggered by a fast shaping chip – TA32c in both cases – followed by a discriminator.

The system allows detailed tests on gain uniformity, gain linearity with applied voltage, photoelectron resolution – illustrated on Fig.5 with the Poisson spectrum seen by the HPD (left) and the single p.e. spectrum seen by the MaPMT (right) –, trigger efficiency (using a pulsed blue LED and its pulse as external trigger), dark current measurement (which indicates a dark current less than 3 Hz per pixel in the case of the MaPMT).

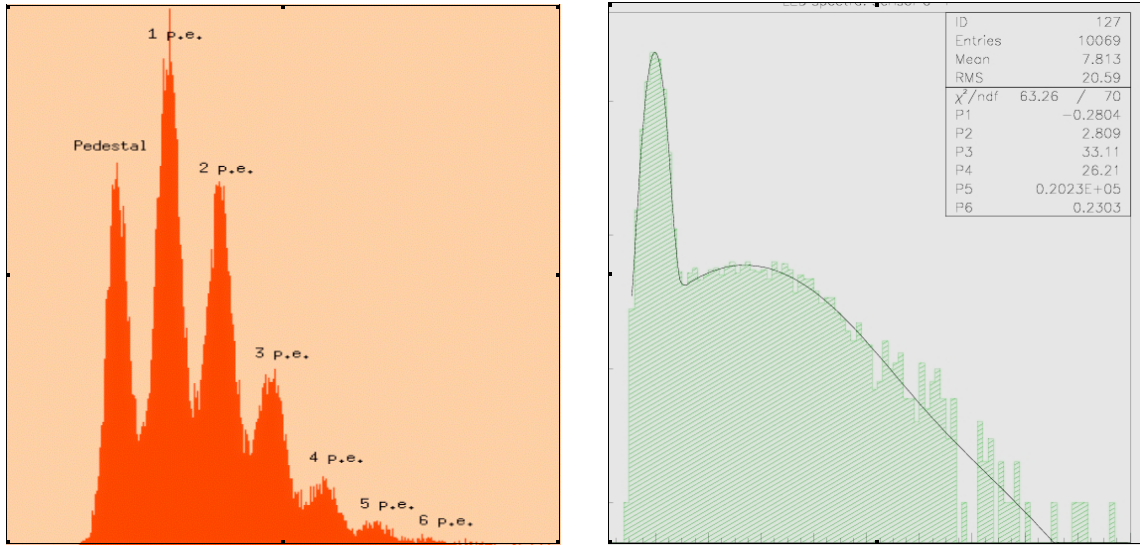


Figure 5: photoelectron resolution obtained with the BFOOT readout system : HPD case (left) and MaPMT case (right).

The results obtained on the HPD tests with the 1st version of BFOOT board lead to the development of an upgraded and compact system.

-2/ The BFOOT version 2 acquisition system

The second version of BFOOT Ethernet controller has been developed as a backup solution for the final R/O chain of the OPERA experiment, dedicated to the MaPMT R/O at the test facility in the OPERA scintillator module assembly site.

The R/O can be performed either in auto trigger mode, using the internal trigger generated by the TA chip, or in external trigger mode (NIM signal input). The system performance is limited by the 1Mbps data transfer capability of the BFOOT processor. This corresponds to roughly 100Hz per pixel data rate given the data format used for the tests.

The system specifications are listed below:

- R/O of VA-TA HDR11(PMT) ($f_{\text{max}} = 5 \text{ MHz}$)
- 4 DACs: 1 for the threshold setting + 3 biases VA-TA
- 12 bits ADC (10 MHz) for the multiplexed output digitisation
- 7 NIM I/O connectors (trigger in/out, busy out, ADC out, PPS in)

- Ethernet controller: BFOOT
- 1 external trigger input
- 1 time reference input
- event timestamp: 10 ns resolution (typ.), 5 ns (min.)
- Read/Write register access through HTTP commands
- FIFO FPGA: 2048 x 32 bits words, buffer BFOOT: 1 Mbytes
- Data Streaming mode (1 Mbits / sec): TCP/IP

The block diagram of the R/O system is displayed below (Fig.6)

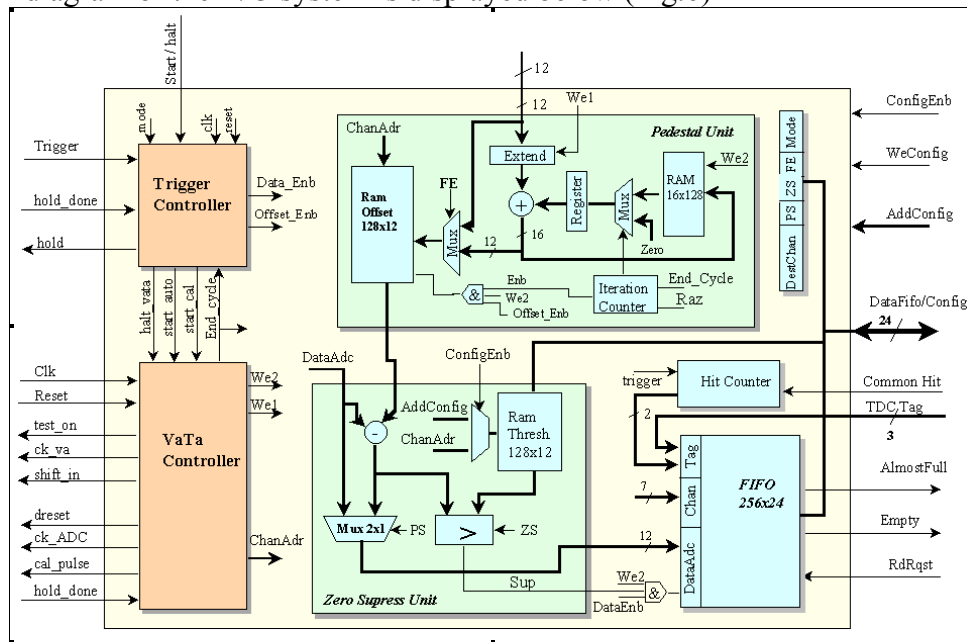


Figure 6: Block diagram of the BFOOT board.

The sequencer (FPGA APEX from Altera) manages the following operations:

- readout sequence,
- event timestamp,
- data formatting (including possible zero suppress),
- data temporary storage in a FIFO.

The BFOOT processor gets the data from the FIFO at a fixed and programmable frequency (min. refreshing period = 17ms).

The BFOOT processor is host on a daughter board (so-called “mezzanine” board) plugged on the main board. The VA-TA and the BFOOT boards have been directly connected through an ERNI 50 pins connector for all the required I/O signals. On Fig.7 one sees a picture of the readout electronics elements (VA-TA front-end board, BFOOT mezzanine and BFOOT mother board). The MaPMT is plugged directly on the front-end board.

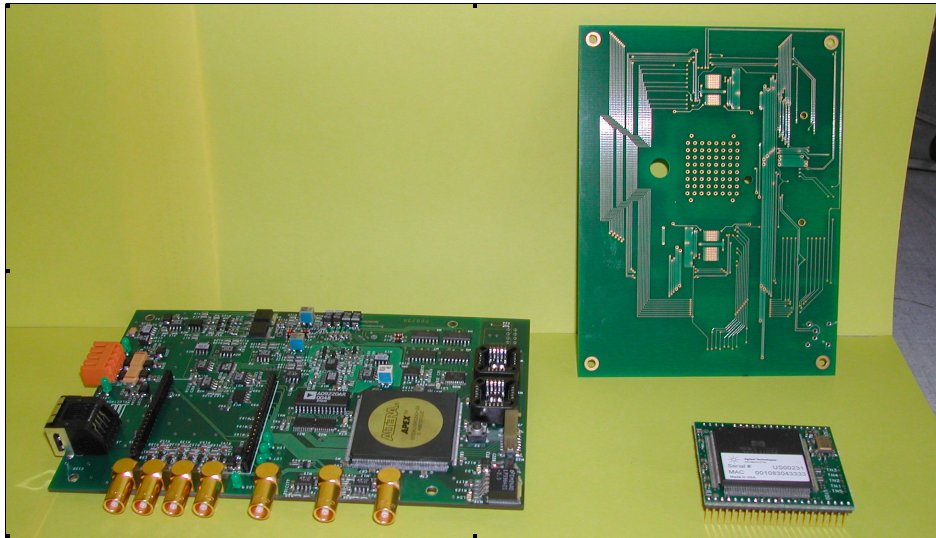


Figure 7 : Picture of the readout electronics elements of BFOOT V2 acquisition system. The component on right is the Ethernet processor.

-3/ Software control

The system is totally manageable through *http* commands, the processor hosting a *WEB* server (see its “applications homepage” below). A LabView interface has also been developed with all embedded commands in a more standard “user friendly” format. The program allows all the slow control, monitoring (front-end biases settings, acquisition mode, trigger source selection...) and acquisition commands.

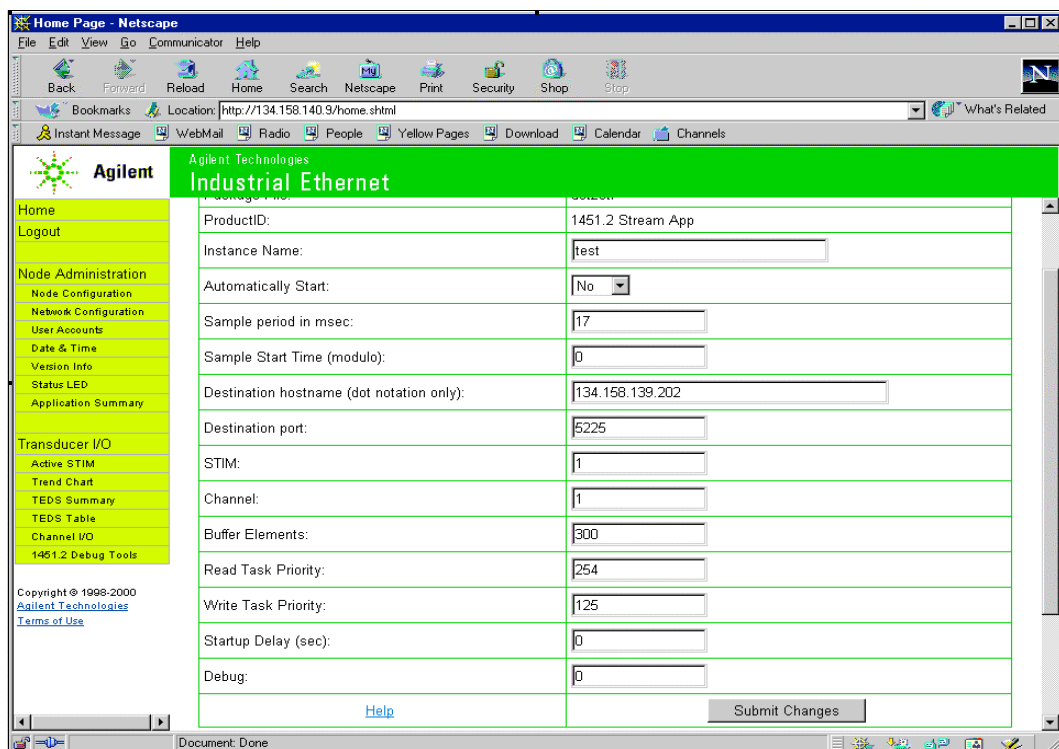


Figure 8: Applications homepage running on the BFOOT WEB server.

Results and Analysis

-1/ Pulse Shape Discrimination

To enhance the sensitivity of a Micro-PET system, longer crystals are required to improve the stopping power and therefore the sensitivity of the scanner. Nevertheless with longer crystals parallax error occurs when the region of interest is far from the center of the field of view. To perform DOI measurement, pulse shape discrimination can be achieved using the difference of pulse shape between two crystal types (LSO and LuAP in our test bench). The PSD can be performed either on the slow component or on the fast component of the LuAP (~20 ns). We evaluated the efficiency and the purity of the fast component discrimination. The pulses from the MaPMT were collected at the level of the last dynode (12th) by a numerical oscilloscope (Lecroy LT402) and each pulse was digitized with a maximum sampling rate of 1GHz and transferred to a computer. Pulse sampling allows to store pulse height spectra as function of time. For each value being in the photo-peak, the time gravity center of the pulse has been calculated (this corresponds more or less to the mean decay time of the crystal) following the formula:

$$\tau = \frac{\sum_{t_i=t_0}^{t_{end}} t_i y(t_i)}{\sum_{t_i=t_0}^{t_{end}} y(t_i)}$$

where t_0 was set at the maximum of the decay and different t_{end} have been tried in order to estimate the best LSO/LuAP discrimination. Different values from $t_{end}=10\text{ns}$ up to $t_{end}=400\text{ns}$ were tried.

An event by event analysis has been performed using this PSD method with LuAP and LSO pure samples. Fig.10 shows the corresponding results. Efficiency and purity of the PSD has been estimated to be around 90 % with a 250 MHz sampling rate.

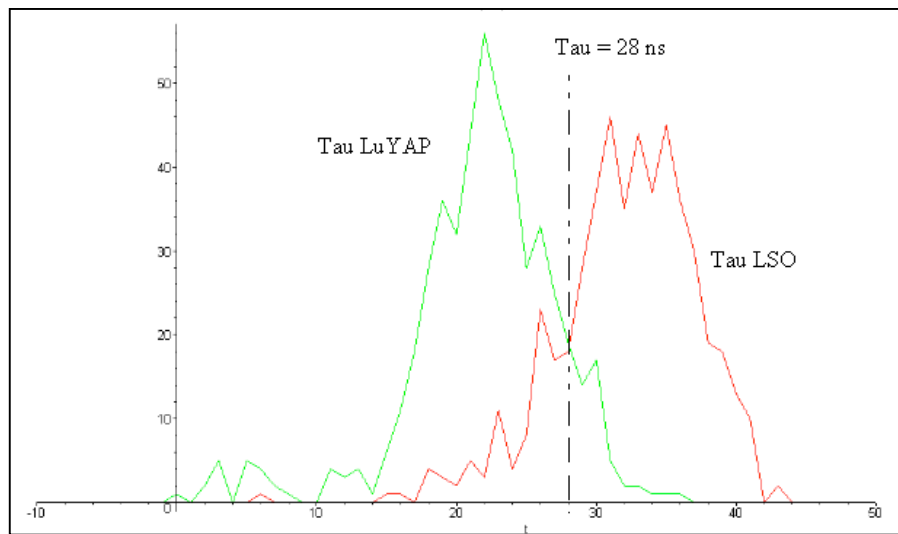


Figure 9: PSD distribution example on real DATA between LuAP and LSO crystals. 90% of efficiency and purity has been achieved but at 250 MHz sampling rate.

The PSD results versus the crystal quality have been extensively discussed in [1]. Nevertheless we conclude that the light emitted by the LuAP was too weak to perform a good PSD on its fast component and a Front-End electronic with a 250 MHz sampling would be necessary to perform a good PSD with an efficiency around 99%.

-2/ Single electron calibration method

The main drawback of the MaPMT vs. the HPD is the pixel to pixel gain spread, which can be as large as 1:3. On the other side, the gain of the MaPMT is sufficiently high (typ. 10^6) to avoid an extra pre-amplifier stage in the front-end electronics. The VA chips can not compensate the MaPMT's gain spread. The only "correction" of the system is applied at the level of the trigger mask where individual thresholds can be set for all the channels. It ensures a trigger efficiency equal for all the channels, although the recorded charge spectra differ. The off-line gain correction to be applied implies a good calibration of the MaPMT pixels gain.

The calibration method is derived from the so-called Bellamy method [3] which is a fitting procedure involving 11 individual parameters. In the case of this application, we retain only a sub-set of those parameters, all the individual crystals producing an intense light yield, far from the pedestal region where most of the fitting procedure difficulties are concentrated.

Therefore we adopted a fitting function taking into account:

- the Poisson fluctuation of the photoelectrons numbers: $P_k = e^{-\mu} \frac{\mu^k}{k!}$ where μ stands for the average number of photoelectrons,
- the Gaussian shape of pedestal and photoelectron peaks: $G_p = G(m_p, \sigma_p)$ where
 - $G()$ is standard normalized Gaussian distribution;
 - the position of each peak is computed as: $m_p = m_0 + p \times g$ ($p \in \mathbb{N}$), g being the single photoelectron gain and m_0 the position of the pedestal peak;
 - the width of each peak is given as: $\sigma_p^2 = \sigma_0^2 + p \times \sigma^2$ ($p \in \mathbb{N}$), σ being the width of a photoelectron peak without noise.
- a possible extra exponential component between the pedestal and the 1st p.e. peak
- an overall normalization constant.

The convergence of the fit depends very sensitively of the initial values given to all these parameters. The pedestals parameters (position and width) are fixed via an independent run done with the same high voltage applied on the MaPMT and an uncorrelated trigger. This gives the most realistic pedestals values between the pedestal and the LED runs.

The initial average number of p.e. value is taken directly from the Poisson statistics:

$\mu = \ln \left(\frac{P_{1 \dots \infty}}{P_0} + 1 \right)$, which implies to count the number of counts in the pedestal w.r.t. the total number of entries.

The individual gains are derived from the mean value of the spectrum \bar{m} :

$$g = \frac{\bar{m} - m_0}{\mu}$$

The width of each p.e. peak is taken in a reasonable range. The normalization constant depends directly of the number of entries of the run (usually 10^5 to 10^6).

All the pixels are illuminated by a diffusing system (segmented cylindrical plexiglass block with 3 LEDs at 120° of each other, all the LEDs driven by the same input signal). With a typical frequency of 500Hz the calibration of each MaPMT is a rather fast procedure. The light yield chosen to perform the fit is relatively large (2 to 5 p.e. in average) to minimize the weight of the pedestal region but to ensure that the pedestal is nevertheless still visible. Typical results are shown in the next Fig. with various values of $\bar{\mu}$ for different channels:

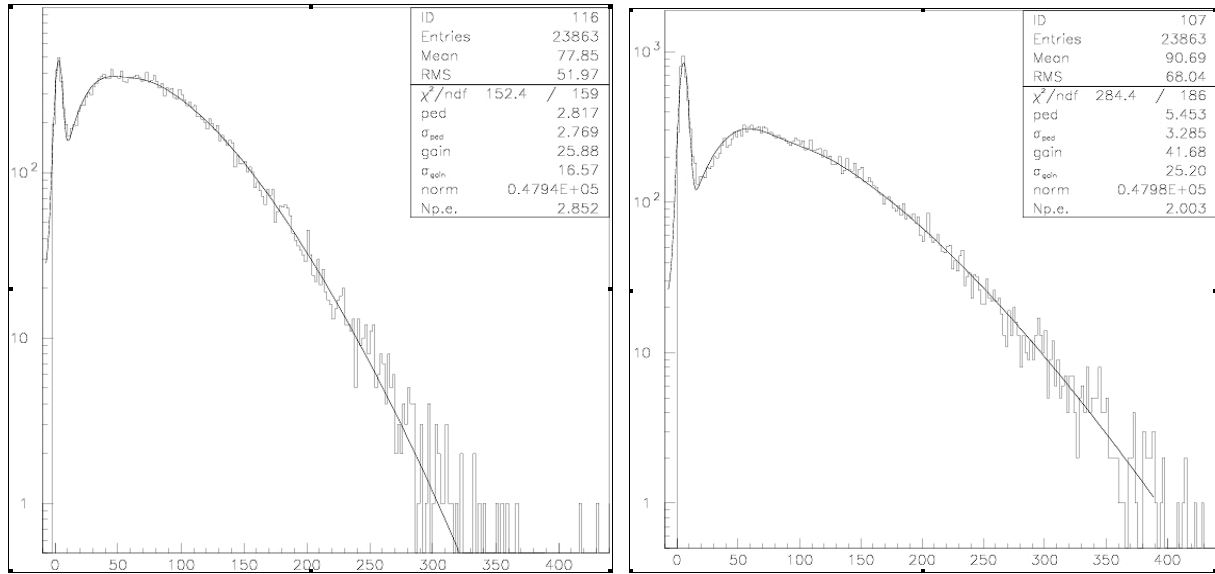


Figure 10: LED spectra obtained with an average number of p.e. ranging from 2.8 (left) to 2.0 (right).

Low light yield spectra (see Fig.11, left) exhibit strange behaviour in the pedestal definition which implies the use of an extended fit function. The gain distribution over the 64 pixels (Fig.11, right) shows the typ. 1:3 gain spread for the MaPMT between min. and max. values (20:60 ADC counts, mean value: 40 ADC counts).

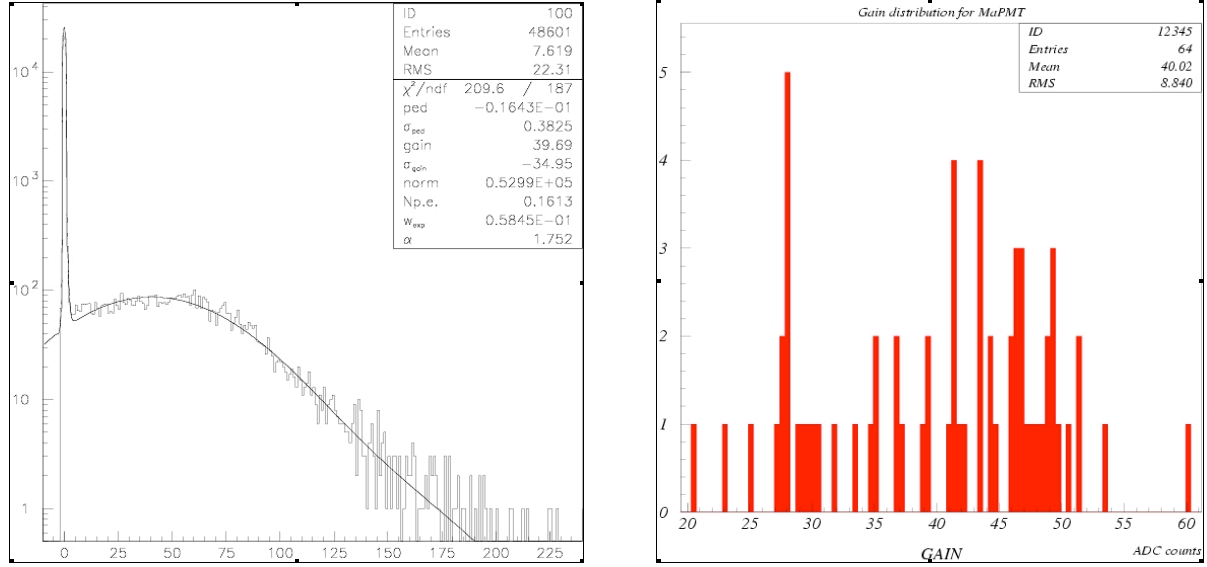


Figure 11 : LED spectra obtained with a low number of p.e. (less than 0.2) (left). Also shown is the gain distribution over the 64 PMT pixels (right).

-3/ Light sharing and matrices mapping

The readout electronics described in the previous section has the major advantage to store energy information (ADC values) of the 64 MaPMT channels for each triggered event. This information has been extensively used to characterize the two detection heads. Information giving only the position of the pulse (anger method) is completely blind to the effect of the trigger threshold adjustment, light sharing between pixels, off-axis displacement between the matrix and the MaPMT.

Selecting event triggered by one pixel allowed to perform specific event studies based on the 64 ADC values recorded. Such recorded events are shown in Fig.12.

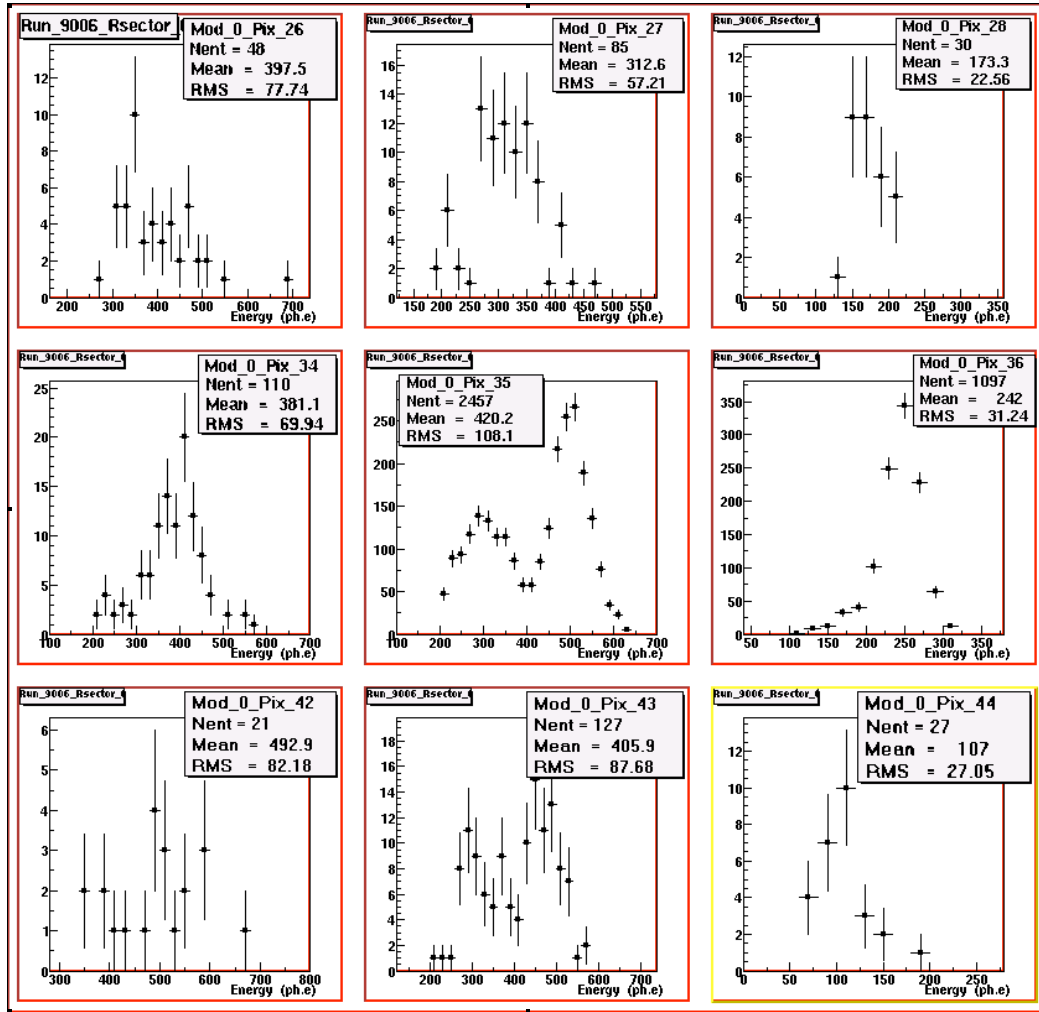


Figure 12: Full spectrum obtained for nine pixels when the central pixel is auto-triggered and the nine ADC values are recorded. Light sharing between neighbour pixels is well seen.

-3.1/ Energy resolution

The first study was dedicated to the photo-peak energy resolution taking into account the energy sum of the neighbour pixels. Fig.13 represents the evolution of the energy resolution as a function of the cluster size. The ratio FWHM/Mean decreased from 21% to 19%, 18% and to 16% when the sum is performed on 5, 9 and 21 neighbour pixels. We concluded from this study that energy resolution would be increasing by sampling the 20 neighbours of the triggered pixel. This feature has to be put in balance with the dead time due to the ADC sampling. The best solution to optimize in the same time the energy resolution and dead time should be a smart ASIC with a serial output of only 9 or 25 pixel values. The readout electronic developed here could be used with some logic implemented in the FPGA or in the Ethernet Processor.

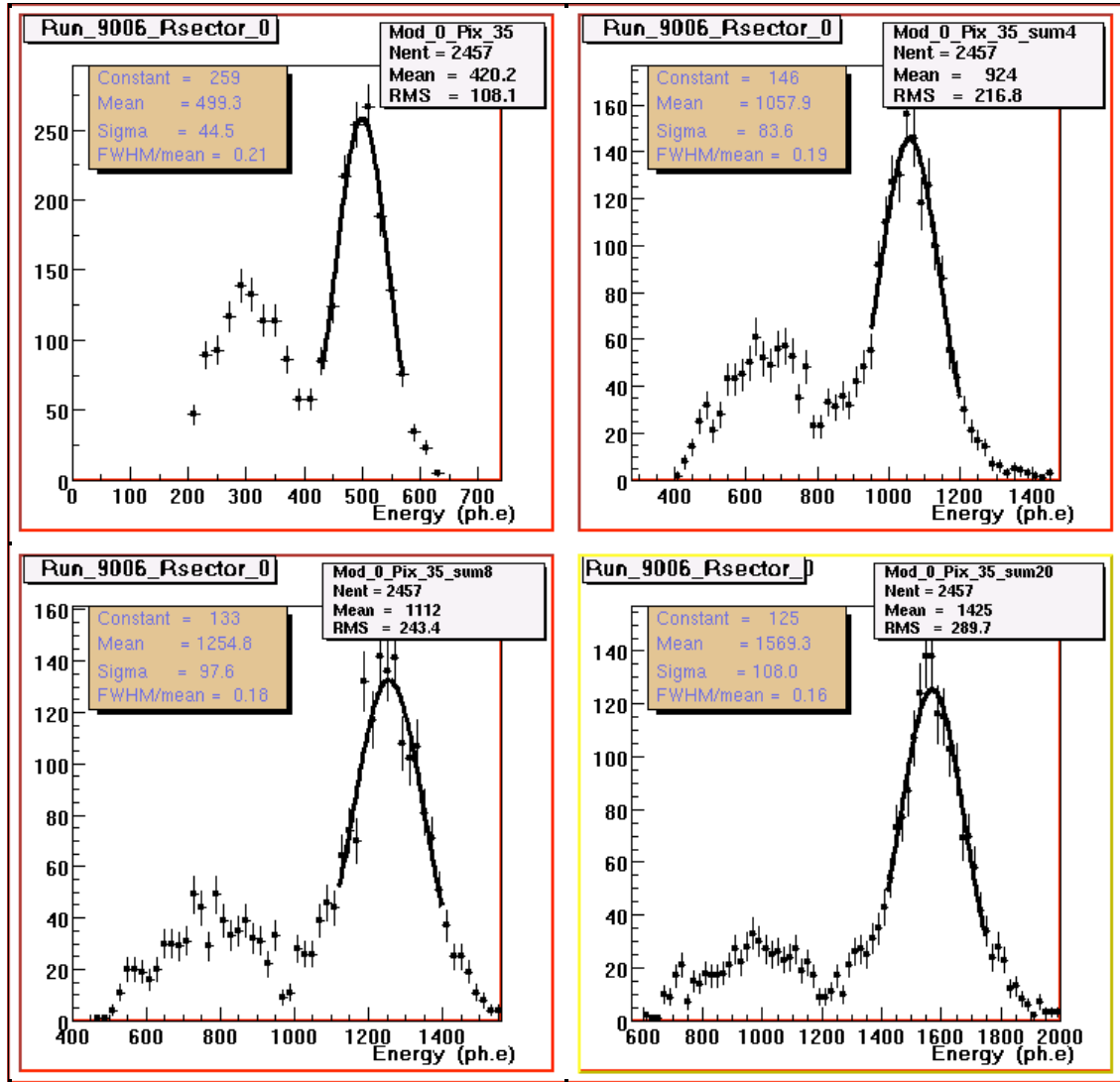


Figure 13: The full spectrum obtained with Pixel 35 (upper left plot). The 5 pixel energy sum distribution (upper right plot). The 9 pixel energy sum distribution (lower left plot). The 21 pixel energy sum distribution (lower right plot).

-3.2/ Matrices mapping control from light sharing.

Information obtained from light sharing has been used to perform a control of the mapping between crystal matrix and MaPMT grid. We computed the energy fraction of light loss in the neighbours. Fig.14 shows the results. We have shown that a mechanical mismatch (0.1 mm estimated) could be seen with this method (Fig. 15).

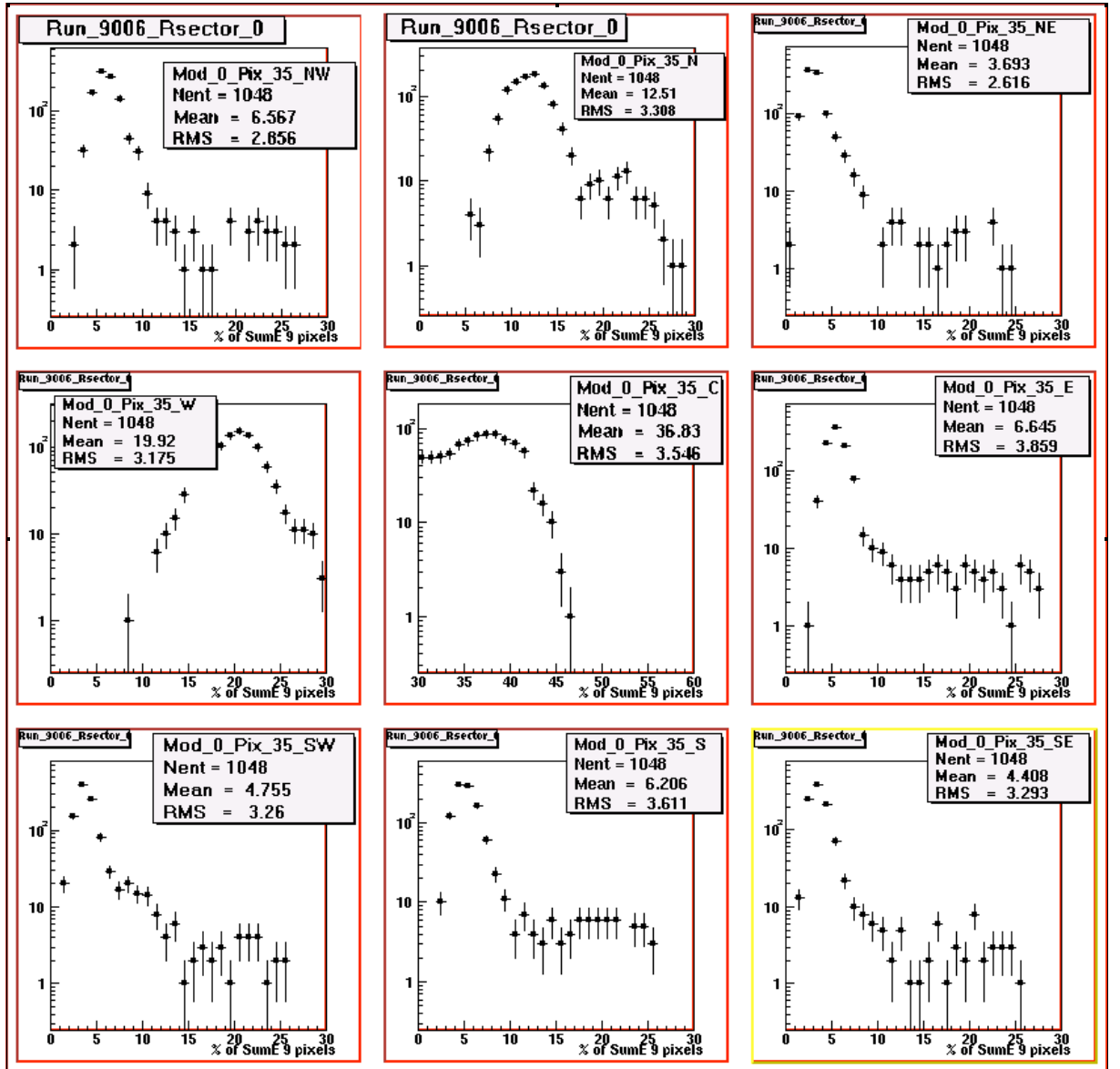


Figure 14 : Energy fraction (in %) obtained after summation of the nine pixel energies. The central pixel number 35 has been triggered. Notice the deviation discrepancy between the values of the West and the East pixels.

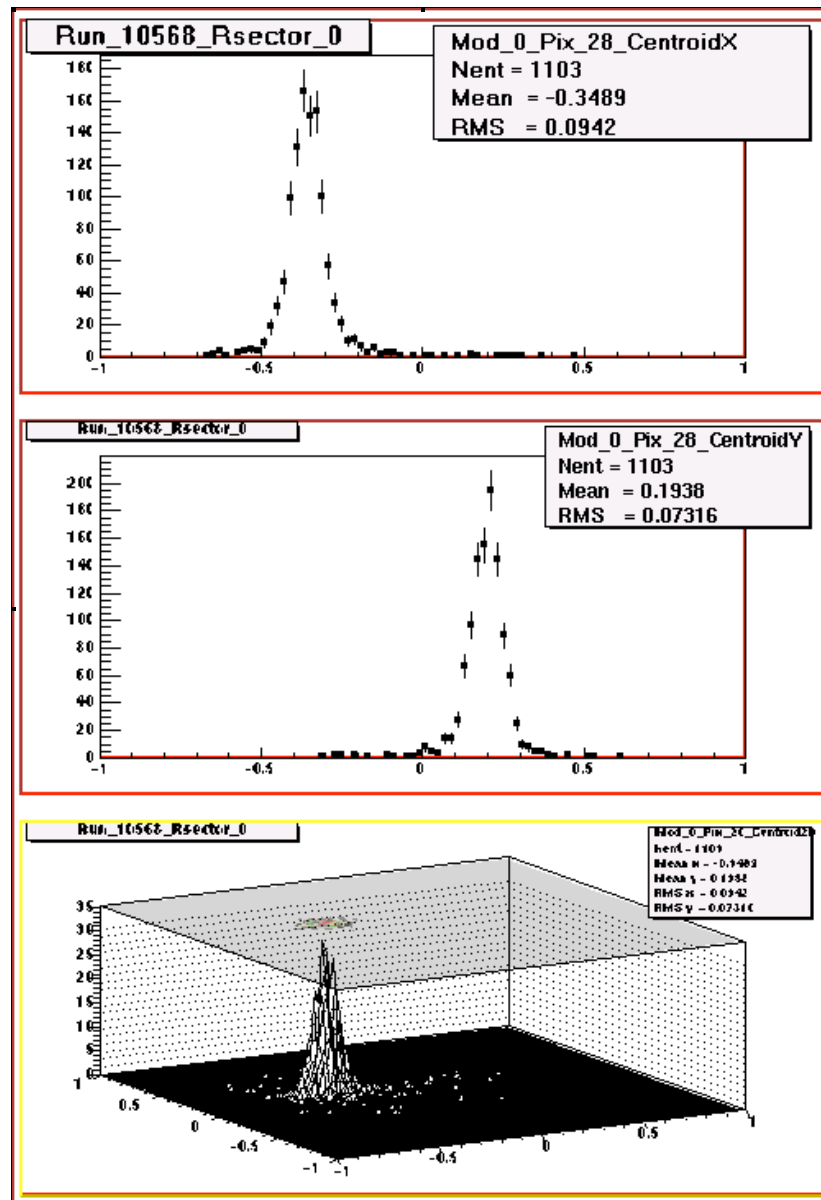


Figure 15: Off axis centre of the crystal position estimated with real data from the discrepancy between West and East pixels light sharing for X direction and between North and South Pixels for Y direction. X and Y Axis are in mm.
Bottom a 2D representation.

-3.3/ Compton events studies

One way to increase the image resolution could be the use of information on the type of interaction occurred in the crystals (remind that a 250 keV cut is the common threshold in PET scanner). It could be really interesting to differentiate the Compton events occurred in

the crystals to the Compton events occurred in the mouse. For this purpose we selected only the off-peak events (Compton events). The Compton spectrum is shown in Fig. 16 for the nine pixels with the seed pixel in the center.

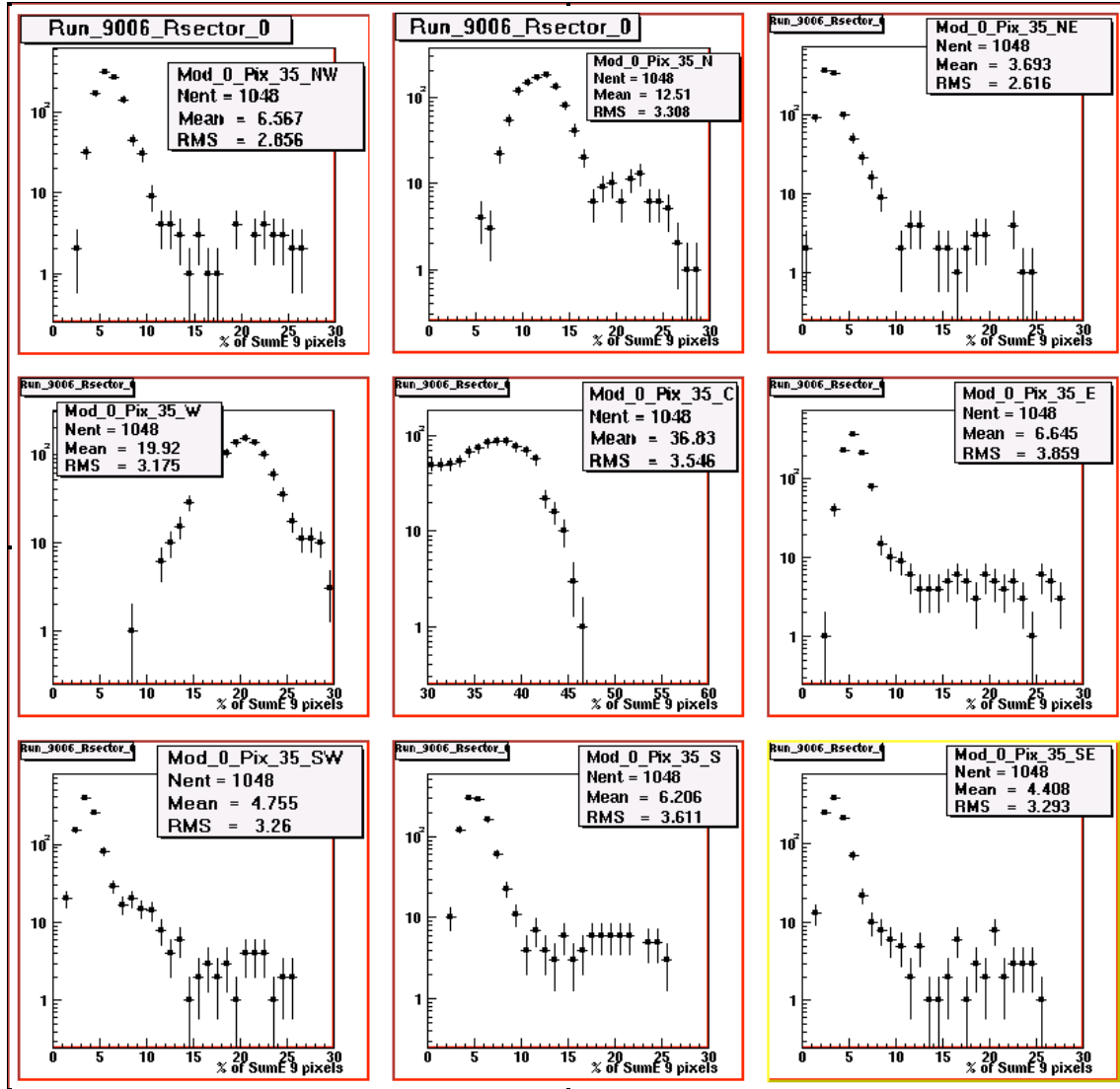


Figure 16 : Energy fraction (in %) obtained after summation of the nine pixel energies. The central pixel has been auto-triggered. The selected events are the events with a 9 pixel energy sum below the full energy peak. This should corresponds to Compton events.

The energy sum of 5, 9 and 21 neighbour pixels is shown in Fig.17. From this plot we can conclude that 50 % of selected events can be classified as Compton events in the crystal. And this information could be used by statistical algorithm for PET image reconstruction.

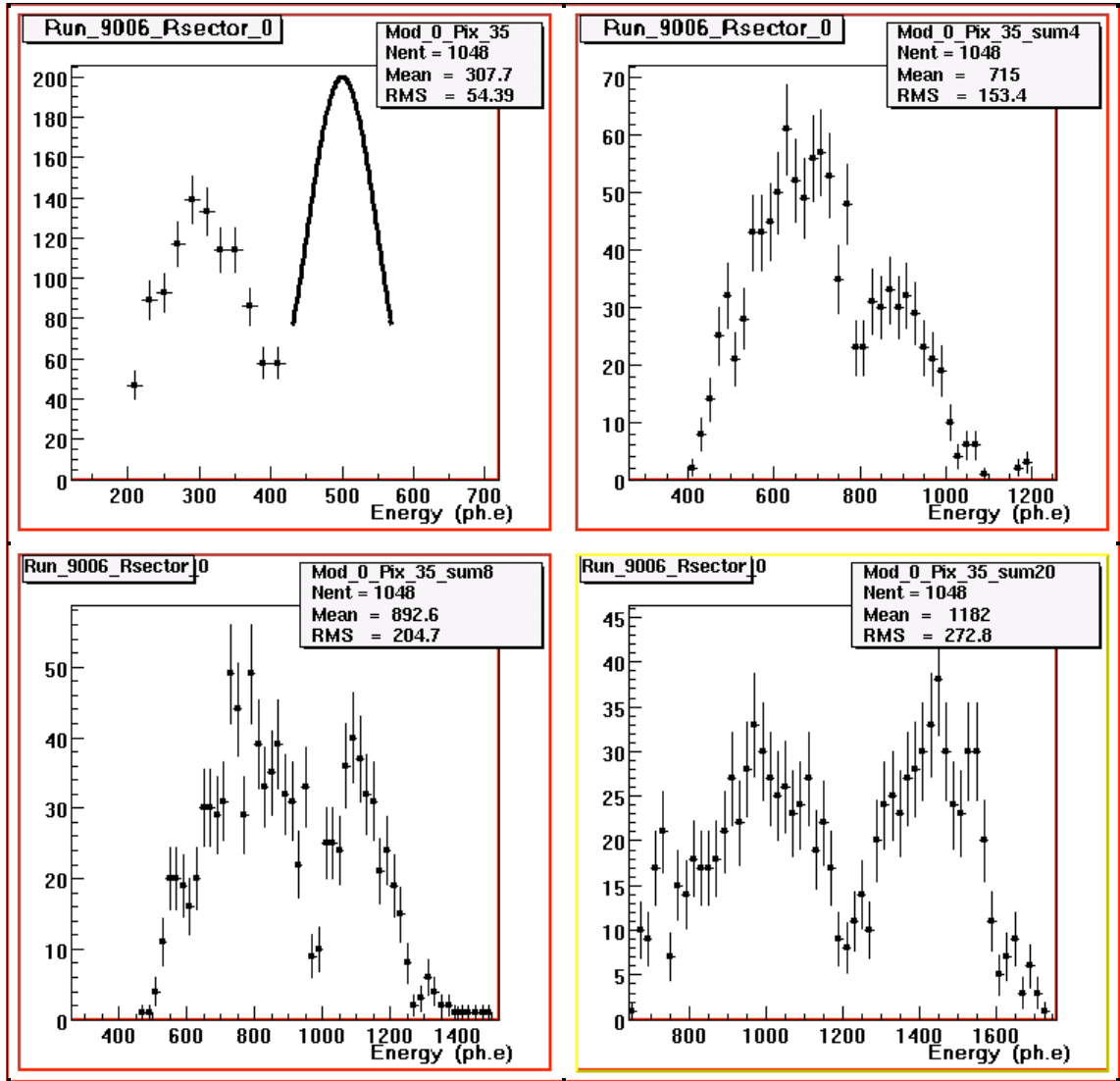


Figure 17: Compton selected events obtained with one auto-triggered pixel (upper left). Energy sum distribution is shown for 5 pixels (upper right), 9 pixels (lower left) and 20 (lower right). We can see the photo-peak reconstruction for 50 % of the events with 20 or 9 pixel clusters.

-3.4/ Flood diagram trigger rates

A crucial issue of the 64 crystal matrix and MaPMT mapping is the gain variation between the 64 channels since on trigger threshold is used. This can be seen with the flood diagram of

Fig.18. This exercise has been performed in order to show the interest of adjustable trigger level for each channel. This is a strong advantage of the new version of the ASIC developed for the OPERA experiment [4]. This effect has to be taken into account in the normalisation before the image reconstruction.

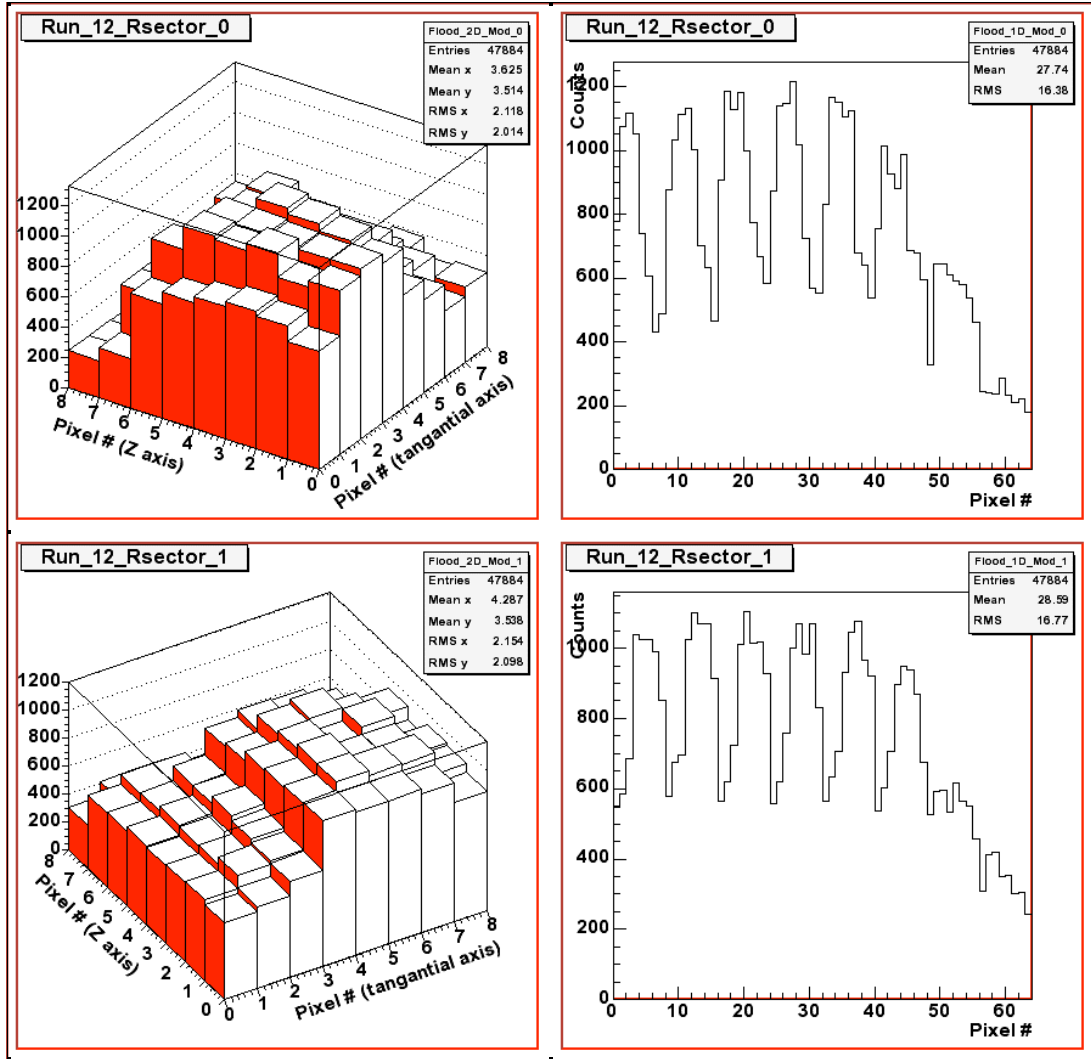


Figure 18 : Flood diagram of the two detection heads used for the image reconstruction of the Sodium source. Notice the loss of events at the border of the matrix. The shift in the X and Y direction is also visible.

-4/ Image reconstruction with off-line coincidence sorting

The major difference with classical acquisition PET system is that the coincidence is performed off-line with the event time stamping information. Although the prototype Ethernet board was not really optimised for this purpose from the dead time point of view, we recorded 9 positions of the two heads (20 degree rotation step) to simulate a full ring imaging of a sodium source. The raw data was processed in the List Mode Format of CCC [5]. To reconstruct the image of the source we used a private interface to the STIR software [6] developed by our CCC collaborators.

Fig.19 shows an image obtained by the two LSO detection head set-up of Fig.3.

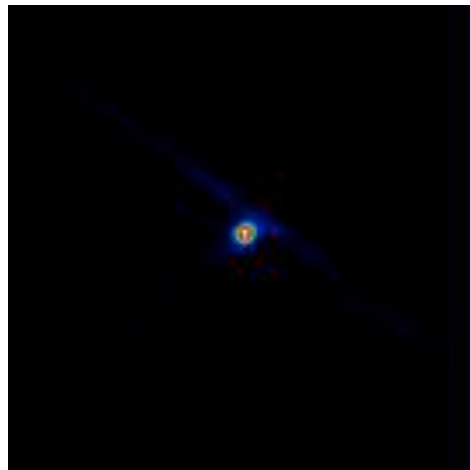


Figure 19: The reconstructed image of the ^{22}Na source obtained with the coincidence set-up. The reconstruction software used is the STIR package. The Raw DATA has been first processed in LMF Crystal Clear Format.

Conclusion

This paper describes the results obtained with a 2-heads micro-PET prototype using lutetium crystals (LSO/LuAP), MaPMTs and a dedicated, fully developed by IPNL, DAQ readout chain, completely driven through an Ethernet processor.

Detailed results have been obtained using this set-up in the overall prototype calibration (single p.e. resolution, trigger efficiencies, energy resolution) and in its tracking and imaging capabilities. The limitations of DOI reconstruction using the fast components of LSO/LuAP have been demonstrated together with the possibility to use part of the Compton events in the detection head.

The feasibility of producing images has also been given. Such a system is easily scalable and can be upgraded using different photo detectors (flat panel PMTs have been characterized with the same R/O chain) and more powerful electronic chain (for example à la OPERA where the front end chip allows the gain spread compensation and the Ethernet DAQ system allows a 100 larger bandwidth for data transfer).

References:

- [1] R. Barbier, Y. Déclais, C. Dujardin, N. Garnie, M. Janier, I.A. Kamenskikh, G. Langeron, J. Marteau, C. Pedrini, D. Sappey Marinier, *Nucl. Instr. Meth. A* **527** (2004) 175-179.
- [2] C. Girerd, et al., *IEEE Nuclear Science Symposium and Nuclear Imaging Conference*, , Lyon, 15-20 October 2003. **Patent Id WO2005081121**.
- [3] E.H. Bellamy et al, *Nucl. Instr. Meth. A* **339** (1994) 468-476.

[4] S. Bondil et al. Performance of the 32-channels front-end electronic chip, OPERA internal note n°34 (2005).

[5] Ch. Morel et al. Clear PET Project List Mode Format Implementation V1.3.2, IPHE/UNIL 2002, private communication.

[6] C Labbé et al. Software for Tomographic Image Reconstruction, STIR package; *Proc. Of 3D99*, **June 1999**, Egmond aan Zee, The Netherlands.

Chapitre 2

Tomographie muonique de structures géologiques

2.1 Introduction

Contexte général — Lancé en 2008, le projet **DIAPHANE**, en Collaboration avec l’Institut de Physique du Globe de Paris (IPGP) et Géosciences Rennes (GR), réalise des tomographies en ligne de volcans actifs et de structures géologiques vues depuis des sites souterrains. La motivation initiale est de répondre à la demande croissante des Sciences de la Terre en méthodes d’imagerie. Les performances des méthodes d’imagerie classiques restent inégales soit en raison des moyens de R&D plus ou moins importants qui leur ont été consacrés, soit à cause d’une limitation physique fondamentale. Par exemple, les méthodes sismiques, qui constituent la méthode privilégiée dans le domaine pétrolier, ont bénéficié d’investissements considérables et atteint un niveau de sophistication remarquable. A contrario, les méthodes fondées sur l’analyse des champs de potentiel souffrent d’une non unicité et d’une faible résolution inhérentes à la physique même des champs mesurés. Les propriétés physiques des roches qu’il est possible d’imager ne sont donc pas toutes logées à la même enseigne et certaines, comme l’impédance acoustique, peuvent être tomographiées à haute résolution contrairement à d’autres comme la masse volumique ou la résistivité électrique. Actuellement, les méthodes géophysiques permettant de déterminer la densité des roches sont la sismique et la gravimétrie. Dans le cas de la sismique, cette détermination est faite indirectement via celle des vitesses des ondes de compression et de cisaillement. Il en résulte une non-unicité qui ne peut, au moins théoriquement, être levée que par l’utilisation de données gravimétriques. La gravimétrie utilise des mesures de la pesanteur reliée à la densité des roches via une intégrale de volume qui fait de la gravimétrie une méthode à basse résolution accompagnée d’une non-unicité fondamentale du problème inverse (référence).

Problématique volcanologique — Les questions scientifiques dans le domaine de la volcanologie sont :

- La tomographie en densité de dômes de lave fortement altérés peut apporter d’importantes contraintes aux modèles de déstabilisation : géométrie des unités structurales composant l’édifice et masses en jeu. Le dôme de la Soufrière de Guadeloupe est bien adapté à ce genre d’étude. Formé en 1530 et soumis à une intense circulation hydrothermale, il a fait l’objet d’expériences de tomographie électrique et de relevés gravimétriques. L’expérimentation de tomographie en densité de la Soufrière a commencé en juillet 2010 avec un petit télescope de première génération. Le but est de pouvoir parvenir à une expérience complète de tomographie 3D à l’aide des télescopes de seconde génération ayant une acceptance et une résolution angulaire optimales.

- La tomographie de dômes de lave en formation et la caractérisation de la partie supérieure du système du conduit d'alimentation présente un grand intérêt pour évaluer la quantité de gaz présents dans le magma et prévoir le type, explosif ou non, d'une éruption. Le site de la Soufrière de Montserrat est une cible idéale mais il représente un défi à la fois par l'impossibilité d'approcher le volcan et par la nécessité d'utiliser des télescopes à forte acceptance et haute résolution angulaire. La mauvaise connaissance de la topographie du dôme en formation peut être partiellement compensée par l'emploi de plusieurs télescopes placés autour du dôme et fournissant, même par temps couvert, une image du profil topographique.
- La tomographie en densité d'un cône volcanique jeune soumis à un début d'altération. Le cône du cratère sud-est de l'Etna s'est formé il y a une vingtaine d'année et nous y avons déjà effectué quelques expériences en collaboration avec nos collègues de l'INVG de Catane. Il représente un état intermédiaire entre la Soufrière de Guadeloupe et celle de Montserrat, et une organisation de l'activité hydrothermale semble s'y être installée.
- Un autre problème volcanologique concerne la détermination de la densité de colonnes d'éjectas au-dessus d'une bouche éruptive pour lesquelles les mesures radar sont inopérantes. Cet objectif constitue un défi particulièrement difficile car il concerne des objets géologiques de faible opacité (équivalente à environ 10 mètres d'eau) où seuls les muons de faible énergie sont stoppés.
- Enfin les premiers retours d'expérience nous ont montré qu'il est possible de contraindre fortement l'évolution de la densité en fonction du temps et donc de suivre le système hydrothermal.

Détecteurs — Le principe général de la tomographie est le même que celui de l'imagerie médicale par rayons X : il s'agit de réaliser une densitométrie (mesure de la densité ou de la masse volumique) par contraste entre les zones les plus denses susceptibles d'absorber plus efficacement un rayonnement pénétrant et les zones les moins denses plus perméables. En disposant un détecteur à muons sur le flanc de la structure à étudier, on peut mesurer le flux (nombre de particules par unité de temps et unité de surface) de muons traversants et le comparer au flux que l'on obtiendrait en absence d'obstacle. Cette comparaison permet de mesurer l'opacité de la structure et de remonter à la répartition de densité de matière à l'intérieur de la structure, moyennant une connaissance minimale à priori de la géologie de la structure, sa topographie etc.

Le détecteur utilisé est un trajectographe, capable de signer le passage d'une particule chargée (en particulier d'un muon) par la détection en coïncidence de 3 impacts sur des plans de détection (appelés "matrices" de détection) distincts. Chaque matrice est constituée de 2×16 barres de scintillateur plastique lus par fibre optique et photomultiplicateur. Les barres sont disposées en damier (16 barres en x et 16 en y). La coïncidence temporelle des couples de points sur les 3 matrices nous permet de reconstruire la trajectoire de la particule incidente. La précision du marquage temporel, initialement de 10ns, a été considérablement améliorée par la mise au point de "ring-TDC" embarqués dans le FPGA de chaque carte d'acquisition. Cette technique de "vernier" utilisant deux oscillateurs câblés en dur dans le FPGA, de fréquence proche mais non identique, permet de descendre à des précisions de l'ordre de quelques dizaines de picosecondes. Le marquage temporel du passage de la particule permet aussi de compter le nombre de muons ayant traversé le détecteur par unité de temps dans une direction donnée. On obtient ainsi une carte de flux détaillée dans toutes les directions auxquelles le détecteur est sensible (qui constituent son acceptance). Les premiers télescopes construits ont été installés pour leur commissioning dans le tunnel du Mont-Terri en Suisse ("Mont-Terri project") pour déterminer avec précision la structure géologique supérieure et en particulier la concavité des veines de roches à basse densité.

Depuis d'autres télescopes ont été placés auprès de volcans actifs (Etna en Sicile, Soufrière de Guadeloupe, Mayon aux Philippines) et ont permis d'imager les structures internes des dômes de ces volcans avec une précision et une fiabilité sans équivalent actuellement. Le but de cette

recherche est de contraindre les modèles d'évolution des dômes de volcans, structures lacunaires et instables, d'identifier la présence de failles et/ou de grottes susceptibles de favoriser une éruption de type phréatique etc. A cet égard la "tomographie muons" fournit des données capitales pour les géophysiciens car extrêmement simples à inverser, contrairement aux méthodes classiques ne disposant que d'informations en surface (tomographie électrique) ou notoirement complexes à inverser (gravimétrie). Les premiers résultats obtenus montrent clairement sur la soufrière de Guadeloupe la présence de failles et de lacunes et poussent fortement à la formation d'une image 3D du dôme pour mieux appréhender la totalité de la structure. De nombreux développements méthodologiques (suppression du flux arrière parasite de particules, analyse du temps de vol des particules, couplage "muons"-gravimétrie etc) ont permis d'améliorer la qualité de l'analyse depuis les débuts du projet.

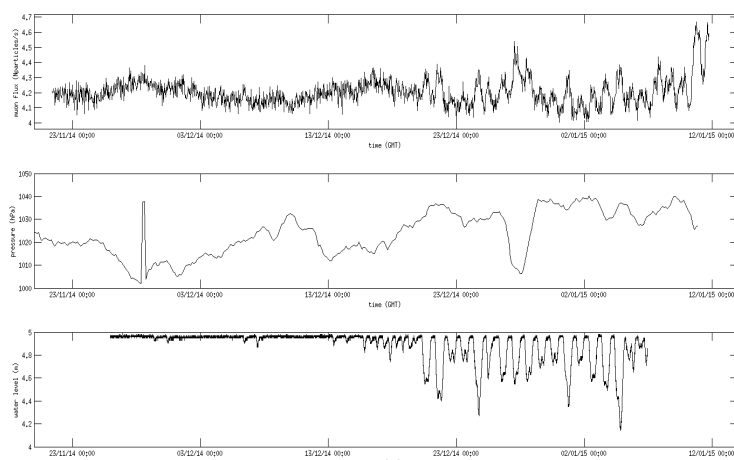


FIGURE 2.1 – *Suivi de la hauteur d'eau d'un château d'eau avec la radiographie muons (haut) en fonction du temps. Les relevés des niveaux effectués par le syndicat des eaux correspondent à la distribution du bas. La variation de densité maximale est de l'ordre de 10%. La distribution du milieu donne la pression atmosphérique.*

Le projet DIAPHANE a reçu en 2014 le soutien de l'ANR pour une période de 4 ans.

Récemment une collaboration au sein de l'Université de Lyon (ILM-IPNL) réalise une étude exploratoire d'un couplage LIDAR-"muons" pour contraindre l'influence des rayons cosmiques très ionisants de la haute atmosphère dans la nucléation. Les prochains télescopes sont d'ores et déjà bâtis pour d'autres études pionnières comme la radiographie du dôme d'un volcan en éruption (Soufrière Hills de Montserrat) et des applications industrielles dans le domaine du génie civil.

Le premier article présenté dans ce chapitre décrivent la faisabilité d'une expérience en fonction de l'acceptance théorique du détecteur, le temps de pose et la résolution souhaitée sur la densité (*Feasibility and limits of the muon tomography technique*, [6]). Le second décrit différentes approches de cette tomographie par muons cosmiques (*Muons tomography applied to geosciences and volcanology*, [7]). Le troisième article présente un développement original, initié par le besoin de réduire le bruit de fond provenant des particules venant de l'arrière, en mesurant leur temps de vol (*Implementation of sub-nanoseconds TDC in FPGA : applications to time-of-flight analysis in muon radiography*, [14]). Pour cela, compte tenu des contraintes en termes de consommation et de puissance de *processing* disponible, un système de vernier temporel embarqué dans un FPGA a été mis au point. L'idée est de cabler physiquement à l'aide des éléments logiques du FPGA, deux horloges de fréquence proche mais pas identique. La résolution du vernier est donc donnée par la différence des fréquences. Enfin le dernier article (*Muon tomography and gravimetry joint inversion*, [15]) présente une méthode exploratoire de couplage de la tomographie muons avec une mesure gravimétrique.

2.2 Geophysical muon imaging : feasibility and limits, [6]

N. Lesparre¹, D. Gibert¹, J. Marteau², Y. Déclais², D. Carbone³ and E. Galichet⁴

¹ Institut de Physique du Globe de Paris (UMR CNRS 7154), Sorbonne Paris Cité, Paris, France.

² Institut de Physique Nucléaire de Lyon (UMR CNRS 5822), Lyon, France.

³ Istituto Nazionale di Geofisica e Vulcanologia, Sezione di Catania, Sicilia.

⁴ Conservatoire National des Arts et Métiers, Paris, France.

Paper submitted to *Geophysical Journal International*, April 2010

SUMMARY

We study the possibilities of muon radiography as a tool to investigate space and time changes in the internal density distribution inside geological structures. Previous works have shown the practical applicability of this method. Nevertheless, quantitative information on factors which impose limitations on it are still sorely lacking in the literature. We discuss the main issues that can influence the final result of a geophysical imaging experiment. In particular, with the view of optimizing the signal-to-noise ratio, we address issues concerning (i) the energy spectrum for muons arriving at different zenith angles, (ii) the muon propagation model through matter, and (iii) the characteristics of the muon detector (telescope) that we have designed to perform experiments of muon radiography against the harsh environment usually encountered in the active zone of a volcano. We thus identify factors that can induce either static or dynamic effects and that should be taken into account. We also define a *feasibility equation* relating the geometrical characteristics of the telescope and the duration of the experiment to the expected density resolution, in turn a function of the geometrical characteristics of the target structure. This relation is especially important to define the applicability domain of muon radiography and it is utilized to test the suitability of the method to investigate the density distribution inside some candidate target structures.

Key words: cosmic rays – spatial analysis – tomography – inverse theory.

1 INTRODUCTION

The interest in using muon tomography for Earth Sciences purposes soon arose after the discovery of cosmic rays (Auger 1941; Leprince-Ringuet 1945; Gaisser 1990; Crozon 2005) and muons (Neddermeyer and Anderson 1937, 1938), and, in particular, when it was realised that muons of cosmic origin are able to cross hundredths of meters, and even kilometres, of rock with an attenuation mainly related to the amount of matter encountered along their trajectory (Nagamine 2003). The very first studies relevant to muon tomography were motivated by the need to characterise the geological burden overlying underground laboratories hosting particles detectors (George 1955). Later, interest for applications other than those directly related to underground laboratories emerged when lighter and mobile detectors became available for field experiments. Early examples are the archaeological investigations performed in the Egyptian Chephren pyramid by Alvarez *et al.* (1970) and the theoretical study of Malmqvist *et al.* (1979), concerning the utility of muon tomography in mining geophysics.

More recently, the interest for muon tomography has been renewed following significant improvements in particle detectors and miniaturised electronics, allowing experiments in out-of-the-lab conditions. In particular, a Japanese team (Nagamine 1995; Nagamine *et al.* 1995; Tanaka *et al.* 2005, 2007a,b,c, 2008a,b, 2009a,b) demonstrated the feasibility of the method to detect both spatial and temporal changes of density inside volcanoes.

Up to now, muon imaging has been performed according to a radiography concept, where the amount of matter of the target (in the following we will call it opacity ϱ) is deduced by comparing the flux of muons, Φ , crossing the geological target to the incident flux, Φ_o , measured at the surface of the Earth in open sky condition. The opacity is converted into density integrated along the trajectories L of the particles,

$$\varrho(L) \equiv \int_L \rho(\xi) d\xi, \quad (1)$$

where ϱ is expressed in g cm^{-2} , ρ is the density, and ξ is

the coordinate measured along the trajectory L of the muon crossing the volume of rock.

To perform 3D tomography imaging, it is necessary to combine a set of radiographies, as done in medical 3D X-ray computed tomography. Mathematically, this can be done by combining a set of ρ values for an as large as possible range of directions of trajectories, L_j , in order to obtain a model of the density distribution, $\rho(x, y, z)$. Contrarily to medical scans which, thanks to the huge spatial sampling performed by modern scanners, use an inverse Radon transform algorithm to compute ρ , muon tomography will suffer from a very poor spatial sampling due to the limited number of locations available to place muon telescopes on the field. This limitation makes the tomography inversion both under-constrained and ill-posed.

Another difference between X-ray scan and muon tomography concerns the weak signals (i.e. fluxes) used in muon tomography and their low signal-to-noise ratio. This characteristic sets a tight constraint on the density contrasts which can be detected in a given amount of time, in turn limiting the time resolution at which geophysical phenomena can be observed. This could lead to a situation of infeasibility of temporal tomography if the period of the studied phenomena is shorter than the integration time needed to resolve the tiny density changes produced by the same phenomena.

In the remaining of this paper we address the influence of the rock thickness, scattering and integration time on both the density and time resolution of a muon tomography experiment. We place particular emphasis on the characteristics of the muon telescope to be used in the field. The combination of the above items leads to the definition of a tomography feasibility domain which is presented and discussed in the context of typical geological situations.

2 SPECTRUM OF INCIDENT COSMIC MUONS

2.1 The muon spectrum

Excepted in very particular situations where artificial sources of muons could be used to perform tomography of geological objects (see Nagamine (2003) for a discussion about such a possibility), all tomography experiments performed to date used muons of cosmic origin, belonging to the so-called secondary cosmic rays. The latter are produced high in the atmosphere (typically 15 km) through interactions between primary cosmic rays, coming from outer space (mainly protons – 90 % – and α particles – 9 %), and atmospheric molecules (Gaisser 1990; Crozon 2005). When measured at the sea level, charged cosmic rays are mainly (63%) composed of muons with a mean energy $\langle E_0 \rangle \approx 4$ GeV (Gaisser 1990). However, the muon spectrum at sea level has a complex form, due to the competition between the interaction and decay of pions and kaons parents and the power-law behaviour inherited from the spectrum of primary cosmic rays and observed for energy $E_0 > 2$ TeV.

The flux of incident cosmic muons is of critical importance for geophysical tomography since it is used to determine the attenuation produced by the geological target. Consequently, any bias in the incident flux of muons will be converted into a bias in the density distribution inside the target. A huge amount of data is available to determine the

surface flux of muons for energies up to 1TeV and for different zenith angles $0 \leq \theta \leq \pi/2$. Despite the large data set available, significant discrepancies still exist among models recently published by several authors, and we present some of them in order to derive a reasonable uncertainty concerning the muon source.

There are two ways to derive the differential flux of muons $\Phi \equiv dN(E_0, \theta)/dE_0$ (given in $\#cm^{-2}sr^{-1}s^{-1}GeV^{-1}$). The first approach consists in performing a full Monte Carlo simulation, through which a large number of air showers, induced by primary nuclei, are generated. The computed muon production is then propagated and attenuated through the atmosphere, in order to obtain the flux at a given altitude. These computations can be accomplished through simulation codes like CORSIKA (Heck *et al.* 1998), which also allow to take into account the geomagnetic and altitude dependence. A second class of flux models is obtained by fitting more or less complicated empirical parametric curves to muon flux data measured at the sea level. The choice of a particular parameterization of the fitting curves may either be inspired by the physics involved in the production of muons from their parents (e.g. Gaisser 1990; Bugaev *et al.* 1998) or be guessed to provide a tight fit, regardless of the physical meaning of the parameters.

Some models of the above second class only consider the production of muons from the two-body decays of pions and kaons and assume a primary proton flux of the form $P_0 E_p^{-\gamma}$, with $P_0 \approx 1.8 \#cm^{-2}sr^{-1}s^{-1}GeV^{\gamma-1}$ and $\gamma \approx 2.7$. This approach yields the analytical form of the muon spectrum initially proposed by (Bugaev *et al.* 1970) and popularised by Gaisser (1990), which reads:

$$\Phi_G(E_0, \theta) = A_G E_0^{-\gamma} \left(\frac{1}{1 + \hat{E}_0 \cos \theta / E_{0,\pi}^{cr}} + \frac{B_G}{1 + \hat{E}_0 \cos \theta / E_{0,K}^{cr}} + r_c \right), \quad (2)$$

where the adjustable parameters are the scale factor A_G , the power index γ , the balance factor B_G , which depends on the ratio of muons produced by the kaons and the pions, and the ratio r_c of the prompt muons to pions.

\hat{E}_0 represents the energy of muon on top of the atmosphere. The energies $E_{0,\pi}^{cr}$ and $E_{0,K}^{cr}$ may be interpreted as critical energies of pions and kaons for the vertical incidence (i.e. $\theta = 0$). These physical quantities should be non-adjustable parameters and should be determined through quantum mechanical calculus. However, most authors consider $E_{0,\pi}$ and $E_{0,K}$ as adjustable parameters when fitting model (2) to data sets. Table 2 recalls the best estimates of these parameters published by several authors.

The θ dependence in eq. (2) accounts for the larger thickness of the atmospheric layer crossed by the muons when the zenith angle increases. However, for large angles $\theta > 70^\circ$, a modified version θ^* is often used in (2) to account for the spherical geometry of the Earth. In fact, the curvature of Earth significantly reduces the thickness of atmospheric layer to be crossed by muons. We have,

$$\cos \theta^* = \sqrt{1 - \frac{1 - \cos^2 \theta}{(1 + H_{atm}/R_{Earth})^2}} \quad (3)$$

Table 1. Meaning and physical unit of principal symbols used in the present study.

| symbol | unit | meaning |
|----------------|--|--|
| L | m | length of ray path |
| D | m | distance between matrices of telescope |
| d | m | size of matrix pixels |
| ΔT | s | duration of measurement period |
| θ | rad or degrees | zenith angle |
| θ^* | rad or degrees | zenith angle corrected for Earth's sphericity |
| Ω | sr | total angular coverage of telescope |
| $\delta\Omega$ | sr | angular resolution of a telescope |
| $N_x N_y$ | | size of telescope matrix |
| \mathcal{T} | cm^2sr | telescope acceptance |
| ρ | g cm^{-3} | rock density |
| ϱ | g cm^{-2} | opacity of rock layer |
| $1 - \alpha$ | | probability level of confidence interval |
| N | | number muons detected |
| ΔN | | discrepancy between the number muons detected for two different rock volumes |
| δN | | half-width of confidence interval of N |
| p | $\text{GeV } c^{-1}$ | momentum |
| E_0 | GeV | energy of muon at sea level |
| \hat{E}_0 | GeV | energy of muon on top of atmosphere |
| ΔE_0 | GeV | energy loss of muon across the atmosphere |
| E_{\min} | GeV | minimum muon energy to cross a given opacity |
| Φ | $\#\text{cm}^{-2}\text{sr}^{-1}\text{s}^{-1}\text{GeV}^{-1}$ | differential flux of muons |
| γ | | power-law exponent of differential spectrum |
| A | | scale factor (i.e. amplitude) of differential spectrum |
| I | $\text{cm}^{-2}\text{sr}^{-1}\text{s}^{-1}$ | integrated flux |

where $R_{\text{Earth}} = 6370$ km is the Earth radius and $H_{\text{atm}} = 32$ km is the altitude of production for muons with a trajectory at large angles.

The empirical spectrum model given by eq. (2) strongly overestimates the incident flux for $E_0 < 100/\cos\theta$ GeV, and Tang *et al.* (2006) proposed a modified version of the original Gaisser's model. A version of this modified spectrum is used in the MUSIC Monte Carlo simulation code (Kudryavtsev 2009) with $r_c = 10^{-4}$ and:

$$\hat{E}_0 = E_0 + \Delta E_0, \quad (4)$$

$$A_T = A_G \left(\frac{120 \cos\theta^*}{1030} \right)^{\frac{1.04}{(E_0 + \Delta E_0/2) \cos\theta^*}}, \quad (5)$$

where

$$\Delta E_0 = 0.00206 \left(\frac{1030}{\cos\theta^*} - 120 \right). \quad (6)$$

Other empirical models departing from the Gaisser's formula (2) and accounting for the low-energy range of the spectrum have been proposed by several authors. For instance, Bugaev *et al.* (1998) derived the following model equation:

$$\Phi_B(p) = A_B p^{-(\alpha_3 y^3 + \alpha_2 y^2 + \alpha_1 y + \alpha_0)}, \quad (7)$$

with $y \equiv \log_{10} p$ and where the momentum p verifies

$$p^2 c^2 = E_0^2 - E_\mu^2 \quad (8)$$

with $E_\mu = 0.10566$ GeV. When the momentum is expressed in GeV/ c , as is usually the case in the particle physics literature, $c = 1$ in the formula above. Table (3) recalls both the numerical values of the α 's and the E_0 ranges, derived by Bugaev *et al.* (1998).

The class of empirical spectrum models of Bugaev *et al.* (1998) is valid for a wide range of energy and was used as a reference by Hebbeker and Timmermans (2002), who fitted it to experimental datasets and found new normalisations for each set, through an iterative procedure. They obtained a new flux shape, independent of the starting Bugaev *et al.* flux, and described by

$$\Phi_H(p) = A_H 10^{H(y)}, \quad (9)$$

where the function

$$H(y) = h_1 \frac{y^3 - 5y^2 + 6y}{2} + h_2 \frac{-2y^3 + 9y^2 - 10y + 3}{3} + h_3 \frac{y^3 - 3y^2 + 2y}{6} + s_2 \frac{y^3 - 6y^2 + 11y - 6}{3}, \quad (10)$$

with $h_1 = 0.144$, $h_2 = -2.51$, $h_3 = -5.76$, and $s_2 = 2.22$.

A major limitation of the models proposed by Bugaev *et al.* (1998) and by Hebbeker and Timmermans (2002) is that they account only for the vertical incidence, $\theta = 0$. To overcome this limitation, the empirical parameterization proposed by Reyna (2006) can be utilised, which allows to calculate the differential muon intensity for all zenith angles and for a wide range of sea-level energy $1 \text{ GeV} \leq E_0 \leq 2000 \text{ GeV}$:

$$\Phi_R(p, \theta) = \cos^3(\theta) \Phi_B(p \cos\theta), \quad (11)$$

where Φ_B is the Bugaev *et al.* (1998) spectrum given by eq. (7) but with $A_R = 0.00253$, $\alpha_0 = 0.2455$, $\alpha_1 = 1.288$, $\alpha_2 = -0.2555$, and $\alpha_3 = 0.0209$. Φ_B in (11) may be replaced by the Φ_H spectrum of Hebbeker and Timmermans (2002) in eq. (9).

Fig. (1) shows the different spectra discussed in the

Table 2. Values of the parameters of model (2) determined by several authors.

| model | A_G | B_G | γ | $E_{0,\pi}^{\text{cr}}(0)$ | $E_{0,K}^{\text{cr}}(0)$ | r_c | E_0 range (GeV) | Reference |
|-------|-----------------|--------|-----------------|----------------------------|--------------------------|-------|--------------------------------------|--------------------------------|
| MS1 | 0.1258 | 0.0588 | 2.65 | 100 | 650 | 0 | $100 - 10^5$ | <i>Volkova et al.</i> [1979] |
| MS2 | 0.14 | 0.054 | 2.70 | 115/1.1 | 850/1.1 | 0 | $100 - 10^5$ and $\theta < 70^\circ$ | <i>Gaisser</i> [1990] |
| MS3 | 0.175 | 0.037 | 2.72 | 103 | 810 | 0 | $300 - 2.5 \times 10^5$ | <i>Klimushin et al.</i> [2001] |
| MS4 | 0.2576 | 0.054 | 2.77 | 115/1.1 | 850/1.1 | 0 | $2 \times 10^3 - 4 \times 10^4$ | <i>Aglietta et al.</i> [1999] |
| MS5 | 0.26 ± 0.01 | 0.054 | 2.78 ± 0.01 | 115/1.1 | 850/1.1 | 0 | $500 - 2 \times 10^4$ | <i>Ambrosio et al.</i> [1995] |

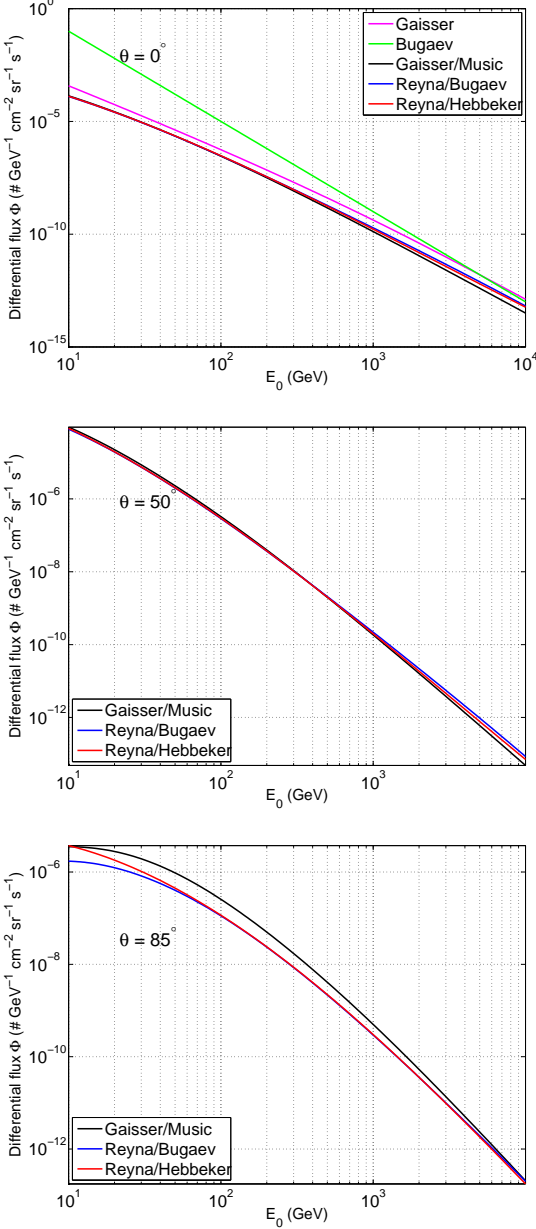


Figure 1. Power spectra discussed in the present paper plotted for different zenith angles (see text for details).

present section for a range of energy E_0 and for zenith angle, θ , equal to 0° , 50° and 85° . For $\theta = 0^\circ$ the Bugaev spectrum strongly departs with unrealistic low-energy flux values up to three orders of magnitude larger than those predicted by the other four spectra. The Gaisser spectrum also predicts significantly larger values than the Gaisser-Music,

Reyna-Bugaev and Reyna-Hebbeker spectra. These latter three spectra are remarkably grouped at low energy while the Gaisser-Music spectrum gives a lower flux in the high-energy domain. This behaviour remains for $\theta = 50^\circ$ but is no more observed for $\theta = 85^\circ$ where the three spectra give flux differing by a factor of 2 in the low-energy domain. For this high zenith angle, the Reyna-Hebbeker spectrum displays a spurious appearance at low energies.

2.2 Effects that may influence the muon flux

Some factors can induce either static (time-independent, locational) or dynamic (time dependent) effects on the observed muon flux. Possible causes of static effects are altitude and geomagnetic latitude, while solar modulation and atmospheric variations may induce temporal fluctuations.

2.2.1 Altitude

The dependence of the muon flux on the altitude, driven by the changing distance between air shower cores and observation point, has been mainly investigated by comparing numerical results of simulation codes with data from balloon-borne experiments (Liu *et al.* 2003). In the latter, atmospheric muon spectra at different altitudes were measured through high-resolution superconducting spectrometers on board of balloons (e.g. Sanuki *et al.* 2002). Bellotti *et al.* (1996) and Hebbeker and Timmermans (2002) found that, for momenta above 10 GeV and altitudes within 1000 m a.s.l., a satisfactory interpolation of both numerical values and measured data is given by a relation of the form:

$$\frac{\Phi(h)}{\Phi(h=0)} = \exp(-h/h_0), \quad (12)$$

where h is the altitude (in m), while h_0 is an empirical characteristic length. According to Hebbeker and Timmermans (2002), $h_0 = 4900 + 750p$, with p being the muon momentum in GeV. Relying on (12), it results that, if the observation point is moved from the sea level to an altitude of 1000 m, a 5 (3)% increase in the flux will be observed, for a muon momentum of 20 (40) GeV.

2.2.2 Geomagnetic latitude

The geomagnetic field acts as a filter against low energy primary cosmic rays, when they propagate through the magnetosphere, down to Earth's atmosphere. Allowed primaries reach the atmosphere and produce secondary muons and neutrinos, while forbidden ones do not contribute to secondary fluxes. Thus, at any geomagnetic latitude, a cut-off

Table 3. Parameters of the fitting formula (7) for the vertical energy spectrum of conventional muons at sea level (data taken from Bugaev *et al.* (1998)).

| p range (GeV) GeV/ c | A_B ($\text{cm}^2 \text{ sr s GeV}^{-1}$) ⁻¹ | α_0 | α_1 | α_2 | α_3 |
|-----------------------------|--|------------|------------|------------|------------|
| 1 – 930 | 2.950×10^{-3} | 0.3061 | 1.2743 | -0.263 | 0.0252 |
| 930 – 1590 | 1.781×10^{-2} | 1.791 | 0.304 | | |
| 1590 – 4.2×10^5 | 1.435×10^1 | 3.672 | | | |
| $> 4.2 \times 10^5$ | 10^3 | 4 | | | |

rigidity (threshold) can be defined. The cutoff values are negligible at high geomagnetic latitudes (near the geomagnetic poles), while, at low latitudes, primary particles need to have a minimum rigidity to reach the atmosphere and this minimum value is higher for positive particles from the East than from the West. According to Cecchini and Sioli (2000), in the equator region the geomagnetic cutoff is about 15 GeV and it causes an effect on the muon spectrum at sea level over momenta up to about 5 GeV.

2.2.3 Solar modulation

Variations in the solar wind velocity modulate the low energy spectrum of cosmic ray particles in the Earth's atmosphere. The dependence of the primary proton spectrum on solar activity follows the form (Bhattacharyya 1978):

$$P_0(E_p + C_p)^{-\gamma}, \quad (13)$$

where $P_0 \approx 1.8 \text{ \#cm}^{-2}\text{sr}^{-1}\text{s}^{-1}\text{GeV}^{\gamma-1}$, $\gamma = 2.7$, and C_p varies from 1.8 during solar minimum to 3 for solar maximum. On the grounds of this parameterization, it results a 3 (1.6)% decrease in the primary proton flux at 50 (100) GeV, when passing from maximum to minimum solar activity. According to Bhattacharyya (1978) and Hebbeker and Timmermans (2002), this effect in the primary flux causes an uncertainty in the muon flux of 1 (10)% at a momentum of 10 (1) GeV. The uncertainty is proportionally lower at higher momenta.

2.2.4 Atmospheric variations

Variations in atmospheric conditions induce changes in the characteristics of the cosmic ray interactions, and thus changes in muon intensity observed at the Earth's surface. In particular, changes in the temperature of the upper layers of atmosphere, and hence changes in the air density, imply that a varying fraction of π – mesons is captured by nuclei and thus a different number of pions decays into muons. The coupling between muon intensity variations and atmospheric temperature can be described by introducing the effective temperature, T_{eff} , i.e. the weighted average of temperatures from the Earth's surface to the top of the atmosphere (Barret *et al.* 1952, 1954; Ambrosio *et al.* 1997),

$$\frac{\Delta I}{I_0} = \alpha_T \frac{\Delta T_{\text{eff}}}{T_{\text{eff}}}, \quad (14)$$

where I_0 is the muon intensity obtained by integrating the flux Φ between the detector threshold and infinity, and assuming an isothermal atmosphere. ΔI represents the fluctuations about I_0 and α_T is the depth-weighted temperature coefficient.

Through underground detectors (MACRO detector, in the Gran Sasso laboratory, Italy, and IceCube observatory, deep in the Antarctic ice), Ambrosio *et al.* (1997) and Tilav *et al.* (2009) found, respectively, a $\pm 5\%$ and a $\pm 10\%$ seasonal fluctuation in the high energy muon rate. In both cases, the fluctuation in the muon rate was shown to be highly correlated with temperature variations in the stratosphere above the two observation points (± 5 and ± 10 K) and α_T was experimentally found to be equal to 0.9. According to Ambrosio *et al.* (1997), for zenith angles $\theta \approx 0$, α_T scales as,

$$\alpha_T = \left(1 + \frac{70}{p_{\text{th}}}\right)^{-1}, \quad (15)$$

where p_{th} is the minimum momentum of the muon flux, I_0 . Accordingly, the effect of atmospheric temperature is important only for muons with high energy.

The barometric effect on the muon flux is a consequence of the mass absorption of muons in the Earth's atmosphere: an increase of barometric pressure above the detector causes a greater absorption and thus a lower detection rate. While the temperature effect is determined by the temperature profile along the Earth's atmosphere, from its top to the detection level, the barometric effect is determined only by the pressure at the observation level.

The pressure coefficient, α_P , which relates changes in muon intensity to atmospheric pressure changes, depends on geomagnetic latitude (the coefficient is greater for detectors located at high latitudes), altitude of the observation point (it is greater at higher altitudes) and average energy of the particles (inverse proportionality). Values of α_P reported in the literature are of the order of -0.5 \%mbar^{-1} for energies around 10 GeV. That implies negligible muon intensity fluctuations for standard atmospheric pressure changes (a few tens of mbar), even at low energies.

2.2.5 Relevance for geophysical muon imaging

Among the factors that induce time-independent effects on the muon flux, the altitude of the observation point may become relevant for geophysical muon imaging. In fact, over the lower energy part of the spectrum, a significant discrepancy might be found between measured and modelled flux, if the latter is referred to the sea level, while the experiment is carried out at high elevations (e.g. the summit zone of a large volcano, usually a few km a.s.l.). Conversely, the geomagnetic cutoff can be disregarded since the effect it induces is small and influences only the lower energy part of the muon spectrum, likely below the threshold energy needed to cross even the smallest opacity of rock (see section 3.1).

Among the factors that may induce time-dependent effects, the solar modulation can be disregarded because of (i)

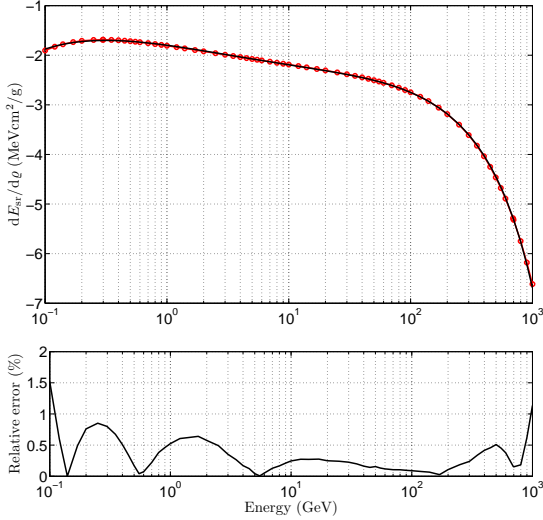


Figure 2. Top: Energy loss for standard rock provided by the Particle Data Group (symbols) and 4th order polynomial fit (solid line). Bottom: relative error between Particle Data Group values and polynomial approximation.

the relatively low amplitude of the fluctuations that it can cause on the muon flux and (ii) the period of its main component (11 years), much longer than the return time of the geophysical phenomena that could be investigated through muon experiments. On the other hand, the seasonal fluctuation that the atmospheric temperature induces on the higher energy part of the muon spectrum may become important, and thus it is to be taken into account, if muon radiographies are repeated at different times to identify time changes in the internal density distribution of the target object.

3 ATTENUATION OF THE MUON FLUX BY ROCK

3.1 Energy loss in matter

High-energies muons are relativistic particles which weakly interact with matter, mainly through ionisation (Adair and Kasha 1976). Bremßstrahlung, nuclear interactions and direct e^-e^+ pair production are the other physical processes by which muons loose energy. The loss of energy may be summarised by,

$$-\frac{dE}{d\rho} = a(E) + b(E)E, \quad (16)$$

where a and b are functions depending on the material properties through which muons propagate. $\rho(L)$ is the density integrated along the trajectory of the muons (see eq. (1)), and the energy loss given by (16) is expressed in $\text{MeV g}^{-1} \text{cm}^2$

The a function represents the energy loss due to ionisation while b is for Bremßstrahlung, nuclear interactions, and e^-e^+ pair production. The determination of these functions requires the computation of cross-sections and Monte Carlo modelling of interactions (Bugaev *et al.* 1998), and the main parameters influencing a and b are the average $\langle Z/A \rangle$ ratio and the bulk density of the material. In practice, computations may either be done with the general purpose software GEANT-4 or with computer programs dedicated to

muon propagation through matter like MUSIC (Kudryavtsev 2009), MMC or MUM (Sokalski *et al.* 2001).

Numerical values for a and b are provided by the Particle Data Group (<http://pdg.lbl.gov>), for a variety of materials and a wide range of energy. Fig. 2 shows the energy loss corresponding to the so-called standard rock ($\langle Z/A \rangle = 0.5$ and $\rho_{\text{sr}} = 2650 \text{ kg m}^{-3}$). When drawn in the log-log domain, the $dE_{\text{sr}}/d\rho$ curve varies smoothly and may be accurately fitted with a polynomial in a wide range of energy. Fig. 2 shows such a fit performed for $E_\mu \leq E \leq 1000 \text{ GeV}$ with a 4th order polynomial and with a relative error never exceeding 2 %. This fit gives:

$$\frac{dE_{\text{sr}}}{d\rho} = -10^{l_4 y^4 + l_3 y^3 + l_2 y^2 + l_1 y + l_0}, \quad (17)$$

where $y = \log E$, with E in GeV, and $l_4 = 0.0154$, $l_3 = -0.0461$, $l_2 = 0.0368$, $l_1 = 0.0801$, $l_0 = 0.2549$.

Excepted for rare instances, almost all types of rocks share the same $\langle Z/A \rangle$ ratio and the only varying quantity is the density. Consequently, the curves a_{sr} and b_{sr} , computed for the standard rock may safely be used to determine the attenuation of the flux of muons across all common rock types. Accordingly, in the remaining of the present paper, we shall use eq. (17) to compute the attenuation of the muon flux regardless of the kind of rock considered.

By knowing the energy loss of muons across rock, it is possible to determine the minimum initial energy, E_{min} , necessary for a muon to cross a given opacity, ρ_L , of rock before hitting the telescope. Practically, E_{min} is found by solving

$$E_{\text{min}} - \int_0^{\rho} \frac{dE}{d\rho} d\rho = E_\mu, \quad (18)$$

where E_μ is the rest energy whose value is given after eq. (8).

The minimum energy, E_{min} , may then be used to compute the integrated flux,

$$I[\varrho, \theta] = \int_{E_{\text{min}}(\varrho)}^{\infty} \Phi(E_0, \theta) dE_0 \quad (\# \text{cm}^{-2} \text{sr}^{-1} \text{s}^{-1}). \quad (19)$$

Eq. (19) gives the time-average number of muons emerging from the geological body as a function of opacity, ϱ .

Because of the power-law nature of the differential spectrum, $\Phi(E_0, \theta)$, the cutoff represented by the E_{min} limit results in a dramatic reduction of the output flux, $I[\varrho(L)]$. That is shown in Fig. (4), which represents the integrated flux computed for several zenith angles and for the Gaisser-Music, Reyna-Bugaev and Reyna-Hebbeker spectra. The similarities and differences observed in the spectra shown in Fig. (1) are retrieved in Fig. (4) and, while both the Gaisser-Music and the Reyna-Bugaev flux appear very similar, the Reyna-Hebbeker significantly departs, especially at high zenith angles.

3.2 Scattering of muons

Despite their low cross-section, muons are continuously scattered along their travel-path across matter through Coulomb scattering with electrons. Indeed, this property is the one exploited in tomography of high-Z material (i.e. with many electrons) for nuclear waste detection (e.g. Jenneson *et*

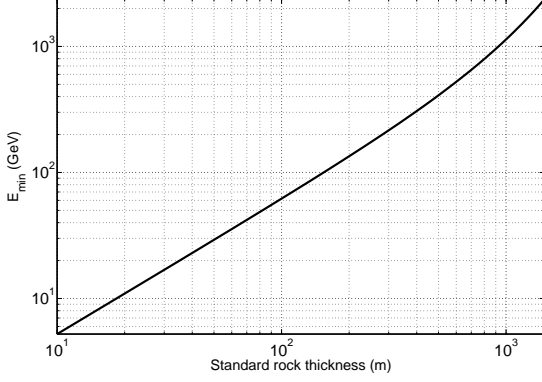


Figure 3. Minimum energy $E_{\min}[\varrho(L)]$ obtained by solving eq. (18) as a function of the standard rock thickness L .

al. 2007; Stanley *et al.* 2008). Experimental study of muon scattering has, for instance, been performed in the Fréjus experiment accounted for by Berger *et al.* (1989). Accounting for the random nature of scattering, the trajectories of the muons are deviated by an angle $\delta\theta$ from their original direction θ with a probability given by a Rayleigh distribution:

$$P(\delta\theta) = \frac{\delta\theta}{\sigma_\theta^2} \exp\left[-\frac{\delta\theta^2}{2\sigma_\theta^2}\right]. \quad (20)$$

The Rayleigh parameter, σ_θ , is given by,

$$\sigma_\theta = \frac{\alpha}{E} \sqrt{\frac{\varrho}{\xi_0}} \left[1 + \kappa \ln \frac{\varrho}{\xi_0}\right], \quad (21)$$

where $\alpha = 13.6$ MeV, $\kappa = 0.038$, and $\xi_0 = 26.54$ g cm⁻² is the radiation length for standard rock.

This equation shows that the scattering dispersion σ_θ of a muon hugely depends on its energy; consequently, it cannot directly be applied to long trajectories across rock since muons lose energy along their paths. For such a situation, when a muon with $E > E_{\min}$ penetrates the rock, it scatters more and more while its energy decreases, according to (16). It is then necessary to integrate a differential form of eq. (21), combined with eq. (16), to obtain the total scattering dispersion. However, due to the E^{-1} dependence of σ_θ , most of the scattering occurs in the very last part of the trajectory where the muon energy is minimum.

As shown in Fig. (3), a minimum energy of 200 GeV is necessary for a muon to cross a rock layer of 300 m and, at this energy level, the scattering, σ_θ , is 0.53 mrad, after a 10 metres-long path. This scattering angle is negligible when compared to the angular resolution $\sim 50 - 100$ mrad of our telescopes (see Section below). This is no more the case if we consider the last 10 metres of the trajectory where the muon energy is reduced by several GeV, leading to a scattering of 80 mrad. The net scattering dispersion may be obtained by summing the squared σ_θ 's (i.e. the variances), computed along the muon trajectory, taking into account the energy loss. For the present example, we obtain a net dispersion $\hat{\sigma}_\theta = 50$ mrad. This value is for the low-energy muons emerging from the rock and, to obtain the total dispersion, we must further integrate (from E_{\min} to ∞) the squared $\hat{\sigma}_\theta$'s, weighted by the differential energy spectrum. Pursuing with the present example where $L = 300$ m of standard rock, the total dispersion falls to ≈ 12 mrad. This values

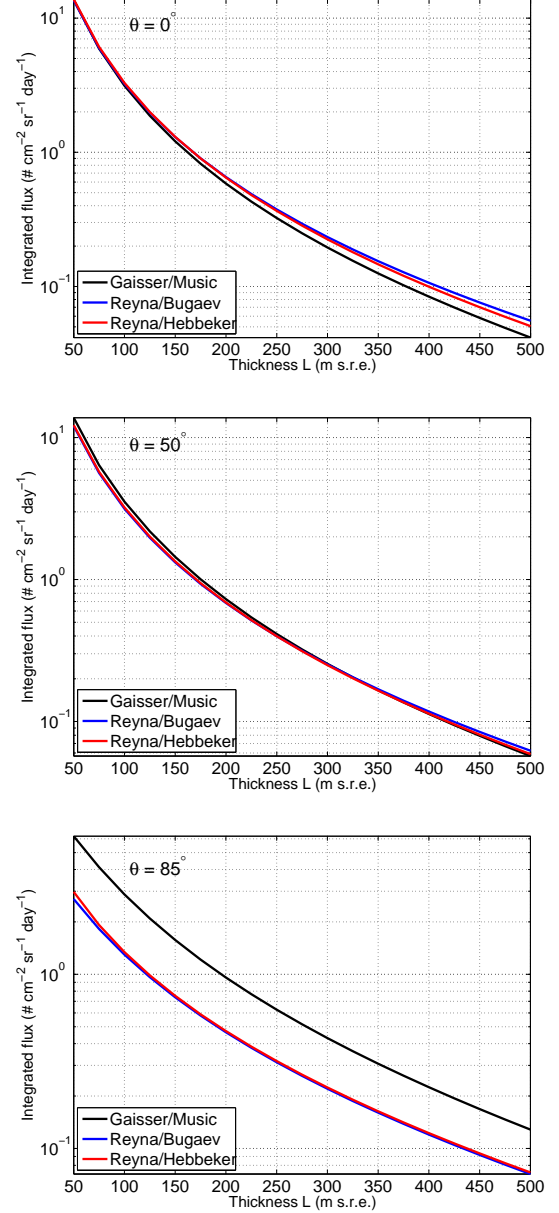


Figure 4. Integrated flux $I[\varrho(L), \theta = 0^\circ, 50^\circ, 85^\circ]$ (19) as a function of the standard rock thickness L expressed in standard rock equivalent metres (m s.r.e.).

risks to ≈ 20 mrad for $L = 50$ m, since more low-energy muons are able to cross.

4 AN EXAMPLE OF MUON TELESCOPE

A central element in muon tomography experiments is the telescope whose influence may be summarised by an acceptance function, \mathcal{T} , given in cm²sr and taking into account the geometrical characteristics of the instrument: the pixel size, the number of pixels, and the distance between the matrices. In practise, the acceptance is the function by which the integrated flux is converted into a number, N , of muons:

$$N(\varrho) = \Delta T \times \mathcal{T} \times I(\varrho), \quad (22)$$



Figure 5. Small-size telescope in operation in the Mont Terri underground laboratory. This telescope is equipped with two 16×16 matrices with 5^2 cm^2 pixels separated by $D = 120 \text{ cm}$ for this setup.

where the integrated flux, I , is given by eq. (19) and ΔT is the duration of the measurement period. Of course, the acceptance depends on the type of telescope and, to give the reader an idea of what the \mathcal{T} function may be, we now briefly describe the telescope we have designed to perform muon tomography experiments in the harsh conditions usually encountered in the summit zone of an active volcano. A complete description of our telescopes (Fig. 5) is given in Gibert *et al.* (2010) and in Lesparre *et al.* (2010). Another telescope with an acceptance similar to ours is described by Uchida *et al.* (2009).

Among the different detection systems available – emulsions (Tanaka *et al.* 2007b), resistive plate chambers (De Asmundis *et al.* 2007), micromegas (Giomataris *et al.* 2006), scintillators (Pla-Dalmau *et al.* 2001) – matrices made with scintillator strips are favoured by the teams doing experiments on volcanoes (Uchida *et al.* 2009; Gibert *et al.* 2010). A detection matrix consists of two series of strips aligned in the x and y directions and forming an array of pixels. A telescope is obtained by placing such matrices on the opposite faces of an imaginary parallelepiped as shown in Fig. 5. The matrices of the telescope we designed are mounted on a modular aluminum frame which can be easily transported to the installation site and assembled in the field. The frame features adjustable legs, to cope with uneven terrains. It also features an upper structure that can pivot 90 degrees with respect to a bottom frame structure, allowing precise orientation of the matrices toward the geological target. Waterproof cases house the matrices and all the other electronics. The above technical features allow our telescopes to be installed in extreme environmental conditions and where hosting facilities are not available. When a muon hits the matrices, the detection system records the front and the rear pixels flashed by ionisation, and the direction of the muon trajectory can be determined.

The total solid angle, Ω , covered by the telescope, and the angular resolution, $\delta\Omega$, depend on the number of pixels, $N_x \times N_y$, their size, d , and the distance, D , separating the two matrices. $\delta\Omega$ covers all muon trajectories able to hit a given pair of pixels, $\{P_{i,j}^F, P_{k,l}^R\}$. All pairs of pixels with the same relative position, $\{m = i - k, n = j - l\}$, share

the same average direction, $\mathbf{r}_{m,n}$, and the same $\delta\Omega(\mathbf{r}_{m,n})$ is assigned to all muons, whatever their actual trajectories. The direction $\mathbf{r}_{0,0}$ is normal to the matrices and corresponds to $N_{0,0} = N_x \times N_y$ pairs of homologue pixels $\{P_{i,j}^F, P_{i,j}^R\}$. For $\mathbf{r}_{m,n}$ with $\{m, n\} \neq \{0, 0\}$, $N_{m,n} < N_{0,0}$ and the larger the shifts m and n , the smaller $N_{m,n}$. Consequently, the directions near $\mathbf{r}_{0,0}$ have a large detection area (i.e. number of pairs of pixels) and those departing too much have a negligible one. The acceptance is obtained multiplying the detection area by the angular resolution,

$$\mathcal{T}(\mathbf{r}_{m,n}) = S(\mathbf{r}_{m,n}) \times \delta\Omega(\mathbf{r}_{m,n}). \quad (23)$$

A telescope with two matrices of $N_x \times N_y$ pixels has $(2N_x - 1) \times (2N_y - 1)$ discrete directions, $\mathbf{r}_{m,n}$, spanning Ω . For instance, the telescope of Fig. 5 has 961 discrete directions. The upper part of Fig. 6 shows the angular resolution, $\delta\Omega(\mathbf{r}_{m,n})$, for this telescope with $N_x = N_y = 16$, $d = 5 \text{ cm}$ and $D = 80 \text{ cm}$. The total angular aperture of the telescope is roughly $\pm 30^\circ$ as can be seen on the X and Y axes of Fig. 6. The acceptance $\mathcal{T}(\mathbf{r}_{m,n})$ is shown in the bottom part of Fig. 6 and, as expected, the largest detection surface corresponds to the normal direction, $\mathbf{r}_{0,0}$, and reaches $\simeq 25 \text{ cm}^2\text{sr}$ in this example. The acceptance is almost zero for a margin corresponding to the directions which most depart from $\mathbf{r}_{0,0}$ and only a fraction of all possible directions of detection will be efficient. Accounting for this effect, the total angular aperture of the telescope is actually restricted to a cone of 15° around $\mathbf{r}_{0,0}$.

Besides the telescope shown in Fig. 5 we plan to produce another one differing only in the number of pixel: $N_x = N_y = 32$ and $d = 5 \text{ cm}$. Depending on its geometrical configuration, this telescope can have an acceptance up to $\approx 250 \text{ cm}^2\text{sr}$ for an angular resolution not exceeding 0.03 sr . However, such a large telescope probably represents the upper limit of what can be done for instruments being installed on rough topography through helicopter hauling. The telescope described by Uchida *et al.* (2009) has $N_x = N_y = 12$ and $d = 7 \text{ cm}$. For $D = 100 \text{ cm}$ this gives $\mathcal{T} \approx 30 \text{ cm}^2\text{sr}$ and an angular resolution less than 0.018 sr .

5 IMAGING CONDITIONS FOR MUON IMAGING

We now use the results obtained in the preceding Sections to establish a link between the data, i.e. the number, N , of muons recorded during a given amount of time, ΔT , the telescope acceptance, \mathcal{T} , and the physical parameter $\varrho(L)$. Taking an acceptance of $15 \text{ cm}^2\text{sr}$ (Fig. 6) and the I -curve of Fig. (4), we find that N may be as high as 1000 muons per day for a rock thickness $L \approx 100 \text{ m}$ or as low as 1 muon per day for $L \approx 1000 \text{ m}$. An important issue is to determine the experimental conditions to be satisfied to be able to distinguish two nearby opacities ϱ_0 and $\varrho_0 + \delta\varrho$ or, equivalently, to statistically make the difference between $N(\varrho_0)$ and $N(\varrho_0 + \delta\varrho)$. Starting from (22) and using (19), we have:

$$\Delta N(\varrho_0, \delta\varrho) \equiv N(\varrho_0 + \delta\varrho) - N(\varrho_0) \quad (24)$$

$$= \Delta T \times \mathcal{T} \times \left. \frac{dI(\varrho)}{d\varrho} \right|_{\varrho=\varrho_0} \delta\varrho \quad (25)$$

$$= \Delta T \times \mathcal{T} \times \Delta I(\varrho_0, \delta\varrho), \quad (26)$$

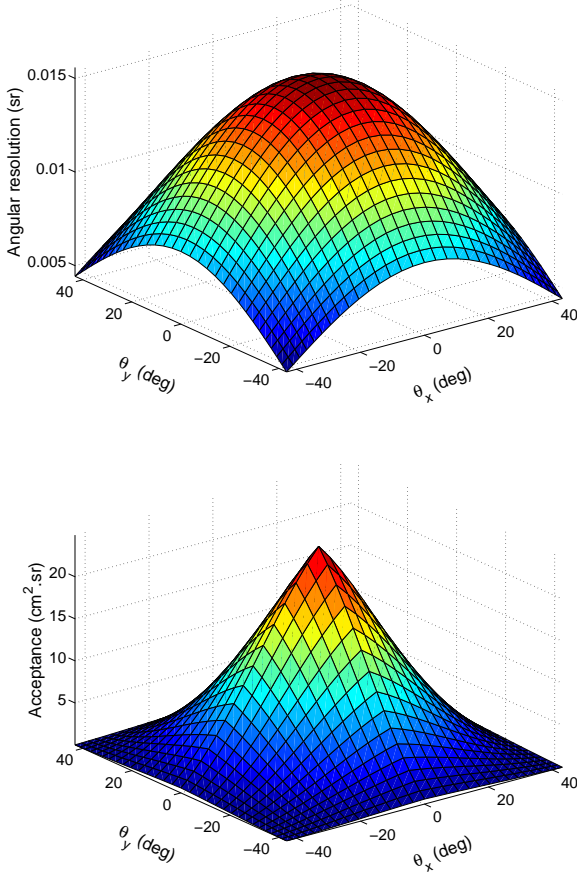


Figure 6. Azimuthal angular properties of the telescope of Fig. 5 equipped with two 16×16 matrices with pixel size $d = 5$ cm and separated by $D = 80$ cm as for the data shown in Fig. 7. Top: Angular resolution $\delta\Omega(\mathbf{r}_{m,n})$ for each discrete direction of sight $\mathbf{r}_{m,n}$ of the pair of matrices. Bottom: Acceptance $\mathcal{T}(\mathbf{r}_{m,n})$.

with

$$\Delta I(\varrho_0, \delta\varrho) = \Phi[E_{\min}(\varrho_0)] \times \left. \frac{dE_{\min}}{d\varrho} \right|_{\varrho=\varrho_0}. \quad (27)$$

Let δN be the half-width of the confidence interval assigned to the measured number of muons $N(\varrho_0)$. The opacity variation $\delta\varrho$ will be resolvable if,

$$\Delta N(\varrho_0, \delta\varrho) = \Delta T \times \mathcal{T} \times \Delta I(\varrho_0, \delta\varrho) > \delta N. \quad (28)$$

Assuming that the sequence forming the N detected events is described by a Poisson process with constant rate N , the central confidence interval, $[N_l, N_u]$, at probability level $1 - \alpha$ is such that:

$$\sum_{n=0}^{N_l} \frac{N^n e^{-N}}{n!} = \sum_{n=N_u}^{\infty} \frac{N^n e^{-N}}{n!} = \frac{\alpha}{2}. \quad (29)$$

Since the Poisson distribution is defined on the set of positive whole numbers, the equalities (29) may not be satisfied exactly, and several intervals with the same confidence level can sometimes be obtained (Conrad *et al.* 2003).

For large enough N (say $N > 50$), the Poisson distribution may be reasonably approximated by a Gaussian with mean N and standard deviation \sqrt{N} . However, the so-called

continuity correction, $n \rightarrow n + 0.5$, must be applied to the Gaussian variable, in order to account for the fact that the Poisson distribution is defined only for integer values, while the Gaussian is for real variables. In practise, we have:

$$\frac{N^n e^{-N}}{n!} \approx \frac{1}{\sqrt{2\pi N}} \exp\left(-\frac{(n + 0.5 - N)^2}{2N}\right). \quad (30)$$

When the Gaussian approximation holds, the confidence interval is obtained through standard procedure, and we have $\delta N = 2\sqrt{N}$ for $1 - \alpha = 0.95$ and $\delta N = \sqrt{N}$ for $1 - \alpha = 0.68$. For this latter case, condition (28) gives,

$$\Delta T \times \mathcal{T} \times \Delta I(\varrho_0, \delta\varrho) > \sqrt{N}. \quad (31)$$

Using expression (22) this equation rewrites as,

$$\Delta T \times \mathcal{T} \times \frac{\Delta I^2(\varrho_0, \delta\varrho)}{I(\varrho_0)} > 1. \quad (32)$$

The left-hand term of condition (32) is determined both by the fixed total opacity of the medium, which depends on the characteristics of the geological target, and by the desired resolution level $\delta\varrho$. This sets the minimum value for the product $\Delta T \times \mathcal{T}$ and the question is to determine whether it is reachable or not. This will clearly depend on the particular constraints attached to a given experimental situation. For instance, one can easily imagine experiments where both the acceptance of the telescope (i.e. its size) and the duration of the measurement period cannot exceed some limits. In such a case, eq. (32) will fix the minimum value for $\delta\varrho$.

6 DISCUSSION OF SEVERAL GEOLOGICAL SITUATIONS

We now present several experimental conditions corresponding to typical applications of muon tomography on the field. We successively briefly discuss experiments in the Mont Terri and Roselend underground laboratories, on La Soufrière volcano and on Mt. Etna volcano.

6.1 Underground laboratories

The Mont Terri underground laboratory (Switzerland) is located in an anticline formed with layers of Opalinus clay and limestones with densities $\rho_{\text{clay}} = 2.4$ and $\rho_{\text{lime}} = 2.7$ (Bossart and Thury 2008). The thickness of the geological cover varies from 250 m to 500 m, depending on the topography of the mountain (Fig. 7) and on the inclination of the telescope presently in operation on this site (Fig. 5). The laboratory is at an altitude of 500 m and the top of the mountain is at ≈ 900 m. Taking a zenith angle of 0° and an average thickness, L , of 400 m, equally divided between clay and limestone, we obtain an integrated flux $I = 0.2516 \text{ \#cm}^{-2}\text{sr}^{-1}\text{day}^{-1}$ in excellent agreement with the data (bottom part of Fig. 7). The structure of the Mont Terri is such that its geometry is invariant in a direction parallel to the axis of the anticline. In such particular circumstances, the telescope may be reconfigured by merging its pixels along the direction parallel to the anticline axis. By doing so, the effective acceptance of the telescope is magnified while the angular resolution is reduced in the same proportions. In the experiment presently discussed, pixels

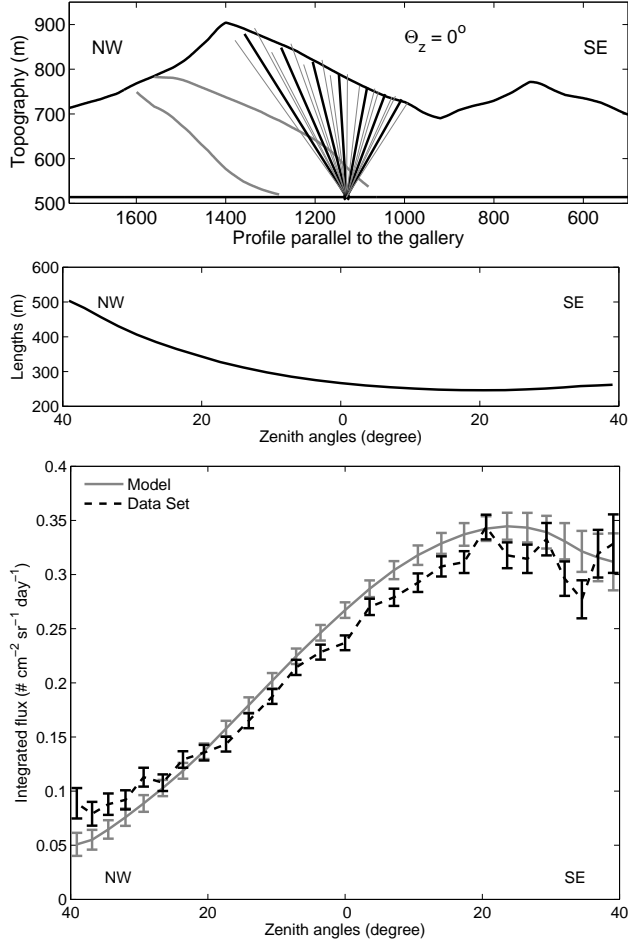


Figure 7. Mont-Terri experiment – Top: cross-section showing the topography profile of the Mont-Terri mountain above the underground laboratory. The fan-like rays symbolise the angular coverage of the telescope. The curved thin line represent the interface between geological layers. Middle: ray length as a function of the zenith angle. Bottom: muon flux recorded by the telescope during one month. Also shown is the theoretical integrated flux I (eq. 19).

were merged by groups of seven, leading to an acceptance, \mathcal{T} , of about $100 \text{ cm}^2 \text{sr}$. Let us suppose that we want to detect a variation of $\pm 10 \text{ m}$ in the position of the interface between clay and limestone, over a total thickness of 300 m , this implies a flux variation of $0.00472 \text{ #cm}^{-2} \text{sr}^{-1} \text{day}^{-1}$ for $I = 0.2175 \text{ #cm}^{-2} \text{sr}^{-1} \text{day}^{-1}$, and eq. (32) gives $\Delta T > 100 \text{ days}$.

The Roselend underground laboratory (French Alps) offers very different conditions from those encountered at the Mont Terri site, with a thickness, L , of the geological cover varying from 10 m to 50 m , depending both on the location along the gallery and on the inclination of the telescope. This gives a much larger integrated flux I comprised between 13 and $185 \text{ #cm}^{-2} \text{sr}^{-1} \text{day}^{-1}$ for $\rho = 2.7 \text{ g cm}^{-3}$. For a density variation $\delta\rho = 0.01 \text{ g cm}^{-3}$ the fluctuation ΔI varies from 0.098 to $0.848 \text{ #cm}^{-2} \text{sr}^{-1} \text{day}^{-1}$. To resolve this density variation with $\mathcal{T} \approx 20 \text{ cm}^2 \text{sr}$, eq. (32) gives a duration ΔT comprised between 13 and 70 days .

6.2 Volcanoes

La Soufrière of Guadeloupe is an andesitic volcano whose lava dome is about five hundred years old (Boudon *et al.* 2008) and which presents a diversified number of hazards including phreatic eruption, flank collapse and explosive magmatic eruption (Komorowski *et al.* 2008). Using electrical resistance tomography, Nicollin *et al.* (2006) found that the lava dome is highly heterogeneous, with massive lava volumes embedded in more or less hydrothermalized materials. Knowing the internal structure of the dome is an important issue because of its implications on flank destabilization models. For this reason, La Soufrière is a priority target for muon imaging (Gibert *et al.* 2010). Gravity data measured on and in the vicinity of the volcano show that the local bulk density varies from 2.2 to 2.7 g cm^{-3} (Gunawan 2005). However, densities as low 1.5 g cm^{-3} may be encountered.

One expected site for a telescope is located at the Col de l'Échelle, on the Eastern side of the volcano. This place is particularly interesting since there is no topographic high present behind the lava dome (i.e. on its western side) to produce perturbing shadow effect. To embrace the whole volcano in a single view, the telescope must have an effective horizontal aperture angle of 90° and zenith angles comprised between 55° and 90° . Accounting for the fact that the extreme angles are useless (top part of Fig. 6), this fixes the matrix distance $D = 80 \text{ cm}$ and the maximum acceptance $\mathcal{T} \approx 20 \text{ cm}^2 \text{sr}$ (bottom part of Fig. 6). The thickness, L , of rock varies from tens of meters at the summit to about 800 m at the base of the volcano, and the corresponding integrated flux, I , is comprised between 0.01 and $10 \text{ #cm}^{-2} \text{sr}^{-1} \text{day}^{-1}$ for a mean density $\rho = 2.2 \text{ g cm}^{-3}$ (Fig. 8). Let us consider a volume of massive andesite (2.7 g cm^{-3}) with a diameter of 100 m embedded in altered rock (2.2 g cm^{-3}), this gives $I \approx 0.076 \text{ #cm}^{-2} \text{sr}^{-1} \text{day}^{-1}$ and $\Delta I \approx 0.009 \text{ #cm}^{-2} \text{sr}^{-1} \text{day}^{-1}$, for a ray length, L of 550 m . Taking an acceptance, \mathcal{T} , of $20 \text{ cm}^2 \text{sr}$, eq. (32) gives a duration $\Delta T > 50 \text{ days}$.

Mt. Etna is a large (1200 km^2) strato-volcano sited on the East coast of Sicily (Italy). It has a base diameter of about 40 km and a height of about 3350 m . The scale of this volcano implies that, at the current state of the art, only a small portion of its edifice can be investigated through muon imaging. In fact, to have a sufficient flux, the thickness of rock to be crossed by muons should not exceed a few kilometers and the time interval needed to resolve a given density contrast, using a mobile detector of limited dimensions, should not exceed the typical period of volcanic processes able to change the internal density distribution of the target structure. One of the active craters in the summit area of the volcano would be a suitable target for the first experiment of muon radiography at Mt. Etna. In particular, the Southeastern Crater would be the more appropriate due to both its size and position. This crater is about 240 m tall (from 3050 to 3290 m a.s.l.), with a base diameter of about 500 m (Fig. 9). Simulations we carried out show that a good installation point for a muon telescope is located on the southern slope of the crater. This point is easily reachable from the dirt track road that crosses the summit zone of the volcano.

Muon rays crossing the middle part of Etna's Southeast crater to reach a detector placed at its base, would have a

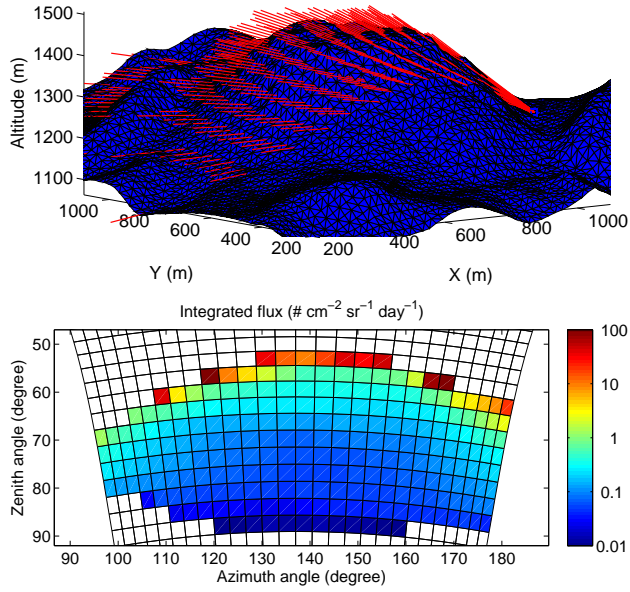


Figure 8. La Soufrière of Guadeloupe model - Top : model of topography in blue, the telescope is located at Col de l'Échelle, the red rays represent some of the muons trajectory across the volcano detected by a 16×16 pixels telescope with a distance between matrices of 80 cm. Bottom : the integrated flux of each trajectory passing through the volcano.

zenith angle of about 68° and would cross about 500 m of rock. This imply a flux of $0.085 \text{ \#cm}^{-2}\text{sr}^{-1}\text{day}^{-1}$, assuming an average density of the crater of 2.5 g cm^{-3} . Let us assume we perform a muon radiography experiment during the period when the summit zone of Etna is free from the snow cover (roughly June - October, $\Delta T \approx 150$ days). Using equation (32) and assuming that \mathcal{T} is $15 \text{ cm}^2\text{sr}$, it results a minimum ΔI of $0.006 \text{ \#cm}^{-2}\text{sr}^{-1}\text{day}^{-1}$. This result can be converted into the minimum resolvable opacity change, $\delta\rho$, which results to be equal to $1.5 \times 10^3 \text{ g cm}^{-2}$. Thus, an inner structure with size exceeding the space resolution of the telescope (about 10 m, assuming a 500 m distance to the target) will be recognized if the density contrast is at least 0.5 g cm^{-3} . Larger inner structures will need proportionally smaller density contrasts in order to be recognized. In any case, even if inner structures have size of the order of a few tens of meters, density contrasts close to 0.5 g cm^{-3} are likely to be encountered if a part of the crater is filled with a low density foamy magma. Hence, as already found by Tanaka *et al.* (2009a), detailed info on the inner architecture (presence and position of conduits, chambers, etc.) and functioning (e.g. convective recycling of degassed magma) of the crater could be retrieved through muon imaging. It is worth stressing that the effect of altitude on the energy spectrum of muons arriving on the summit zone of Etna (above 3000 m a.s.l.) is to be taken into account (see section 2.2.1).

7 CONCLUSIVE REMARKS

We comprehensively discuss the constraints on geophysical imaging using cosmic muons. In our study we take into account the three key elements involved in muon imaging for Earth Sciences purposes, namely: (i) the characteristics of

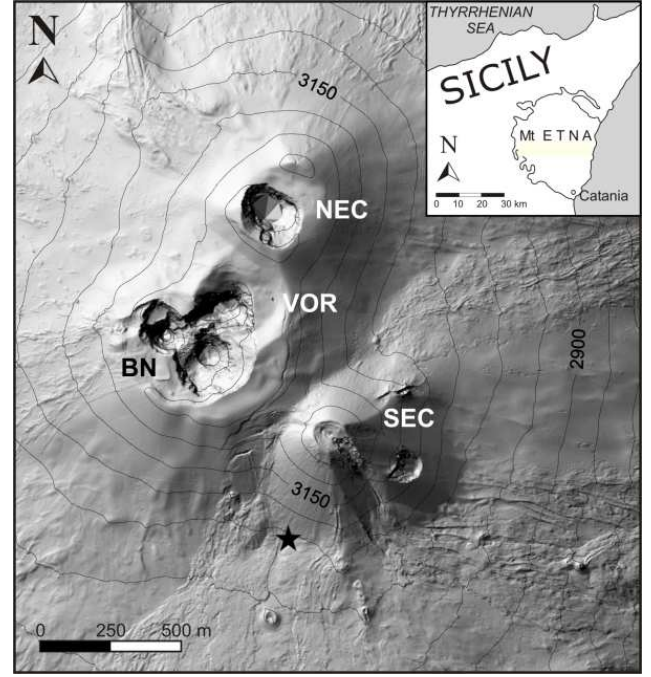


Figure 9. Sketch map of the summit zone of Mt. Etna (topographic map by Favalli *et al.*, 2009) showing the position of the four Summit Craters (NEC = Northeast Crater, VOR = Voragine, BN = Bocca Nuova, SEC = Southeast Crater). The black star marks the planned installation site for the muon telescope. The inset at the top right shows the location of Mt. Etna with respect to Sicily (Italy).

the flux of incident cosmic muons, (ii) the attenuation of the muon flux by rock and (iii) the geometrical characteristics of the detector. The intersection of the constraints imposed by each of these three elements determine the feasibility of muon imaging, under a given set of geological conditions.

The choice of a suitable model describing the flux of incident cosmic muons is of primary importance since errors in the incident flux will be propagated to the resulting density distribution inside the target object. Ideally, the differential flux of muon should be derived through a full Monte Carlo simulation (e.g. CORSIKA; Heck *et al.*, 1998). However, in the framework of a feasibility study, it is advisable to utilise more manageable tools. Many authors have proposed empirical parameter curves to fit observed muon flux data (e.g., Gaisser, 1990; Bugaev *et al.*, 1998; Hebbeker and Timmermans, 2002; Reyna, 2006; Tang *et al.*, 2006). Nonetheless, in spite of the large amount of measured data, there exist significant discrepancies between the different proposed parameterizations. For example, we have shown that, at low energies, the model proposed by Bugaev *et al.* (1998) overestimates the flux by up to three orders of magnitude with respect to the other four models considered. This difference is especially significant when the density distribution inside thin layers of rock is to be investigated and thus even low energy particles contribute to the integrated flux. Among the flux models considered, at last two show a remarkably similar behaviour and can be safely used for the ensuing calculations. Moreover, we show that both the elevation of the observation point and the atmospheric temperature may induce relevant effects on the muon flux that should be taken into account.

The loss of energy that muons undergo when they travel through rock (due to ionization and other interactions) is usually determined through further Monte Carlo modeling (e.g. GEANT or MUSIC; Kudryavtsev 2009), which considers the possible interactions, including muon-nucleus inelastic scattering. However, we show that, using the numerical values provided by the Particle Data Group, an equation can be obtained describing, with sufficient accuracy, the attenuation of the muon flux, as a function of the crossed opacity. In practise, the proposed equation allows to retrieve the minimum initial energy, E_{\min} , that a muon needs to cross a given opacity of rock. E_{\min} is then used as the lower limit of integration to compute the time-average number of muons crossing the target object, starting from the equation of the incident flux.

We have designed a muon detector (under production at the time of this writing) which can work outdoor, even under the harsh conditions that may be encountered when performing geophysical campaigns (e.g. in the summit zone of an active volcano). Thanks to a modular mounting frame, the telescope can be easily transported and, when assembled in the field, can cope with uneven terrains and can be precisely oriented towards the target object. The detection system is based on plastic scintillator bars, forming two matrices at a given distance, and the timing and direction of the hitting muon is retrieved by recording the pixels flashed by ionization in the two matrices. The geometrical characteristics of the telescope (pixel size, number of pixels, distance between the two matrices) determine the acceptance, the function by which the integrated flux is converted into a number of muons.

After discussing the three above key elements, we propose a feasibility equation relating (i) the duration of the muon experiment, (ii) the acceptance of the telescope, (iii) the integrated flux of muons and (iv) the variation in the integrated flux caused by a structure inside the target object, with different density than the surrounding rock. By means of this relation it is possible to delineate a domain of applicability of the muon imaging, in different geological situations. For example, using our results, we show that, after 50 to 150 days of data acquisition, it is possible to distinguish, inside target objects with size of some hundreds of meters and at the $1-\sigma$ confidence level, inner structures with size of $20 \div 100$ m, if they have a density contrast of the order of 0.5 g cm^{-3} with respect to the surrounding material. Such density contrasts can be found inside above-ground volcanic structures due to, e.g., different alteration degree of the rock or presence of conduits filled with low density foamy magma. Thus, even after relatively short observation periods, muon imaging can supply valuable information about the internal structure of a volcano.

Our study is broadly relevant to other research groups as it provides the tools to assess the space/density resolution capabilities of muon imaging, in the allocated time slot and under the conditions imposed by a given geological situation.

ACKNOWLEDGMENTS

This paper is dedicated to the memory of our friend and colleague Albert Tarantola who participated with us to the

launch of the DIAPHANE muon tomography project. The design and the construction of the telescopes greatly benefited from the skilled expertise of Bruno Carlus (computer), Bruno Kergosien (electronics), Pascal Rolland (mechanical engineering), and Sylvain Vanzetto (optical fibres). The DIAPHANE project is financially supported by the IPGP (www.ipgp.fr) BQR grant, the DOMOSCAN ANR (www.agence-nationale-recherche.fr) project, the CNRS/IN2P3 (www.cnrs.fr) Astroparticles program and the MD experiment of the Mont Terri project (www.mont-terri.ch) funded by Swisstopo and CRIEPI partners. Daniele Carbone benefited from a 6-months sabbatical stay in IPGP funded by the Research in Paris grant program (www.paris.fr). This is IPGP contribution ****.

REFERENCES

- Adair, R.K. & Kasha, H., 1976. in: V.W. Hughes, C.S. Wu (Eds.), *Muon Physics*, vol. 1, 323 pp., Academic Press, New York.
- Aglietta, M. & the LVD Collaboration, 1999. Upper limit on the prompt muon flux derived from the LVD underground experiment, *Phys. Rev. D*, **60**, 112001.
- Alfaro, R., Belmont-Moreno, E., Cervantes, A., Grabski, V., Lopez-Robles, J.M., Manzanilla, L., Martinez-Davalos, A., Moreno, M. & Menchaca-Rocha, A., 2003. A muon detector to be installed at the pyramid of the sun, *Revista Mexicana de Fisica*, **49**, 54-59.
- Alvarez, L.W., Anderson, J.A., Bedwei, F.E., Burkhard, J., Fakhry, A., Giris, A., Goneid, A., Hassan, F., Iverson, D., Lynch, G., Miligy, Z., Mousaa, A.H., Sharkawi, M. & Yazolinio, L., 1970. Search for hidden chambers in the pyramids, *Science*, **167**, 832839.
- Ambrosio, M. & the MACRO Collaboration, 1997. Seasonal variations in the underground muon intensity as seen by MACRO, *Astroparticle Physics*, **7**, 109-124.
- Auger, P., 1941. *Les rayons cosmiques*, 136 pp., PUF, Paris.
- Barrett, P.H., Bollinger, L.M., Cocconi, G., Eisenberg, Y. & Greisen, K., 1952. Interpretation of Cosmic-Ray Measurements Far Underground, *Rev. modern Phys.*, **24**, 133-178.
- Barrett, P., Cocconi, G., Eisenberg, Y. & Greisen, K., 1954. Atmospheric Temperature Effect for Mesons Far Underground, *Phys. Rev.*, **95**, 1573-1575.
- Berger, Ch. & the Fréjus Collaboration, 1989. Experimental study of muon bundles observed in the Fréjus detector, *Phys. Rev. D*, **40**, 2163-2171, doi:10.1103/PhysRevD.40.2163.
- Bhattacharyya, D.P., 1978. Effect of solar modulation on the low energy sea level muon spectrum near the geomagnetic equator, *Aust. J. Phys.*, **31**, 451-453.
- Bellotti, R., Cafagna, F., Circella, M., de Cataldo, G., de Marzo, C. N., Giglietto, N., Spinelli, P., Golden, R. L., Stephens, S. A., Stochaj, S. J., Webber, W. R., de Pascale, M. P., Morselli, A., Picozza, P., Ormes, J. F., Streitmatter, R. E., Massimo Brancaccio, F., Papini, P., Piccardi, P., Spillantini, P., Basini, G., Bongiorno, F., Ricci, M., Brunetti, M. T., Codino, A., Grimani, C., Menichelli, M. & Salvatori, I., 1996. Measurement of the negative muon spectrum between 0.3 and 40 GeV/c in the atmosphere, *Phys. Rev. D*, **53**(1), 35-43.
- Borozdin, K.N., Hogan, G.E., Morris, C., Priedhorsky, W.C., Saunders, A., Schultz, L.J. & Teasdale, M.E., 2003. Radiographic imaging with cosmic ray muons, *Nature*, **422**, 277.
- Bossart, P. & Thury, M. (eds), 2008. Mont Terri Rock Laboratory Project, Programme 1996 to 2007 and Results, Rep. Swiss Geological Survey 3, Wabern, Switzerland.
- Boudon, G., Komorowski, J.-C., Villemant, B. & Semet, M.-P., 2008. A new scenario for the last magmatic eruption of La Soufrière of Guadeloupe (Lesser Antilles) in 1530 A.D. Evidence from stratigraphy radiocarbon dating and magmatic evolution of erupted products, *J. Volcanol. Geotherm. Res.*, **178**, 474-490, doi:10.1016/j.jvolgeores.2008.03.006.

- Bugaev, E.V., Kotov, Yu D. & Rosental, I.L., 1970. Cosmic muons and neutrinos, *Atomizdat*, Moscow.
- Bugaev, E.V., Misaki, A., Naumov, V.A., Sinegovskaya, T.S., Sinegovsky, S.I. & Takahashi, N., 1998. Atmospheric muon flux at sea level, underground, and underwater, *Phys. Rev. D*, **58**, 054001.
- Cecchini, S. & Sioli, M., 2000. Cosmic Ray Muon Physics, arXiv:hep-ex/0002052v1.
- Conrad, J., Botner, O., Hallgren, A. & Pérez de los Heros, C., 2003. Including systematic uncertainties in confidence interval construction for Poisson statistics, *Phys. Rev. D*, **67**, 012002.
- Crozon, M., 2005. *Quand le ciel nous bombarde*, 246 pp., Vuibert, Paris.
- De Asmundis, R., Avella, P. & Toglia, F., 2007. Using RPC detectors as cosmic rays monitors, *IEEE Trans. Nucl. Sci.*, **54**, 670-676, doi: 10.1109/TNS.2007.895505.
- Dorman, L.I., 2004. *Cosmic Rays in the Earth's Atmosphere and Underground*, Kluwer Academic Publishers, Dordrecht, The Netherlands, 855 pp.
- Favalli M, Fornaciai, A. & Pareschi, M.T., 2009. LiDAR strip adjustment: application to volcanic areas, *Geomorphology*, **111**, 123-135, doi:10.1016/j.geomorph.2009.04.010.
- Gaisser, T., 1990. *Cosmic rays and particle physics*, Cambridge University Press.
- Gibert, D., Beauducel, F., Déclais, Y., Lesparre, N., Marteau, J., Nicollin, F. & Tarantola, A., 2010. Muon tomography: Plans for observations in the Lesser Antilles, *Earth Planets Space*, **62**, 153165.
- Giomataris, I., De Oliveira, R., Andriamonje, S., Aune, S., Charkpak, G., Colas, P., Fanourakisc, G., Ferrera, E., Giganon, A., Rebourgeard, Ph. & Salin, P., 2006. Micromegas in a bulk, *Nuclear Instr. Methods A*, **560**, 405-408.
- Girerd, C., Gardien, S., Burch, J., Katsanevas, S. & Marteau, J., 2000. Ethernet network-based DAQ and smart sensors for the OPERA long-baseline neutrino experiment, *Nuclear Science Symposium Conference Record, 2000 IEEE*, **2**, 12/111-12/115.
- George, E.P., 1955. Cosmic rays measure overburden of tunnel, *Commonwealth Engineer*, 455457.
- Gunawan, H., 2005. Gravity and microgravity applied to volcanology: Examples of La Soufrière of Guadeloupe and of Merapi (Indonesia), PhD Thesis, IPG Paris (in french).
- Hebbeker, T. & Timmermans, C., 2002. A compilation of high energy atmospheric muon data at sea level, *Astroparticle Physics*, **18**, 107-127.
- Heck, D., Knapp, J., Capdevielle, J.N., Schatz, G. & Thouw, T., 1998. CORSIKA: A Monte Carlo code to simulate extensive air showers, Karlsruhe University, Forschungszentrum Karlsruhe Report FZKA 6019.
- Jenneson, P.M., Gilboy, W.B., Simons, S.J.R., Stanley, S.J. & Rhodes, D., 2007. Imaging large vessels using cosmic-ray tomography muon energy-loss techniques, *Chemical Engineering Journal*, **130**, 75-78.
- Klimushin, S.I., Bugaev, E.V. & Sokalski, I.A., 2001. Parametrization of atmospheric muon angular flux underwater, *Phys. Rev. D*, **64**, 014016, doi: 10.1103/PhysRevD.64.014016.
- Komorowski, J.C., Legendre, Y., Caron, B. & Boudon, G., 2008. Reconstruction and analysis of sub-plinian tephra dispersal during the 1530 A.D. Soufrière (Guadeloupe) eruption: Implications for scenario definition and hazards assessment, *J. Volcanol. Geoth. Res.*, **178**, 491-515.
- Kudryavtsev, V.A., 2009. Muon simulation codes MUSIC and MUSUN for underground physics, *Computer Physics Communications*, **180**, 339-346 doi:10.1016/j.cpc.2008.10.013.
- Leprince-Ringuet, L., 1945. *Les rayons cosmiques. Les mésotons*, Albin Michel ed., Paris.
- Lesparre, N., Marteau, J., Déclais, Y. & Gibert D., 2010. Design and operation of a field telescope for cosmic ray geophysical tomography, *Nucl. Instr. Meth. Phys. Res. A*, in preparation.
- Liu, Y., Derome, L. & Buénerd, M., 2003. Atmospheric muon and neutrino flux from 3-dimensional simulation, *Phys. Rev. D*, **67**(7), 073022-(23 pages).
- Malmqvist, L., Jönsson, G., Kristiansson, K. & Jacobsson, L., 1979. Theoretical studies of in-situ rock density determination using cosmic-ray muon intensity measurements with application in mining geophysics, *Geophysics*, **44**, 1549-1569.
- Nagamine, K., 2003. *Introductory Muon Science*, 208 pp, Cambridge University Press, Cambridge UK.
- Nagamine, K., 1995. Geo-tomographic observation of inner-structure of volcano with cosmic-ray muons, *J. Geography*, **104**, 998-1007.
- Nagamine, K., Iwasaki, M., Shimomura, K. & Ishida, K., 1995. Method of probing inner-structure of geophysical substance with the horizontal cosmic-ray muons and possible application to volcanic eruption prediction, *Nucl. Instr. Meth. A*, **356**, 585-595.
- Neddermeyer, S.H. & Anderson C.D., 1937. Note on the nature of cosmic-ray particles, *Phys. Rev.*, **51**, 884-886.
- Neddermeyer, S.H. & Anderson C.D., 1938. Cosmic-ray particles of intermediate mass, *Phys. Rev.*, **54**, 88-89.
- Nicollin, F., Gibert, D., Beauducel, F., Boudon, G. & Komorowski, J.-C., 2006. Electrical tomography of La Soufrière of Guadeloupe Volcano: Field experiments, 1D inversion and qualitative interpretation, *Earth Planet. Sci. Lett.*, **244**, 709-724.
- Pla-Dalmau, A., Bross, A.D. & Mellott, K.L., 2001. Low-Cost Extruded Plastic Scintillator, *Nucl. Instr. Meth. A*, **466**, 482-491.
- Reyna, D., 2006. A Simple parameterization of the cosmic-ray muon momentum spectra at the surface as a function of zenith angle, arXiv:hep-ph/0604145.
- Sanuki, T., Fujikawa, M., Abe, K., Anraku, K., Asaoka, Y., Fuke, H., Haino, S., Imori, M., Izumi, K., Maeno, T., Makida, Y., Matsui, N., Matsumoto, H., Matsunaga, H., Motoki, M., Nishimura, J., Nozaki, M., Orito, S., Sasaki, M., Shikaze, Y., Sonoda, T., Suzuki, J., Tanaka, K., Toki, Y., Yamamoto, A., Yamamoto, Y., Yamato, K., Yoshida, T. & Yoshimura, K., 2002. Measurements of atmospheric muon spectra at mountain altitude, *Phys. Lett. B*, **541**, 234-242, doi: 10.1016/S0370-2693(02)02265-7.
- Schultz, L.J., Borozdin, K.N., Gomez, J.J., et al., 2004. Image reconstruction and material Z discrimination via cosmic ray muon radiography, *Nucl. Instr. Meth. A*, **519**, 687-694.
- Sokalski, I.A., Bugaev, E.V. & Klimushin, S.I., 2001. MUM: flexible precise Monte Carlo algorithm for muon propagation through thick layers of matter, *Phys. Rev. D*, **64**, 074015.
- Stanley, S.J., Rhodes, D., Jenneson, P.M., Gilboy, W.B. & Simons, S.J.R., 2008. See inside: The development of a cosmic ray muon imaging system to aid the clean up of the UKs nuclear waste legacy, *Annals of Nuclear Energy*, **35**, 507-517.
- Tanaka, H., Nagamine, K., Nakamura, S.N. & Ishida, K., 2005. Radiographic measurements of the internal structure of Mt. West Iwate with near horizontal cosmic ray muons and future developments, *Nucl. Instr. Meth. A*, **555**, 164-172.
- Tanaka, H., Nakano, T., Takahashi, S., Yoshida, J., Ohshima, H., Maekawa, T., Watanabe, H. & Niwa, K., 2007a. Imaging the conduit size of the dome with cosmic ray muons: The structure beneath Showa Shinzan Lava Dome, Japan, *Geophys. Res. Lett.*, **34**, L22311, doi:10.1029/2007GL031389.
- Tanaka, H., Nakano, T., Takahashi, S., Yoshida, J., Takeo, M., Oikawa, J., Ohminato, T., Aoki, Y., Koyama, E., Tsuji, H. & Niwa, K., 2007b. High resolution imaging in the inhomogeneous crust with cosmic ray muon radiography: The density structure below the volcanic crater floor of Mt. Asama, Japan, *Earth Planet. Sci. Lett.*, **263**, 104-113.
- Tanaka, H., Nakano, T., Takahashi, S., Yoshida, J. & Niwa, K., 2007c. Development of an emulsion imaging system for cosmic-ray muon radiography to explore the internal structure of a volcano, Mt. Asama, *Nucl. Instr. Meth. A*, **575**, 489-497.
- Tanaka, H. & Yokoyama, I., 2008a. Muon radiography and deformation analysis of the lava dome formed by the 1944 eruption of Usu, Hokkaido – Contact between high-energy physics and volcano physics, *Proc. Jpn. Acad.*, **B84** 107-116.
- Tanaka, H., Nakano, T., Takahashi, S., Yoshida, J., Takeo, M., Oikawa, J., Ohminato, T., Aoki, Y., Koyama, E., Tsuji, H., Ohshima, H., Maekawa, T., Watanabe, H. & Niwa, K., 2008b. Radiographic imaging below a volcanic crater floor with cosmic-ray muons, *American Journal of Science*, **308**, 843-850.
- Tanaka, H., Uchida, T., Tanaka, M., Shinohara, H. & Taira, H., 2009a. Cosmic-ray muon imaging of magma in a conduit: Degassing process

- of Satsuma-Iwojima Volcano, Japan, *Geophys. Res. Lett.*, **36**, L01304, doi:10.1029/2008GL036451.
- Tanaka, H., Uchida, T., Tanaka, M., Takeo, M., Oikawa, J., Ohminato, T., Aoki, Y., Koyama, E. & Tsuji, H., 2009b. Detecting a mass change inside a volcano by cosmic-ray muon radiography (muography): First results from measurements at Asama volcano, Japan, *Geophys. Res. Lett.*, **36**, L17302, doi:10.1029/2009GL039448.
- Tang, A., Horton-Smith, G., Kudryavtsev, V.A. & Tonazzo, A., 2006. Muon simulations for Super-Kamiokande, KamLAND, and CHOOZ, *Phys. Rev. D*, **74**, 053007, doi:10.1103/PhysRevD.74.053007.
- Tarantola, A., 2005. *Inverse Problem Theory and Methods for Model Parameter Estimation*, 342 pp., Society for Industrial and Applied Mathematics, Philadelphia.
- Tilav, S., Desiati, P., Kuwabara, T., Rocco, D., Rothmaier, F., Simmons, M. & Wissing, H., for the IceCube Collaboration, 2009. Atmospheric Variations as observed by IceCube, Proceedings of the 31st ICRC, Łódź.
- Uchida, T., Tanaka, H. & Tanaka, M., 2009. Space saving and power efficient readout system for cosmic-ray muon radiography, *IEEE trans. Nuclear Sci.*, **56**, 448-452.
- Volkova, L.V., Zatsepin, G.T. & Kuzmichev, L.A., 1979. *Sov. J. Nucl. Phys.*, **29**, 645.

2.3 Muons tomography applied to geosciences and volcanology, [7]

J. Marteau^{a,*}, D. Gibert^b, N. Lesparre^b, F. Nicollin^c, P. Noli^a, F. Giacoppo^e

^a*Institut de Physique Nucléaire de Lyon (UMR CNRS-IN2P3 5822), Université Lyon 1, Lyon, France.*

^b*Institut de Physique du Globe de Paris (UMR CNRS 7154), Sorbonne Paris Cité, Paris, France.*

^c*Géosciences Rennes (CNRS UMR 6118), Université Rennes 1, Bât. 15 Campus de Beaulieu, 35042 Rennes cedex, France.*

^d*Università degli studi di Napoli Federico II & INFN sez. Napoli, Italy.*

^e*Laboratory for High Energy Physics, University of Bern, Sidlerstrasse 5, CH-3012 Bern, Switzerland.*

Abstract

Imaging the inner part of large geological targets is an important issue in geosciences with various applications. Different approaches already exist (e.g. gravimetry, electrical tomography) that give access to a wide range of informations but with identified limitations or drawbacks (e.g. intrinsic ambiguity of the inverse problem, time consuming deployment of sensors over large distances). Here we present an alternative and complementary tomography method based on the measurement of the cosmic muons flux attenuation through the geological structures. We detail the basics of this muon tomography with a special emphasis on the photo-active detectors.

Keywords: cosmic rays, muon, volcano, tomography, telescope

PACS: 14.60.-z, 95.55.Vj, 91.40.-k, 93.85.-q

1. Introduction and motivations

Monitoring natural events such as earthquakes, volcanic eruptions, landslides and tsunamis has immense importance, both scientific and societal. The interest of volcano radiography arose in the last decades in Japan [1–4], which has a large volcanic and seismic activity, like other places in the world such as Italy and Iceland in Europe or the Antilles belt in the Atlantic ocean. Because of the possible vicinity of populated areas, volcanoes require careful monitoring of their activity and precise modelling of their geophysical evolution.

Consider for instance Lesser Antilles, a subduction volcanic arc with a dozen of active volcanoes located in populated areas. The volcanoes of Martinique (La Montagne Pelée), Guadeloupe (La Soufrière), and Montserrat (The Soufrière Hills) presented an eruptive activity since the beginning of the 20th century. It is therefore crucial to

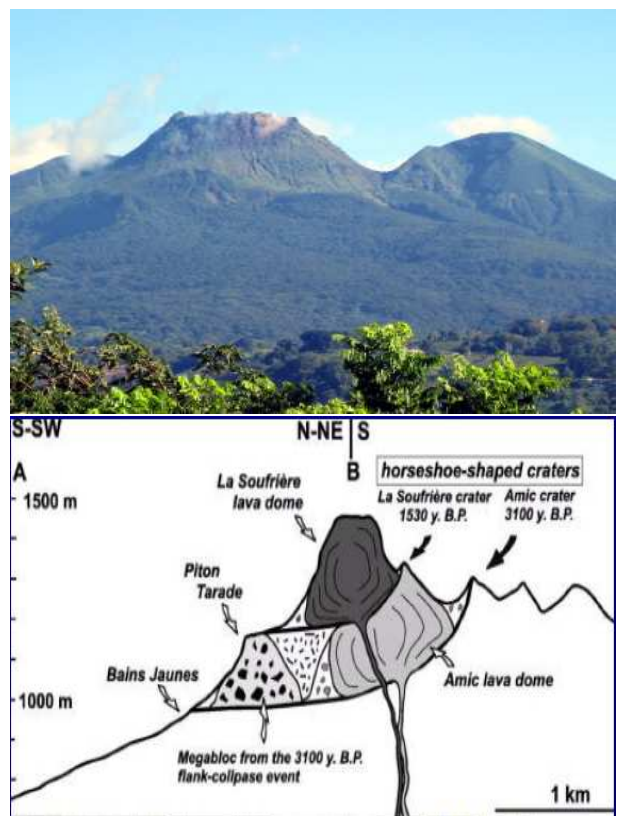


Figure 1: La Soufrière of Guadeloupe: picture and model.

*Corresponding author

Email address: marteau@ipnl.in2p3.fr (J. Marteau)

18 evaluate their eruptive evolution in the near future to and 55
19 quantify the associated risk for surrounding inhabitants. 56
20 Reaching these goals requires accurate imaging of the vol- 57
21 cano's inner structure and quantitative estimates of the 58
22 related parameters (variations of volume, density, strain, 59
23 or pressure) associated with fluid transports (magma, gas, 60
24 or water) or physical and chemical evolution of the volcanic 61
25 materials. La Soufrière of Guadeloupe, an andesitic vol- 62
26 cano whose lava dome is about five hundred years old [5], 63
27 is particularly relevant since it presents a diversified num- 64
28 ber of hazards including phreatic eruption, flank collapse 65
29 and explosive magmatic eruption [6]. Its dome is very het- 66
30 erogeneous, with massive lava volumes embedded in more 67
31 or less hydrothermalized materials [7]. Given the constant 68
32 erosion of the volcano due to the tropical intensive rain 69
33 activity, the evolution of such a lacunary structure may be 70
34 rapid, with formation of cavities, that may be filled with
35 pressurized and likely very acid fluids, resulting in flank
36 destabilization. On top of that present structural mod-
37 els show that the dome sits on a 15° N-S inclined plane,
38 leading to an overall very unstable structure (Fig.1). This
39 particular example shows that a precise knowledge of the
40 dome's internal structure is a key issue for the global mod-
41 elling and understanding of the volcanoes. For this reason,
42 La Soufrière has been chosen as priority target for muon
43 imaging [8], which constitutes one of the most promising
44 tools to obtain direct information on the density distribu-
45 tion inside geological objects.

46 2. Tomography basics

47 The interest of muon tomography for Earth Sciences
48 purposes soon arose after the discovery of cosmic rays and
49 of the muon. The cross-section of that particle at those
50 typical energies makes it a perfect probe since it is able
51 to cross hundredths of meters of rock with an attenua-
52 tion related to the amount of matter along its trajectory
53 [9]. Since it is a charged particle, its detection is quite 71
54 straightforward. The first studies relevant to tomography 72

in geosciences, were motivated by the need to characterise
the geological burden overlying underground structures, in
particular laboratories hosting large particles experiments
aimed at detecting rare events in a silent environment (the
so-called “cosmic silence” [10]). This type of “underground
tomography” is pursued nowadays in the applications of
long-term storage where detailed knowledge is required on
the geological environment (nature and borders of vari-
ous layers) and for mining geophysics. Applications other
than those directly related to underground physics require
smaller, modular, autonomous detectors movable on the
field and able to reject efficiently the background. The
pioneering archaeological investigations performed in the
Egyptian Chephren pyramid by Alvarez et al. in the seven-
ties [11], looking for some hidden room inside the pyramid,
reveal the feasibility of the method.

A muon radiography uses the same basic principles
than a standard medical radiography: measuring the at-
tenuation of a beam (cosmic muons versus X-rays) when
crossing matter (rock vs human flesh) with a sensitive de-
vice. A detailed discussion of all parameters is given in
[12]. The measurement gives access to the opacity ϱ
of the geological structures by comparing the muons flux Φ
after crossing the target to the incident open sky flux, Φ_o .
Various models give analytical expressions of the muon
flux from the two-body decays of pions and kaons and
assuming a primary proton flux spectrum roughly follow-
ing a power law $\approx E_p^{-2.7}$ [13–15]. The opacity is con-
verted to density ρ by inverting the integral equation :
 $\varrho(\text{kg.m}^{-2}) \equiv \int_L \rho(\xi) d\xi$, L denoting particles trajectory with
local coordinate ξ . The muons energy loss (and potential
absorption) on their way through rock accounts for the
standard bremsstrahlung, nuclear interactions, and e^-e^+
pair production physical processes, taken as :

$$-\frac{dE}{d\varrho}(\text{MeV g}^{-1} \text{ cm}^2) = a(E) + b(E)E, \quad (1)$$

where the functions a and b depend on the crossed mate-
rial properties [16]. The flux of muons emerging from the

target is the integral of Φ over the energy, ranging from $E_{\min(\varrho)}$, the minimum initial energy necessary to cross given opacity ϱ , to infinite (Fig.2). This flux is influenced

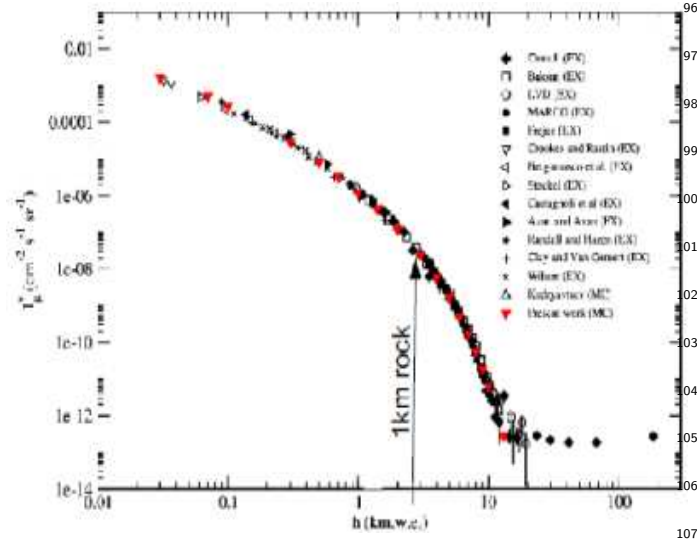


Figure 2: Integrated flux computed as a function of the standard rock thickness L in meters-water-equivalent (m.w.e.) compared to experimental points.

by various environmental parameters such as altitude, geomagnetic cut-off, solar modulation, atmospheric variations to be accounted for in the simulation models. Finally the number of detected muons is the convolution of the muons flux crossing the target, the data taking duration and the telescope acceptance, which is the key experimental parameter that one may evaluate from the simulation and/or from the data themselves.

3. Photo-active detectors for tomography

3.1. The DIAPHANE project

DIAPHANE is the first european project of tomography applied to volcanology. It started in 2008 with a collaboration between three French institutes : IPG Paris, IPN Lyon and Géosciences Rennes to promote muon tomography in the French Earth Science and Particle Physics communities [8]. The first objectives of the project were to make technological choices for the muon telescopes and

to define a design suitable for the difficult field conditions encountered on the Lesser Antilles volcanoes. The detector's design : plastic scintillator, optical fibres, pixelized photomultipliers and triggerless, smart, Ethernet-capable readout electronics, is based on the state-of-the-art opto-electronics technology, known for its robustness and stability in extreme working conditions. Modularity and limits in weight are also imposed by transportation constraints, some positions on the flank of the volcanoes being accessible only by helicopter. A standard detector (or "telescope") comprises 3 independant XY detection planes with autonomous and low power consumption readout system recording and timestamping their own hits in auto-trigger mode. The event-building is performed quasi on-line, via software procedures, by sorting all raw data in time and looking for time coincidences between hits passing the various trigger cuts. Data are transferred continuously via Ethernet wifi and are directly accessible remotely. No shift on-site are needed (concept of the unmanned sensors). The detector is powered through solar panels. Weight, power consumption, robustness and costs have been optimized to the best achievable compromises for that type of field operating detector [17].

Detection matrices. Two layers (X & Y) scintillator bars are glued between 1.5 mm thick anodised aluminium plates. The scintillator bars were provided by Fermilab with a rectangular cross-section of $5 \times 1 \text{ cm}^2$ and are co-extruded with a TiO_2 reflective coating and a 1.5 mm diameter central hole to host an optical fibre [18]. Two different fibres are used to optimize the emission-absorption spectra matching and decrease the attenuation length : wavelength shifting (WLS) fibre (Bicron BCF 91A MC) glued with standard optical cement (Bicron BC-600) in the bar and, through a custom PEEK optical connector, a clear fibre (Bicron BCF-98 MC) down to the photosensor. Three matrices are used in coincidence in a complete telescope. The total aperture angle and the angular resolution of the

telescope may be adjusted by changing the distance between the matrices.

Photodetectors. Hamamatsu 64 channels multi-anode photomultipliers are used baseline photosensors (H8804-mod5 and its upgraded version H8804-200mod). These PMTs are robust and do not exhibit any temperature/humidity dependance. Their gains and pedestals are monitored regularly and are stable within a few percents. The present design also foresees optional upgrade with Hamamatsu MPPC (S10362-11-050C) directly connected onto the optical plugs of the scintillator bars w/o the clear fibres. The MPPCs have very attractive performances in terms of single photon sensitivity and photon resolution power, which are key features to improve the muon detection efficiency. Nevertheless their dark count rates and thermal fluctuations are a concern and require careful commissioning. Dedicated electronics, adapted from the PMT's one, is presently under tests.

Readout system. The global data acquisition system is built as a network of “smart sensors” [19, 20]. The PMT data are collected by two multichannel front-end chips, then digitized and pre-processed by an Ethernet Controller Module (hosting a 32-bit RISC CPU with a Linux 2.4 OS, a FPGA and a FIFO) plugged on a Controller Mother Board (including a fast ADC, a HV module and a clock decoding system). The same type architecture is also valid for the MPPC option where only the front-end stage has to be adapted. The distributed client/server software is based on the CORBA standard. Since the telescope is running in triggerless mode, event timestamp accuracy is a critical issue. A clock broadcasting system synchronizes all sensors with a common clock unit regulated by GPS.

Mechanical structure. The frame of the telescope is built with slotted and anodised aluminium profiles. The detection matrices and R/O system fit in a single box made with 4 profiles and two 1 mm thick aluminium plates. Tightness against water and light is obtained with a seal applied

between the aluminium plates and the profiles. Four connectors complying with the IP67 norm are used to ensure power supply and data transfer, and a valve equipped with a Gore Tex membrane allows evacuation of water vapour without letting liquid water to penetrate into the box. The supporting structure of the telescope is made with the same type of profiles, the full structure being articulated to change the inclination of the matrices. Pictures of the telescope are shown in Fig.3.



Figure 3: Left: detection plane with 16×16 scintillator bars, connected via optical fibres to the PMT+R/O system. Right: a3-planes detector installed on La Soufrière (Ravine Sud).

3.2. First results and comparisons with other methods

As stated above, the acceptance of the telescope is a key parameter since the goal of the project is to assign an opacity and therefore a density to the target from an absolute measurement of flux. Many corrections may be inferred to the theoretical acceptance deduced from solid angles calculations. The experimental inefficiencies are corrected either directly from the light yield measurement or indirectly from the overall data sets themselves. Details on the methods may be found in Ref.[12, 21]. Typical acceptance curves and corrected open sky muons flux (showing the expected symmetry) are shown in Fig.4.

Three DIAPHANE telescopes have been built and have been recording data on the field. The first one was put in the Mont-Terri underground laboratory (Switzerland), located in an anticline formed with layers of Opalinus clay and limestones with densities $\rho_{\text{clay}} = 2.4$ and $\rho_{\text{lime}} = 2.7$ [22]. This place was chosen to fully commission in-situ a

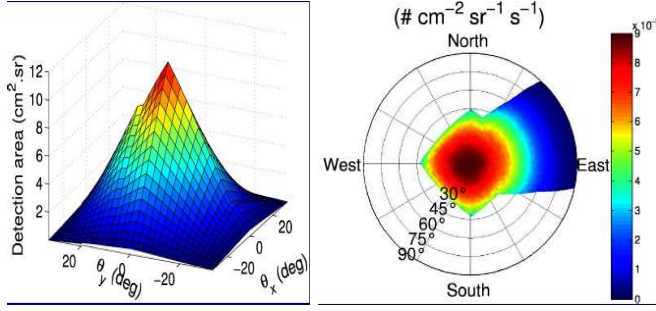


Figure 4: Left: acceptance function of a 16×16 3-planes detector before correction. Right: corrected open sky muons flux.

muon telescope and constrain detector performance, data analysis and simulations models since the geological layers and topography are well known. This telescope is still taking data and is deployed in various places of the gallery to sample the geological layers and make redundant measurements.

The second telescope has been deployed on the Etna volcano for a short trial period during summer 2010 and was able to see within a few days the profile of the volcano. The scale of this volcano implies that, at the current state of the art, only a small portion of its edifice can be investigated through muon imaging. Further campaigns are planned on the Etna following preliminary studies detailed in [12].

The third telescope has been installed on La Soufrière of Guadeloupe, one of the volcanoes with hardest environmental conditions. The geophysics case of this volcano was discussed in the previous sections. Two sites have been already explored, roughly at 90° of each other (“Ravine Sud”, accessible by car and “Roche Fendue” only accessible by helicopter). These two orthogonal views show not only a very good compatibility with each other but also with other measurements carried out with different methods on the same place (gravimetry and electrical tomography). Fig.5 shows the large density variations observed in the inner structure. Preliminary analysis indicates presence of large low density volumes within the cone, also seen in electrical tomographic data (highly conductive zones be-

ing inferred either to hydrothermally washed zones or to acid zones), and reveals the existence of large hydrothermal channels to be accurately monitored. The DIAPHANE

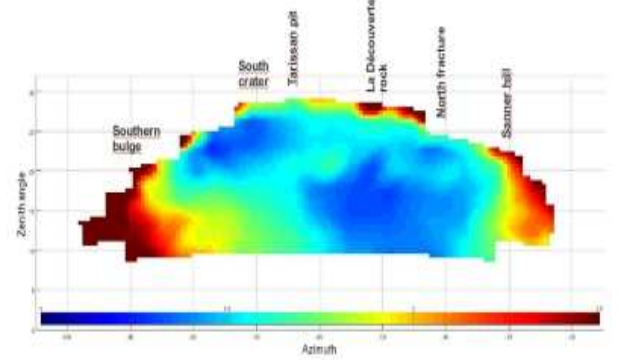


Figure 5: Density profile obtained at the Roche Fendue site.

project has very rich and intense perspectives with the exploration of other fields of view and at a short-term scale the deployment of a network of telescopes (with larger acceptance) running in parallel to perform real-time 3D tomography of the volcano and sample some particularly sensitive zones (like recently opened faults) that may evolve quickly in time.

3.3. The MURAY project

The MU-RAY project [23] aims at the construction of muon telescopes with angular resolution comparable with that obtainable with emulsions, but with real-time data acquisition and larger sensitive area. The telescopes are required to be able to work in harsh environment imposing a modular structure, each module being light enough to be easily transported by hand. Further requirements are mechanical robustness and easy installation. Power budget must fit a small solar panel system’s capability. Good time resolution can improve background suppression by measuring the muon time of flight.

Scintillator features. A telescope prototype is built in Naples University laboratory and it consists of three $1 \times 1 \text{ m}^2 XY$ stations (Fig.6). The third station will be used to study possible backgrounds, as the one induced by cosmic-ray

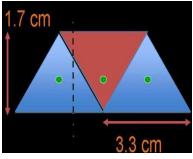


Figure 6: Left: triangular shape of the scintillator bars used in the MURAY project. Right: a3-planes detector in the lab.

showers. Each station is made by two planes disposed in orthogonal way. Each plane is composed by two adjacent modules made by 32 triangular plastic scintillator strips. Scintillator bars are produced by extrusion process at Fermilab, for D0 [24] and Minerva [25] experiments, in pieces as long as 6m, with a hole along the center. The core (Dow Styron 663W) is doped with blue-emitting fluorescent compounds (PPO 1% and POPOP 0.03%). The surface has a co-extruded TiO₂ coating (0.25mm thick) to increase internal reflectivity and to shield from environment light. The use of isosceles triangular shape allows the construction of very compact, crack-free planes. Moreover, the measurement of the light output produced by two adjacent strips enables the determination of the particle crossing distance between two contiguous fibers, improving the spatial resolution. The triangular bars are glued to each other and over two 2mm thick fibreglass plates, creating a very solid module. Light from scintillator is collected by 1mm diameter WLS fibre BICRON BCF92, glued inside the bar to maximize light collection efficiency. Fibres are mirrored at one end using the Al sputtering facility of the Frascati INFN laboratory [26].

Photodetectors and electronics. The light is readout by silicon photomultipliers (SiPM) [27, 28] which offer several advantages. Their robustness is mandatory for the environmental conditions; their very low power consumption (less than 1mW per channel) is relevant due to limited power budget. One of main SiPM drawbacks is the gain temperature dependence that affects the detector perfor-

mance. For this reason the SiPMs' temperature will be controlled using Peltier cells. In order to optimize the power consumption, we decided to group together 32 die SiPMs in a single connector (PCB). The fibres are glued to a custom 32-channel optical connector, which will be fixed to the module chassis and mechanically coupled with the PCB. One side of the Peltier cells is thermally in contact with the back side of the PCB while plastic guarantees a good thermal insulation with respect to the environmental temperature. A rubber O-ring around the sensitive area is used to ensure light and air tightness. Two temperature sensors are located on the PCB for the Peltier cells control circuit. The SiPM front-end electronics readout is based on SiPM Read-Out Chip (SPIROC) ASIC developed by OMEGA group (LAL, CNRS-IN2P3 [29]).

Geophysics case. Today around 600,000 people are living at the base and along the slopes of the Vesuvius volcano, in a so-called "red" area which has been classified at the highest volcanic risk in Europe. Mt. Vesuvius is therefore among the most studied volcanoes in the world. The knowledge of the inner structure of the volcano edifice and subsoil structure is of the greatest importance to build realistic scenarios of the next eruption through accurate simulations (magma upraising mechanism and eruption). Even if the Vesuvius has been thoroughly investigated using the traditional geophysical methods (gravimetric, seismological, electromagnetic), muon radiography may help by improving the resolution of the cone inner structure by one order of magnitude.

4. Other techniques : gaseous detectors and nuclear emulsions

4.1. Gaseous detectors

Since there is not an unique way to detect muons, various projects arose recently using gaseous detectors: glass RPC for the TOMUVOL project (radiography of the Puy-de-Dôme, Clermont-Ferrand, France) and gas TPC for the

313 T2DM2 project (hydrogeology of the karst complex around
 314 the LSBB, Rustrel, France). Those projects have taken
 315 their first data this year and interesting results are awaited
 316 soon.

317 4.2. Probing matter with emulsions

318 Nuclear emulsion particle detectors feature incompa-
 319 rable high spatial and angular resolution ($< 1 \mu m$ and a
 320 few $mrad$, respectively) in the measurement of ionizing
 321 particles tracks. With the advent of fast electronic detec-
 322 tors, the emulsion technique has experienced a period of
 323 decline up to 20 years ago since when impressive progress
 324 in the high-speed automated scanning and industrial pro-
 325 duction have determined a new boost in the application
 326 of this technique in high-energy physics experiments. A
 327 nuclear emulsion is essentially a photographic plate where
 328 silver halide crystals with a typical size of $0.2 \mu m$ are ho-
 329 mogeneously dispersed in a gelatin matrix of about $50 \mu m$
 330 thickness. When such an emulsion is exposed to ionizing
 331 radiation or light, clusters of silver atoms are produced.
 332 These form latent image centres that became visible un-
 333 der an optical microscope when they are reduced to metal-
 334 lic silver filaments (grains) through a chemical developing
 335 process. A typical emulsion film produced industrially by
 336 FUJI Film Co., as a result of a joint R&D program with
 337 the OPERA Collaboration [30], consists of $\sim 10^{14}$ silver
 338 halide crystals. Each of them has a detection efficiency
 339 of 20% for minimum ionizing particle and a sensitivity of
 340 $30 \div 40$ halide grains per $100 \mu m$.

341 In addition to their spatial and angular resolution, tracker
 342 detectors based on nuclear emulsions are ideal for muon
 343 radiography for their data storage capability, portability
 344 and rather simple implementation in difficult environments
 345 such as, for examples, volcanoes. Moreover, nuclear emul-
 346 sion films do not need power supply and electronic front-
 347 end readout systems. The high spatial resolution of nu-
 348 clear emulsion films was first exploited by Tanaka and his
 349 co-workers for the muon radiography of some volcanoes in

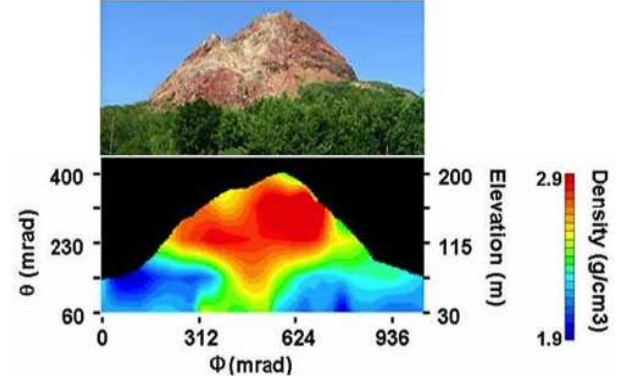


Figure 7: Top: view of the Showa-Shinzan lava dome. Bottom: average density distribution projected onto the detector's plane.

Japan. In 2007 they performed a test measurement for
 imaging the conduit of the Showa-Shinzan lava dome, on
 the east flank of Usu volcano by using quasi-horizontal
 cosmic-ray muons [31]. A muon detector consisting in a
 set of emulsion chambers with an area of $6000 cm^2$ was
 exposed for three months. Fig. 7 shows the reconstructed
 average density of the dome summit. Recently the Labora-
 tory for High Energy Physics (LHEP) of the University of
 Bern has started an R&D program on nuclear emulsion de-
 tectors for muon radiography in the framework of the Inno-
 vative Nuclear Emulsion Technologies (INET) project, fi-
 nanced by the Switzerland-Russian Scientific and Techno-
 logical Cooperation Programme. A proof-of-principle test
 has been conceived in 2010 aimed at the detection of an
 existing (and known) mineral deposit inside a mine. Dedi-
 cated modular devices have been designed (see Fig. 8) and
 ten samples (emulsion film total area of $5000 cm^2$) have
 been placed along the mine tunnel in order to measure the
 underground muon flux at different locations. The combi-
 nation of data from several modules would eventually lead
 to a 3D image of the inner structure of the mountain.

Each emulsion chamber consists of two rectangular stain-
 less steel covers, containing four stacks of two emulsion
 doublets each. In order to reduce the effects of radiation
 coming from natural radioactivity, a lead plate is posi-
 tioned in the middle of each stack. The module mechan-
 ics is conceived to be tight to preserve the emulsion sur-

face from light and humidity. After an exposure of 4.5 months the detector have been disassembled *in situ* inside a portable dark room and the emulsion films developed and sent back to Bern. LHEP is one of the largest



Figure 8: Left: emulsion module hosting 16 emulsions. Middle: module station during data taking. Right: reconstructed passing-through tracks.

emulsion scanning laboratories in the world where 5 state-of-the-art high speed automatic microscopes are installed and routinely operating for the OPERA experiment [32]. In addition, a new scanning station has been dedicated to muon radiography. The automated scanning system consists of a microscope equipped with a computer-controlled motorized stage, a dedicated optical system and a CMOS camera [33]. For each field of view, several tomographic images of the emulsions are taken at equidistant depths by moving the focal plane across the emulsion thickness (Z direction). Images are grabbed and processed by a vision multi-processor board, hosted in the control PC. The tracks are then reconstructed by combining grains from different layers with a dedicated software program (see Fig. 8-(right)). For the extension of muon radiography measurements to deeper structure as well as for reducing the exposure time, a larger emulsion surface would be needed. For this reason an upgrade of the current scanning system is foreseen, in order to reduce the scanning time. One promising solution seems to be the use of high speed GPU (Graphic Processing Unit) to replace standard CPU for faster track reconstruction. In the framework of INET, the LHEP group has set up a facility for “in-house” pouring and development of emulsion films. Several tests

are ongoing with the aim of producing suitable emulsion detectors (large area, high sensitivity, low noise) for muon radiography and other applications, especially in the medical field. Connections with specialized companies providing emulsion gel have been established for potential future large-scale production.

5. Conclusions and perspectives

Muon tomography reaches a new era with mature, robust, adapted to harsh field conditions technologies developed and commissioned around the world. Volcanoes are more and more targeted by muon tomographic imaging since the alternative methods often reveal limited or difficult to work out in their environments. The complementarity of the muon tomography with gravimetric or electric tomography is emerging strongly since it offers direct volume information with quasi straight lines of responses relatively easy to invert. The measurements are also taken in a rather short timescale with a limited number of “shootings”. Promising real-time 3D tomographies may offer to the community a powerful tool to monitor, understand and better predict the behaviour of volcanoes, with an obvious and crucial societal impact.

Acknowledgements

Authors from the DIAPHANE project warmly thank K.Mahiouz, F.Mounier, P.Rolland, S.Vanzetto (opto-mechanics), B.Carlus (informatics), S.Gardien, C.Girerd, B.Kergosien (electronics) and colleagues from the Observatoire Volcanologique et Sismologique de Guadeloupe : A.Bosson, F.Randriamora, T.Kitou, C.Lambert and V.Daniel. The DIAPHANE project is financially supported by the IPGP BQR grant, the DOMOSCAN ANR project, the CNRS/IN2P3 Astroparticles program, and the MD experiment of the Mont Terri project funded by Swisstopo and CRIEPI partners. The author would like to thank C.Carloganu and

P.Salin who contributed to the oral presentation. Emulsions tomography project benefits from the strong support and expertise of the LHEP group.

References

- [1] K. Nagamine, J. Geogr. 104 (1995) 998–1007.
- [2] K. Nagamine, M. Iwasaki, K. Shimomura, K. Ishida, Nucl. Instr. and Meth. A 356 (1995) 585–595.
- [3] H.K.M. Tanaka, K. Nagamine, N. Kawamura, S.N. Nakamura, K. Ishida, K. Shimomura, Hyperfine Interact. 138 (2001) 521–526.
- [4] H.K.M. Tanaka, K. Nagamine, N. Kawamura, S.N. Nakamura, K. Ishida, K. Shimomura, Nucl. Instr. Meth. A 507 (2003) 657–669.
- [5] G. Boudon, J.-C. Komorowski, B. Villemant, M.-P. Semet, J. Volcanol. Geotherm. Res., 178, 474–490, doi:10.1016/j.jvolgeores.2008.03.006.
- [6] J.-C. Komorowski, Y. Legendre, B. Caron, G. Boudon, J. Volcanol. Geoth. Res., 178, 491–515.
- [7] F. Nicollin, D. Gibert, F. Beauducel, G. Boudon, J.-C. Komorowski, Earth Planet. Sci. Lett., 244, 709–724.
- [8] D. Gibert, F. Beauducel, Y. Déclais, N. Lesparre, J. Marteau, F. Nicollin, A. Tarantola, Earth Planets and Space 62 (2010) 153–165.
- [9] K. Nagamine, *Introductory Muon Science*, 208 pp, Cambridge University Press, Cambridge UK, 2003.
- [10] A. Zichichi, *Subnuclear physics: the first 50 years : highlights from Erice to ELN*, 210pp, World Scientific Publishing, 2000.
- [11] L.W. Alvarez, J.A. Anderson, F.E. Bedwei, J. Burkhard, A. Fakhry, A. Girgis, A. Goneid, F. Hassan, D. Iverson, G. Lynch, Sci. 167 (1970) 832–839.
- [12] N. Lesparre, D. Gibert, J. Marteau, Y. Déclais, D. Carbone, E. Galichet, Geophys. J. Int., 183, 1348–1361.
- [13] E.V. Bugaev, Yu D. Kotov, I.L. Rosental, *Cosmic muons and neutrinos*, Atomizdat, Moscow.
- [14] E.V. Bugaev, A. Misaki, V.A. Naumov, T.S. Sinegovskaya, S.I. Sinegovsky, N. Takahashi, Phys. Rev. D, 58, 054001.
- [15] T. Gaisser, *Cosmic rays and particle physics*, 279pp, Cambridge University Press, 2000.
- [16] <http://pdg.lbl.gov>
- [17] N. Lesparre, J. Marteau, Y. Déclais, D. Gibert, B. Carlus, F. Nicollin, B. Kergosien, Nucl. Instr. Methods A, in revision.
- [18] A. Pla-Dalmau, A.D. Bross, K.L. Mellott, Nucl. Instr. and Meth. A 466 (2001) 482–491.
- [19] C. Girerd, S. Gardien, J. Burch, S. Katsanevas, J. Marteau, IEEE Nucl. Sci. Symposium and Nucl. Im. Conference (2000) 7903.
- [20] J. Marteau, Nucl. Instr. and Meth. A 617 (2010) 291–293.
- [21] N. Lesparre, D. Gibert, J. Marteau, Geophys. J. Int., in revision.
- [22] P. Bossart, M. Thury, *Mont Terri Rock Laboratory Project, Programme 1996 to 2007 and Results*, Rep. Swiss Geological Survey 3, Wabern, Switzerland.
- [23] <http://mu-ray.fisica.unina.it>
- [24] P. Baringer, et al., Nucl. Instr. and Meth. A 469 (2001) 295.
- [25] <http://minerva.fnal.gov>
- [26] <http://www.lnf.infn.it/esperimenti/alice/emcal/sputtering/index.php>
- [27] Z. Sadygov, Avalanche Detector, Russian Agency for Patents and Trademarks, Patent No. RU 2102820 (1998).
- [28] V. Golovin, Avalanche Photodetector, Russian Agency for Patents and Trademarks, Patent No. RU 2142175 (1999).
- [29] <http://omega.in2p3.fr>
- [30] T. Nakamura et al., Nucl. Instr. & Meth. A 556 (2006) 80.
- [31] H. K. M. Tanaka et al. , Geo. Res. Lett. 34 (2007) L22311.
- [32] R. Acquafredda et al., JINST 4 (2009) P04018.
- [33] L. Arrabito et al., JINST 3 (2008) P04006.

2.4 Implementation of sub-nanoseconds TDC in FPGA : applications to time-of-flight analysis in muon radiography, [14]

Jacques Marteau¹, Jean de Bremond d'Ars², Dominique Gibert^{2,3}, Kevin Jourde³, and Serge Gardien¹, Claude Girerd¹, Jean-Christophe Ianigro¹

¹ Institut de Physique Nucléaire de Lyon, Univ Claude Bernard, UMR 5822 CNRS, Lyon, France.

² Géosciences Rennes, Univ Rennes 1, UMR 6118 CNRS, Rennes, France.

³ Institut de Physique du Globe de Paris, Sorbonne Paris Cité, Univ Paris Diderot, UMR 7154 CNRS, Paris, France.

Abstract. Time-of-flight (*tof*) techniques are standard techniques in high energy physics to determine particles propagation directions. Since particles velocities are generally close to c , the speed of light, and detectors typical dimensions at the meter level, the state-of-the-art *tof* techniques should reach sub-nanosecond timing resolution. Among the various techniques already available, the recently developed ring oscillator TDC ones, implemented in low cost programmable logic circuits like FPGA (Field Programmable Gate Array), feature a very interesting figure of merit since a very good timing performance may be achieved with limited processing ressources. This issue is relevant for applications where unmanned sensors should have the lowest possible power consumption. Actually this article describes in details the application of this kind of *tof* technique to muon tomography of geological bodies. Muon tomography aims at measuring density variations and absolute densities through the detection of atmospheric muons flux's attenuation, due to the presence of matter. When the measured fluxes become very low, an identified source of noise comes from backwards propagating particles hitting the detector in a direction pointing to the geological body. The separation between through-going and backward-going particles, on the basis of the *tof* information is therefore a key parameter for the tomography analysis and subsequent previsions. This paper describes a time-to-digital converter (TDC) implementation fulfilling the requirements of a *tof* measurement applied to muon tomography.

PACS numbers: 1315, 9440T

1. Introduction

Density radiography with atmospheric muons aims at determining the density variations or the absolute densities of geological or large volume bodies. The density is measured through the screening effect on the incident muons flux induced by the presence of matter, like for the X rays in a standard medical radiography. A detector is deployed on the slopes of the studied volcano and records the hits left by the muons which crossed volcano's matter. The collection of hits enables the muon trajectory reconstruction (tracking detector). During a given exposure time, which depends on the overall features of the volcano e.g. the cone dimensions, the muon flux is measured in all directions accessible to the detector. The comparison with the well-known “free” muons fluxes, i.e. the fluxes of muons propagating in “open” sky without any screening due to the presence of matter, gives access to the attenuation induced by the volcano's matter. Inverting this problem allows to determine the volcano density since the external topography of the volcano is known. The details of muons tomography may be found elsewhere (Alvarez 1970; Nagamine 1995; Nagamine et al. 1995; Tanaka et al. 2001; Lesparre et al. 2010). For a detailed presentation of recent applications of this muon tomography technique, like the dynamics of the aquifers, please refer to Jourde et al. (2013), and references therein.

We will focus in this article on applications in volcanology, where the maximal dimension of the volcano to probe is typically at the kilometer scale. This is for instance the case of La Soufrière de Guadeloupe in the Lesser Antilles or the top craters of Mount Etna in Sicily, Italy (Lesparre et al. 2010; Carbone et al. 2013, Jourde et al. 2013). In both cases, the detectors used in the measurements are set on the slopes of the volcano and their orientation is such that they may catch muons incident from the “open” sky, and muons which propagated through the volcano. Given the position of the detector and the harsh environmental conditions, the instrument may be designed as robust as possible and totally autonomous (remote control, low power consumption compatible with solar panels or wind wings power sources). Despite these constraints the figure of merit of those detectors is the signal-to-noise ratio to reach the best possible sensitivity. In particular recent applications aimed at detecting small-density contrasts, which translates in small variations in the muons flux to be detected, and put severe constraints on the sensitivity (Nagamine 2003; Lesparre et al. 2010).

Muons “telescopes” are standard high energy physics trackers that count the particles arriving from a given direction during a known time slot (typically one month for the present applications). Different detection techniques are used world-wide and our telescopes are scintillator XY hodoscopes, readout by multi-anodes photomultiplier tubes (MaPMT) and self-triggered electronics, with three active planes. A picture of one telescope deployed on the slopes of the Soufrière de Guadeloupe is displayed on Fig. 1.

The coincidence and majority logics within those three planes enable to practically eliminate the random coincidences and to reduce the contamination from particles

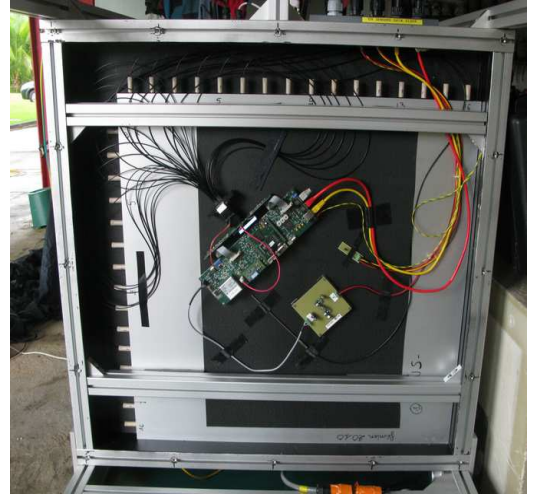


Figure 1. Left : Picture of a muon telescope in horizontal position. The three detection planes are protected by the yellow frames. Right : The inner part of a matrix : active XY scintillator planes, PMT and readout electronics.

bundles when combined with track selection filters. The basic timing resolution step used in these telescopes is set by the master clock frequency of 20MHz which is then multiplied locally by a factor 5 via a Phase-Lock Loop (PLL). Therefore a 10ns timing resolution was used in the first version of the telescopes to perform event timestamping and coincidence logic between the three active planes. Although sufficient to perform standard structural imaging, this timing resolution was shown to be quite limited for more sensitive studies and should have been upgraded to reach the sub-nanosecond domain. In particular we showed in the early data taking on Mount Etna and on La Soufrière of Guadeloupe (Lesparre et al. 2012b, Jourde et al. 2013) that muons propagating downwards, from below the horizontal plane, and passing through the telescope may mimic muons that would have crossed the volcano. Indeed in both cases the telescopes were located on the steep flanks of the volcanoes and their rear-side was facing large and deep valleys allowing even low energy particles to reach and cross the telescope. The only way to remove this noise it to use high-resolution *tof* criterion and therefore improve the timing resolution by at least one order of magnitude, as proposed for example in muon radiography applications in (Anastasio et al. 2012). The paper is organized as follows. In the first Section is described the data acquisition (DAQ) and timing system of the telescopes. In the second Section the general features of the TDC implementation in the FPGA are detailed. In the third Section we present the calibration procedure and the corrections obtained on the measured flux when the backward contribution is subtracted.

2. Description of the distributed DAQ and timing systems

2.1. General features

Each detection plane is read out by its own Ethernet-capable autonomous electronics and sends its data after pre-processing to a central, low-power consumption, rugged computer for the global event building and track selection. The computer (Ref.MMI-4087AD-R2A18320 from KEP, 1.8GHz processor running under Linux) is hosted in a compact and isolated “electronics box”. This box also includes a network switch, low voltage regulators, a ten-relay module with a built-in web server (WebRelay-10 from Xytronix Research & Design, Inc.) and the Master Clock board (see below).

The readout electronics system is directly derived from the one of the OPERA neutrino experiment (Acquafredda et al. 2009; Aganovfona et al. 2013). This experiment aimed at detecting the $\nu_\mu \rightarrow \nu_\tau$ neutrino oscillations between the CERN (Geneva, Switzerland) and the Gran Sasso underground laboratory (L’Aquila, Italy). The Target Tracker of the OPERA detector, a scintillator hodoscope, was meant to build the trigger signal and to identify the volume inside the detector where the neutrinos interacted.

The DAQ system, common to the OPERA and to the muons telescopes, has been designed on the concept of the so-called “smart sensors” in which each detecting element is readout by an independent micro-processor board and sends its data over a standard Ethernet network (Marteau 2010). The DAQ system fulfills the requirements of triggerless operation, event timestamping (with 10ns steps) locked on external clock for off-line correlation, continuous running capability, high availability and low deadtime, modular and flexible hardware/software architecture (trigger schemes, on-line and off-line filters etc).

2.2. Electronic readout system

The muons energy loss in a scintillator strip (Pla-Dalmau et al. 2001) is converted into scintillation photons trapped in a wavelength shifting optical fibre and directed on one MaPMT pixel, where it is converted into a charge signal with a typical gain of 160fC per photo-electron. The readout electronics is divided into a front-end stage (two dedicated 32 channels ASICS developed in LAL, Orsay, France), a mother-board and a mezzanine board (constituting the hereafter so-called controller board).

Front-end electronics The ASICS developed is based on a standard slow/fast shaper architecture. Each channel starts with a gain-adjustable preamplifier which feeds a fast shaper, followed by a discriminator, and a slow shaper, used for precise charge readout. If an event occurs (signal above threshold on one channel’s fast shaper) a track&hold logic blocks the charges in the 32 channels slow shapers after an adjustable delay. The 32 values of the charges are then multiplexed and sent to the controller board for further processing (digitization, zero suppression, formatting and compression). The timing processes are described in Fig. 2. The clock line in the figure refers to the multiplexed

outputs readout.

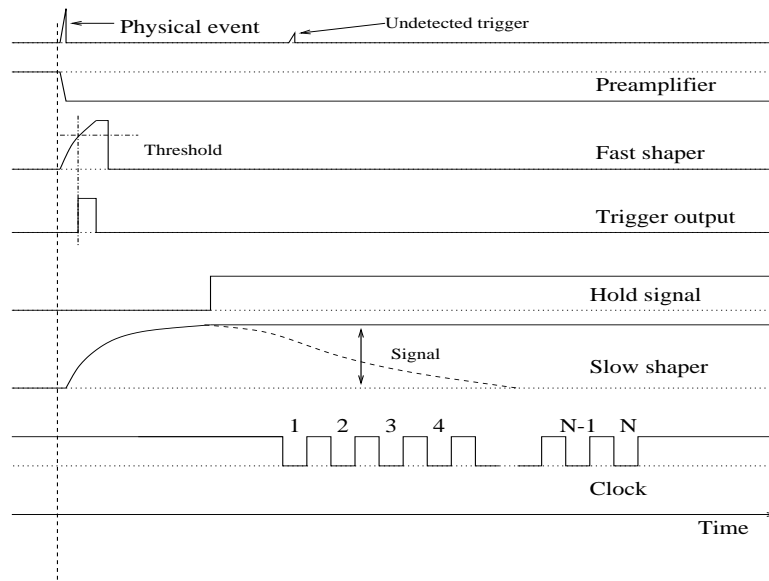


Figure 2. Timing diagrams of the front-end electronics ASICS readout sequence.

Processor boards The mezzanine board hosts three main elements:

- A micro-processor, the ETRAX 100LX from AXIS (www.axis.com), which is a 32-bit RISC CPU with Linux 2.4 OS running at 100MHz and presented in a Multi Chip Module (MCM) with 4 Mbytes of flash memory, 16 Mbytes of SDRAM and Ethernet transceiver.
- A FPGA, ALTERA EP1C4F324C6 from the low-cost cyclone series.
- An intermediate buffer, the 131kwords FIFO 72V36110 from IDT.

The mezzanine is designed to interface and control the F/E electronics, to handle the readout sequence, sort the data in time and transfer them to the event builder computer. It also manages the slow control processes. All communications are performed through Ethernet, see Fig. 3. The readout sequence starts with the occurrence of an event trigger. The FPGA generates a timestamp on this trigger (see below), performs some control logic if required (e.g. fast coincidence between two different chips) and sets the track&hold logic. Multiplexed data are sent to the ADC (the maximal processing frequency is 5MHz which leads to an overall $6,4\mu s$ dead-time for 32 channels. The ADC values are zero suppressed, formatted, stored into the FIFO and finally passed to the micro-processor. The data sharing between the FPGA and the micro-processor is performed via IRQ generation either on a PPS basis or on an adjustable threshold on the FIFO occupancy.

Motherboards The motherboard hosts, on top of the mezzanine board, the following elements:

and the measurement of the propagation delays in the cables. The CLK and PPS signals are chained from one sensor to the other. Up-to 8 sensors may be chained in this way following the M-LVDS specifications and 2 clock bus are available on a single MC (therefore feeding up-to 16 sensors).

On each sensor the “clock unit” (Fig. 3) receives and processes the clock signals. The CLK signal is used to generate locally, in a PLL, a 100MHz clock signal. This signal drives all the readout sequences and the event timestamping process.

The PPS signal (also called DAQ cycle) resets the value of the local counter running at 100MHz. This procedure avoids the long-term drifts of local counters due to the bad quality of the local quartz oscillators embedded in the mezzanines. At the reception of a new PPS signal, a flag is set and a word is inserted in priority inside the FIFO. In this way, data are naturally time-ordered and subdivided in periods corresponding to the PPS duration. An incremental number is attributed to each DAQ cycle (with a maximal of 255, corresponding to a few minutes for a real PPS signal). The event-building computer sends requests to all sensors to check whether data of cycle N are available. If not, the request is repeated until either all sensors answer or the maximal timeout value is exceeded. When data are available, the corresponding block is sent from the ETRAX micro-processor to the event-building computer. The same procedure is repeated for cycle $N + 1$. If a sensor does not answer in due time, a warning is emitted to the computer, stating that data are missing for that specific cycle. This DAQ architecture has shown very efficient behaviour during the entire OPERA data taking period, from August 2006 (commissioning run) to December 2012 (last neutrinos from CNGS).

2.4. Event timestamping

The standard event timestamping procedure is based on the latching of the current local counter generated at 100MHz inside the FPGA, on the occurrence of a trigger from the front-end electronics. As described above this launches the readout sequence (track&hold, multiplexing, analog-to-digital conversion, Fig. 2).

Two special time flags are inserted into the data flow, one for the cycle number (which is then common to all data recorded within that cycle) and one timestamp is attached to each individual event in 10ns units (the ultimate timing accuracy at this level). Since the computer links the DAQ cycle time to the UTC, the absolute timing of each event is then known by summing the cycle time value and the 10ns timestamp. The timestamp procedure and the propagation of delays are displayed in the right part of Fig. 4.

Although the 10ns accuracy is enough for standard applications, it has been already discussed that it may reveal insufficient for smarter data analysis. Of course a basic idea is to increase the CLK frequency in order to get finer timing steps. But the precision to reach, below one nanosecond, makes this option unpractical and too critical in terms of power consumption, a key feature of the unmanned sensors.

Since the system was not designed initially neither for precise time measurements nor for

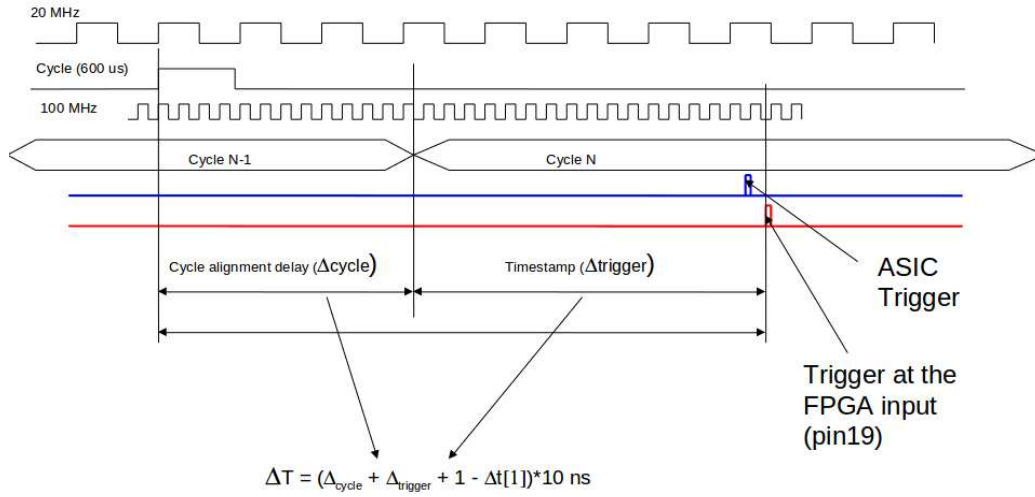


Figure 4. Timestamp generation diagram. Δ_{cycle} accounts for the propagation delays within the chained clock bus. Δ_{trigger} is the raw timestamp given in the data (ranges from 0 to 1000ms by steps of 10ns). $\Delta t[1]$ is the delay for the trigger to go from front-end chip to the FPGA. The absolute time T (from the starting point of the clock chain) is given by the following formula :

$$(\Delta_{\text{cycle}} + \Delta_{\text{trigger}} + 1 - \Delta t[1]) * 10ns < T < (\Delta_{\text{cycle}} + \Delta_{\text{trigger}} + 2 - \Delta t[1]) * 10ns.$$

All delays to reach the 1st controller board in the clock chain should be added.

particles time-of-flight determination, no specific hardware was foreseen. A remaining interesting option is the use of TDC techniques like tapped delay lines, delay locked loop, vernier delay lines or trigger ring oscillator. Most of those techniques are implemented in dedicated ASICs which obviously was not possible here. The idea was therefore to integrate TDC modules within the existing FPGA of each mezzanine board (Lin et al. 2006; Song et al. 2006; Junnarkar et al. 2008; Junnarkar et al. 2009). This technique allows a significant improvement of the system performances, simply by reconfiguring the FPGA via hardware description language (HDL). The techniques used for this particular upgrade implied no new hardware, allowed many tests on different configurations and are easily implemented (the use of an emulated JTAG bus in the case of the sensor mezzanine between the microprocessor and the FPGA enables the reconfiguration without direct connection of a programming tool).

3. Upgrade of the timing system

With a standard counter the measurement of a time interval relies on the number of clock counts recorded. The intrinsic error on the measurement equals the quantization error and the resolution is limited to the clock period. The idea to overcome this limitation is to use a vernier with two slightly different and controllable frequencies T_{slow} and T_{fast} and to use the difference in periods as the new timing step. A phase detector is used to perform the coincidence between the two counters (Fig. 5, left). Of course, the key parameter is the generation of the two nearby clocks in a controlled and reproducible

way.

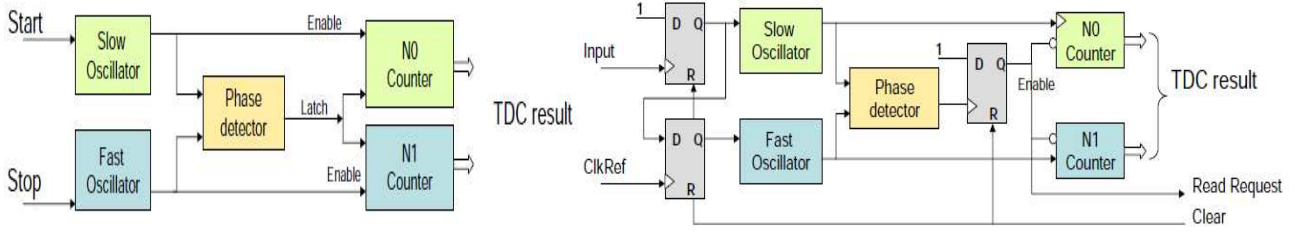


Figure 5. Left : block diagram of a generic ring oscillator TDC. Right : block diagram of a ring oscillator TDC with external reference clock signal used to generate the STOP signal of the TDC.

3.1. Ring oscillator TDC

In the present applications the 100MHz clock generated on the mezzanine is used as the reference STOP signal. The physical signal under study generates the START. The schematics is displayed in Fig. 5, right. The two elements of this type of TDC system are the controllable ring oscillators and the phase detector.

Ring oscillators The oscillators are generated following simple schemes. An example of ring oscillator developed and validated in the present application is detailed in Fig. 6. An odd number of logical cells is required to generate the oscillation through the feedback loop. The oscillation starts as soon as the ENABLE signal flips from 0 to 1. The period of the final signal (S_3 in this example) depends on the delays cumulated in the logical elements themselves and in the propagation from one to the other. Given the asymmetry of the logic when it goes from high state (H) to low state (L) or in the opposite direction (from (L) to (H)), we denote the various periods respectively T_{pHLn} and T_{pLHn} , with $n = 0..3$ (see Fig.6). The final frequency is then given by the following formula :

$$f = \frac{1}{\sum_{n=0}^{n=3} T_{pHLn} + T_{pLHn}}$$

It is worth noticing that the final frequency is given by the routing within the FPGA. Therefore the way the oscillators are implemented into the FPGA may be as controlled as possible to grant a good level of reproducibility.

Phase detector The phase detector (Lin et al. 2006) developed and validated for this application is displayed in Fig. 7. Also shown is the timing diagram of this phase detector. The phase detector is actually the most limiting part of the system to reach very small time resolution because of the setup time of the flip-flops. They may be left in metastable positions and require some time to recover. To avoid this potential problem, we always take a margin factor wrt the minimal timing steps we could achieve. In this configuration the flip-flops are stable and bring no limitations on the performance.

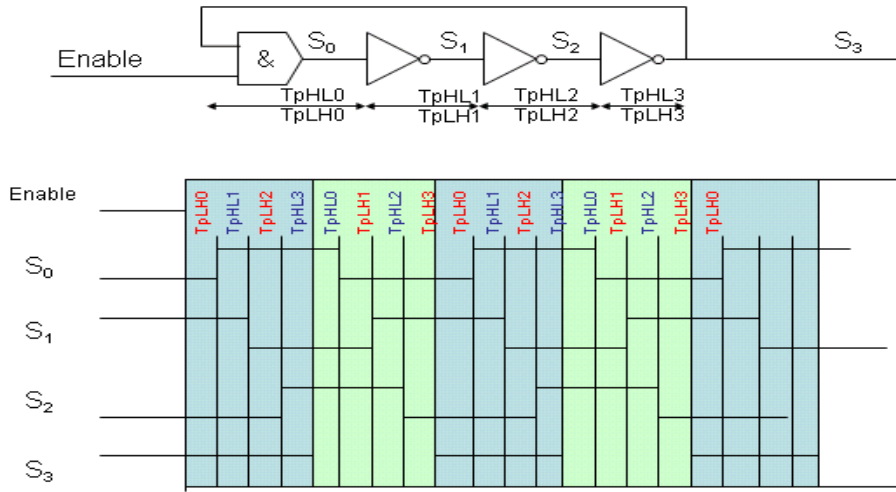


Figure 6. Simple ring oscillator and its timing diagram. T_{pHLn} and T_{pLHn} denote the times of the logic when it goes from state high (H) to low (L) and vice-versa.

3.2. Implementation in FPGA

Since the idea is to generate two oscillators with close frequencies due to small difference in the FPGA routing, it is worth using special procedures to freeze the design in a controlled way. Indeed a direct synthesis may give random results and differing from one synthesis to the other. The target being the tens of pico-seconds time resolution, a careful design is mandatory.

Using standard design tools available from ALTERA, the following design sequence has been used in this project :

- creation of a separate project for the ring oscillators
- creation of regions for each oscillator
- open loop synthesis with SDC constraints
- Timequest analysis
- Post compilation Editing (ECO) with chip planner
- regions export

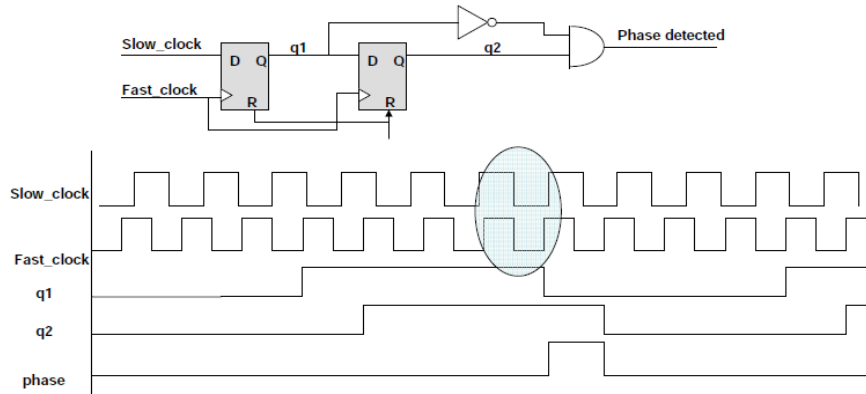


Figure 7. The phase detector and its timing diagram.

In particular the regions should be located to their final position in the TOP project, and the in/out pins should be inserted manually. During the final regions import, the netlist-type should be set to Post-fix in order to protect the region. Following this design sequence allows to generate, in a reproducible way, ring oscillators with close frequencies to achieve TDC measurements.

3.3. Timing sequence

The ring oscillators, called “fast” and “slow” oscillators have period $T_{fast} = T_1$ and $T_{slow} = T_0$ respectively ($T_0 \geq T_1$). The slow oscillator is launched on the rising edge of the signal trigger while the fast one starts on the rising edge of the local 100MHz clock. The timing sequence is summarized in Fig. 8.

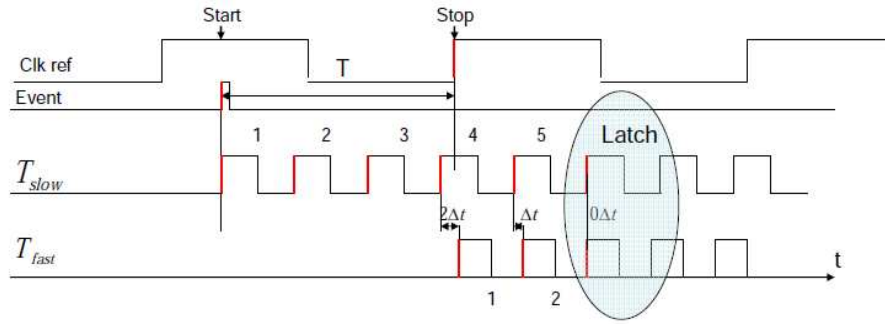


Figure 8. TDC vernier principle.

The determination of the coincidence, using the phase detector, between the two signals gives access to two values, N_0 and N_1 , representing the number of counts for the slow and the fast clock respectively. The timestamp of the signal, wrt the local counter, is therefore given by:

$$T = (N_0 T_0 - N_1 T_1) = (N_0 - N_1) \cdot T_0 + N_1 \cdot \Delta t,$$

In the previous equation

$$\Delta t = T_0 - T_1$$

represents the time resolution of the system. The deadtime of the system depends on the ratio of the two quantities : $T_0/\Delta t$.

Obviously the 2 parameters to be calibrated are Δt and T_0 . Typical values obtained for these parameters in the ALTERA EP1C4 FPGA of the mezzanines are $\Delta t \sim 0.2\text{ns}$ and $T_0 \sim 2.2\text{ns}$. This leads to a factor ~ 50 improvement in the time resolution wrt the 10ns steps of the original design. In the next Section we detail the calibration procedures and the results obtained in the physics analysis.

4. Calibration and results

In the previous sections we described the global DAQ and timing system developed for the DIAPHANE project of cosmic muons tomography. In particular we saw how the

design of ring oscillators TDC enables to increase significantly the timing resolution of the system. It has been also pointed out that the design may be performed in a careful way and that the TDC parameters should be calibrated since they strongly depend on the routing procedures.

4.1. Calibration procedures

The T_0 value is calibrated with the help of the local reference 100MHz clock. The method consists in counting the number $N_{cal;0}$ of T_0 periods corresponding to N_{ref} 10ns periods (labelled T_{ref}). Typical values are $N_{cal;0} \sim 256$ (8 bits counter). Therefore :

$$T_0 = N_{ref} \times \frac{T_{ref}}{N_{cal;0}} \quad \text{ns.}$$

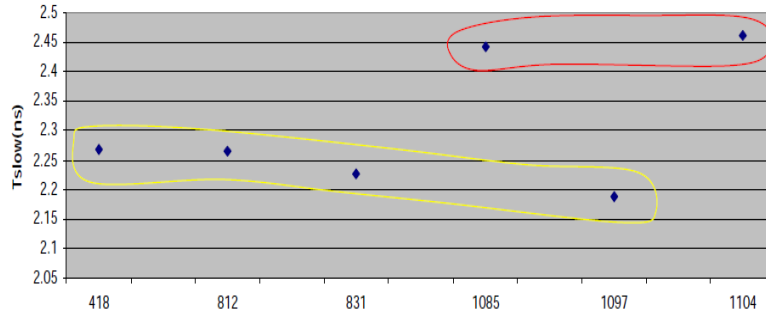


Figure 9. T_0 measurements on 6 different FPGA. On the X-axis we reported the serial number of the FPGA.

The error on the measurement is of the order of $\frac{T_0}{N_{cal;0}}$. Results obtained on a sample of 6 different mezzanines are displayed in Fig. 9. We identified the effect of the different production batch on the T_0 value's dispersion. This result clearly shows that each sensor should be individually calibrated.

To determine the value of Δt an internal trigger is started with the slow oscillator and the fast oscillator starts on the next rising edge of the 100MHz clock. Then we count the number $N_{cal;1}$ of T_0 periods between two consecutive phase detections. The measurements are repeated and the average value of $N_{cal;1}$ is computed. Through this procedure we get the desired value of the timing resolution from the following formula :

$$\Delta t = \frac{T_0}{N_{cal;1}} \text{ns.}$$

Results are available from Fig. 10.

4.2. Linearity tests

We tested the linearity of response of single sensors by using an external delay unit (HP 8131A, adjustable steps of 10 to 100ps). The tests procedure is the following. A

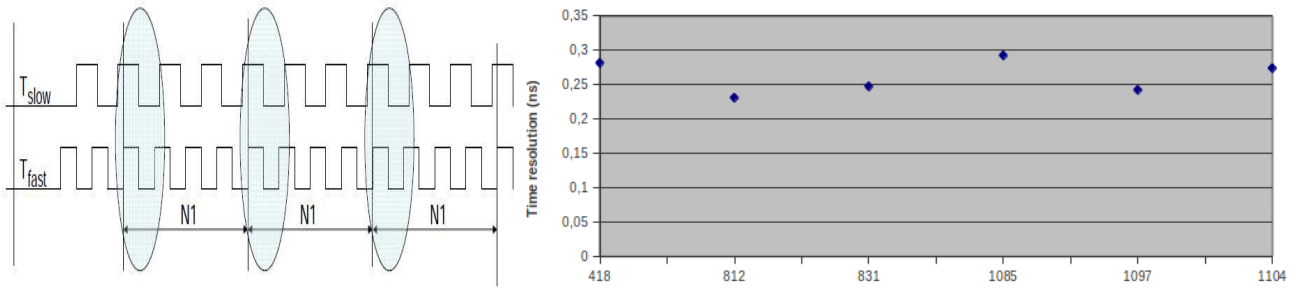


Figure 10. Left : Δt calibration principle. Right : Δt measurements on 6 different FPGA. The FPGA are the same as those used for the calibration in Fig. 9, identified by their serial number.

signal trigger is generated in the FPGA, synchronous with the 100MHz clock, using the LED PULSE MODE of the system. This channel is usually devoted to the generation of a fast pulse, synchronous to the local clock, to be sent to a blue LED illuminating the PMT. This procedure enables to measure the PMT photo-electrons response and therefore its gain.

To test the linearity of the TDC response we take out the generated trigger and feed an external delay unit with a resolution of 100ps. The delayed signal is then sent back to the sensor as an external trigger (a dual LEMO connector is available on the motherboard). The TDC starts on the rising edge of this external trigger and stops on the next rising edge of the 100MHz. This gives the position of the received trigger inside the 10ns period. A READY status flag and a CLEAR signal manage the current measurement sequence and enable the next measurement. Between two consecutive measurements the external delay is increased by steps of 100ps. Measurements are repeated over more some 10ns local clock periods. Typical calibration curves for 6 different mezzanines are displayed on Fig. 11. The sign of the slope in a 10ns period depends on the way

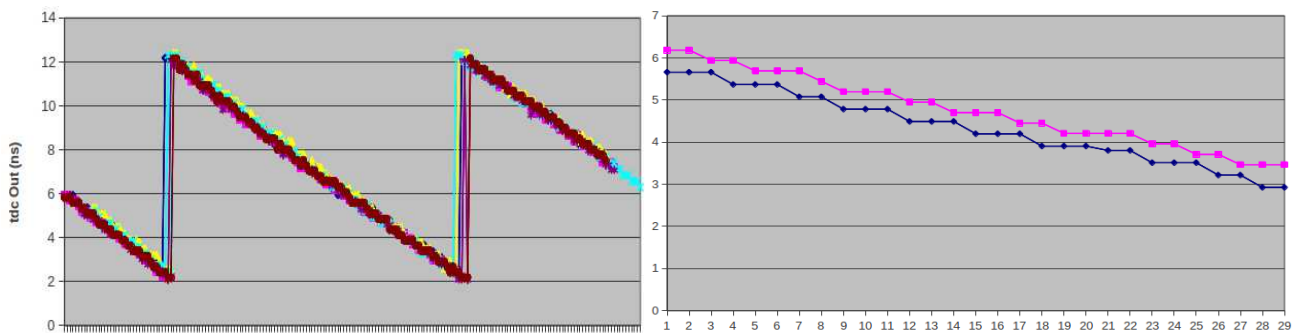


Figure 11. Left : calibration curves for the same set of 6 sensors. The Y-axis represents the TDC output, while the X-axis corresponds to the external delay steps. Right : zoom a measurement sequence for 2 different sensors. The offset between the two is clearly visible. The 'plateau' observed and lasting 2-3 external delay steps are compatible with the measured 240ps.

the START and STOP are generated. The linearity of the TDC is clearly seen from the curves, all compatible with an average time resolution of 240ps. Also visible, the

differences in offsets from one sensor to the other, which have to be corrected in a multi-TDC system implementation. The residuals of a linear fit to one calibration curve are displayed in Fig. 12.

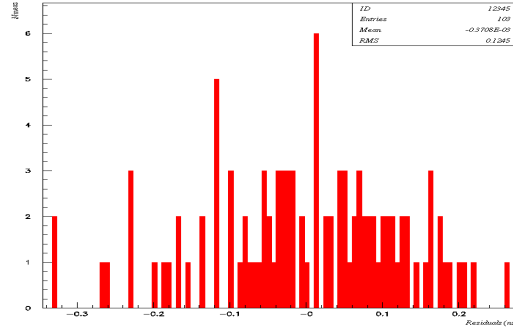


Figure 12. Linear fit of the calibration curves: distribution of the residuals.

4.3. Comparative tests between sensors

We use simultaneously two different sensors. The first one (Master Sensor) works in LED PULSE MODE like in the previous test. This signal is delayed externally and then resent, as EXT TRIGGER, to the two sensors. All cables paths are identical. The 20MHz clock signals from the Master Clock are transmitted by Ethernet cables with same length. This test outlines the dispersion effects between two sensors in a single measurement sequence. The systematic offsets on a series of measurements for each combination of two sensors are reported in Fig. 13.

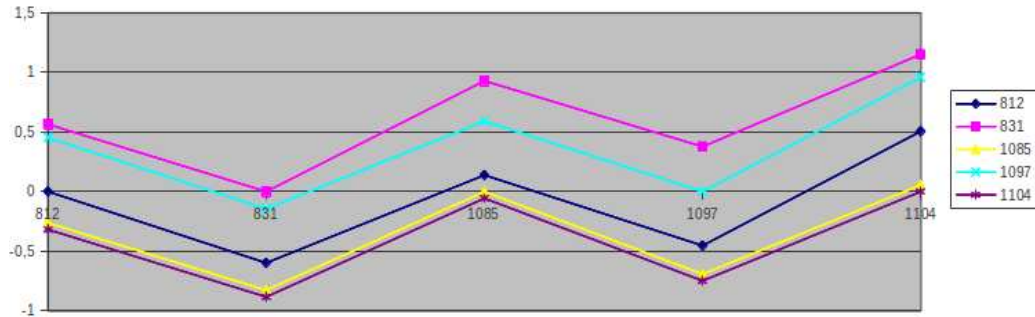


Figure 13. Systematic offsets (in ns) in a series of measurements between the raw TDC output of two different sensors.

The effect of the FPGA's batch production is particularly sensible for serial number 1085 and 1104, belonging to same batch, and which curve shows quasi identical responses wrt to each other and to the four remaining sensors. This result points out the requirement of a complete calibration procedure, as described in the preceeding subsections, to fully exploit the fine resolution of the TDC.

4.4. Results obtained on field

Detailed results are given in (Jourde et al. 2013). Fig. 14 displays the time-of-flight distribution of recorded muons as measured on a three-planes telescope. The most accurate TOF value is computed as the difference in the TDC outputs of the 2 extreme sensors because of the large lever arm. The information of partial TOF, derived from the information of the middle plane is included in the analysis as well since it provides an independant set of data to be mixed with the main one.

Propagation delays (in the signal cables and in the optical fibres from the scintillator to the PMT's) are corrected for. Dedicated calibration tests have been carried out for those corrections, already at the time of the OPERA experiment (Marteau 2009).

The telescope was set on the top of a small hill without any matter on any side. The slow slope of the hill allowed particles also to propagate upwards from below the horizon. Left part of Fig.14 describes all variables and terms used in the analysis. According to our conventions, the upwards propagating muons correspond to negative values of the zenith angle if they propagate backwards, and positive values if they propagate forwards. Of course, given the properties of the cosmic muons flux which is maximal

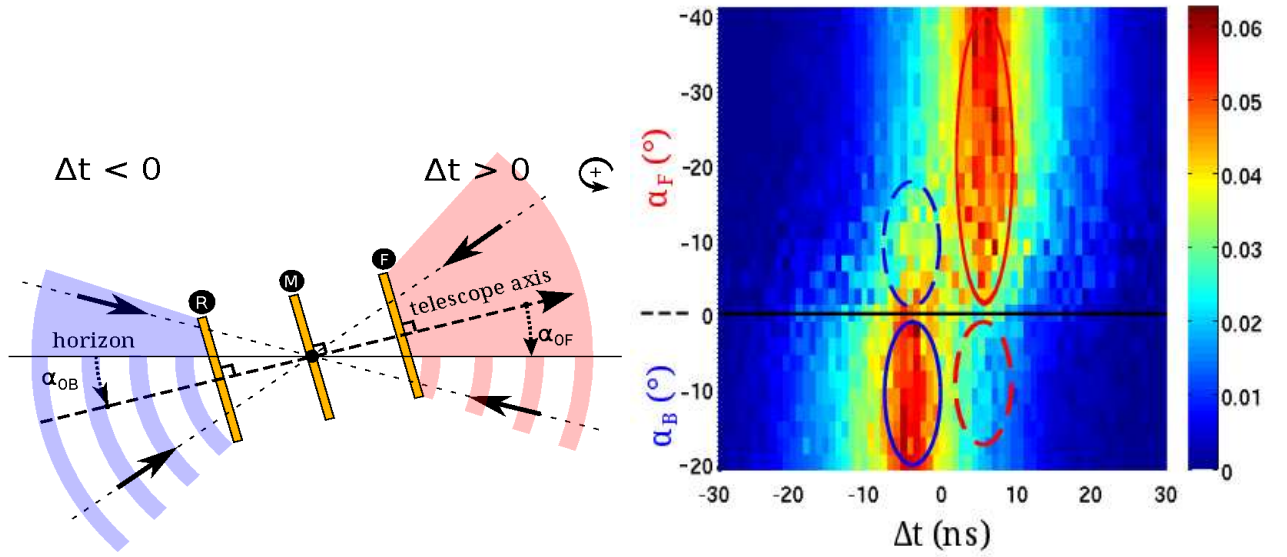


Figure 14. Left : orientation convention for the muons propagation. The telescope is seen from the side. Right : time-of-flight distribution wrt to the zenith angle. The horizon is represented by the dashed line. The blue and red solid ellipses respectively show the backward ($\alpha_B < 0$ and $\Delta t < 0$) and forward ($\alpha_F < 0$ and $\Delta t > 0$) events corresponding to the downward fluxes. The dashed ellipses show events corresponding to upward-going muons from forward (red ellipse, $\alpha_B < 0$ and $\Delta t > 0$) and backward (blue ellipse, $\alpha_F < 0$ and $\Delta t < 0$).

at the zenith, the level of backwards propagating muons is expected to be rather low. The 2D-histogram shows the TOF distribution as a function of the zenith angle. The solid ellipses correspond to downwards propagating muons (the main component of the flux). The dashed ellipses clearly point out the existence of an upwards propagating muons sample that are identified thanks to the fine-grained TDC implemented in the

sensors and calibrated following all the procedures described in the text. The main contamination is expected close to the horizon where the rock obstruction behind the telescope is the smallest. In the configuration used for the measurement presented in Fig.14, this maximal contamination amounts to 70% of the total flux. It decreases to 30% at -10 angles and is close to zero above -20 angles. Details analysis has been performed for different sites and is presented in (Jourde et al. 2013). This result allows to correct the images obtained for a large geophysical structure, like a volcano, where the lowest part of the image corresponds to the largest amount of matter to be crossed by the muons, therefore to the lowest fluxes and also to the closest-to-horizon propagation directions. If an upwards-going muon is misidentified, it may be falsely accounted for a crossing-through muon. This results in a wrong evaluation of the global volcano density which then seems less dense than in reality. This background source is extremely important and has to be reduced as much as possible for the small values of the fluxes or when one addresses physical situation where small differential fluxes may be measured.

5. Conclusions and perspectives

As demonstrated in muon tomography data analysis applied to volcanology, a good timing resolution is mandatory for background rejection and signal-to-noise ratio improvement. For instance the rejection of the upward-going muons whose trajectories might be confounded with those of downward-going muons crossing the volcano is absolutely necessary to measure the density of the structure under study. This background rejection is based on a time-of-flight analysis. Since the typical size of the instrument is of the order of 1 meter, the time-of-flight of a relativistic muon amounts to some nanoseconds. This imposes severe constraints to the timing resolution of the detector which has limited resources on field in terms of available power and embedded electronics.

In this article we describe the implementation of fine-resolution ring oscillators TDC inside existing FPGA. A simple vernier technique between two oscillators with close frequencies leads to timing resolution down to tens of pico-seconds. The generic DAQ and clock distribution systems are also detailed. The implementation of the oscillators and the freezing of their routing before the general synthesis is outlined.

The implementation on the instrument was performed remotely, while the instrument was on site. We show that simple calibrations may be achieved on site, with the instrument running, without connecting any specific test setup. The use of a common reference clock, already available for synchronization purposes, allows to measure separately one of the two frequencies and the vernier step (i.e. the TDC timing resolution). The technique has been validated on the slopes of La Soufrière de Guadeloupe in the Lesser Antilles and a dedicated commissioning run has been organized to check the presence of upward-going muons by time-of-flight analysis. The results obtained, published separately and summarized in the present article, clearly show the presence of this

upward-going muons flux and the rejection power of the TDC data. Direct implications on the quality of the radiographies of the volcano and their consequences on the density analysis are detailed in Jourde et al. (2013).

We outline that this technique has been upgraded recently after the validation of the concept on the field to improve the timing resolution. The new design consists in changing the oscillators configuration online to adjust their frequency and then combine different slow/fast oscillators to get different resolution. In this approach, optimal resolution may be designed for any application. Technically one varies the position of the cells and the routing. When the design is completed a calibration of all possible oscillators combinations is mandatory. One gets a catalog of TDC's with different resolutions. We point out here that resolutions as good as 20ps have been obtained. All details of this new adjustable-TDC technique are being published (Girerd 2013). It is planned to implement and test this new system in our muons telescopes.

Acknowledgments Field operations in Guadeloupe received the help from colleagues of the Volcano Observatory, from the crews of the helicopter station of the French Civil Security (www.helicodragon.com) and from members of the National Natural Park of Guadeloupe (www.guadeloupe-parcnational.fr). On-field maintenance and servicing of the telescope are ensured by Fabrice Dufour. Field operations on Mount Etna received the help of colleagues of the Volcano Observatory at Catania. Logistic organization was ensured by the ULISSE-IN2P3 department of CNRS (ulisse.cnrs.fr). We acknowledge the financial support from the UnivEarthS Labex program of Sorbonne Paris Cité (ANR-10-LABX-0023 and ANR-11-IDEX-0005-02). This is IPGP contribution ****.

- [1] Acquafredda, R. et al., the OPERA collaboration, 2009. *JINST* **4**, P04018.
- [2] Agafonova, N., et al., the OPERA collaboration, 2013. New results on $\nu_\mu \rightarrow \nu_\tau$ appearance with the OPERA experiment in the CNGS beam, accepted for publication in JHEP, arXiv:1308.2553.
- [3] Alvarez, L.W., Anderson, J.A., Bedwei, F.E., Burkhard, J., Fakhry, A., Girgis, A., Goneid, A., Hassan, F., Iverson, D., Lynch, G., Miligy, Z., Mousaa, A.H., Sharkawi & M., Yazolinio, L., 1970. Search for hidden chambers in the pyramids, *Science*, **167**, 832–839.
- [4] Anastasio, A. et al., 2012. *Nucl. Instr. and Meth. A* (2012), <http://dx.doi.org/10.1016/j.nima.2012.08.065>.
- [5] Carbone, D., Gibert, D., Marteau, J., Diamant, M., Zuccarello, L., Galichet, E., An experiment of muon imaging at Mt. Etna (Italy), *Geophys. J. Int.*, GJI-13-0406 in press.
- [6] Gibert, D., Beauducel, F., Déclais, Y., Lesparre, N., Marteau, J., Nicollin, F. & Tarantola, A., 2010. Muon tomography: Plans for observations in the Lesser Antilles, *Earth Planets Space*, **62**, 153–165.
- [7] Girerd, C., 2013. *Nucl. Instr. and Meth. A*, in preparation.
- [8] Jourde, K., Gibert, D., Marteau, J., De Bremond D'Ars, J., Gardien, S., Girerd, C., Ianigro, J.-C., Carbone, D., 2013. Effects of upward-going cosmic muons on density radiography of volcanoes, *Geophys. J. Int.*, GJI-S-13-0495 in press, oai:hal.in2p3.fr:in2p3-00848135.
- [9] Junnarkar, S.S., O'Connor, P., Fontaine R., 2008. FPGA based self calibrating 40 picoseconds resolution, wide range Time to Digital Converter, *IEEE Nuclear Science Symposium Conference Record*, **64-6**, 3434–3439.
- [10] Junnarkar, S.S., O'Connor, P., Vaska, P., Fontaine R., 2009. FPGA-Based Self-Calibrating Time-

to-Digital Converter for Time-of-Flight Experiments, *IEEE Trans. of nuclear Science*, **56-4**, 2374–2379.

- [11] Lesparre, N., Gibert D., Marteau J., Déclais Y., Carbone D. & Galichet E., 2010. Geophysical muon imaging: feasibility and limits, *Geophys. J. Int.*, **183**, 1348–1361.
- [12] Lesparre, N., J. Marteau, Y. Déclais, D. Gibert, B. Carlus, F. Nicollin & B. Kergosien, 2012a. Design and Operation of a Field Telescope for Cosmic Ray Geophysical Tomography, *Geosci. Instrum. Method. Data Syst.*, **1**, 33–42.
- [13] Lesparre, N., D. Gibert & J. Marteau, 2012b. Bayesian Dual Inversion of Experimental Telescope Acceptance and Integrated Flux for Geophysical Muon Tomography, *Geophys. J. Int.*, **188**, 490–497, doi: 10.1111/j.1365-246X.2011.05268.x.
- [14] Lesparre, N., D. Gibert, J. Marteau, J.-C. Komorowski, F. Nicollin & O. Coutant, 2012c. Density Muon Radiography of La Soufrière of Guadeloupe Volcano: Comparison with Geological, Electrical Resistivity and Gravity data, *Geophys. J. Int.*, **190**, 1008–1019.
- [15] Lin, M-C., Tsai, G-R., Liu, C-Y., Chu, S-S., 2006. FPGA-based high area efficient time-to-digital IP design, *Proc. IEEE Technology, Education and Networking Conf*, 1–4.
- [16] Marteau, J., 2010. *Nucl. Instr. and Meth. A* **617**, 291–293.
- [17] Marteau, J., D. Gibert, N. Lesparre, F. Nicollin, P. Noli, F. Giacoppo, 2012. Muons tomography applied to geosciences and volcanology, *Nucl. Instr. Meth. A*, **695**, 23–28.
- [18] Nagamine, K., 1995. Geo-tomographic observation of inner-structure of volcano with cosmic-ray muons, *J. Geography*, **104**, 998–1007.
- [19] Nagamine, K., 2003. *Introductory Muon Science*, 208 pp, Cambridge University Press, Cambridge UK.
- [20] Nagamine, K., Iwasaki, M., Shimomura, K. & Ishida, K., 1995. Method of probing inner-structure of geophysical substance with the horizontal cosmic-ray muons and possible application to volcanic eruption prediction, *Nucl. Instr. Meth. A*, **356**, 585–595.
- [21] Pla-Dalmau, A., Bross, A. D. & Mellott, K. L., 2001. Low-cost extruded plastic scintillator, *Nucl. Instr. Meth. A*, **466**, 482–491.
- [22] Song, J., An, Q., Liu, S., 2006. A High-Resolution Time-to Digital Converter Implemented in Field-Programmable-Gate-Arrays, *IEEE Trans. of nuclear Science*, **53-1**, 236–241.
- [23] Tanaka, H., Nagamine, K., Kawamura, N., Nakamura, S.N., Ishida, K. & Shimomura, K., 2001. Development of the cosmic-ray muon detection system for probing internal-structure of a volcano, *Hyperfine Interact.*, **138**, 521–526.
- [24] Tanaka, H., Nagamine, K., Nakamura, S.N. & Ishida, K., 2005. Radiographic measurements of the internal structure of Mt. West Iwate with near horizontal cosmic ray muons and future developments, *Nucl. Instrum. Methods A*, **555**, 164–172.
- [25] Tanaka, H., Uchida, T., Tanaka, M., Shinohara, H. & Taira, H., 2009. Cosmic-ray muon imaging of magma in a conduit: Degassing process of Satsuma-Iwojima Volcano, Japan, *Geophys. Res. Lett.*, **36**, L01304.

2.5 Muon tomography and gravimetry joint inversion, [15]

Kevin Jourde¹, Dominique Gibert^{1,2}, Jacques Marteau³

¹ Institut de Physique du Globe de Paris, Sorbonne Paris Cité, Univ Paris Diderot, UMR 7154 CNRS, Paris, France

² Géosciences Rennes, Univ Rennes 1, UMR 6118 CNRS, Rennes, France

³ Institut de Physique Nucléaire de Lyon, Univ Claude Bernard, UMR 5822 CNRS, Lyon, France

E-mail: jourde@ipgp.fr, dominique.gibert@univ-rennes1.fr, marteau@ipnl.in2p3.fr

September 2014

Abstract. Both muon tomography and gravimetry are geophysical methods that provide information on the density structure of the Earth's subsurface. Muon tomography measures the natural flux of cosmic muons and its attenuation produced by the screening effect of the rock mass to image. Gravimetry generally consists in measurements of the vertical component of the local gravity field. Both methods are linearly linked to density, but their spatial sensitivity is very different. Muon tomography essentially works like medical X-ray scan and integrates density information along elongated narrow conical volumes while gravimetry measurements are linked to density by a 3-dimensional integral encompassing the whole studied domain. We develop the mathematical expressions of these integration formulas – called acquisition kernels – to express resolving kernels that act as spatial filters relating the true unknown density structure to the density distribution actually recoverable from the available data. The resolving kernels provide a tool to quantitatively describe the resolution of the density models and to evaluate the resolution improvement expected by adding new data in the inversion. The resolving kernels derived in the joined muon/gravimetry case indicate that gravity data are almost useless to constrain the density structure in regions sampled by more than two muon tomography acquisitions. Interestingly the resolution in deeper regions not sampled by muon tomography is significantly improved by joining the two techniques. Examples taken from field experiments performed on La Soufrière of Guadeloupe volcano are discussed.

1. Introduction

Muon tomography is a geophysical method that offers a new way to determine the density of large rock volumes by measuring their screening effect on the natural cosmic muons flux crossing the rock volume to probe (e.g. Nagamine 2003, see Tanaka 2013 for a brief review). The small cross-section of muons in ordinary matter (Barrett et al. 1952) allows the hard component of the muon spectrum (Tang et al., 2006; Gaisser & Stanev 2008) to cross hectometers, and even kilometers, of rock. Most muons crossing the rock volume have a

negligible scattering relative to the instrument angular resolution and travel along straight trajectories ranking muon tomography among the class of straight-ray scanning imaging methods (Marteau et al., 2011). In practice, muon tomography is performed by using a series of pixelated particle detectors that allow to determine the trajectories of the muons passing through the rock body. Portable field telescopes presently used sample hundredths of directions and allow to scan an entire volcano from a single view-point in a couple of weeks (Fig. 1). By counting the number of muons passing through the target, the attenuation onto the incident muon flux is determined for each sampled direction and used to produce a radiography of the object opacity (expressed in g.cm^{-2}) or of average density along ray-paths if the object geometry is known.

Since the pioneering works by Nagamine et al. (1995a,b) and Tanaka et al. (2001), recent studies illustrate the interest of the method to image spatial and temporal variations of the density inside volcanoes (Tanaka et al. 2005, 2007a,b, 2008, 2009a,b, 2013; Gibert et al., 2010; Cârloganu et al., 2012; Lesparre et al. 2012c; Shinohara & Tanaka, 2012; Portal et al., 2013). When compared with the relatively large number of publications devoted to qualitative applications of muon tomography, only a small number of studies address methodological issues and quantitative assessments of the method. Lesparre et al. (2010) establish a feasibility formula where the achievable density resolution is related to the measurement duration (i.e. time resolution), the total apparent rock thickness (i.e. total opacity) and the telescope acceptance (i.e. the detection capacity of the matrices). The feasibility formula writes as an inequality and gives practical hints to design field experiments and evaluate which density heterogeneities can be resolved inside a given geological target, for a given amount of time and a given telescope. In a more recent study, Jourde et al. (2013) present experimental evidences of a flux of upward-going particles that occurs in certain field conditions. These particles have trajectories parallel to those of the muons emerging from the rock body to radiography but they travel through the telescope from rear to front. These upward-going particles may constitute a huge Poissonian noise that could strongly alter the radiographies. Jourde et al. (2013) give practical recommendations for choosing experimental sites likely to give an as best as possible signal-to-noise ratio, and they also puts strong constraints on the time resolution of the electronic detection chain necessary to statistically recognize particles coming from the rear face of the telescopes.

In the present study, we extend our methodological work by quantitatively examining how the combination of muon tomography and gravity data may improve the reconstruction of the density distribution inside geological bodies. Studies combining muon data and gravity measurements remain scarce, and we emphasize the early study by Caffau et al. (1997) who compared muon tomography with gravity measurements. More recently, Davis & Oldenburg (2012) and Nishiyama et al. (2014) presented joined inversions of gravity data and muon tomography using a straightforward linear regularized inversion based on block models. Combining density radiographies and gravity measurements is a quite natural intention since both methods provide information directly related to the density distribution. However, both methods sample the density structure in very different ways, and the scanner-like principle of muon tomography confers to this method a high-resolution that could question the interest

to perform a costly complementary gravimetry survey. Conversely, muon tomography has limitations due to difficulties to install muon telescopes at a large number of places around the geological body to image. Consequently the number of opacity radiographies available to perform the tomography reconstruction is always small with, eventually, wide uncovered angular sectors that make the inverse Radon transform ill-posed to perform the tomography reconstruction. Another strong limitation of muon tomography comes from the fact that it at best only samples the density structures located above the horizontal plane passing through the telescope location.

Considering these issues, gravity data may bring useful information to better constrain the recovery of the density distribution, and it is the purpose of the present study to quantitatively document the benefits of a joint inversion of gravity and muon data to recover the density structure. In order to obtain results independent of any particular parametrization (e.g. block discretization), we adopt a formulation in terms of resolving kernels whose expression only depend on the geometrical properties of the data acquisition (i.e. locations of measurement points and telescope acceptance functions). We begin by establishing the relationships between the density structure and both muon tomography and gravity data. Next, we derive the resolving kernels respectively corresponding to individual gravity and muon inversions and to joint gravity–muon inversion. The resolving kernels translate the information contained in the data into information concerning the density structure. We conclude the article with examples taken from real field experiments conducted on La Soufrière of Guadeloupe to illustrate the practical interest to combine muon radiographies and gravity measurements. The muon tomographies experiments were already described in various articles (Lespare et al., 2012 and Jourde et al. 2013). Three sites called Ravine Sud, Rocher Fendu and Savane à Mulets were explored and are represented on Fig. 1(a). The gravimetry survey is currently running, for the purpose of this article we simulated one hundred measurements regularly spaced on a grid that covers the dome (Fig. 1(b)).

2. The sampling of the density distribution by muon tomography and gravimetry

Here, we recall the main formula relating the density distribution to the data, i.e. fluxes of muons and gravity measurements. In the inverse problem framework, these formula describe the forward problem for each method. In the remaining, we suppose that the muon data have been cleaned from perturbing effects such as upward going fluxes of particles as described in Jourde et al. (2013).

2.1. Muon tomography

The primary information used in muon tomography consists in cosmic muons flux attenuation measurements resulting from the screening produced by the geological volume to scan. Attenuation is measured by counting the number of muons emerging from the volume for each observation axis: $s_m = (\mathbf{r}_m, \mathcal{P}_m(\varphi, \theta))$, of the telescope (Fig. 1(a)). \mathbf{r}_m represents the position of the telescope, \mathcal{P}_m the observation axis acceptance pattern which depends on (φ, θ)

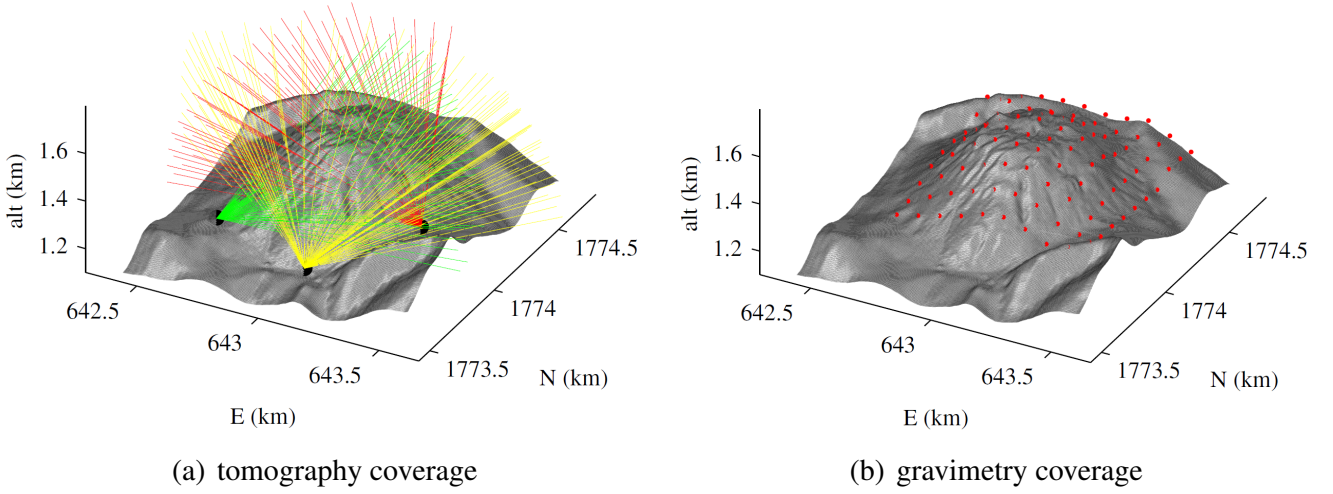


Figure 1. (a): muon tomography data coverage on the Soufrière of Guadeloupe. The lines represent the observation axes of the muon telescope when located at Rocher Fendu (red), Ravine Sud (yellow) and Savane à Mulets (green). (b): the red dots represent the positions at which we simulated gravimetry measurements

the azimuth and zenith angles referenced at \mathbf{r}_m (see Fig. 2). Note that \mathbf{r}_m is the same for all the observation axes on a given site. \mathcal{P}_m depends on the telescope geometry and angular orientation on the site. Our standard field telescopes count 31×31 observation axes and, in a field experiment where the telescope successively occupies several places around the target, the number, M , of data may easily reach several hundredths. For example if we use the muon tomography data from the 3 Soufrière sites $M = 3 \times 31 \times 31$. In practice M is lower as many axes point downward or above the volcano.

\mathcal{P}_m ($\text{cm}^2.\text{sr}.\text{rad}^{-2}$) shape depends on the detection matrices structure (see Lesparre et al. 2012a,b for further details). It has a steep peak centered on a small solid angle region Ω_m . It is identically null outside Ω_m (Fig. 2 and Fig. 3). Observe that \mathcal{P}_m must not be confounded with the integrated pixel acceptance \mathcal{T}_m ($\text{cm}^2.\text{sr}$) used for instance in Lesparre et al. (2010),

$$\mathcal{T}_m = \int_0^{2\pi} \int_0^\pi \mathcal{P}_m(\varphi, \theta) \times \sin(\theta) d\theta d\varphi = \int_{\Omega_m} \mathcal{P}_m(\varphi, \theta) d\Omega. \quad (1)$$

The number of muons attributed to a given line of sight actually corresponds to all muons detected in Ω_m . Inside the geological volume the trajectories of these muons describe a conical volume whose apex is located at the telescope, \mathbf{r}_m .

The attenuation of the muon flux caused by the rock screen depends on the amount of matter encountered by the particles along their trajectories. For a given straight trajectory $\mathbf{t} = (\mathbf{r}, \varphi, \theta)$ (\mathbf{r} is a telescope site and (φ, θ) the azimuth and zenith angles referenced at \mathbf{r}) it is quantified by the density line integral along \mathbf{t} , the opacity

$$\varrho = \int_{\mathbf{t}} \rho(\xi) d\xi = L \times \bar{\rho}, \quad (2)$$

where ρ is the density, L the particle path length, and $\bar{\rho}$ is the average density along \mathbf{t} . The differential flux associated with \mathbf{t} may be expressed as a function $\delta\phi_{\mathbf{t}} =$

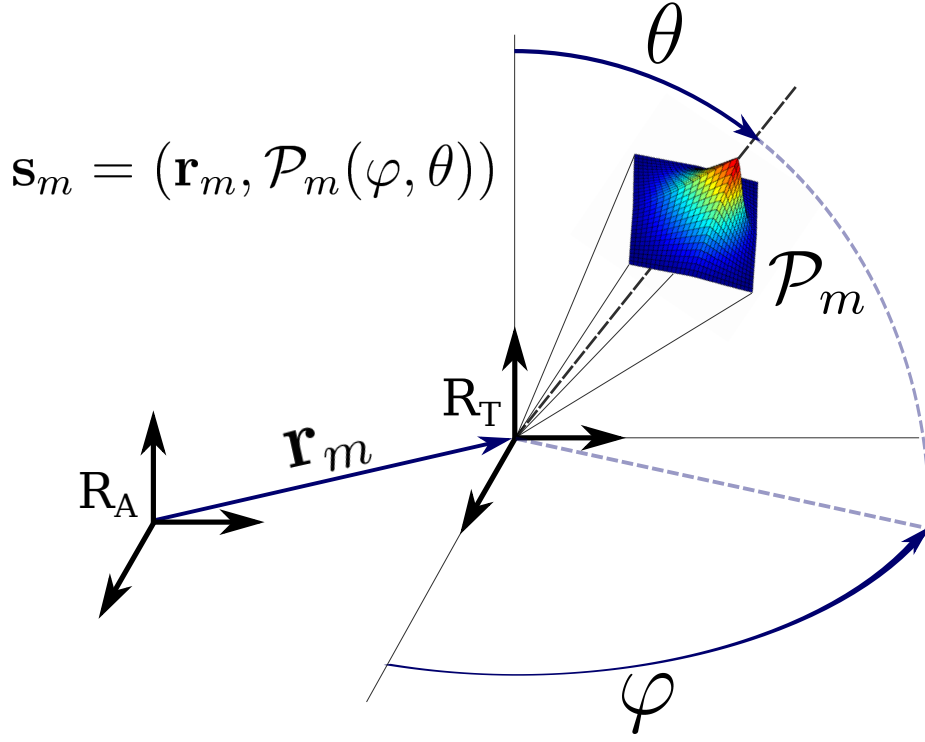


Figure 2. Muon tomography reference frame and notations. R_A and R_T respectively are the absolute orthonormal and the instrument reference frames. An observation axis $\mathbf{s}_m = (\mathbf{r}_m, \mathcal{P}_m(\varphi, \theta))$ is represented with \mathbf{r}_m the vector that localizes the telescope position and \mathcal{P}_m its acceptance pattern (restrained to the solid angle Ω_m). The spherical coordinates (φ, θ) are here localizing the steep acceptance peak mentioned in section 2.1.

$\frac{\partial^3 \phi}{\partial \Omega \partial S}(\varrho, \varphi, \theta)$ [$\text{s}^{-1} \cdot \text{cm}^{-2} \cdot \text{sr}^{-1}$] that accounts for the muon flux that reaches the instrument. Then the measured flux ϕ_m for the m^{th} line of sight relates to the opacity *via* the relationship,

$$\phi_m = \mathcal{T}_m^{-1} \int_{\Omega_m} \mathcal{P}_m(\varphi, \theta) \times \delta\phi_t(\varrho, \varphi, \theta) d\Omega. \quad (3)$$

Note that the integration is restricted to the small solid angle Ω_m because of the compact support of the observation axis acceptance \mathcal{P}_m (Fig. 3).

$\delta\phi_t$ is not linearly related to ϱ , however for small opacity fluctuations we assume that $\delta\phi_t$ may be approximated by its first order development around the local average density, $\rho_0(\mathbf{r})$. $\rho_0(\mathbf{r})$ is the prior density model of the geological structure. For a given path \mathbf{t} it reads,

$$\delta\phi_t(\varrho) = \delta\phi_t(\varrho_0) + (\varrho - \varrho_0) \times \frac{d\delta\phi_t}{d\varrho}(\varrho_0) + o(\varrho), \quad (4)$$

where $\varrho_0 = \int_{\mathbf{t}} \rho_0(\xi) d\xi$. Rearranging the terms and letting $\alpha_t = \frac{d\delta\phi_t}{d\varrho}(\varrho_0)$, we obtain,

$$\delta\phi_t(\varrho) - \delta\phi_t(\varrho_0) \approx \alpha_t \int_{\mathbf{t}} [\rho(\xi) - \rho_0(\xi)] d\xi. \quad (5)$$

Inserting eq. 5 into eq. 3 we get the approximate equation

$$\phi_m - \phi_0 \approx \int_{\Omega_m} d\Omega \int_{\mathbf{t}} \frac{\mathcal{P}_m(\varphi, \theta)}{\mathcal{T}_m} \times \alpha_t \times [\rho(\xi) - \rho_0(\xi)] d\xi \quad (6)$$

where $\phi_0 = \phi_m(\rho_0)$ is the flux corresponding to the prior density model $\rho_0(\mathbf{r})$ and $\mathbf{t} = (\mathbf{r}_m, \varphi, \theta)$.

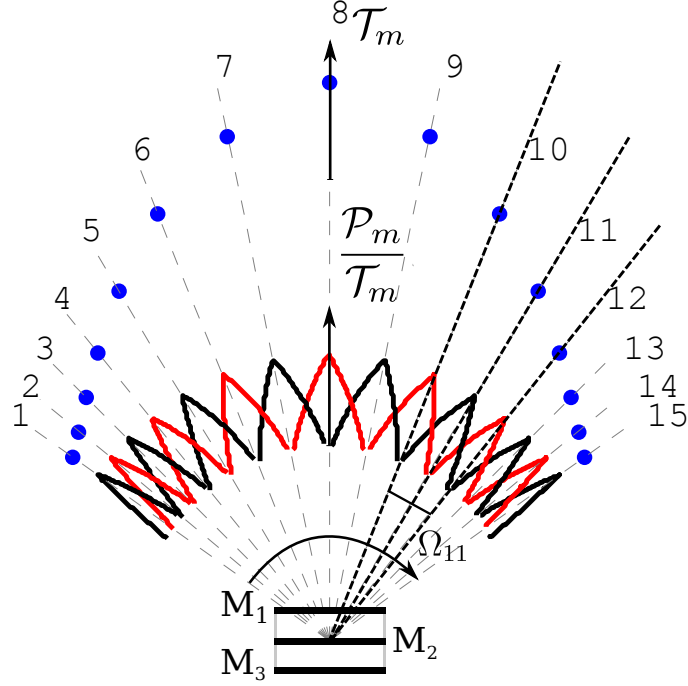


Figure 3. Representation of the acceptance. The horizontal bars labelled M_1 , M_2 and M_3 represent the pixelated detection matrices of the telescope. We draw \mathcal{T}_m and $\mathcal{P}_m/\mathcal{T}_m$ for 15 observation axes \mathbf{s}_m symmetrically distributed on the left and right sides of the main axis of the telescope (arbitrarily indexed for m going from 1 to 15, we do not represent all the observation axes for clarity purposes). The red and black sawtooth-like curves are a merging of the normalized intra-pixel acceptance $\mathcal{P}_m/\mathcal{T}_m$ for even and odd lines of sights respectively. The blue dots represent the 15 discrete values of the integrated pixel acceptance \mathcal{T}_m obtained by integrating each \mathcal{P}_m on the unit sphere (eq. (1)). Observe that the solid angle Ω_m associated with a given \mathbf{s}_m (here represented for $m = 11$) overlaps the solid angle of the neighbour lines of sight. The dashed lines are plotted along the acceptance steep peaks discussed in section 2.1.

In the remaining of the present paper, we shall use the centred and normalized flux,

$$\tilde{\phi}_m = \frac{\phi_m - \phi_m(\bar{\rho}_0)}{\phi_m(\bar{\rho}_{\min}) - \phi_m(\bar{\rho}_{\max})} = \frac{\phi_m - \phi_0}{C_{\phi,m}}, \quad (7)$$

where $\bar{\rho}_{\min}$ and $\bar{\rho}_{\max}$ are expected extreme values of the density.

2.2. Gravimetry

Gravimetry aims to estimate the gravity field generated by surrounding objects measuring locally the vertical acceleration they produce. The vertical acceleration g is directly related to the density spatial distribution through the Newton law:

$$g_n = G \int_V \frac{(\mathbf{r}_n - \mathbf{r}) \cdot \mathbf{e}_z}{\|\mathbf{r}_n - \mathbf{r}\|^3} \times \rho(\mathbf{r}) d\mathbf{r} \quad (8)$$

where the vector \mathbf{r}_n represents the location of the n^{th} measurement point (in our example n runs from 1 to 100). As for muon tomography we use the normalized gravity anomaly \tilde{g}_n

defined as

$$\begin{aligned}\tilde{g}_n &= \frac{g_n - g_n(\rho_0)}{C_{g,n}} \\ C_{g,n} &= |g_n(\bar{\rho}_{\min}) - g_n(\bar{\rho}_{\max})|\end{aligned}\tag{9}$$

3. Resolving kernel approach

3.1. The acquisition kernels

We define X , the space that contains the set of continuous L^2 functions going from \mathbb{R}^3 into \mathbb{R} . The 3D density distribution ρ belongs to X and it is related to the muon flux measurements, $\tilde{\phi}_m$, and to the gravity data, \tilde{g}_n , through the action of acquisition kernels \mathcal{G} and \mathcal{M} which also belong to X . This reads,

$$\tilde{\phi}_m = \langle \mathcal{M}_m, \rho - \rho_0 \rangle_X, \quad m = 1, \dots, M \tag{10}$$

$$\tilde{g}_n = \langle \mathcal{G}_n, \rho - \rho_0 \rangle_X, \quad n = 1, \dots, N, \tag{11}$$

where $\langle \cdot, \cdot \rangle_X$ is X inner scalar product, and M and N are respectively the number of muon tomography and gravimetry data. From eq. (6) (7) (8) and (9) we obtain explicit expressions for \mathcal{M} and \mathcal{G} ,

$$\mathcal{M}_m(\mathbf{r}) = \frac{\mathcal{P}_m(\varphi, \theta)}{\mathcal{T}_m} \times \frac{\alpha_t}{C_{\phi,m} \xi^2}, \tag{12}$$

$$\mathcal{G}_n(\mathbf{r}) = \frac{G}{C_{g,n}} \times \frac{(\mathbf{r}_n - \mathbf{r})}{\|\mathbf{r}_n - \mathbf{r}\|^3} \cdot \mathbf{e}_z. \tag{13}$$

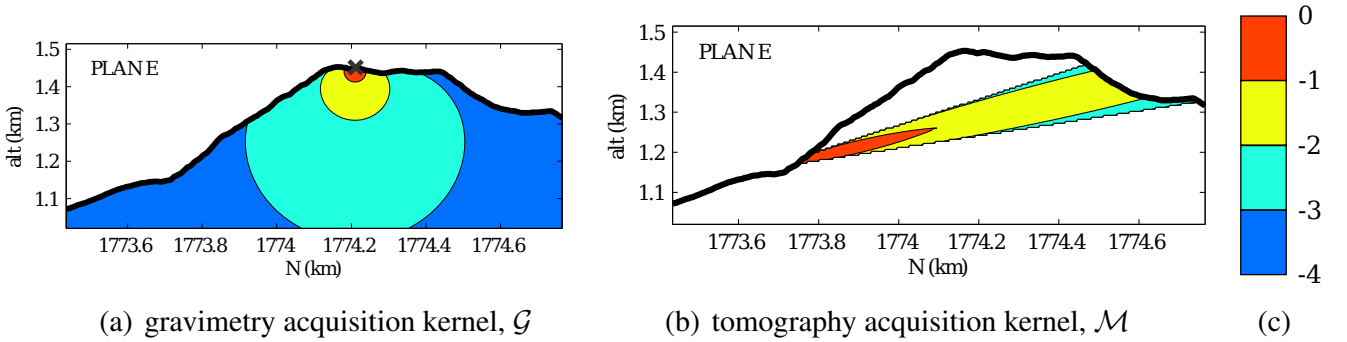


Figure 4. Acquisition kernel of a gravimetric measurement, (a), and of a tomographic measurement (for one observation axis) on the right, (b). The acquisition kernels are normalized with reference to their maximum value and printed in a \log_{10} scale.

Observe that the $1/\xi^2$ term in eq. (12) comes from the spherical coordinates elementary volume expression, $\xi^2 d\xi d\Omega$, inserted in eq. (6). Examples of acquisition kernels are plotted in Fig. 4 and discussed in sections 4.1 and 4.2. The X structure allows to introduce prior information into the problem. For instance, the classical inner product of L^2 continuous functions,

$$\langle f, g \rangle_X = \int_V f(\mathbf{r}) \times g(\mathbf{r}) d\mathbf{r}, \tag{14}$$

can be replaced by the weighted inner product,

$$\langle f, g \rangle_X = \int_V \int_V w(\mathbf{r}', \mathbf{r}'') \times f(\mathbf{r}') \times g(\mathbf{r}'') d\mathbf{r}' d\mathbf{r}'', \quad (15)$$

where the weight function w ($w(\mathbf{r}', \mathbf{r}') > 0$, $w(\mathbf{r}', \mathbf{r}'') = w(\mathbf{r}'', \mathbf{r}')$), plays the role of a covariance function that may be used to neglect the impact of the free air zone around the studied structure for gravimetry and muon tomography (see eq. (25) and its comment below). It may also serve to introduce a correlation length for the density variations.

3.2. The resolving kernel

The 3D density distribution, $\hat{\rho}(\mathbf{r})$, obtained by solving the set of linear equations (10,11) is a degraded version of the true density distribution, $\rho(\mathbf{r})$, both because of the limited number of data available and of the filtering (i.e. blurring) effect of the acquisition kernels. In the remaining, we shall use the set of undifferentiated acquisition kernels

$$\{\zeta_k\} = \{\mathcal{G}_n\} \cup \{\mathcal{M}_m\} \quad k = 1, \dots, K = M + N, \quad (16)$$

and the set of undifferentiated normalized data,

$$\{d_k\} = \{\tilde{g}_n\} \cup \{\tilde{\phi}_m\} \quad k = 1, \dots, K = M + N. \quad (17)$$

We now formulate the inverse problem in the framework of functional spaces where the family of acquisition kernels constitutes a set of generating functions of a subspace X_K of X of dimension K (Tarantola & Nercissian, 1984; Bertero et al., 1985). This implicitly assumes that the ζ_k are linearly independent with respect to the retained inner product, i.e. no acquisition kernel can be written as a linear combination of the other kernels. The noticeable instances where this important assumption is not satisfied correspond to situations where several data have been acquired identically, i.e. either at the same location for gravity measurements or with the same position and orientation of the telescope for muon tomography. In such cases the dimension of X_K is reduced since the redundant data may be merged (i.e. averaged) into a single one.

The best density distribution that can be recovered through the inversion process (it is the best because it takes all the information contained in the data and makes the less hypotheses about X_K complementary subspace) is a linear combination of the generating functions,

$$\hat{\rho}(\mathbf{r}) - \rho_0(\mathbf{r}) = \sum_{k=1}^K a_k \times \zeta_k(\mathbf{r}). \quad (18)$$

The components a_k of eq. (18) are obtained by minimizing the quadratic distance ϵ_Y between the data and the corresponding values given by the density model,

$$\epsilon_Y = \|\langle \{\zeta_k\}, \rho - \rho_0 \rangle_X - \{d_k\}\|_Y = \sum_{k=1}^K W_k \times (\langle \zeta_k, \rho - \rho_0 \rangle_X - d_k)^2 \quad (19)$$

Y is the weighted Euclidean space that contains the measurements. The weights W_k permits to introduce prior information about the measurements quality. It is possible to introduce crossed terms W_{ij} if the measurements are not independent, but it is not the case here. We get

$$a_k = \sum_{j=1}^K W_j \times S^{k,j} \times \langle \zeta_j, \rho - \rho_0 \rangle_X \quad (20)$$

where $S^{k,j}$ is the (k, j) component of the Gram matrix inverse defined as $S_{k,j} = W_j \times \langle \zeta_k, \zeta_j \rangle_X$. Using eq. (20), eq. (18) becomes,

$$\hat{\rho}(\mathbf{r}) - \rho_0(\mathbf{r}) = \sum_{k=1}^K \zeta_k(\mathbf{r}) \sum_{j=1}^K W_j \times S^{k,j} \times \langle \zeta_j, \rho - \rho_0 \rangle_X. \quad (21)$$

The presence of $\langle \zeta_j, \rho \rangle_X$ in the right hand part of this equation indicates that the density distribution actually recovered, $\hat{\rho}(\mathbf{r})$, is assembled from projections of the true unknown density, $\rho(\mathbf{r})$, onto the acquisition kernels. The recovered density is a filtered version of the true density distribution, and the filter (i.e. the resolving kernel) depends on the data. This can be made more explicit by rewriting eq. (21) as (Bertero et al., 1985),

$$\hat{\rho}(\mathbf{r}) - \rho_0(\mathbf{r}) = \int_V \Delta(\mathbf{r}, \mathbf{r}') \times (\rho(\mathbf{r}') - \rho_0(\mathbf{r}')) d\mathbf{r}', \quad (22)$$

where we introduce the resolving kernel,

$$\Delta(\mathbf{r}, \mathbf{r}') = \sum_{j=1}^K b_j(\mathbf{r}) \times \tilde{\zeta}_j(\mathbf{r}'), \quad (23)$$

with

$$b_j(\mathbf{r}) = \sum_{i=1}^K W_i \times \zeta_i(\mathbf{r}) \times S^{i,j}, \quad (24)$$

$$\tilde{\zeta}_j(\mathbf{r}') = \int_V w(\mathbf{r}', \mathbf{r}'') \times \zeta_j(\mathbf{r}'') d\mathbf{r}''. \quad (25)$$

$\tilde{\zeta}_j$ is the acquisition kernel ζ_j modulated by the prior information represented by the w function. For instance, w may be an indicator function used to limit the support of the acquisition kernels to the volume of interest.

4. Characterisation of the resolving kernel

A resolving kernel, $\Delta(\mathbf{r}, \mathbf{r}')$, is a function defined in the whole space that plays the role of a spatial filter. When applied to the true density distribution, it gives the reconstructed density. The amplitude and the shape of Δ render the achievable resolution of the reconstructed density structure. According to eq. (23) it is a linear combination of the acquisition kernels. Δ may be characterized in different ways by using several properties to quantify its resolution and anisotropy. These properties should be the least possible dependant to a specific resolving kernel and allow the user to easily appreciate the resolution and its eventual bias. In the present study, we simply compare the resolving kernels against the ideal kernel represented

by a Dirac distribution $\delta(\mathbf{r} - \mathbf{r}')$. This is achieved through the projection γ of $\Delta(\mathbf{r}, \mathbf{r}')$ onto a $\delta(\mathbf{r} - \mathbf{r}')$,

$$\gamma(\mathbf{r}) = \langle \Delta(\mathbf{r}, \mathbf{r}'), \delta(\mathbf{r} - \mathbf{r}') \rangle_X = \int_V w(\mathbf{r}, \mathbf{r}') \times \Delta(\mathbf{r}, \mathbf{r}') d\mathbf{r}' \quad (26)$$

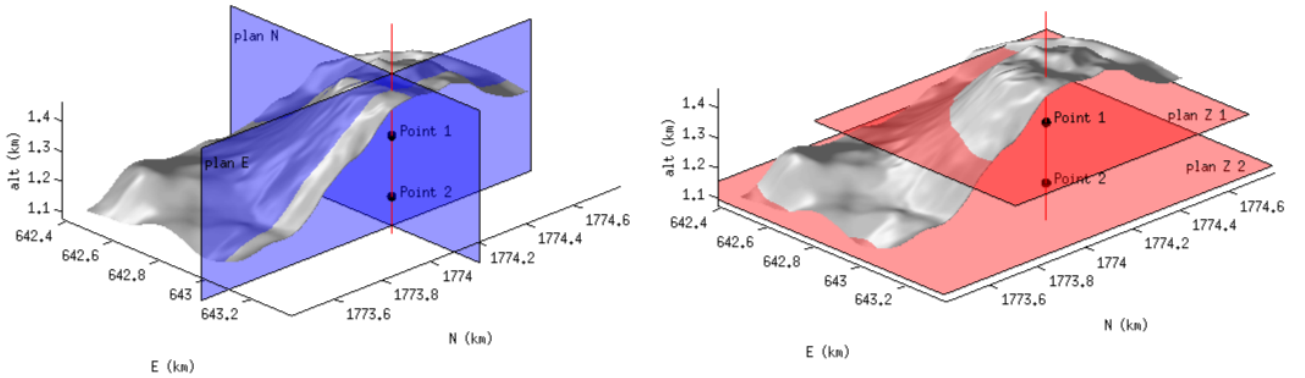
where the X scalar product is defined by eq. (15). Here, the Hamming function is used as the weight function

$$w(\mathbf{r}, \mathbf{r}') = \frac{H_L(\|\mathbf{r} - \mathbf{r}'\|)}{K_w} \times \left[1 + \cos \left(\frac{2\pi \times \|\mathbf{r} - \mathbf{r}'\|}{L} \right) \right] \quad (27)$$

where K_w is a normalising constant, H_L is a rectangular pulse that restricts w to $\|\mathbf{r} - \mathbf{r}'\| \in [-L/2; L/2]$, and $L = 25$ m. If \mathbf{r} or \mathbf{r}' is located outside the volcano we take $w(\mathbf{r}, \mathbf{r}') = 0$. This choice is explained in section 4.4.

We now display resolving kernels corresponding to the data acquisition shown in Fig. 1(a) for muon tomography and in Fig. 1(b) for gravimetry. Muon radiographies are taken from three sites equidistantly located along the Southern edge of the volcano. Gravity measurements are assumed to be done on a regular grid over the entire lava dome.

Accounting for the fact that the acquisition kernels ζ_k are either for gravity or for muon tomography (eq. (16)), we successively consider the case of resolving kernels obtained for muon tomography alone, for gravity data alone, and for a combination of muon tomography and gravity data. We compute $\Delta(\mathbf{r}, \mathbf{r}')$ for two positions $\mathbf{r} = \{\mathbf{r}_1; \mathbf{r}_2\}$ located along a vertical line that goes through the center of the dome (Fig. 5). Points \mathbf{r}_1 and \mathbf{r}_2 are respectively inside and below the volume of the lava dome spanned by the lines of sight of the telescopes (Fig. 1(a)). The parameter γ is computed and plotted on the four characteristic slices represented on Fig. 5.



(a) vertical observation planes

(b) horizontal observation planes

Figure 5. 3D views of the cross-sections used to represent the resolving kernels in figures 6 and 7. The resolving kernels are computed at points 1 and 2. Point 1 is located at a level Z1 in the part of the lava dome scanned by the lines of sight of the muon telescope (Fig. 1(a)) and point 2 is located at Z2 below the ray coverage of the telescope.

4.1. Gravimetry kernels

Fig. 4(b) shows a gravimetry acquisition kernel \mathcal{G} . Remind that the data used in the present study are normalized relatively to a reference model with density ρ_0 (eq. (9)). The gravimetry acquisition kernels are very sensitive to density fluctuations close to the measurement point because of its $1/r^2$ term. The gravity data are actually the component of the gravity field anomaly taken along the local vertical, and the acquisition kernel becomes less and less sensitive as we get closer to the horizontal plane that contains the measurement point.

The gravimetry inverse problem is systematically ill-posed (e.g. Al-Chalabi, 1971) because no matter the number of measurements the resolving kernel mostly integrates information around the measurement positions, i.e. near the surface. An illustration of this problem is given for the resolving kernels of \mathbf{r}_1 and \mathbf{r}_2 (Fig. 6(a),7(a)). For gravimetry inversions it is more realistic to model $\rho(\mathbf{r})$ by a function that depends on a few discrete parameters (even if it means losing the linearity between the data and the measurements) rather than trying a continuous inversion.

Observe that \mathcal{G} integrates the density over the entire volume and provide information for point \mathbf{r}_2 located below the lines of sight of the telescope.

4.2. Muon tomography kernels

Fig. 4(b) shows a typical muon tomography acquisition kernel \mathcal{M} (eq. (12)). It has a conical shape whose aperture angle depends on the distance between the front and the rear detection matrices of the telescope. The apex of the kernel is located at the telescope, and the kernel widens as we move away from the telescope thus the local sensitivity is decreasing. Moreover the triangular shape of the intra-pixel acceptance \mathcal{P}_m (see Fig. 2 and Fig. 3) makes the sensitivity maximum along the main line of sight \mathbf{s}_m .

The Fig. 4(b) shows we are as sensitive to a density change occurring on a few tenth of meters in front of the telescope as to the same change happening on a few hundred of meters beside the volcano. It reveals how deterministic is the telescope position. If one desires to image or monitor a specific region belonging to a bigger structure, the measurement will be much more sensitive if the telescope is in front of it. The important heterogeneities inside the muon tomography acquisition kernels forbid us to use the Radon transform mathematical corpus. For an equivalent resolution and scanning the kernels can be regularized taking the telescope away from the volcano and reducing the angular aperture. We then get into the typical experimental conditions of a medical X-ray tomography. But the consequences are a weaker particle flux (a longer acquisition time) and a greater sensitivity to potential noises. So a compromise has to be found, but the actual lack of understanding of the noises and the already very long acquisition times we are facing lead us to take the telescope the closest we can to the volcano.

We draw the reader's attention to the fact that, despite their compact support, the acquisition kernels overlap each others for neighbour main lines of sight (see Fig. 3). As will be seen below, this characteristic is fundamental to understand the shape of the resolving kernels.

A muon tomography resolving kernel is a linear combination of muon tomography acquisition kernels \mathcal{M} (eq. (23)), and the inversion process optimizes the b_i coefficients to obtain the best density model (eq. (24)). Fig. 6(b) and Fig. 6(c) show the resolving kernel for point \mathbf{r}_1 for different combinations of tomography datasets.

When using data acquired from a single place located at the Southernmost edge of the volcano (Ravine Sud, see Fig. 5(a)), the resolving kernel (Fig. 6(b)) encompasses lines of sight spanning a limited range of azimuths. Consequently, the filtering effect of $\Delta(\mathbf{r}_1, \mathbf{r}')$ integrates ρ along a long narrow cone to give the estimated density $\hat{\rho}(\mathbf{r}_1)$. The fact that $\Delta(\mathbf{r}_1, \mathbf{r}')$ has not a compact support like the \mathcal{M} kernels comes from the overlapping of neighbour acquisition kernels that produces a transfer of information among lines of sight.

When simultaneously using all three muon tomography sites, the resolving kernel includes acquisition kernels that span a wider range of sight azimuths. Consequently, the resolving kernel is more localized onto point \mathbf{r}_1 (Fig. 6(c)). However, the number of radiographies remains small and the kernel has a spider shape visible in the horizontal slice at the far right of Fig. 6(c).

Observe that the resolving kernel $\Delta(\mathbf{r}_2, \mathbf{r}) = 0$ since all acquisition kernels are null in this part of the volcano.

4.3. Joined muon tomography and gravimetry kernels

We now consider resolving kernels computed by using both muon \mathcal{M} and gravity \mathcal{G} acquisition kernels.

Gravimetry does not improve significantly the inversion process at \mathbf{r}_1 , and the resolving kernel $\Delta(\mathbf{r}_1, \mathbf{r}')$ (Fig. 6(d)) looks very similar to the one obtained for the muon radiographies alone (top right of Fig. 6(c)). The information provided by muon tomography is dominant relative to gravimetry excepted at the immediate vicinity of the gravity measurement points.

The situation is very different for point \mathbf{r}_2 where the resolving kernel (Fig. 7(b)) obtained by joining muon radiographies and gravity data appear very different from the gravity kernel (Fig. 7(a)). The most conspicuous effect is that muon data compensates the great sensitivity of gravimetry at near-surface locations by shifting the center of mass of the resolving kernel downward. This considerably improves the vertical resolution achievable in the deepest parts of the volcano.

The conclusions are different if only one tomography acquisition is available. In that case the gravimetry measurements have an impact on the upper part of the dome because they contribute to resolve the ambiguity about the anomaly spatial depth relatively to the acquisition position. But then the zone below the dome will lack data to be properly constrained.

4.4. Impact of prior information

The choice made for the X and Y weight functions $w(\mathbf{r}', \mathbf{r}'')$ (eq. 15) and $W_{i=1\dots K}$ (eq. (19)) has an important influence on the obtained resolving kernels $\Delta(\mathbf{r}, \mathbf{r}')$.

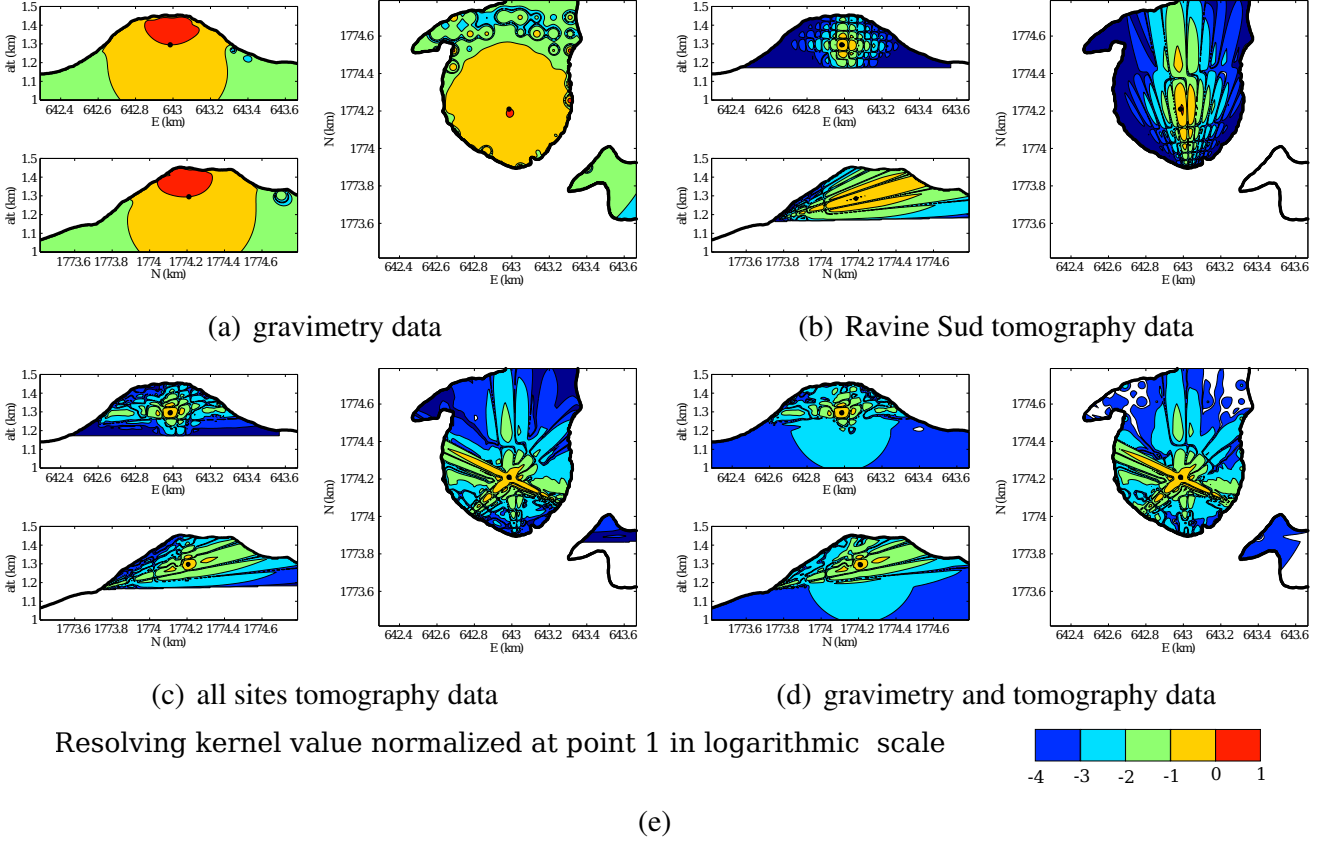


Figure 6. Resolving kernel at point \mathbf{r}_1 (Fig. 5) obtained for the gravity data alone, (a), the Ravine Sud muon tomography alone, (b), all three muon radiographies, (c), and the joined muon and gravity datasets (d). See Fig. 1(b) for the locations of gravity measurements and the three sites for muon radiographies. The resolving kernel absolute value is normalized with reference to the value computed at point \mathbf{r}_1 and represented with a \log_{10} scale.

In the X space, the diagonal term $w(\mathbf{r}', \mathbf{r}'' = \mathbf{r}')$ permits to adjust the local degree of prior knowledge on $\rho(\mathbf{r})$. For instance, $w(\mathbf{r}, \mathbf{r}) = 0$ in regions where $\rho(\mathbf{r})$ is assumed sufficiently well-known to have no impact on our measurements. This corresponds to situations where $\rho_0(\mathbf{r}) = \rho(\mathbf{r})$ and where the concerned regions have not to be accounted for in the inversion process. In our case we use it to cancel the free-air impact on muon tomography and gravimetry, but we can also constrain it to incorporate direct field measurements of the density.

The non-diagonal part $w(\mathbf{r}', \mathbf{r}'' \neq \mathbf{r}')$ may be used to introduce a spatial correlation in ρ . This can be done through $\tilde{\zeta}$ which is the convolution of ζ with w (eq. (25)). Here, we use a simple Hamming function with a 25 m correlation length everywhere in the dome (eq. (27)), and $\tilde{\zeta}$ is a smoothed version of ζ which attenuates the $1/r^2$ effect previously mentioned (for muon tomography it permits to get closer to the X-ray tomography experimental conditions previously detailed). The correlation introduced by the Hamming function increases the acquisition kernels sensitivity further from the measurement point toward the central and the Northern parts of the dome. This produces a better localization of the resolving kernel at \mathbf{r}_2 as can be checked by comparing Fig. 7(c) with Fig. 7(b) where no spatial correlation was applied. The counterpart of this effect is a de-sharpening of the kernel at point \mathbf{r}_2 . w is a regularizing low-pass filter that removes spurious short-wavelength fluctuations in the density model and reduces the ill-conditioning of the inverse problem (e.g. Bertero et al., 1988).

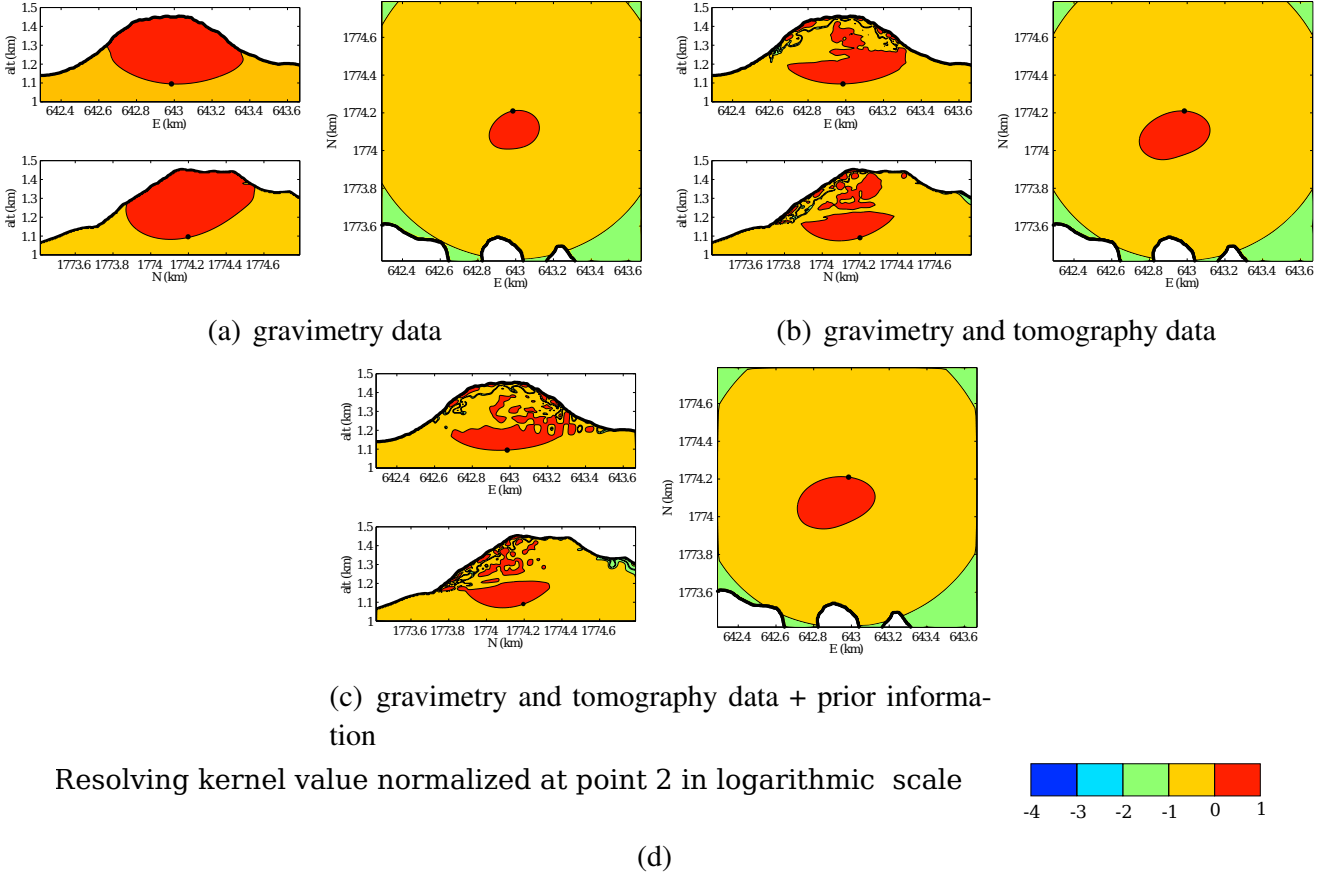


Figure 7. Resolving kernel at point \mathbf{r}_2 (Fig. 5) obtained for the gravity data alone (a) and for the joined muon and gravity datasets (b). Figure (c) is obtained with both muon and gravity datasets and some prior information about the density spatial correlation. See Fig. 1(b) for the locations of gravity measurements and the three sites for muon radiographies. The resolving kernel absolute value is normalized with reference to the value computed at point \mathbf{r}_2 and represented with a \log_{10} scale.

The choice of w is problem-dependent and must be sustained by prior knowledge. The Hamming function acts as a low pass filter with a limited support compatible with the large homogeneous zones observed on the field: massive andesite, hydrothermally altered material and possibly large cavities.

In the Y space, the weights $W_{i=1\dots K}$ allow to assign different quality factors to the available data at one inversion location. For instance, in muon tomography, the W 's permit to account for the fact that all observation axes have not the same integrated acceptance \mathcal{T}_m (Fig. 3). The quality of the gravity data strongly depends on the ground stability (i.e. tilt stability during measurement sequences) and the presence of wind (i.e. vibrations of the gravity-meter). The non-diagonal terms W_{ij} , $i \neq j$ are null as the measurements are independent the ones from the others.

4.5. γ maps

The $\gamma(\mathbf{r})$ index defined in eq. (26) may be used to estimate the resolution achievable everywhere in the volcano. Fig. 8 shows slices of the γ function obtained for the gravity data (left part of Fig. 8) and by joining the three muon tomography data sets together

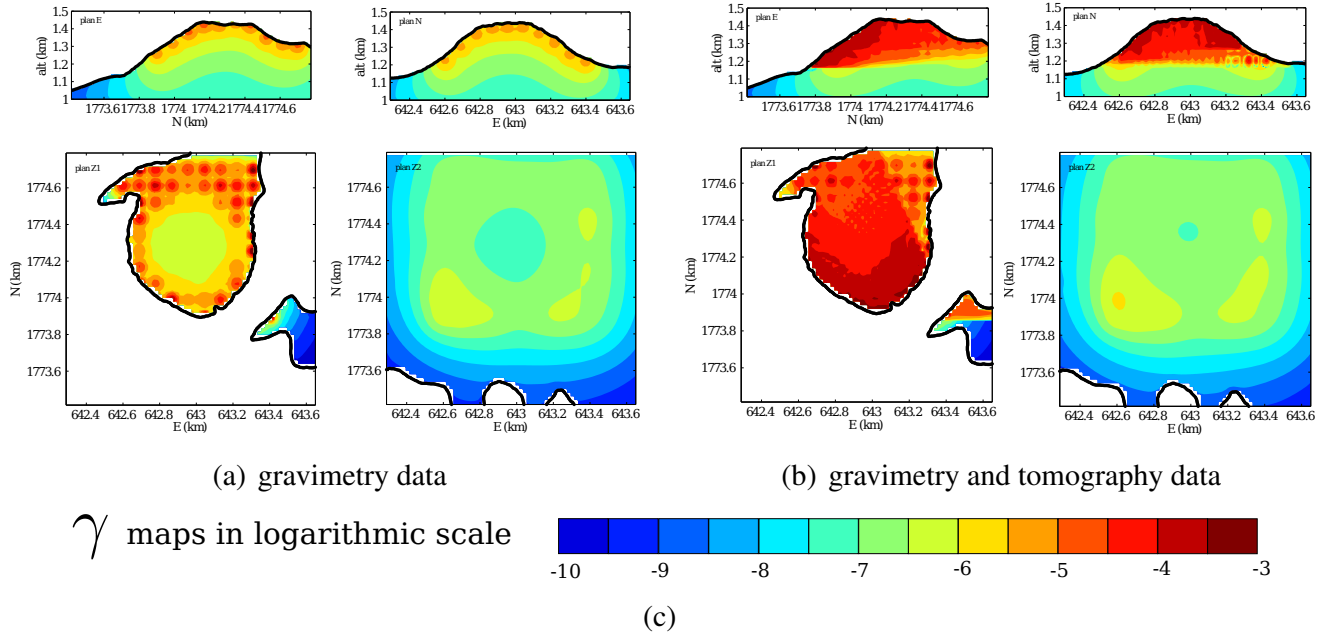


Figure 8. Representation of $|\gamma|$ on the four slices defined in Fig. 5. The results are represented with a \log_{10} scale.

with the gravity measurements (Fig. 8(b)). The gravimetry γ slices clearly reveal the important sensitivity of the data to density variations located in the immediate vicinity of the measurement points and the very low sensitivity to density structure located deeper in the lava dome.

The muon-gravimetry γ slices confirm the results obtained for points $\{\mathbf{r}_1; \mathbf{r}_2\}$ and show the considerable improvement of the resolution obtained when jointly using the muon and gravity datasets. They also reproduce the asymmetric resolution due to the conical shape of the muon acquisition kernels \mathcal{M} . Since the places occupied by the telescope are located along the Southern edge of the volcano, a finer resolution is obtained for the Southern part of the lava dome. This corresponds to the dark-red circular sector visible in the upper horizontal slice in Fig. 8(b). As expected, the resolution is coarser in the central and Northern parts of the dome. The same slice shows that the North-Eastern region of the volcano is resolved by the gravity data alone since no lines of sight of the telescope cross this part of the dome.

The γ map is a useful tool to plan an acquisition survey. One can easily compute how γ is changed with different possible measurement campaigns and select the most pertinent one depending on the region of interest, the available time on the field and the accessibility of the site. This choice is critical as muon tomography acquisitions are long (a few weeks) and gravity measurements delicate. It can also be used to design a mesh for the problem. The meshing elements density can roughly follow the γ map fluctuations.

We emphasize that other definitions may be used for γ and that a single index may prove insufficient to characterize the shape of resolving kernels. Consequently, we recommend to perform a 3D examination of individual resolving kernels at locations of particular importance (i.e. like detecting places where density changes occur).

5. Conclusion

The resolving kernel analysis discussed in the present study allows to quantitatively assess the way by which gravity data and density muon radiographies may be joined to reconstruct the density distribution inside geological bodies. A main result concerns the improvement of the resolution obtained in the deep regions of the density model when joining muon and gravity data, and despite the fact that these regions are not sampled by muon tomography. Part of the information brought by the muon data is transferred to the deep regions of the model through the long-range coupling of the gravity acquisition kernels (Fig. 4(a)) used to construct the joined resolving kernels (eq. (23)).

The compact support of the muon acquisition kernels (Fig. 4(b)) allows muon tomography to obtain high-resolution models of the density structure of La Soufrière but restricted to the upper part of the dome. Gravimetry cannot be used on its own to make a proper continuous inversion because it is too sensitive to the very close subsurface. Therefore coupling the two techniques does not lead to significant improvement of the density model in regions where muon data are available (compare Fig. 6(c) and Fig. 6(d)).

The muon tomography acquisition kernel has a conic shape, and noise considerations obligate us to put the cone apex just in front of the studied structure. It results in a large decrease of the sensitivity between the front and the rear of the volcano. This problem adds to the heterogeneous tomography sampling and forbids us to use the standard Radon transform usually adopted in X-ray tomography medical experiments to inverse the density. It also shows how deterministic is the telescope position if one desires to image or monitor a specific region belonging to a bigger body.

The positive weight function w of the inner product (eq. (15)) may be used to introduce prior information both by limiting the support of the density distribution to reconstruct and by introducing a spatial correlation smoothing the $1/r^2$ effect of muon tomography and gravimetry acquisition kernels. This extends the range of sensitivity of the measurements and results in a solution with a more homogeneous quality.

Finally the γ maps give an overview of the resolving kernel geometry everywhere in the dome which can easily be used to optimally plan future acquisition surveys with respect to data already available.

acknowledgments

This study is part of the ANR-14-CE04-0001 DIAPHANE project. We acknowledge the financial support from the UnivEarthS Labex program of Sorbonne Paris Cité (ANR-10-LABX-0023 and ANR-11-IDEX-0005-02). This study also received funding from Swisstopo through the Mont-Terri MD Project. This is IPGP contribution ****.

References

- [1] Al-Chalabi, M., 1971. Some studies relating to non-uniqueness in gravity and magnetic inverse problems. *Geophysics*, **36**, 835–855.

- [2] Barrett, P.H., Bollinger, L.M., Cocconi, G., Eisenberg, Y. & Greisen, K., 1952. Interpretation of Cosmic-Ray Measurements Far Underground, *Rev. modern Phys.*, **24**, 133–178.
- [3] Bertero, M., De Mol, C., & Pike, E.R., 1985. Linear inverse problems with discrete data. I. General formulation and singular system analysis, *Inv. probl.*, **1**, 301.
- [4] Bertero, M., De Mol, C., & Pike, E.R., 1988. Linear inverse problems with discrete data: II. Stability and regularisation. *Inv. probl.*, **4**, 573.
- [5] Caffau, E., Coren, F. & Giannini, G., 1997. Underground cosmic-ray measurement for morphological reconstruction of the Grotta Gigante natural cave, *Nucl. Instrum. Methods A*, **385**, 480–488.
- [6] Cârloganu, C., Niess, V., Bene, S., Busato, E., Dupieux, P., Fehr, F., Gay, P., Miallier, D., Vulpescu, B., Boivin, P., Combaret, C., Labazuy, P., Laktineh, I., Lenat, J.-F., Mirabito, L. & Portal, A., 2012. Towards a muon radiography of the Puy de Dôme, *Geosci. Instrum. Method. Data Syst.*, **2**, 765–780.
- [7] Davis, K. & Oldenburg, D.W., 2012. Joint 3D of muon tomography and gravity data to recover density, *ASEG Extended Abstracts*, **1**, 1–4.
- [8] Gaisser, T. & Stanev T., 2008. Cosmic Rays, *Phys. Lett. B*, **667**, 254–260, doi:10.1016/j.physletb.2008.07.028.
- [9] Gibert, D., Beauducel, F., Déclais, Y., Lesparre, N., Marteau, J., Nicollin, F. & Tarantola, A., 2010. Muon tomography: Plans for observations in the Lesser Antilles, *Earth Planets Space*, **62**, 153–165.
- [10] Jourde, K., D. Gibert, J. Marteau, J. Bremond d’Ars, S. Gardien, C. Girerd, JC. Ianigro, and D. Carbone, 2013. Experimental detection of upward going cosmic particles and consequences for correction of density radiography of volcanoes, *Geophys. Res. Lett.*, **40-24**, 6334–6339.
- [11] Lesparre, N., Gibert D., Marteau J., Déclais Y., Carbone D. & Galichet E., 2010. Geophysical muon imaging: feasibility and limits, *Geophys. J. Int.*, **183**, 1348–1361.
- [12] Lesparre, N., D. Gibert & J. Marteau, 2012a. Bayesian Dual Inversion of Experimental Telescope Acceptance and Integrated Flux for Geophysical Muon Tomography, *Geophys. J. Int.*, **188**, 490–497, doi: 10.1111/j.1365-246X.2011.05268.x.
- [13] Lesparre, N., J. Marteau, Y. Déclais, D. Gibert, B. Carlus, F. Nicollin & B. Kergosien, 2012b. Design and Operation of a Field Telescope for Cosmic Ray Geophysical Tomography, *Geosci. Instrum. Method. Data Syst.*, **1**, 33–42.
- [14] Lesparre, N., D. Gibert, J. Marteau, J.-C. Komorowski, F. Nicollin & O. Coutant, 2012c. Density Muon Radiography of La Soufrière of Guadeloupe Volcano: Comparison with Geological, Electrical Resistivity and Gravity data, *Geophys. J. Int.*, **190**, 1008–1019.
- [15] Marteau, J., D. Gibert, N. Lesparre, F. Nicollin, P. Noli, F. Giacoppo, 2011. Muons tomography applied to geosciences and volcanology, *Nucl. Instr. Methods A*, doi: 10.1016/j.nima.2011.11.061.
- [16] Nagamine, K., 1995a. Geo-tomographic observation of inner-structure of volcano with cosmic-ray muons, *J. Geography*, **104**, 998–1007.
- [17] Nagamine, K., Iwasaki, M., Shimomura, K. & Ishida, K., 1995b. Method of probing inner-structure of geophysical substance with the horizontal cosmic-ray muons and possible application to volcanic eruption prediction, *Nucl. Instr. Meth. A*, **356**, 585–595.
- [18] Nagamine, K., 2003. *Introductory Muon Science*, 208 pp, Cambridge University Press, Cambridge UK.
- [19] Nishiyama, R., Tanaka, Y., Okubo, S., Oshima, H., Tanaka, H. & Maekawa, T., 2014. Integrated processing of muon radiography and gravity anomaly data toward the realization of highresolution 3D density structural analysis of volcanoes: Case study of ShowaShinzan lava dome, Usu, Japan. *J. Geophys. Res. Solid Earth*, **119**, 699–710.
- [20] Portal, A., Labazuy, P., Lénat, J.-F., Béné, S., Boivin, P., Busato, E., Cârloganu, C., Combaret, C., Dupieux, P., Fehr, F., Gay, P., Laktineh, I., Miallier, D., Mirabito, L., Niess, V. & Vulpescu, B., 2013. Inner structure of the Puy de Dôme volcano: cross-comparison of geophysical models (ERT, gravimetry, muon imaging), *Geosci. Instrum. Method. Data Syst.*, **2**, 47–54.
- [21] Shinohara, H. & Tanaka, H., 2012. Conduit magma convection of a rhyolitic magma: Constraints from cosmic-ray muon radiography of Iwodake, Satsuma-Iwojima volcano, Japan, *Earth and Planet. Sci. Lett.*, **349–350**, 87–97.
- [22] Tanaka, H., Nagamine, K., Kawamura, N., Nakamura, S.N., Ishida, K. & Shimomura, K., 2001.

Development of the cosmic-ray muon detection system for probing internal-structure of a volcano, *Hyperfine Interact.*, **138**, 521–526.

- [23] Tanaka, H., Nagamine, K., Nakamura, S.N. & Ishida, K., 2005. Radiographic measurements of the internal structure of Mt. West Iwate with near horizontal cosmic ray muons and future developments, *Nucl. Instrum. Methods A*, **555**, 164–172.
- [24] Tanaka, H., Nakano, T., Takahashi, S., Yoshida, J., Ohshima, H., Maekawa, T., Watanabe, H. & Niwa, K., 2007a. Imaging the conduit size of the dome with cosmic ray muons: the structure beneath Showa Shinzan Lava Dome, Japan, *Geophys. Res. Lett.*, **34**, L22311, doi: 10.1029/2007GL031389.
- [25] Tanaka, H., Nakano, T., Takahashi, S., Yoshida, J., Takeo, M., Oikawa, J., Ohminato, T., Aoki, Y., Koyama, E., Tsuji, H. & Niwa, K., 2007b. High resolution imaging in the inhomogeneous crust with cosmic-ray muon radiography: The density structure below the volcanic crater floor of Mt. Asama, Japan, *Earth planet. Sci. Lett.*, **263**, 104–113.
- [26] Tanaka, H., Nakano, T., Takahashi, S., Yoshida, J., Takeo, M., Oikawa, J., Ohminato, T., Aoki, Y., Koyama, E., Tsuji, H., Ohshima, H., Maekawa, T., Watanabe, H. & Niwa, K., 2008. Radiographic imaging below a volcanic crater floor with cosmic-ray muons, *American J. Science*, **308**, 843–850.
- [27] Tanaka, H., Uchida, T., Tanaka, M., Shinohara, H. & Taira, H., 2009a. Cosmic-ray muon imaging of magma in a conduit: Degassing process of Satsuma-Iwojima Volcano, Japan, *Geophys. Res. Lett.*, **36**, L01304.
- [28] Tanaka, H., Uchida, T., Tanaka, M., Takeo, M., Oikawa, J., Ohminato, T., Aoki, Y., Koyama, E. & Tsuji, H., 2009b. Detecting a mass change inside a volcano by cosmic-ray muon radiography (muography): First results from measurements at Asama volcano, Japan, *Geophys. Res. Lett.*, **36**, L17302, doi:10.1029/2009GL039448.
- [29] Tanaka, H. K., 2013. Subsurface density mapping of the earth with cosmic ray muons, *Nuclear Physics B-Proceedings Supplements*, **243**, 239–248.
- [30] Tang, A., Horton-Smith, G., Kudryavtsev, V.A. & Tonazzo, A., 2006. Muon simulations for Super-Kamiokande, KamLAND, and CHOOZ, *Phys. Rev. D*, **74**, 053007, doi:10.1103/PhysRevD.74.053007.
- [31] Tarantola, A. & Nercissian, A., 1984. Three-dimensional inversion without blocks, *Geophys. J. Int.*, **76**, 299–306.

Bibliographie

- [1] Auto-triggerable HPD sensors fully readout on ethernet : applications for high-energy physics and medical imaging, S.Katsanevas, G.Largerou, J.Marteau, G.Moret, Nucl. Instrum. Meth. A **504** (2003) 103.
- [2] Two-head small animal PET prototype with LSO/LuAP coupled to a multi-anode PMT R.Barbier, Y.Déclais, C.Dujardin, N.Garnier, M.Janier, I.A.Kamenkikh, G.Largerou, J.Marteau, C.Pédrini, D.Sappey-Marinié, , NIM A 527 (2004) 175-179.
- [3] The ClearPET project : development of a 2nd generation high-performance small animal PET scanner Nuclear Instruments and Methods in Physics Research Section A : Accelerators, Spectrometers, Detectors and Associated Equipment, Volume 537, Issues 1-2, 21 January 2005, Pages 307-311, K. Ziemons et al.
- [4] Muon Tomography : Plans for Observations in the Lesser Antilles, D.Gibert, F. Beauducel, Y.Déclais, N.Lesparre, J.Marteau, F.Nicollin, A.Tarantola, Earth Planets and Space, Vol. 52, 153-165, 2010.
- [5] The MU-RAY project : Summary of the round-table discussions, Beauducel, F. et al, Earth Planets and Space, Vol. 52, 145-151, 2010.
- [6] Geophysical muon tomography : feasibility and limits, N.Lesparre, D.Gibert, J.Marteau, Y.Déclais, D.Carbone, E.Galichet, Geophysical Journal International, Vol. 183, 1348-1361, 2010.
- [7] Muons tomography applied to geosciences and volcanology, J. Marteau, D. Gibert, N. Lesparre, F. Nicollin, P. Noli, F. Giacoppo, Nucl. Instrum. Meth. A **695** (2012) 23.
- [8] Bayesian Dual Inversion of Experimental Telescope Acceptance and Integrated Flux for Geophysical Muon Tomography, N. Lesparre, D. Gibert & J. Marteau, Geophysical Journal International, Vol. 188, 490-497, 2012.
- [9] Design and Operation of a Field Telescope for Cosmic Ray Geophysical Tomography, Lesparre, N., J. Marteau, Y. Déclais, D. Gibert, B. Carlus, F. Nicollin & B. Kergosien, Geosci. Instrum. Method. Data Syst., 1, 33-42, 2012.
- [10] Density muon radiography of La Soufrière of Guadeloupe volcano : comparison with geological, electrical resistivity and gravity data, N. Lesparre, D. Gibert, J. Marteau, F. Nicollin, O. Coutant & J.-C. Komorowski, Geophys. J. Int. (2012) 190, 1008-1019.
- [11] Background noise estimations in geophysical muon tomography experiments, N. Lesparre, J. Marteau & D. Gibert, Geosci. Instrum. Method. Data Syst., in preparation.
- [12] An experiment of muon imaging at Mt. Etna (Italy), Carbone, D., Gibert, D., Marteau, J., Diamant, M., Zuccarello, L., Galichet, E., Geophys. J. Int., Volume 196, issue 2, pages 633-643, 2014.
- [13] Effects of upward-going cosmic muons on density radiography of volcanoes, Jourde, K., D. Gibert, J. Marteau, J. de Bremond d'Ars, S. Gardien, C. Girerd, J.-C. Ianigro & D. Carbone, Geophysical Research Letters, accepted, 2014 [arXiv :1307.6758].

- [14] Implementation of sub-nanoseconds TDC in FPGA : applications to time-of-flight analysis in muon radiography, Marteau, J., J. de Bremond d'Ars, D. Gibert, K. Jourde, S. Gardien, C. Girerd, J.-C. Ianigro,, IOP Measurement Science and Techniques, Measur. Sci. Tech. **25** (2014) 035101 [arXiv :1310.4281].
- [15] Improvement of density models of geological structures by fusion of gravity data and cosmic muon radiographies, K. Jourde *et al.*, gi-2015-3, submitted [arXiv :1411 :5146].

Conclusions

C'est peu de dire que la physique des neutrinos a connu de profondes métamorphoses depuis le temps où j'ai eu l'opportunité, sur une idée originale de J.Delorme et M.Ericson, de débiter une thèse qui m'ouvrait les portes de ce domaine de recherche. De ce qui n'était alors qu'une somme d'"anomalies" – des neutrinos atmosphériques, des neutrinos solaires, de LSND par rapport à KARMEN etc – à la connaissance actuelle des paramètres de la matrice PMNS, que de changements radicaux ! Et quelle chance d'avoir pu assister de si près, et parfois d'en être un acteur parmi tant d'autres collègues, à de tels progrès. L'affirmation de l'existence des oscillations de neutrinos atmosphériques par Super-Kamiokande à la fin du siècle dernier ouvre une voie prometteuse. Dans laquelle s'engouffre SNO et KamLAND pour apporter un éclairage neuf sur les neutrinos solaires. Puis K2K qui lance l'ère des expériences d'oscillations sur faisceau à longue distance (*long baseline*). Et qui observe au passage la disparition des neutrinos muoniques du faisceau, dans le domaine de paramètres des neutrinos atmosphériques.

Je me souviens des discussions passionnées sur l'orientation à donner aux programmes "neutrinos" du début des années 2000. Des "branching point" et des "smoking gun" qui devaient guider l'orientation des expériences, leur *design* ainsi que celui des faisceaux source. Quel projet pousser ? Dans quelle collaboration s'engager ? Les programmes américains et européens se sont dessinés progressivement et nous avons vécu l'entrée sous terre de MINOS d'abord et d'OPERA ensuite. Des faisceaux NuMI et CNGS. Deux stratégies différentes, le mode "disparition" pour la première, impliquant un détecteur proche et un détecteur lointain. Le mode "apparition" pour la seconde, avec un unique détecteur lointain, optimisé pour la mesure du produit de l'oscillation et théoriquement sans bruit de fond. Une statistique importante dans un cas, une mesure d'événements très rares dans le second. Le choix d'OPERA, des émulsions comme trajectographe ultra-fin, de son mode opératoire hors norme plutôt qu'ICARUS, précurseur d'une branche de détecteurs très grand volume candidats au futur, s'est fait sur des critères objectifs de faisabilité. Mais aucune des deux expériences du programme CNGS n'était réellement aisée à opérer.

La construction du détecteur OPERA, de la structure mécanique porteuse reposant sur les deux spectromètres aimantés, au remplissage des murs de briques s'étalera de 2003 à 2007. Les premiers neutrinos parviendront en août 2006, après le gel complet des faisceaux du CERN en 2005, et seront interrompus en 2007 du fait d'un défaut de protection au niveau de la cible du CNGS. Du premier run de physique en 2008 jusqu'aux derniers neutrinos en décembre 2012, il aura fallu être sur la brèche, *on-call*, pour s'assurer que la prise de données se déroulait correctement. Que les neutrinos μ arrivaient à heure fixe, et dans les proportions attendues. Contrairement à d'autres projets que j'ai connus depuis, le *staff* était relativement pauvre en nombre et les *shifts* sur le détecteur très légers.

Mais que dire de la satisfaction ressentie quand le système que vous avez développé en équipe, avec des collègues proches et impliqués, peu nombreux au regard de l'ampleur de la tâche et de la lourdeur de la responsabilité, répond sans relâche et fournit les données attendues par la totalité

de la collaboration. Quand toutes les heures passées en réunion et sur le détecteur, à câbler, tester, réparer, prennent un sens et que les premiers *display* d'événements vous permettent enfin de voir le neutrino jusqu'ici théorique et abstrait. Que les premières analyses vous permettent d'isoler les neutrinos des cosmiques et sont donc la promesse que, malgré les innombrables crises traversées au cours de ce projet, sur les émulsions, le plomb, la remise aux normes du laboratoire du Gran Sasso en plein montage de l'expérience, la désaffectation du CERN, la panne massive du CNGS, la course après les *p.o.t.* et les statistiques, la saga de la mesure de la célérité des neutrinos, le projet pourrait aller à son terme.

Qu'il me soit permis de dire ici concernant la vitesse des neutrinos, que ce fut une expérience tout à fait singulière et instructive, dans laquelle la naïveté plus ou moins réelle des scientifiques a du composer avec celle, plus ou moins feinte, du monde de la communication. Et comment elle a permis de faire tomber un grand nombre de masques. Même si ce n'était évidemment pas le but au moment de la proposition de cette mesure, comme sous-produit des oscillations. Un devoir presque, quand on connaît les sommes engagées sur un tel projet et le prix de revient d'un neutrino τ . Un devoir de physicien que peu de gens auraient pu mener à bien et qu'il a fallu justifier encore et encore, face à l'emballlement de la machine médiatique. En plus des heures passées à techniquement comprendre et tenter de reproduire les mesures. Le plus frustrant étant de ne pas avoir vraiment pu reproduire l'erreur même si le poste défaillant a été identifié. La mesure d'OPERA reste la plus précise à ce jour. Il est bon aussi de le rappeler, car c'était le but de cette mesure.

Je reprends le fil de l'histoire des neutrinos, avec les premières mesures précises de MINOS des paramètres du secteur atmosphérique. Et enfin le premier ν_τ sur OPERA. En 2010. La première véritable apparition d'un neutrino après oscillation. Mesurer les paramètres d'un modèle nous apporte toujours une grande confiance en lui. C'est un peu le fond de commerce du Modèle Standard. Mais "voir" le phénomène lui donne toujours une autre dimension. Un pas important donc. Comme celui qui sera franchi en 2012 avec la double mesure de l'angle θ_{13} . Même dialectique que précédemment : une fois en mode "disparition" avec Daya Bay, une fois en mode "apparition" avec T2K. Quelle excitation, là encore ! Et un clin d'oeil forcément pour CHOOZ qui avait posé une limite juste au-dessus de la valeur mesurée in fine. Pour Y. Déclais dont l'implication dans OPERA et dans le groupe Neutrinos de l'IPNL a été déterminante. Limite qui a pesé presque autant qu'une découverte dans toutes les analyses de la décennie précédente. Et le tableau est donc complet, les angles de mélange sont tous mesurés et re-mesurables. L'ère de la métrologie fine peut commencer. Ainsi que celle de la recherche des effets d'ordre supérieur, la violation de CP dans le secteur leptonique, si elle existe, et la détermination de la hiérarchie de masse.

Le futur de la physique des neutrinos est donc probablement plus proche qu'on le pensait il y a peu. Peut-être accessible avant la mise au point des *neutrino factory*. Mais les défis posés par les neutrinos sont toujours aussi grands et les possibilités de dévisser toujours aussi réelles. WA105, démonstrateur d'un futur LBNO, est la prochaine étape vers cette prochaine génération d'expériences. L'argon liquide comme milieu actif et les défis technologiques qui l'accompagnent. Une ère dans laquelle les acteurs industriels sont impliqués dès la genèse du projet. Peut-être un changement de paradigme dans le domaine.

Plus précisément le projet LAGUNA-LBNO prévoit la recherche de la violation CP et la mesure de la hiérarchie de masse grâce aux oscillations de neutrinos entre le CERN et la Finlande (Pyhäsalmi, 2300km de distance), dans le canal $\nu_\mu \rightarrow \nu_e$. Il est prévu d'installer un détecteur lointain massif (20ktonnes puis 50ktonnes), chambre à projection temporelle géante à argon liquide. L'IPNL est impliqué dans la simulation, la mise au point des outils d'analyse et de reconstruction des événements et dans la R&D sur le système de lecture de la charge : développement d'une électronique froide pour la lecture du signal en charge dans la phase argon gazeuse et développement d'une

chaîne d'acquisition autonome. Cette dernière, au format télécommunications micro-TCA, haut-débit (10GbE ou PCI-express), envoie les données brutes, sans perte, vers des cartes de traitement munies de FPGA (et programmées dans un environnement de type OpenCL). A court terme le projet WA105 (dont le démarrage est prévu en 2016 dans la zone ouest du CERN), démonstrateur (6m x 6m x 6m) représentant 1 :20 du détecteur final, doit permettre de valider le concept final. Il est donc prévu que le système proposé par l'IPNL, et retenu par la collaboration, soit validé. Le projet LBNO, tel que prévu au terme du *design study*, est le seul programme qui propose la mesure à la fois de la hiérarchie de masse et la recherche de la violation de CP. Ce représentant de la génération "mégatonne" remplit le cahier des charges, exigeant, en terme de sensibilité et doit s'inscrire, d'une façon ou d'une autre, en collaboration avec certains projets, en compétition avec d'autres, dans le paysage des grands projets de physique des hautes énergies.

Le chemin est donc encore long vers une compréhension complète des mécanismes opérant dans le secteur des neutrinos. Et les inconnues systématiques telles que les sections efficaces jouent un rôle déterminant. Dans ce domaine également les progrès ont été notables, depuis l'époque pionnière où certains physiciens mettaient en doute la pertinence d'une telle étude et du *revival* des résonances Delta dans le milieu nucléaire. À l'heure où j'écris ces lignes, il n'est plus question de douter de l'importance du calcul, de la simulation et enfin des mesures, des sections efficaces neutrino-noyau, dans un domaine d'énergie où les effets nucléaires jouent un rôle important. Je me souviens là encore de discussions parfois surprenantes sur le gaz de Fermi, en session plénière de *workshop* dédié aux interactions neutrino-noyau. Sur l'implémentation de ce modèle simple dans des simulations Monte-Carlo de collaborations de premier plan. Le modèle de Lyon, basé sur le formalisme des réponses nucléaires, a prouvé avec le temps toute sa pertinence. L'approche semi-classique, analytique, permet en effet de se confronter rapidement aux résultats expérimentaux, peu nombreux au moment de ma thèse, et qui commencent à affluer maintenant avec un nombre croissant de programmes qui incluent un volet "sections efficaces" (MiniBooNE, T2K, Minerva etc). Après avoir durant ma thèse développé ce modèle en collaboration avec le groupe Théorie, et mis au point tous ses aspects techniques, j'ai pu transmettre le flambeau et participer à sa renaissance quelques années après ma soutenance. Actuellement ce modèle a une place reconnue dans ce domaine spécifique et les phénomènes qu'il met en évidence, tels que l'importance des effets collectifs et des excitations multi-nucléon $np - nh$, sont pris en compte (ou tentent de l'être) dans les simulateurs. Les futurs projets utilisant l'argon liquide devraient rapidement inclure les effets de telles prédictions dans leur simulation.

Dans la séquence *Je me souviens* mes souvenirs ne sont pas entièrement tournés vers les neutrinos, même si c'est indirectement par leur entremise que j'ai eu la chance de découvrir d'autres domaines, dits trans-disciplinaires. Et de pouvoir me confronter à d'autres problématiques physiques, d'autres difficultés conceptuelles sur des systèmes complexes biologiques ou géophysiques. Après une R&D très enrichissante sur l'imagerie médicale, qui m'a permis de comprendre également la complexité inhérente à la confrontation du monde universitaire à celui des objectifs industriels, c'est surtout dans le domaine des géosciences que je me suis investi. Un domaine à la frontière entre plusieurs champs de recherche, entre plusieurs instituts, et qui a même reçu un nom, celui des "géoparticules".

Le projet DIAPHANE est maintenant dans une phase stable où les procédures, les méthodes et les détecteurs sont bien maîtrisés. Il a fallu environ cinq ans pour parvenir à ce stade de maturité avec le retour des différents terrains explorés (laboratoires souterrains, volcans actifs, tests méthodologiques en labo). Les retours sur les volcans actifs en particulier permettent de penser que cette discipline, encore totalement exploratoire au moment du démarrage du projet, peut intégrer à court terme le parc des méthodes de surveillance et d'alerte. La collaboration avec les géophysiciens a permis d'aller bien au-delà d'un simple transfert de technologie et/ou de savoir-faire. Actuellement la complémentarité des approches "physique des particules" et "géophysique" permet de valider des modèles

complets allant des générateurs de cosmiques au modèle numérique de terrain.

Le projet DIAPHANE peut donc raisonnablement s'orienter vers des applications plus fines telles que l'inversion 3D, le couplage avec les autres méthodes géophysiques (couplage gravimétrie-muons, résistivité-muons etc), le *monitoring* en temps réel des dômes volcaniques etc. Ce dernier aspect revêt un aspect primordial tant la dimension sociétale de cette recherche est importante, la plupart des volcans étudiés se situant non loin de zones densément peuplées. Le projet en a désormais les moyens avec le soutien de l'ANR, qui fait suite à diverses contributions de nos instituts référents (INSU et IN2P3) et à des contributions ponctuelles (collaborations avec le laboratoire du Mont-Terri, avec l'observatoire de Singapour, avec l'IRSN). Les cibles d'étude vont se concentrer sur l'arc antillais (Soufrière de Guadeloupe et de Montserrat) et tandis que l'on pense conforter les collaborations actuelles. Une expérience exploratoire à Montserrat, dont le volcan est en fin d'éruption et le dôme "tout neuf" permettra de contraindre les modèles d'évolution des volcans depuis leur origine. L'étude actuelle du Mayon va s'orienter vers une étude dédiée du sommet et focaliser sur la sortie du cratère pour corrélérer l'évolution du plume (panache volcanique) avec la répartition en densité proche de l'ouverture. Mais c'est bien la Soufrière de Guadeloupe, particulièrement active, qui reste la cible principale, avec une extension du nombre de détecteurs disposés sur le pourtour du dôme. Enfin d'autres applications en géosciences, au-delà des problématiques de stockage longue durée (laboratoires souterrains du Mont-Terri et de Tournemire) et d'étude des dômes volcaniques (Soufrière, Etna, Mayon), sont prévues, comme les applications en forage (recherche minière, étude des systèmes hydrothermaux proches de la surface etc) ou en génie civil.

Les projets ne manquent pas, preuve de la vitalité des domaines multi-disciplinaires et de la très grande capacité de métamorphoses du neutrino, capable d'oscillations au-delà du domaine des astroparticules.